Some Problems In Hot Rolling Of Al-Alloys Solved By The Finite Element Method

XINJIAN DUAN

A thesis submitted in partial fulfilment of the requirements of Bournemouth University for the degree of Doctor of Philosophy

November 2001

Bournemouth University

Abstract

This thesis is focused on employing the finite element method (FEM) to simulate hot flat rolling process. The relevant work involves selecting a suitable constitutive equation, predicting the rolling load and roll torque, computing temperature changes and lateral deformation, simulating the evolution of substructure, modelling static recrystallisation and designing the rolling pass schedule.

A practical pass schedule supplied by an aluminium company and containing reliable measured data of roll load and torque is analysed by a commercial 3-D thermomechanical coupled FEM program FORGE3 V5.3. The inverse analysis method is adopted to obtain the friction coefficient and heat transfer coefficient. The distribution of pressure, equivalent strain, the stress and damage in the roll gap in breakdown rolling are discussed. The changes of temperature and lateral profile under both laboratory and industrial rolling conditions are computed and compared with experimental measurements, the differences are then investigated. Through applying the Taguchi experimental design method, the influence of each rolling parameter on the spread, i.e. the ratio of width to thickness, the roll radius to thickness, the thickness reduction, and the deformation temperature, the relative contribution of each control parameter is quantitatively estimated and expressed as a percentage. A new spread formula is built up based on a large amount of FE analyses. The new formula is able to deal with both laboratory and industrial rolling conditions with high accuracy.

Critical reviews are presented for the previous work in the modelling of subgrain size and static recrystallisation. Both empirical and physical models are applied to investigate the evolution of subgrain size, dislocation density, misorientation and the flow stress in the roll gap. The predicted subgrain size agrees very well with the experimental measurement. The difference between the use of two models are illustrated and analysed. Studies on modelling of static recrystallisation are carried

out by incorporating the plastomechanical parameters, i.e. strain, strain rate and temperature, into empirical model. Various approaches are proposed to reduce the predicted volume fraction recrystallised at the surface and are verified by the comparison with measurement. Simulation results show that some of the previous work reported in the literature are erroneous. Further work in the modelling of static recrystallisation and texture evolution is detailed. The Taguchi experimental method is also applied to study the influence of the rolling parameters on the fraction recrystallised (X_V). The study shows that rolling temperature has the greatest influence on the X_V, followed by the parameter H_m/L. The roll temperature and roll speed have little influence on the X_V.

Designing a rational rolling pass schedule is critical for the control of strip profile and product quality. In the present thesis, the procedure of designing a rolling pass schedule is illustrated. The formulae used in scheduling are listed and explained. The scheduling program is then performed to check with two existing industrial schedules. The comparison shows that the rolling load, temperature and power model is reliable and shows high accuracy. A multipass simulation by the use of finite element method is also carried out and the results are compared with various model predictions. The problems in the simulation are illustrated and explained.

CONTENTS

List of Figures

List of Tables

List of Publications

Refereed papers

1. X. Duan and T. Sheppard. Prediction of temperature evolution by FEM during multi-pass hot flat rolling of aluminium alloys. Modelling and Simulation in Materials Science and Engineering. 9(6), 2001, 525-538.
2. X. Duan and T. Sheppard. Modelling of subgrain evolution of aluminium alloys under hot working conditions. Aluminum Transaction. 5 (1), 2001.
3. X. Duan and T. Sheppard. Lateral deformation during the hot flat rolling of aluminium alloys. Materials Science and Technology. May, 2002.
4. X. Duan and T. Sheppard. Shape optimisation using FEA software: a v-shaped anvil as an example. Journal of Materials Processing Technology. 120(1-3), 2002, 426-431.
5. X. Duan and T. Sheppard. Three dimensional thermal mechanical coupled simulation during hot rolling of aluminium alloy 3003. International Journal of Mechanical Sciences. (Submitted).
6. X. Duan and T. Sheppard. Computation of substructural strengthening by the integration of metallurgical models into finite element code. Computational Materials Science. (Submitted).
7. X. Duan and T. Sheppard. Factors involved in pass schedule design for hot flat rolling of aluminium alloys. Modelling and Simulation in Materials Science and Engineering. (Submitted).
8. X. Duan and T. Sheppard. Some problems in the modelling of static recrystallisation. Material science and Technology.(Submitted).
9. X. Duan and T. Sheppard. Influence of forming parameters on static recrystallisation behaviour during hot rolling aluminium alloys. Modelling and Simulation in Materials Science and Engineering. (Submitted).

10. X. Duan and T. Sheppard. Development of a new spread formula by the combination of finite element method with the Taguchi experimental design method. Modelling and Simulation in Materials Science and Engineering. (Submitted).

Contributions to symposia

1. X.Duan and T.Sheppard. Modelling of static recrystallisation by combining FEM with empirical models. The Second International Conference on Advanced Forming and Die Manufacturing Technology. Pusan, Korea, June 17-19, 2002. (Accepted).
2. X.Duan and T.Sheppard. The influence of process parameters on the evolution of subgrain size during hot flat rolling of Al. alloy. The Second International Conference on Advanced Forming and Die Manufacturing Technology. Pusan, Korea, June 17-19, 2002. (Accepted).
3. X.Duan and T.Sheppard. Three dimensional simulation of subgrain size evolution during hot rolling of commercial purity aluminium alloy. 9th ISPE International Conference on Concurrent Engineering: Research and Applications. (Accepted).

ACKNOWLEDGEMENTS

The author would like to thank the many who have helped during the production of this thesis, especially the following:

School of Design, Engineering & Computing

For financial support through a bursary

Professor T. Sheppard

For his constant supervision, encouragement and help throughout the research

Mr. X. Velay and Mr. I. Flitta:

For their constant help for the last two years, especially during the starting stages

Dr. C. Geoghegan

For his help in improving my spoken and written English

The members of the design group

For their help and support at various stages

Laminazione Sottile SA, Caserta, Italy

For supplying industrial rolling pass schedule and measured data

Dr. D.S. Wright, Dr. N. Raghunathan, Dr. M.A. Zaidi and **Dr. R.P. Vierod**

For permission to use their excellent experimental work

My wife

For her patience and support

Nomenclature

$1/R_\rho$	Local lattice curvature in equation (2-22), mm^{-1}
a	Level arm, mm
b^*	Effusivity of the part in chapter 3, $Kg.s^{-5/2}.{}^0K^{-1}$
b	Burgers vector in the remainder equations, m
b^*_{tool}	Effusivity of the die, $Kg.s^{-5/2}.{}^0K^{-1}$
C	Heat capacity, $J.Kg^{-1}.K^{-1}$
C	Capacity matrix in equation (3-26)
D	Roll diameter, mm
D_1	Bearing diameter of work roll, mm
D_2	Bearing diameter of support roll, mm
D_s	Self-diffusion coefficient
dH	Thickness reduction $dH = H_1 - H_2$, mm
dH_{max}	The maximum thickness reduction, mm
$d\varepsilon$	Increment of strain
$d\delta$	Increment of subgrain size, μm
d_0	Initial grain size, μm
d_{rex}	Recrystallised grain size, μm
$E(\dot{\varepsilon}_{ij})$	Work function
F_i	Traction, N
G	Universal gas constant, $J.Kg^{-1}.mole^{-1}$
G'	Growth rate of recrystallised grains
G^*	Shear modulus, Pa
H	Conductivity matrix in equation (76)
H_1	Entry thickness, mm
H_2	Exit thickness, mm
H_C	Convective heat transfer coefficient, $W.m^{-1}.K^{-1}$

H_R Heat transfer coefficient between the rolls and the stock, $W.m^{-1}.K^{-1}$

h_{cd} Transfer coefficient, $W.m^{-1}.K^{-1}$

k Conductivity, $W.m^{-1}.K^{-1}$

k_h Stress concentration factor in walls

K Material consistency, MPa

$K_{bearing}$ Power absorbed by the bearings, kW

K_{def} The power required for deforming the slab, kW

$K_{\lim}$ The maximum power limit, kW

K_{total} Total power required, kW

l Contact length, mm

L_1 Slab length before rolling, mm

L_2 Slab length after rolling, mm

L_C Length of dislocations annihilated

M Taylor factor

M_{GB} Grain boundary mobility

MSD Mean square deviation

N Roll speed, rpm

N_{TOT} Total number of nuclei

N_V Number of nucleation at grain boundary

O_p Overload coefficient of power

P Roll force, MN

P' Modified roll force, MN

P_D Total stored energy, J/m^3

Q_F Factor to account for pass geometry and fractional conditions

Q_{def} Activation energy for deformation, $J.mol^{-1}$

Q_{rex} Activation energy for recrystallisation, $J.mol^{-1}$

Q_S Sim's factor

R Roll radius, mm

R' Deformed roll radius, mm

s	Deviatoric stress tensor
s	Spacing in cell walls in equation(2-14)
S	Surface
S_w	Spread coefficient, defined as $S_w = Ln(W_2/W_1)/Ln(H_1/H_2)$
S/N	Signal-to-noise
$\overline{S/N}$	Overall mean Signal-to-noise
t	Time, s
t'	Time of the slab passing the roll gap, s
$t_{0.5}$	Time to 50% recrystallisation, s
t_b	Back tension, MN
t_f	Forward tension, MN
t_{lead}	Time of the lead exposed in air, s
t_{tail}	Time of the tail exposed in air, s
t_{total}	Total time of each pass, s
T	Temperature in ^{0}C in equation (1-3) and ^{0}K in the remainder equations
T	Nodal temperature vector
T_a	Annealing temperature, ^{0}K
T_{amb}	Ambient temperature, ^{0}C
T_{mat}	Material temperature, ^{0}C
T_0	Outside temperature, ^{0}C
J	Roll torque, N-m
T_{tool}	Tool temperature, ^{0}C
u_i	Velocity component, mm/s
V	Tangential roll velocity in chapter 6, or volume in equations (84) to (90)
V_{bite}	Volume of material in the roll gap, mm^3
$\bar{v}_m$	Mean velocity of viscous glide
w	Work, N.m
W_1	Entry width, mm
W_2	Exit width, mm

x	Distance of penetration of temperature profile, mm
X_V	Volume fraction recrystallised %
Z	Zener-Hollomon parameter
α	Thermal diffusivity in equation (1-3)
β	Drag force, N
θ	Misorientation across subgrain boundaries, degree
θ_C	Critical misorientation for a high angle boundary, of the order of 15^0
θ_{ss}	Misorientation across subgrain boundaries in steady state regime, degree
δ	Subgrain size, μm
δ_{ss}	Subgrain size in steady state regime, μm
δx	distance increment, mm
ε	Strain
ε_m	Critical strain
$\bar{\varepsilon}$	Equivalent strain
$\dot{\varepsilon}$	Strain rate, s^{-1}
ε_r	Emissivity parameter
ε_δ	Characteristic strain for subgrain size growth
ε_θ	Characteristic strains for misorientation growth
ϕ_b	Bite angle, degree
$\dot{\bar{\varepsilon}}$	Equivalent strain rate, s^{-1}
μ	Friction coefficient
$\bar{\sigma}$	Flow stress, MPa
$\bar{\sigma}'$	Modified flow stress, MPa
$\sigma_{\exp}$	Measured stress at the steady state regime, MPa
σ_f	Fractional stress, MPa
σ_n	Normal stress, MPa
σ_s	Yield stress, MPa

σ_r Stephan-Boltzmann constant, J.^{0}K^{-1}

Δt Time increment, s

ΔT_{lead} Temperature change at the slab tail, ^{0}C

ΔT_{mat} Temperature change of the slab, ^{0}C

ΔT_{roll} Temperature change of the roll, ^{0}C

ΔT_{tail} Temperature change at the slab tail, ^{0}C

ΔV Velocity difference at the interface, mm/s

π Functional

ρ Density in chapter 3 and 6; dislocation density in chapter 2 and 5

ρ_b Boundary dislocation density, m^{-2}

ρ_g Geometrically necessary dislocation density, m^{-2}

ρ_i Internal dislocation density, m^{-2}

ρ_r Boundary dislocation density, m^{-2}

Λ_r Average distance a dislocation density travels before being stopped, m

Chapter 1 Introduction

1.1 Aluminium alloys

A unique combination of properties make aluminium alloys one of the most versatile engineering and construction materials. In addition to good mechanical properties, it has low density, high corrosion, no toxic reactions, and good electrical and thermal conductivity.

According to the major principal alloy elements, wrought aluminium alloys are generally divided into seven major classes, identified by four digits. In other way, aluminium alloys can be categorised into non-heat treatable and heat treatable, in terms of whether or not they can be strengthened by heat treatment. Table 1 briefly illustrates the designation.

Table 1 Designation of aluminium alloys

Designation	**Major alloying element**	**Properties**	**Heat treatable?**	**Typical Alloys**
1XXX	⩾ 99% aluminium	Excellent corrosion High electrical and thermal conductivity	No	AA1050 AA 1100
2XXX	Cu, Si	High Strength-to-weight ratio	Yes	AA2014 AA 2024
3XXX	Mn	Medium strength	No	AA3003 AA3104
4XXX	Si	Lower melting point	Generally not	
5XXX	Mg	Good corrosion resistance high strength	No	AA5083 AA 5052
6XXX	Mg, Si	Good formability, machinabilty, weldability	Yes	AA6061 AA 6063
7XXX	Mg, Zn	Moderate to very high strength	Yes	AA7075

In addition to strength, properties such as stress corrosion resistance, machinability, toughness and fatigue strength can be achieved by a careful control of alloying elements and by a special thermal treatments (Woodward 1994). Copper (Cu) has appreciable strengthening effect. Magnesium (Mg) has a marked strength effect, due to both its solubility and formation of intermetallic compounds. Silicon (Si) mainly influences the microstructure through its strong tendency to form intermetallic compounds with Al, Fe, Mg and Mn. Manganese (Mn) is present in the alloy both as precipitates and dissolved in the matrix. Zinc (Zn) improves general corrosion behaviour and compromises between good extrudability and required strength.

Currently, aluminium alloys are widely used in building, construction, transportation, and packaging industries. There is increasing use in the manufacture of automobiles, and the average proportion of aluminium in body panel has been rapidly increasing in order to reduce weight and enhance stiffness (Vöhringer 1999).

1.2 Hot flat rolling and rolling pass schedule

Flat rolled products, i.e. sheet, plate and foil constitute almost 50% of all aluminium alloys used. More than 1/3 of sheet and foil are consumed for making cans (Sanders 2001). The raw material for most rolled products is the DC (Direct Chill semi-continuous cast) slab. Slabs up to over 20 tons in weight and 500-600 mm thick, 2000 mm wide and 8000 mm long are produced. The slab is usually reduced in thickness to about 25 mm in a single stand hot reversing mill (see Fig.1-1). This process is always referred to as breakdown rolling or roughing rolling in the literature.

The breakdown rolling usually constitutes 9-25 passes depending upon the capacity of mill. After breakdown rolling, the strip is further deformed to 2.3-5.0mm in

thickness usually in a 4-stand or 5-stand mill, which is often referred to as tandem rolling. In some plant, tandem rolling is replaced by extended rolling in a single stand reversing mill. That is becoming more normal as the extended costs of plant increases.

The number of rolling passes and the allocation of the amount of reduction directly determine the forming feasibility and the product quality. Deciding the number of pass, allocating the amount of reduction, controlling the temperature variation are the main tasks of designing an acceptable rolling pass schedule.

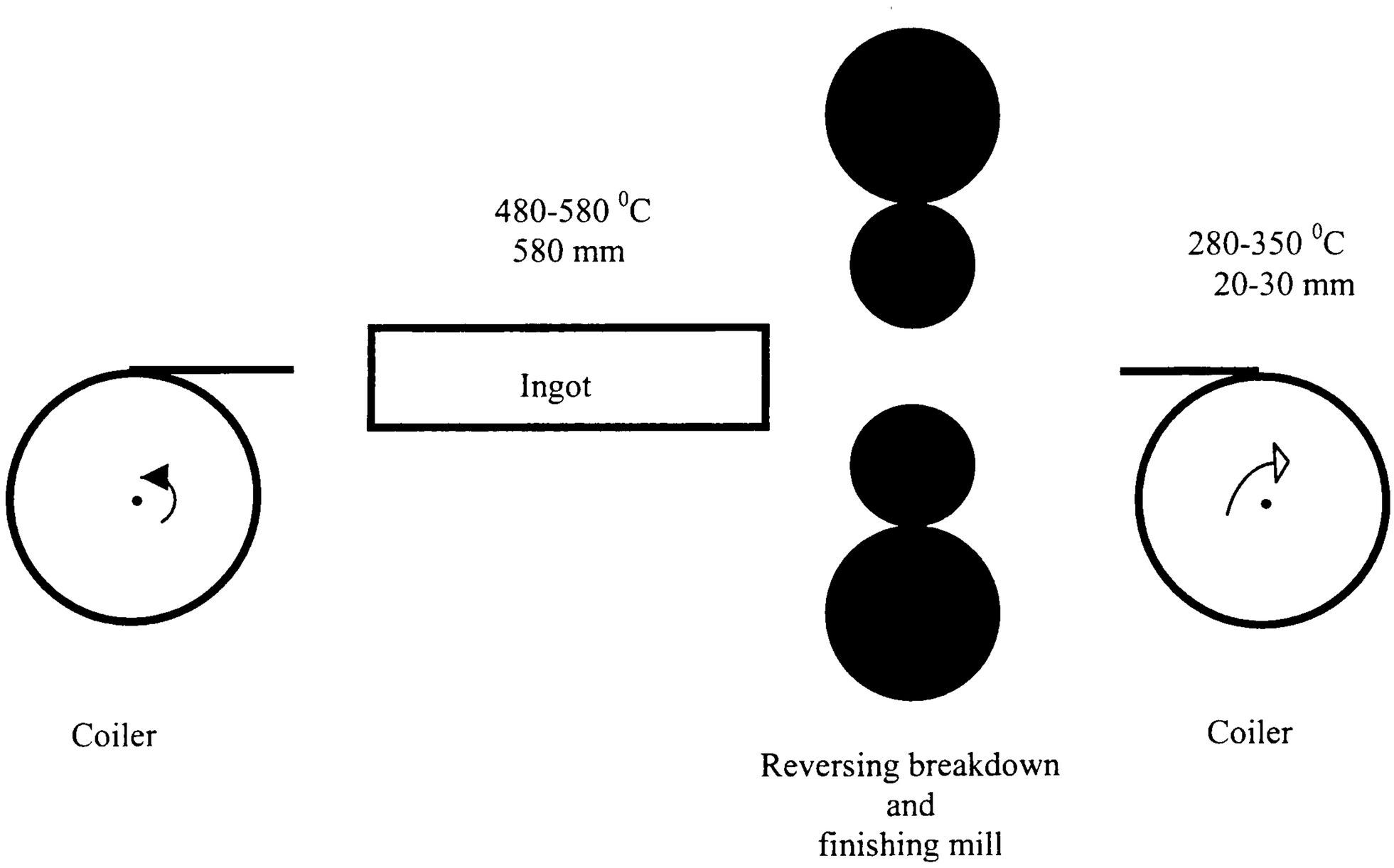

Fig. 1-1 Conceptual view of single stand hot reversing mill

1.3 Finite element method in metal forming

Applying the finite element method (FEM) to aid predictions on the metal forming industry has been an international research focus during the last decade. This could

be proved from the proceedings of any of the recent conferences on metal forming. The reason can be attributed to the characteristics of the metal forming processes: large deformation, thermomechanical coupled, non-linear boundary conditions and non-linear material behaviour. Presently, there is no method that could tackle all these problems satisfactorily except FEM. Applications of the plastic finite element method into metal forming started at the end of the 1970's. It has been widely used in both industry and academia since the beginning of the 1990's as computer hardware and software make significant advance. The main advantages of FEM, compared with other numerical methods and analytical techniques are:

- Avoid the need to assume homogeneous deformation
- Detail the deformation information, such as strain, stress, temperature, velocity
- Consider the complex interactions between strain, strain rate, temperature, microstructure, and the flow stress
- Use very realistic models to represent real process behaviour, such as the coefficient of friction, heat transfer etc.
- Visualise the deformation process
- Replace the experimental phase partially or completely

There are three main techniques dealing with the movement of the node in the FEM computation. In the Eulerian technique, the finite element mesh is spatially fixed, material is considered to flow through it. The main disadvantage is that it can not predict the deformation history with time. It is only applicable to the steady state deformation. The remeshing is avoided, thus computation time is greatly reduced. In the Lagrangian technique, the finite element mesh is deformed incrementally over time with the material. This techniques is commonly used by the major commercial FEM programs. One disadvantage is that remeshing is frequently required. The Aribitrary Lagrange Euler (ALE) was shown to be efficient in metal forming to avoid remeshing. The basic idea is to define a mesh velocity, which is different from the kinetics velocity, but preserves the free surface evolution. The

mesh velocity is imposed so that, during the deformation process, the mesh distortion remains at a minimum (Chenot et al 1996).

The FEM used in metal forming can be generally categorised into rigid-plastic FEM, elastic-plastic FEM and visco-plastic FEM, in terms of the type of material constitutive model employed (Hartley 1993). For some hot processes, such as forging, rolling and extrusion, plastic strains outweigh elastic strains; the material is regarded as a non-Newton fluid, and rigid-visco-plastic FEM is usually adopted to simulate these processes. Well recognised commercial programs used in bulk deformation include EASY-FORM®, DEFORM®, FORGE2&3®, MARC/AUTOFORGE®, MSC/SUPERFORGE® and Qform® (Bramley 1999). Each commercial code has its speciality. For rolling, the capabilities of automatic meshing and remeshing, thermomechanical coupling and easy transfer of deformation history from one pass to another pass are crucial.

The analysis accuracy is affected by three main elements: analyst, program and the input data. Choosing an appropriate program is a choice, followed by preparing the various input parameters, such as flow stress, heat conductivity etc. The analyst's job involves: establishing the analysis model, running the program and analysing the results. Although the present FEM programs are more user friendly and intelligent than those 10 years ago, the analyst still plays a very important role to ensure a good result. Further requirement for the analyst is the capability of programming user routine with FORTRAN or C language.

1.4 Microstructure changes during hot working condition

The microstructural changes during hot working conditions have been extensively studied. The temperature in hot working conditions is considered greater than $0.6T_m$, where T_m is the melting temperature. The deformation of rolling is applied in a series of passes, which are necessarily separated by periods of time. The

microstructural changes occurring during deformation are termed dynamic recovery or recrystallisation, and those taking place in the time intervals after deformation is termed static recovery or recrystallisation.

The structural changes during deformation are the competing results of work hardening and of softening by dynamic recovery and possibly by dynamic recrystallisation. Whether dynamic recrystallisation occurs or not depends primarily on the rate of dynamic recovery. Generally, aluminium alloys have high stacking fault energy. The movement of dislocation, such as climb and cross-slip, takes place easily at high temperature. Previous researches have shown that dynamic recovery is relatively rapid (Zaidi and Sheppard 1982). Dynamic recrystallisation does not occur in most circumferences. It has only been reported to occur in some aluminium-magnesium alloys when large strains were applied, which is not common in industrial production (Sheppard and Tutcher 1981a; Raghunathan and Sheppard 1986). Hence, dynamic recrystallisation can not be considered in the present thesis.

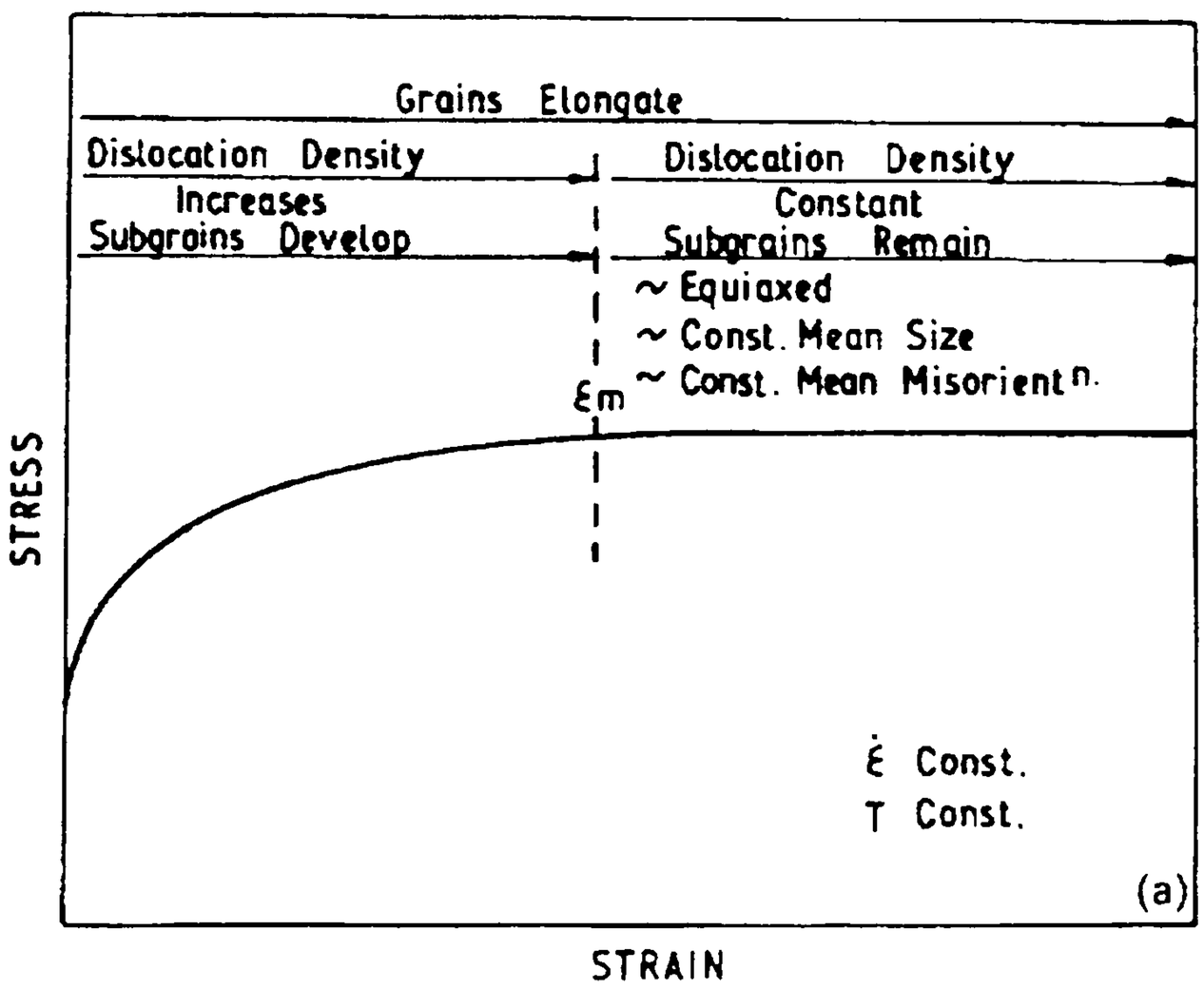

Fig.1-2 Schematic stress-strain curve and microstructural Changes (after Sellars 1990).

The microstructural changes are summarised in relation to the stress-strain curve in Fig.1-2. Before the deformation reaches the strain ε_m, the flow stress increases with increase of dislocation density. Rearrangements of dislocation lead to the formation of subgrain boundaries. At the strain ε_m, the hardening and softening process balance, a steady state regime is attained. The flow stress and dislocation density remains dynamically constant. A main feature of the steady state regime is that subgrains are well developed, approximately equiaxed, of constant mean size and of nearly constant mean misorientation, even after very large strains.

After deformation, further structural changes occur by the process of static recovery and recrystallisation. They are equivalent to the processes that take place during annealing of cold worked metals, although the driving forces are lower. These processes occur because the substructures produced by deformation are thermodynamically unstable. Static recovery produces smaller microstructural changes than does static recrystallisation. Therefore, it is difficult to observe by optical or electron metallography, but Sheppard and Zaidi (1982) did find the evidence to show that static recovery happens during interpass delay. Compared with static recovery, static recrystallisation has a marked softening effect and is easily observed. The process of static recrystallisation includes two stages; nucleation and growth. Nucleation always takes place at the original grain boundaries, deformation bands or large participates. The mechanism of growth include subgrains coalesce, the migration of sub-boundaries and subgrain growth. The rate of recrystallisation is dominated by total stored energy and its distribution, the availability of nucleation sites and the holding temperature.

1.5 Layout of the thesis

The present work has focused on employing the finite element method to simulate the hot flat rolling process, from breakdown rolling to tandem rolling. The relevant aspects involve choosing an appropriate constitutive equation; predicting rolling

load and torque; simulating the evolution of dislocation substructure in the roll gap, modelling static recrystallisation and designing the rolling pass schedule. Although no experiments have been carried out, reliable data have been extracted from external PhD theses and the literature, supplied by the aluminium companies in Italy and the UK, and provided by other academic research groups in the UK. The total data is far greater than that available or used and reported in the existing literature. It should be emphasised that the data provided by the aluminium companies are especially valuable because they are usually commercially sensitive.

Basic concepts on aluminium alloy, hot flat rolling and microstructural changes are briefly introduced in chapter 1. Detailed research history and critical reviews are given in chapter 2. Principal formulation and analysis techniques of the FEM programs FORGE2/3® are recalled in chapter 3

In the early stages of the breakdown rolling, the lateral spread of a slab is significant, leading to a three-dimensional deformation. The influence of rolling parameters, such as reduction, temperature and slab geometry on the roll load and torque are first investigated. Attention is then paid to the heat transfer coefficient and friction coefficient, which are very difficult to measure. The changes of temperature and lateral profile under both laboratory and industrial rolling conditions are the major objectives in chapter 4. The Taguchi experimental design method is applied to analyse the influence of four main parameters (the ratio of width to thickness, the ratio of roll radius to the slab thickness, reduction and deformation temperature) on the spread, and to express the contribution of each parameter in percentage. A new formula is then established by analysing a large amount of FE analyses and the laboratory data from external PhD theses, which makes the formula valid for both laboratory rolling and industrial practice.

In chapter 5, both empirical and physical based models are adopted to study how subgrain size, dislocation density, misorientation and the flow stress vary in the roll

gap. Studies on static recrystallisation are carried out by incorporating the plastomechanical parameters, i.e. strain, strain rate and temperature, into the empirical model. Further work is also detailed in this chapter.

The pass schedule optimisation is the most difficult but also the most valid method to achieve good strip profile and high product qualities. In chapter 6, the procedure of designing an acceptable rolling pass schedule is illustrated. All achievements on temperature, lateral deformation, and the friction presented in Chapter 4 and Chapter 5 are applied into the design of rolling pass schedules. The computed rolling load, pass temperature, and power are then compared with industrial measurement and the predictions by the FEM. The design package shows a very high accuracy.

Chapter 7 concludes all the work carried out in the present thesis and suggests further work in the modelling of hot rolling.

Chapter 2 Review of literature

2.1 Simulation of breakdown rolling

Rolling force, power, temperature and width are four basic rolling parameters required in the mill setup. Accurate prediction of these parameters is crucial for producing qualified products efficiently and safely. In the breakdown rolling passes, the slab thickness is of the same order as the rolls. The width-to-height ratio is usually less than 4. Lateral deformation cannot therefore be ignored. This is a three-dimensional deformation process and can only be described accurately by the use of suitable FEM or FD analyses.

Nearly all theories concerning the calculation of the rolling force and torque in current rolling publications are based on a plane strain assumption and assume that the contact pressure distribution is distributed over a circular arc. Wright (1978) compared various assumptions with measured pressure distributions. The conclusions on the pressure distribution in the roll gap in breakdown passes are confusing. It is impossible to conceive a suitable mathematical algorithm because of the complexity of the deformation. Presently there is no method that could provide more detailed local deformation information than FEM. During the last decades, various FE models have been adopted to simulate the 3-D hot flat slab rolling processes. Li et al (1984) used 3-D rigid-plastic FEM in their analyses. Betrand-Corini et al (1988) applied 3-D visco-plastic model. Liu et al (1987) employed elastic-plastic analyses.

The calculation of rolling force is the most important task for the mill setup. Accurate prediction of rolling force can greatly reduce the pressure over the controlling system to adjust the mill setup. Although each rolling plant has invested to establish their own empirical rolling model by various methods such as regression, neural networks, FEM and analytical approaches, these models are

usually not useful when rolling a new product. The reasons are due to the dearth of deep study on the influence of some factors, i.e. friction coefficient, temperature evolution and lateral deformation. Hence, hot rolling model development has proceeded slowly. In the following sections, reviews will focus on these factors.

2.1.1 Friction coefficient

Friction in the roll gap possibly affects the mode of deformation more than any of the geometrical features of the rolling slab or strip since its coefficient is affected by a multitude of factors, including temperature, lubricant and emulsion, reduction, and the interface velocity etc. The nature of the hot rolling process makes it extremely difficulty to verify the contact condition. Lenard, Pietrzyk and Cser (1999) have reviewed the techniques for the evaluation of friction coefficient in flat rolling. These techniques include: (1) direct measurement methods, measuring the average frictional shear stresses or the average coefficient of friction at the interface; (2) deriving a constant friction factor or coefficient of friction from the measured deformation load; (3) determining the constant friction shear factor or coefficient of friction by measurements of deformation or other indirect indices, and (4) calculating the coefficient of friction from measured values of the forward slip. The most commonly adopted methods are (1) and (2). When using FEA, the inverse analysis (trial and error) appears to be the best choice. By using an inverse analysis method, FEA is iteratively run until the appropriate friction coefficient is found to match the computed rolling force with the measurement satisfactorily. Clearly, industrial or experimental data is required for this method.

However, none of the above methods appear to be capable of dealing with the variations experienced throughout a complete pass schedule. Moreover, most of the published work has been concerned with cold rolling and considered to be under plane strain conditions. Specific results on the measurement of friction during hot rolling of aluminium alloys is scarce. General conclusions are that the coefficient of

friction falls as the rolling speed is increased and it increases when the reduction is increased. Atack and Abbott (1986) concluded that sticking friction does not exist when hot rolling aluminium alloys. This conclusion contradicts many authors' observation. But it does indicate that more research work is necessary in this area.

There are three friction laws, which have been widely used in the current simulations. They are the Tresca friction law, coulomb friction law, and viscoplastic friction law. The form of various laws will be detailed in chapter 3.

2.1.2 Temperature evolution

It is generally accepted that, in hot deformation processes, temperature is the most significant parameter for the determination of product properties. Ductility, strength, texture etc. are each significantly influenced by the formation and development of microstructure. Meanwhile, temperature also has a considerable effect on the deformation load and torque. It is therefore necessary to ascertain the magnitude of any temperature change during the deformation and dwell time. Temperature variation during hot rolling is caused by the combined effect of two factors. One is the heat generated by the friction work and plastic deformation. Another is the heat loss to the rolls through conduction and to the surroundings by convection and radiation.

Three different approaches, the analytical approach, the finite difference (FD) and the finite element method (FEM) are currently in use to calculate the temperature variation through the slab thickness in the roll gap. There are quite significant differences between these approaches in their consideration of heat generation and heat loss. The analytical approach usually only takes into account heat transfer between the slab and roll by conduction. The calculated temperature is only rigorously true under certain conditions. FD gives a better prediction than the analytical approach by assuming heat generation through the slab thickness and

applying friction work to the surface elements, in addition to the conduction between roll and slab. Due to the convergence problem and the difficulty of dealing with the distorted mesh during deformation, currently all researchers have only adopted two-dimensional FD models. FEM is theoretically the best method because it considers all factors, such as changing thermal properties or differing rates of internal heat generation with position and time. The problem when employing FEM is that the analysis takes a good deal of computer time, especially for three-dimensional deformation. For this reason analytical methods and FD are usually adopted for the design of rolling pass schedules.

2.1.2.1 The analytical approach

The usual assumptions implemented are:

- Heat conduction occurs in one direction – only radial in the rolls.
- The heat transfer coefficient between slab and rolls is infinite
- Uniform thermal properties exist in rolls and slab.

Equations adopted to calculate the temperature distribution in slab and roll are expressed as (Carslaw and Jaeger 1959):

$$T_1 = A\left\{1+\left[\frac{k_2}{k_1}\sqrt{\frac{\alpha_1}{\alpha_2}}\right]erf\left[\frac{x}{2\sqrt{\alpha_1 t}}\right]\right\} \tag{2-1}$$

$$T_2 = A\left\{erfc\left[\frac{|x|}{2\sqrt{\alpha_2 t}}\right]\right\} \tag{2-2}$$

where T_2 is the roll temperature, T_1 is the slab temperature, A is defined as

$$A = \left[\frac{T_{initial}}{1 + \frac{k_2}{k_1}\sqrt{\frac{\alpha_1}{\alpha_2}}} \right] \tag{2-3}$$

These relationships are limited by the lack of any terms for either internal heat generation or friction at the interface. Their validity is only rigorously true so long as the slab appears infinite, e.g. whenever $x < \sqrt{12\alpha t}$. Assuming a quadratic temperature profile with the integral profile approach derives this latter limit.

2.1.2.2 The Finite difference (FD)

Wilmotte et al (1972) first used the finite difference approach to calculate temperature distribution in strip rolling. In their calculation, a uniform increase of temperature in the roll gap was assumed and Carslaw and Jaeger's (1959) equation was employed to calculate cooling during contact with the work rolls. Bryant and Heselton (1982) carried out similar calculations, neglecting the effect of friction and assuming uniform distribution of heat caused by plastic deformation and uniform temperature across the width of the strip. Sheppard and Wright (1978, 1980) calculated the temperature distribution for slab rolling by taking into account non-uniform heat generation in the deformation zone and the effect of friction. Sellars and Kawai (1993) determined the temperature changes in the stock without computing conduction in the rolls, leading to a method termed "the phantom roll". Critically we should note that this method requires the input of considerable experimental data and is limited to two-dimensional geometry. Recently, Hand et al. (2000) calculated temperature changes for multi-deformation schedules during hot plane strain compression. The temperature rise due to plastic deformation and friction is obtained by considering the area under the equivalent pressure-strain curve over the appropriate strain interval. This requires actual test data.

In recent years, the application of FEM into the rolling process has made the FD techniques redundant. Compared with many available FEM codes, there are few commercial FD packages, and there exists inherent theoretical disadvantage, such as mesh generation and remeshing, and convergence. All these factors help to explain why the development of FD proceeds so slowly in the simulation of metal forming. In the current study, the method adopted by Sheppard and Wright (1980) is chosen as a representative for the FD. It should be stated that this method is not the best among various FD methods. The reason of selecting this method is attributed to that FD is not the major research interest in the current thesis. It is only adopted to give a general comparison of the predicted temperature evolution between FD and FEM.

2.1.2.3 Finite element method

Rebelo and Kobayashi (1980) first simulated the combined effects of viscoplastic deformation and heat transfer for cylinder compression and ring compression processes by introducing separate functions for the equilibrium and for the energy balance equations in FEM. The first application of the finite element method to analyse the temperature distribution during hot rolling was by Zienkiewicz et al.(1981). Lenard and Pietrzyk (1992) reviewed the research work on the heat transfer coefficient and described the effect of variation in the heat transfer coefficient on the calculation of load for warm and cold rolling of aluminium.

In addition to the experimental method (Atack, Round and Wright 1988), the inverse analysis (trial and error) by FEM is another way to ascertain the heat transfer coefficient. When using this method, FEA is run iteratively until the computed temperature histories match the recorded temperature satisfactorily. The reported values of heat transfer coefficient show great differences from 10,000 to 80,000 $Wm^{-2}K^{-1}$ by this method (Chen et al 1992, Wells et al 1998, and Mirza et al 2001). These differences may be attributed to the thickness reduction (which

influences the pressure and hence the true contact area), and finally the thickness of the lubricant layer, this last factor alters the heat transfer characteristics across the interface.

2.1.3 Lateral deformation

In the hot flat rolling of slabs, plane strain condition prevails in the middle portion of the product width, and lateral flow occurs at the edges. The consequences of this spread are many:

- It reduces the pressure for a given reduction.
- There is a propensity for the fibers near the edge to be short, resulting in a residual tensile stress state, thus making shape and flatness control more difficult.
- It may cause edge cracking, depending on the initial geometry and the process parameters.
- The material loss increases because cracked edges and bad edge profile must be trimmed.

All these considerations emphasize the necessity for a deep understanding of lateral flow during slab rolling. Earlier work has predicted the spread by empirical formulae constructed from regression of laboratory experimental data (Hill 1950, Wusatowski 1958, Sparling 1961, Helmi & Alexander 1967, Sheppard & Wright 1981, Raghunathan & Sheppard 1989, Silk & Winden 1999). The relaevant formulae are given below.

Hill' equation

$$S_w = 0.5 \exp\left[-0.525\left(W_1 / \sqrt{D * dH}\right)\right] \tag{2-4}$$

Wusatowski's equation

$$S_w = \exp\left\{-1.9872\left[W_1 / H_1\right] * \left[H_1 / R\right]^{0.556}\right\} \tag{2-5}$$

Sparling's equation

$$S_w = 0.981\exp\left\{-1.615 * \left[W_1^{\,0.9} / \left(R^{0.55} H_1^{\,0.1} dH^{0.25}\right)\right]\right\} \tag{2-6}$$

Helmi & Alexander's equation

$$S_W = 0.95\left(\frac{W_1}{H_1}\right)^{-1.1} \exp\left[-0.707\left(\frac{W_1}{H_1}\right)^{-0.971} \frac{W_1}{(R * dH)^{1/2}}\right] \tag{2-7}$$

Sheppard & Wright's equation

$$\ln\frac{W_2}{W_1} = \left(0.11 + 0.032T_H - 0.01\frac{R}{H_1}\right)\left[\frac{W_1}{(R * dH)^{1/2}}\right]^{-3.5}\left(\frac{W_1}{H_1}\right)^{1.375T_H + 0.233(R/H_1) - 0.1} \tag{2-8}$$

Raghunathan & Sheppard's equation

$$\ln\frac{W_2}{W_1} = 2.45\left(\frac{W_1}{H_1}\right)^{-0.71}\left(\ln\frac{Z}{A}\right)^{0.002}\left(\frac{R}{H_1}\right)^{-0.04} * \exp\left\{-\left(2.72 - 0.125\ln\frac{Z}{A}\right)\left(\frac{R}{H_1}\right)^{0.55}\left(\frac{W_1}{H_1}\right)^{-1}\left[\frac{W_1}{(R * dH)^{1/2}}\right]\right\} \tag{2-9}$$

Winden's equation

$$\frac{W_2}{W_1} = -C^{spread}\left(\frac{H_2}{H_1}\right) + \left(1 + C^{spread}\right) \tag{2-10}$$

Notes:

$$S_W = Ln(W_2 / W_1) / Ln(H_1 / H_2)$$

T_H: Homologues temperature

$dH = H_1 - H_2$: Thickness reduction

The conclusions drawn on the spread for hot flat rolling are that the spread increases with

- decrease of the width/ thickness ratio of the slab
- increase of the roll radius/ initial thickness ratio
- increase of the reduction
- increase of the entry temperature
- Other factors such as the interface friction, roll speed, and the material flow stress exert minor influence on the spread.

Due to the limitation of laboratory conditions, small-scale experiments are always conducted to simulate the industrial condition by trying to obey the principle of similitude. Since some factors are very difficult to reproduce, such as the friction condition on at the slab/roll interface, the temperature changes along the slab thickness and the roll temperature, workers have tended to ignore these factors unconsciously or intentionally. Consequently, the formulae developed are only valid for a limited range of rolling conditions.

More recently, Winden (1999) managed to simulate the industrial rolling on a conventional laboratory rolling mill through employing some new techniques. The regressed spread formula gave a good prediction than the previous formulae for his experimental data. However, since only one parameter, the ratio of entry thickness to exit thickness, is employed, its application range must be greatly reduced. Strictly

speaking, this equation is not correct because possibly the most important factor, the ratio of entry width to entry thickness, is not included.

The three-dimensional rolling process has been analysed either by FEM (Yamada et al 1992, Kobayashi et al. 1989, and Liu et al 1987) or the energy method (Yoon and Kim 1991). However none has systematically studied the spread behaviour in both laboratory and industrial rolling processes. In industrial practice, the slabs before entering the breakdown pass usually have a curved edge profile."Broadside" rolling is adopted before the normal reduction when the required product width is significantly wider than the initial cast slab width. The consequence of "broadside" rolling is in producing a distinctly concave profile. Slabs not treated in this way are rolled, as cast, with a slight convex initial profile.

At the present time, there would appear to be no published papers dealing with width variation predicted by FEA for industrial rolling which must also include multipass rolling.

2.2 Modelling dislocation substructure changes

2.2.1 Dislocation substructure evolution

Up to date, a considerable amount of work has been reported on the dislocation substructure evolution for aluminium alloys under various hot work conditions: hot rolling, hot torsion and plane strain compression (Immarigeon 1969) (Zaidi 1982) (Rahunathan 1989) (Sheppard 1982) (Knustad 1985) (Poschmann 1995) (Zhu 1996) (Mcqueen 1998) (Nieth 1996) (Baxter 1999) (Sellars 2000). Dislocation substructure can be described by three internal state variables: dislocation density (ρ), subgrain size (δ) and misorientation across subgrain boundaries (θ). Prior to discussing the modelling of the substructure changes, it would be useful to review the previous investigations on substructure evolution.

To give a clearly description of the dislocation density evolution, a schematic representation of substructure is taken from the literature (Nes 1998). In Fig.2-1, total dislocation density consists of the internal dislocation density ρ_i and the boundary dislocation density ρ_b.

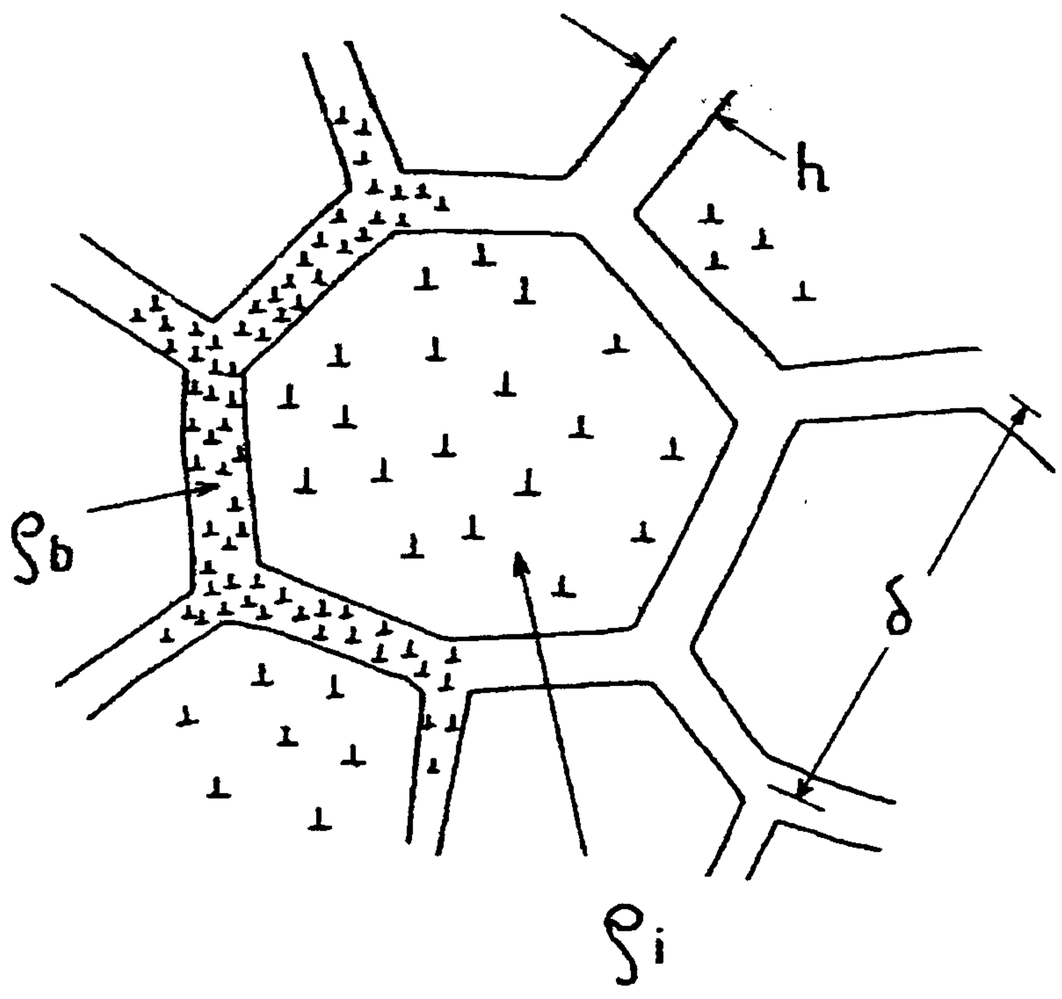

Fig.2-1 A schematic representation of the microstructure; cell diameter, δ, cell wall thickness,h,cell wall dislocation density, ρ_b and dislocation density with the cells, ρ_i (after Nes 1998)

During the early stages of deformation, dislocation multiplication occurs, and the total dislocation density (ρ), $\rho = \rho_i + \rho_b$, increases from $10^8 \sim 10^{10}$ m^{-2} to $10^{11} \sim 10^{12}$ m^{-2} at the commencement of macroscopic flow. Dislocations move, and interact with each other to form tangles. This terminates in a cellular structure with the dislocations clustering tightly into the cell walls separating dislocation free regions. As deformation proceeds, ρ continues increasing, and attains at a constant value of approximately 10^{14} m^{-2} when the steady state regime is reached. The cellular structures are replaced completely by the formation of subgrains due to the additional dislocation reactions. Subgrains can be regarded as an extension of a

cellular structure in that the dislocations are arranged in the form of planar networks in subgrain boundaries, while the cellular boundaries consist of three-dimensional network and tangles of dislocation. The ability to form a cellular or subgrain structure depends on several factors: the stacking fault energy, the applied stress, the strain, the temperature, and the presence or absence of obstacles.

An interesting feature of subgrains is that they are equiaxed and maintain their equilibrium size and shape in the steady state regime even at very large strains, whereas the grains are always elongated in the direction of the extension. There are up to date two interpretations. The first considers that sub-boundaries are constantly migrating in such a way as to keep the substructure equiaxed. The second possible interpretation is by the repeated unravelling of the sub-boundaries and the subsequent reformation of new sub-boundaries at locations which keep their average spacing and dislocation density constant, termed "repolygonisation" (Jonas et al 1969).

The critical strain required for subgrain formation varies with the deformation mode and materials, and increases with Z, the temperature compensated strain rate, defined as

$$Z = \dot{\bar{\varepsilon}} * \exp\left(\frac{Q_{def}}{GT}\right) \tag{2-11}$$

At strain rates of 0.05 – 1 s^{-1}, the critical value of strain for general hot working conditions is usually within 0.2-0.3; but for creep, the critical strains are only 0.01-0.1 (Jonas et al 1969). According to Zaidi et al's (1982) observation on the subgrain evolution for commercial pure aluminium throughout roll gap, the subgrain size is stabilised at 10mm from entry bite (the total contact length is 35 mm) in the slab centre, and no further change in size could be observed. The equivalent strain at this

position is about 0.15, computed by FEM. Sellars (1990) proposed an equation to calculate the critical strain ε_m, see Fig.1-2,

$$\varepsilon_m = 0.002 * Z^{0.2} \tag{2-12}$$

The calculated value of ε_m for commercial purity aluminium is 0.314 when the rolling temperature is 500^0C; there is 40% reduction; and 2 s^{-1} is the strain rate. Obviously, the calculated value of ε_m is too large. The reason may be attributed to the plane strain compression test where ε_m is regressed from experimental data. Raghunathan and Sheppard's (1989) observation for AA5056 showed that a minimum strain of 0.19 is required to attain stabilised subgrains for that alloy.

After the critical strain, the flow stress is independent of strain. The hyperbolic sine function is usually applied to describe the relationship between the rolling parameters and the flow stress. Before reaching ε_m, the flow stress is a function of strain. The relative term in constitutive equation is often described by the power law. The determination of ε_m is hence important for the selection of constitutive equation.

2.2.2 Modelling the change of dislocation density

For steady state deformation, a generally recognised equation relating subgrain size with the internal dislocation density is written as

$$\rho_i^{1/2}\delta_{ss} = C \tag{2-13}$$

C usually varies from 5 to 30 (Sellars 1997, Zhu 1998). Compared with the steady state deformation, there is little reported data for dislocation density during transient

deformation. Several models (McQueen and Blum 1998, Luce et al 1999, Roberts et al 2000, Sellars et al 2000) have been reported to calculate the changes of dislocation density by considering the rate of generation of dislocation density and the rate of annihilation of dislocation density.

McQueen and Blum (1998) predicted the rate of dislocation annihilation ρ^- by

$$\rho^- = A\rho^{1.5}\exp(-Q/RT)\sinh\left(b^2 s k_h \sigma/(Mk'T)\right) \tag{2-14}$$

Where A is constant. The rate of generation of the dislocation density ρ^+ was given by

$$\rho^+ = (2M/b)\dot{\varepsilon}/\left(c\rho^{-0.5}\right) \tag{2-15}$$

It is clear that ρ^+ depends on the strain rate $\dot{\bar{\varepsilon}}$ and the dislocation density ρ.

The three-variable-model distinguishes three dislocation populations (Roters et al 2000): the mobile dislocations ρ_m travelling through the cell structure, the immobile dislocations density ρ_i inside the cell and the density of immobile dislocations ρ_w in the cell walls. For each class of dislocations, the evolution is also made up of a production term and a reduction form.

Sellars and Zhu's work (1997, 2000) is highlighted because it will be adopted and modified in chapter 5.

The internal dislocation density ρ_i is made up of two parts, *i.e.* the so-called "random" dislocation density (ρ_r) and the "geometrically necessary" dislocation density (ρ_g),

$$\rho_i = \rho_r + \rho_g \tag{2-16}$$

For deformation at constant Zener-Hollomon parameter Z, $\rho_g \approx \rho_r$, but for transient deformation, ρ_g is of great significance to describe the evolution of internal dislocation density. ρ_r contributes both to total stored energy and to the flow stress, but ρ_g contributes little to the flow stress.

The increment of random dislocation density due to plastic deformation is expressed as:

$$d\rho_r^+ = \frac{M}{b\Lambda_r} d\varepsilon \tag{2-17}$$

Λ_r is the average distance that a dislocation travels before being stopped. $\Lambda_r = C\rho^{1/2}$ is commonly postulated (Nes 1998, Sellars et al 1997), where ρ is the total density of stored dislocations. To simplify the calculation, ρ is assumed to equal ρ_r (Sellars et al 1997).

The annihilation of dislocation density due to dynamic recovery is given by

$$d\rho_r^- = -\frac{2L_C \bar{v}_m \rho_r}{w} dt \tag{2-18}$$

where w is the length between the sites of cross slip or climb events, L_C is the length of dislocations annihilated, $\bar{v}_m$ is the mean velocity of viscous glide, defined as

$$\bar{v}_m = D_s b \sigma_f / \beta \tag{2-19}$$

where D is the self-diffusion coefficient, β is the drag force and σ_f is the friction stress. The evolution equation for the random dislocation density is then derived as

$$d\rho_r = d\rho_r^+ + d\rho_r^- = \left(C_1 \rho_r^{1/2} - C_2 \frac{\sigma_f}{Z} \rho_r \right) d\varepsilon \qquad (2\text{-}20)$$

where $C_1 = CM/b$, C is a constant and $C_2 = 2D_0 b\beta$. At steady state deformation, $d\rho_r = d\rho_r^+ + d\rho_r^- = 0$, hence

$$C_2 = \left(Z / \sigma_f \rho_r^{1/2} \right)_{ss} C_1 . \qquad (2\text{-}21)$$

ρ_g is derived using

$$\frac{1}{R_\rho} = \rho_g b + \frac{\theta}{\delta} \qquad (2\text{-}22)$$

The local lattice curvature, $1/R_\rho$, within a grain during deformation is assumed to be constant at a given strain in transient deformation. This assumption is not totally true. Further work has been initiated.

2.2.3 Modelling the change of subgrain size

It is generally accepted that the following equation can satisfactorily relate subgrain size with temperature T, and strain rate $\dot{\bar{\varepsilon}}$, or the temperature compensated strain rate Z during steady state deformation:

$$\delta_{ss}^{-m} = A + BLnZ \qquad (2\text{-}23)$$

According to the conclusions given by Zaidi and Sheppard (1982), a good fit could be obtained for m values in equation (2-23) varying from 0.35 to 1.25. This is because the range of subgrain sizes generally obtainable in the hot working range is very small when compared with the range of LnZ values. Constants in equation (2-23) for various alloys are listed in Appendix 1. It can be seen from the appendix 1 that m equals 1 is widely used. It should be noted that equation (2-23) is not the only form of formula that relates subgrain size with process parameters for steady deformation. Other formulae modified from equation (2-23) are given as (Jonas 1969, Raghunathan 1986, Nes et al 1994):

$$\delta_{ss}^{-m} = a + bLn(Z/A) \tag{2-24}$$

$$\delta_{ss}^{-m} = a + \{b + cLn(Z/A)\}\varepsilon \tag{2-25}$$

$$\frac{1}{\delta_{ss}} = \frac{GT}{A} Ln\left(\frac{Z\delta_{ss}^{2}}{B}\right) \tag{2-26}$$

$$\begin{aligned} \frac{1}{\delta_{ss}} &= \frac{kT}{C_1} LnZ\delta_{ss}^{2} C_2 \qquad \text{when } \frac{PV_a^b}{kT} \succ 1 \\ \frac{1}{\delta_{ss}} &= \left[\frac{kTZC_2}{C_1}\right]^{1/3} \qquad \text{when } \frac{PV_a^b}{kT} \prec 1 \end{aligned} \tag{2-27}$$

where P is the driving pressure for subgrain growth, V_a^b is the activation volume, k is geometric constant, $C_1 = 2\gamma_{SB}V_a^b$, $C_2 = 0.0004M/(\nu_D b^2 C_B)$, C_B is a constant, ν_D is the Debye frequency (Nes et al 1994).

It must be emphasised here that the equations (2-23 to 2-27) are just statistical expression from experimental data, strictly they have no physical interpretation, and are not valid to predict subgrains size in transient deformation.

Compared with the work on subgrain size during steady state deformation, there is still a lack of quantitative relationships to relate the subgrain size with the deformation parameters in transient deformation. During the last few years, Furu et al (1999), and Sellars et al (2000) have carried out some exploration work in this field. They have performed transient deformation by altering the strain rate in plane strain compression (PSC) tests. The PSC specimens of $60.0\times50.0\times10.0mm^3$ were machined from homogenised , rolled and annealed material with fully recrystallised grains of major intercept length $(117\pm5)\mu m$. A graphite lubricant was used for all tests. The specimens were quenched within 1.5s of the end of deformation. Their conclusions for internal dislocation density, subgrain size and misorientation are shown in Fig.2-2.

For deformation at constant strain rate, the subgrain size decreases. For deformation at increasing strain rate, the subgrain size also decreases with strain until a steady state size is achieved at a strain of about 1.0. Under transient conditions of reducing strain rate to a strain of 1.0, the subgrain size is smaller than the steady state size. After a strain of 1.0, the subgrain size increases suddenly, interpreted as the dissociation of subgrain boundaries. The steady state value is eventually achieved at a strain of about 1.6.

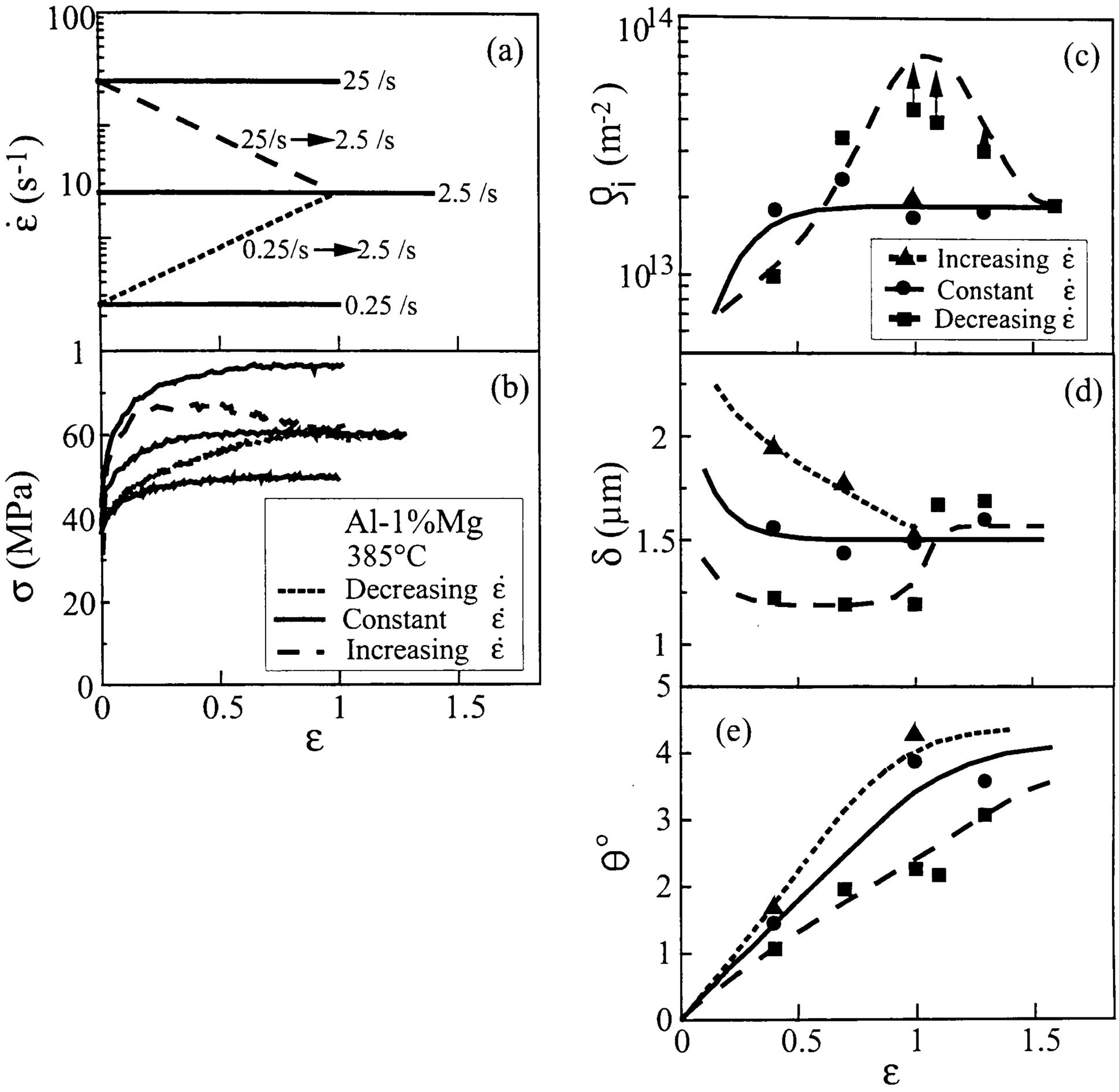

Figure 2-2 Experimental results of evolution of (a) strain-rate, $\dot{\varepsilon}$, (b) flow stress, σ, (c) internal dislocation density, ρ_i, (d) subgrain size δ, and (e) misorientation between subgrains, θ, of Al-1%Mg deformed at 385°C in plane strain compression tests (After Sellars and Zhu 2000).

It is clear from the above analysis that the subgrain size shows a very complex behaviour with strain during transient deformation, especially in the case of decreasing strain rate. Fortunately, for most metal forming processes, subgrain forms and stabilises in the stage of increasing strain rate, such as from the entry bite to the exit in hot flat rolling and from the rear of container to the die mouth in hot rod extrusion. The periods of decreasing strain rate in these two processes are very

short. It should also be noted that measurements of subgrain size before the steady state regime have not been presented in the case of constant strain rate (see Fig.2-2 (d)). It is also clear that the prediction of initial subgrain size has not been logically studied.

Comparing (b) with (c), (d) and (e) in Fig.2-2, it can be seen that the flow stress can not be uniquely expressed as a function of dislocation density, subgrain size and misorientation when the transient deformation condition of decreasing strain rate is applied. This indicates that a simple work hardening and recovery approach is not sufficient. A different mechanism occurs. The sudden increase in dislocation density was attributed to the subgrain boundaries dissolving (Zhu et al 1997).

The following equation has been applied successfully to model the behaviour of Al-1%Mg alloy:

$$d\delta = \frac{\delta}{\varepsilon_\delta \delta_{ss}}(\delta_{ss} - \delta)d\varepsilon \qquad (2\text{-}28)$$

Where "ss" stands for steady state, δ is the instantaneous subgrain size, $d\varepsilon$ is the increment of strain, $d\delta$ is the increment of subgrain size, ε_δ is characteristic strains, which determine the rates of evolution of subgrain size, δ_{ss} is defined as the same as equation (2-23). ε_δ is assumed proportion to Z^n. It is strange that Zhu and Sellars (1997,2000) assigned different values (-0.5 and ¾) to the exponent n in two papers for the same material and experimental conditions. However, it indicates that ε_δ is a function of Z. The specific form relating ε_δ with the Zener-Hollomon parameter may depend upon the deformation conditions and the material.

2.2.4 Modelling of the change of misorientation

For obvious experimental reasons, the variation of misorientation θ has not been extensively investigated. Some work concerned with high purity aluminium is shown in Fig.2-3 (Nes 1998). The figure clearly shows that the average boundary misorientation increases rapidly with strain, reaching about 2^0-3^0 at a strain of about 1, after that it remains constant up to strains as high as 4. According to Fig.2-3, a simple relationship can be derived

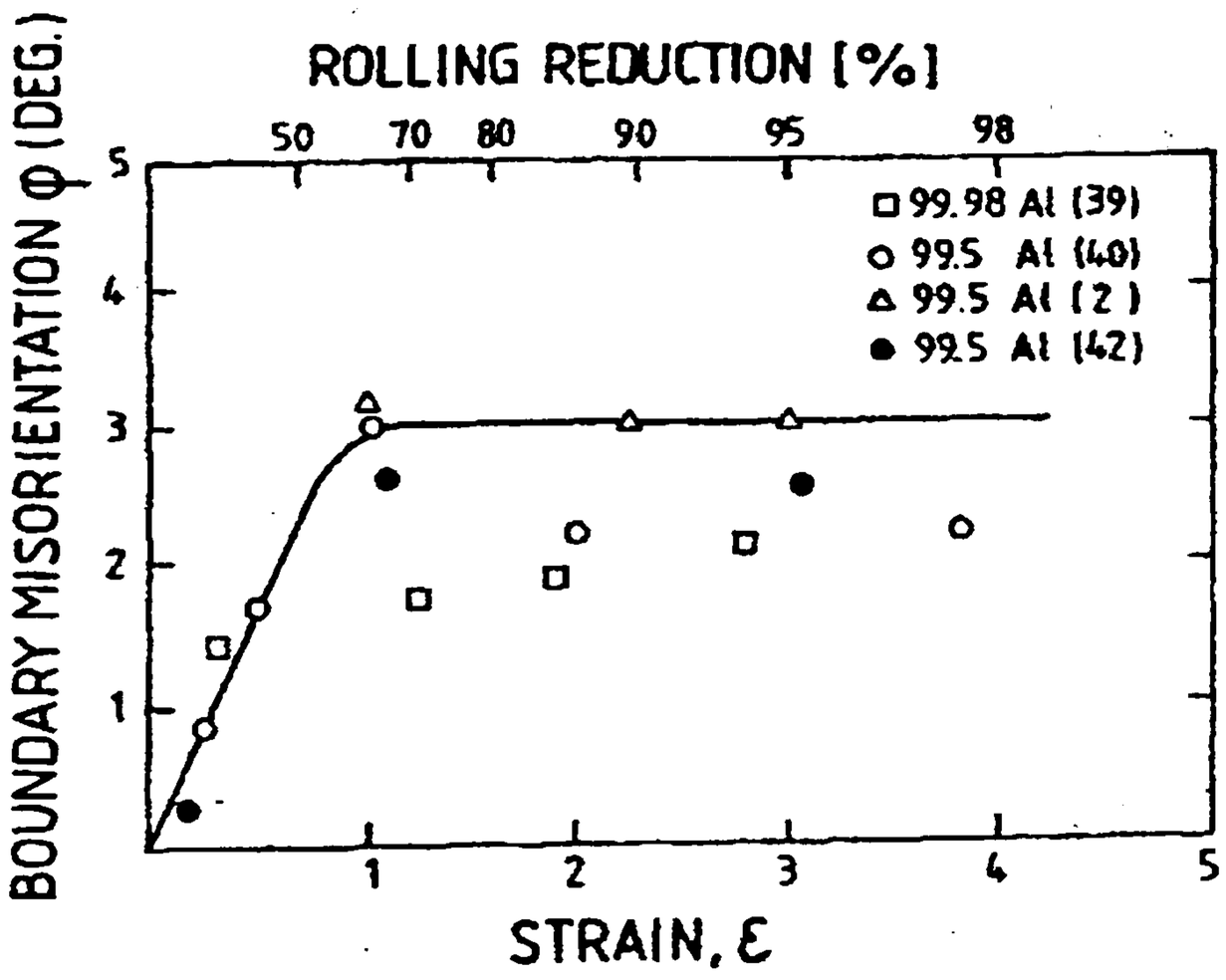

Fig.2-3 Sub-boundary misorientation vs strain (after Nes 1998)

$$\theta = 3. \times \varepsilon \quad \text{if } \varepsilon \leq 1.$$

$$\theta = 3. \qquad \text{if } \varepsilon \succ 1. \tag{2-29}$$

Sellars and Zhu (2000) have recently proposed another relationship for Al-1%Mg alloy during transient deformation conditions:

$$d\theta = \frac{1}{\varepsilon_\theta}(\theta_{ss} - \theta)d\varepsilon \tag{2-30}$$

where ε_θ is a characteristic strain. $\varepsilon_\theta \propto Z^{1/4}$ is assumed in their study. Fig.2-2 (e) shows the comparison between the predicted and the measured misorientation. For increasing and for constant $\dot{\varepsilon}$, the calculated curves show similar shape as the curve presented in Fig.2-3. The variation of misorientation under decreasing $\dot{\varepsilon}$ is more complex. But this condition does not happen in rolling. Therefore, equation (2-29) has adequate capacity to predict the misorientation.

2.2.5 Substructure strengthening

The mechanism of substructure strengthening has been a research focus in metallurgy for some time during the last decades (Jonas et al 1969, Zaidi et al 1982, Nes et al 1994, Marthinsen et al 2001). In the earlier work, when the values for dislocation was not established, and the misorientation was regarded to play only a minor role in determining the flow stress (Jonas et al 1969, Marthinsen et al 2001), only the experimental relationship between subgrain size and the flow stress was established. A modified Hall-Petch relationship is generally accepted for describing this kind of relationship during steady state deformation:

$$\sigma = \sigma_f + k\delta^{-m} \tag{2-31}$$

Where σ_f is the frictional stress, δ is the subgrain size, k is a constant. With the introduction of new techniques into experimental measurement, models based on dislocation, subgrain size, misorientation and grain size have been reported. The most recent formulae include

$$\sigma = \sigma_f + \alpha_1 M G^* b\sqrt{\rho_{tot}} \tag{2-32}$$

$$\sigma = \sigma_f + \alpha_1 M G^* b\sqrt{\rho_i} + \alpha_2 M G^* b/\delta \tag{2-33}$$

$$\sigma = \sigma_f + \sigma_p + \alpha_1 M G^* b\sqrt{\rho_i} + \alpha_2 G^* b[1/\delta + 1/D] \tag{2-34}$$

where α_1 and α_2 are constants, ρ_{tot} in equation (2-32) is the total dislocation density given by :

$$\rho_{tot} = \rho_i + \frac{\kappa\theta}{b\delta} \tag{2-35}$$

where $\kappa = 3$ is a geometric constant (Nord-Varhaug et al 2000), θ is the misorientation between the subgrains.

In the calculations, the following values of parameters mentioned above have been selected: $G^* = 2.99\times10^4 \exp(-5.4\times10^{-4}T)$ (Marthinsen and Nes 2001), $b = 2.86\times10^{-10}$ m. For high purity Al-1%Mg (Zhu et al 1997), σ_f=25, α_1=0.26, α_2=0.83; for commercial Al-1%Mg (Zhu et al 1998), σ_f=25, α_1=0.18, α_2=0.83. Based on a considerable amount of investigation on various aluminium alloys, Nord-Varhaug et al (2000) have found that $\sigma_f = 0.1\sigma_{exp}$, α_1=0.3, α_2=2.0 give a better prediction for samples deformed by hot torsion, PSC (plane strain compression) and uniaxial compression. Nes (1998) and Marthinsen and Nes (2001) have concluded that equation (2-33) and equation (2-34) give a much better prediction than does equation (2-32).

There is another model (Roters et al 2000) which considers the dislocation density as the characteristic state variable. The flow stress is calculated by

$$\sigma = M\left(f_i \cdot \tau_{eff,i} + f_w \cdot \tau_{eff,w}\right) \tag{2-36}$$

where M is the average Taylor factor, f_i and f_w are the weight factors, and $\tau_{eff,i}$ and $\tau_{eff,w}$ are the effective stress inside the cell or cell wall. Theoretically, equation (2-36) is the same as equation (2-33) since the strengthening by dislocation density inside cell walls equals the strengthening effect by subgrain size. However, there is an obvious difference in the application between equation (2-33) and equation (2-36) because the mode of calculations for ρ_w and δ are quite different.

2.3 Modelling of static recrystallisation

There are two types of models: empirical and physical, which deal with the kinetics of static recrystallisation (SRX). Each model has its advantages. In general, empirical models are easy to use and could be accepted by industry for off-line microstructure control. The physical model is advanced in theory and is only studied in academia at the present time. However, the model reveals the physics behind the transformation and if the problem of evaluating the constants can be overcome, it would clearly very useful.

2.3.1 Empirical model

The relationship between the fraction of recrystallised (X_V) and the holding time (t) is generally represented by the Avrami equation:

$$X_V = 1 - \exp\left\{-C\left(\frac{t}{t_f}\right)^k\right\} \tag{2-37}$$

t_f is the time to recrystallise the fixed volume fraction f, k is a constant. In practice k has a value of about 2. C is a constant given by

$$C = -\ln(1-f) \tag{2-38}$$

The usual convention is to fix f at 50% and this leads to the characteristic time for 50% recrystallisation ($t_{0.5}$). In this case, C becomes ln2. Equation (2-37) is rewritten

$$X_V = 1 - \exp\left\{-\ln 2\left(\frac{t}{t_{0.5}}\right)^2\right\} \tag{2-39}$$

The time to 50% recrystallisation is usually given as

$$t_{0.5} = Ad_0^a \varepsilon^b Z^c \exp\left(\frac{Q_{rex}}{RT_a}\right) \tag{2-40}$$

A, a, b, c are constants regressed from experimental data.

Recrystallised grain size is calculated by the following equation

$$d_{rex} = Bd_0^e \varepsilon^f Z^g \tag{2-41}$$

B, e, f, g are constants. The constants in equation (2-40) and (2-41) are listed in the appendix 2 for various aluminium alloys.

From the appendix 2, it is clear that A has a positive value; b and c have negative values. This means that small grain size, high Z, high strains and high annealing temperatures all decrease $t_{0.5}$, and hence increase the fraction recrystallised.

It should be noted that equation (2-37) is not the only form possible. In extrusion, the fraction recrystallised X_V is usually less than 50%. Hence the term $t_{0.5}$ can not be used. A replacement is using t_0, the time to just give zero recrystallisation. The modified expression for X_V is given by the form of equation (Sheppard 1993b)

$$\ln\ln\left(\frac{1}{1-X_V}\right) = K_0 + K_1 \ln d_0 + K_2 \ln Z - K_3 T - K_4 \ln t - K_5 \ln \varepsilon \qquad (2\text{-}42)$$

2.3.2 Physical models

There are two main research groups (Nes et al at the Norwegian University of Science and Technology, Norway; Sellars et al at the University of Sheffield, UK) who have carried out similar researches on the modelling of SRX behaviour for aluminium alloys. All models are built on the calculation of the number of nucleation sites and the total stored energy, which are two key parameters for the occurrence of SRX. Since two groups have different research objectives, and use different materials in their work, the consideration of the number of nuclei is therefore different, resulting in different models.

Nes et al. have mainly concentrated on the cube texture evolution in multi-pass rolling during steady state deformation. The major alloy studied is AA3004 (Vatne 1995,1998, Nes 1998), which is regarded as containing large undeformable particles. These particles are considered as an important and often governing nucleation mechanism. Three types of nucleation sites are involved: deformation

zones around particles, cube sites and grain boundary regions. The total stored energy (or driving force) P_D is expressed as:

$$P_D = 0.5M\left(\frac{bC_\delta}{\delta}\right)^2 + 0.05M\frac{b}{\delta} \tag{2-43}$$

where C_δ is a constant of typical value of the order 5. The fraction recrystallisation $X(t)$ after time t is written:

$$X(t) = 1 - \exp(X_{ext}(t)) \tag{2-44}$$

$X_{ext}(t)$, the corresponding extended volume, is determined by:

$$X_{ext}(t) = \frac{4}{3}\pi N_{ToT}(G' \cdot t)^3 \tag{2-45}$$

G' is the growth rate of recrystallised grains. N_{TOT} is the sum of above three types of nuclei. The recrystallised grin size d_{rex} is given by:

$$d_{rex} = \left(\frac{X}{N_{TOT}}\right)^{1/3} \tag{2-46}$$

Sellars et al. (2000) and Zhu et al (2001) have built their models on the basis of three internal state variables, δ, ρ_i and θ. Al-Mg alloys are deformed by plane strain compression (PSC). Their work has focused on the influence of transient deformation on the substructure evolution and static recrystallisation behaviour. Since deformation is performed by plane strain compression and the material is high purity Al-Mg alloy, there is no cube band before or after deformation; grain boundaries are therefore the dominant nucleation sites. Hence only the nuclei at grain boundaries have been considered in their models. Adopting such a strategy is helpful for understanding one nucleation mechanism thoroughly.

In their work, the total stored energy, $P_{D,}$ is calculated by

$$P_D = \frac{Mb^2}{10}\left[\rho_i\left(1-\ln\left(10b\rho_i^{1/2}\right)\right)+\frac{2\theta}{b\delta}\left(1+\ln\left(\frac{\theta_c}{\theta}\right)\right)\right] \tag{2-47}$$

The time to 50% recrystallisation is expressed as:

$$t_{0.5} = \frac{C}{P_D}\left(\frac{1}{N_V}\right)^{-1/3} \tag{2-48}$$

Where C is a constant. The fraction recrystallisation $X(t)$ after time t is the same as equation (2-39). The recrystallised grin size d_{rex} is written as:

$$d_{rex} = A\left(\frac{1}{N_V}\right)^{1/3} \tag{2-49}$$

Since physical modelling model is still at the exploration stage, there are several uncertain parameters in the above equations, such as G' in equation (2-45), and A in equation (2-49) etc. All these parameters are obtained by fitting the calculated results with experimental data. The reasons for such an analysis are attributed to: (1) these parameters are too difficult to measure by using current experimental equipment; (2) this kind research is just at the starting stage, few experimental data are available; (3) there are still some mechanisms which are not very clear, for example how the microband forms. Previous works have shown that the microbands are a preferential nucleation site (Zaidi and Sheppard 1982, Jonas 1969); (4) the determination of the initial internal dislocation density (ρ_0) of annealed materials. Most workers consider this value to be 10^8 to 10^{10} m^{-2}. The

upper limit is 100 times the lower limit. This is a significant difference. In Sellars and Zhu's work (2000), ρ_0 is even taken as 10^{11}. All these uncertain factors restrict the application of physically based models because they can not be directly applied to other materials. The ambition of obtaining a model, which has the capability of prediction power for cases outside the alloy test conditions, is however one should be pursued.

It should be emphasised again that Nes et al's model is only applicable to steady state deformation with strains greater than 0.5, while Sellars et al's models are proposed for transient deformation. This perhaps explains why equation (2-46) and equation (2-49) do not have the same form and there is the introduction of a coefficient in equation (2-49).

2.4 Prediction of microstructure evolution by FEM

2.4.1 Dislocation density and misorientation

Modelling the evolution of dislocation density by FEM started during the 1980's and was concerned mainly with steels. Lenard et al (1999) has given an excellent review in this aspect in their book. In the present thesis, attention will only be paid on the application of the models introduced in the section 2.2.2, because they are the latest work and must be advanced in theory. They are also the basis for the modelling of other metallurgical phenomena, i.e. the work hardening behaviour, static recrystallisation and texture evolution.

In recent years, only the model proposed by Roters et al (2000) has been incorporated into a commercial FE program to simulate the rolling process for an Al-alloy (Luce et al 2000, Aretz et al 2000). Integrating Sellars and Zhu's model into FE programs has not been reported.

None of the past work has dealt with the simulation of misorientation. From the introduction in section 2.2.4, it can be seen that the modelling of misorientation is easy compared with the simulation of subgrain size and dislocation density. Equation (2-47) indicates that the calculation of misorientation is inevitable if we want to compute the value of P_D, which is the basis of all physical models for the modelling of static recrystallisation.

2.4.2 Subgrain size

There are two ways to predict the subgrain size. The first is using equation (2-23). It would appear to be a trivial task to predict the subgrain size and distribution, just simply substituting nodal strain rate and nodal temperature directly into equation (2-23). However, the work in chapter 5 will show that the computed distribution of subgrain size based on such a computation is incorrect. Hence, some modifications must be made for equation (2-23) when using FEM.

At the present time, the present author is aware of only two attempts to predict the subgrain size by FEM: Dashwood et al's (1996) study on AA7075 during rod extrusion and Chen et al's (1992) prediction for hot rolling of pure aluminium. The predicted result by Dashwood et al. fit reasonably well with the experimental measurement in a small region around the die mouth. The distribution of subgrain size within the container was not given. However, in their study, there is one dubious assumption. The value of activation energy, which is used to calculate Z by equation (2-11), is twice the normal value of activation energy, and the authors did not present relevant experimental data to support this modification. The activation energy is a process parameter. It is approximately 156 KJ/mol for thermal activation during deformation for nearly all aluminium alloys. Of course, there will be somewhat variations from these values according to the fraction of cross-slip, climb, glide etc. of the dislocation movements in the alloy. It is not a parameter,

which can be tuned in order to match the predicted result with experimental measurement.

Chen et al. averaged the Zener-Hollomon parameter over each element in the whole deformation zone and then integrated with time during simulation. This model gave an acceptable result. The relative error between the measured and predicted results is about 20%. There is also a problem with the method presented. That is how to average the Zener-Hollomon parameter over the whole deformation zone and what physical interpretation would justify this action? The authors' interpretation cannot be accepted.

The second way to predict the subgrain evolution is in using physical model. Only Vatne et al (Vatne et al 2000) have applied Nes's subgrain model (Nes 1998) to predict the subgrain size after the deformation pass in order to calculate the driving pressure for subsequent recrystallisation. The predicted subgrain size was reported to be good (no computed distribution of subgrain size was given). However, the predicted subgrain size was not actually adopted in their calculation for static recrystallisation.

2.4.3 Static recrystallisation (SRX)

There are three ways to predict SRX: empirical model, physical model and cellular automaton.

When using the empirical model, the FEA results are postprocessed to produce a mean value of Z and final equivalent strain for the differing through-thickness locations. These two values are then substituted into equation (2-40) to derive the value of $t_{0.5}$, and finally the fraction recrystallised X_f is calculated by the use of equation (2-39). Several attempts have been carried out by using this approach (Dauda& McLaren 1999, Chen et al 1992, McLaren and Sellars 1993, McLaren

1994, Yiu et al 1991, Brand et al 1996, Wells et al 1998, and Mirza et al 2001) and all assumed plane strain deformation.

For the modelling of SRX after single pass deformation, Chen et al (1992) simply incorporated the FE output into equation (2-11) without any modification, and their prediction was not validated by experimental or industrial data. The predicted fraction recrystallised falls from the surface to the centre. McLaren et al compared their prediction with experimental data for commercial purity aluminium in a small mill (roll diameter is 68mm) (McLaren 1994), (see Fig.2-4). An unrealistic measurement of the fraction recrystallised at the surface was presented and not explained. The measured fraction recrystallised at the surface is even smaller than that at the centre, and the value at the centre appears to be too large. The predicted fraction recrystallised is in fact much higher than the measurement at the surface. The poor prediction has been attributed to the geometric factors through the section, such as the ratio of the roll contact length/stock thickness, which determines the homogeneity of the deformation. Recently, Dauda & McLaren (1999) measured and simulated the gradient of fraction recrystallised for high purity Al-3%Mg alloy. Full static recrystallisation in the slab was achieved before rolling. The comparison between the measurement and prediction is shown in Fig.2-5. It is clear that the rate of recrystallisation increases steadily from the slab centre to the surface. But the prediction is still much greater than the measurement at the surface, and the measured gradient from the centre to the surface appears to be lower than the normal industrial measurement. Yiu et al's measurement provided a strong quantitative evidence that the fraction recrystallised should fall from the surface to the centre see Fig.2-6 (Yiu et al. 1990). Compared with Fig.2-5, there is significant difference on the fraction recrystallised between the surface recrystallised and the centre in Fig.2-6a. The value of the fraction recrystallised at the surface is in a reasonable range.

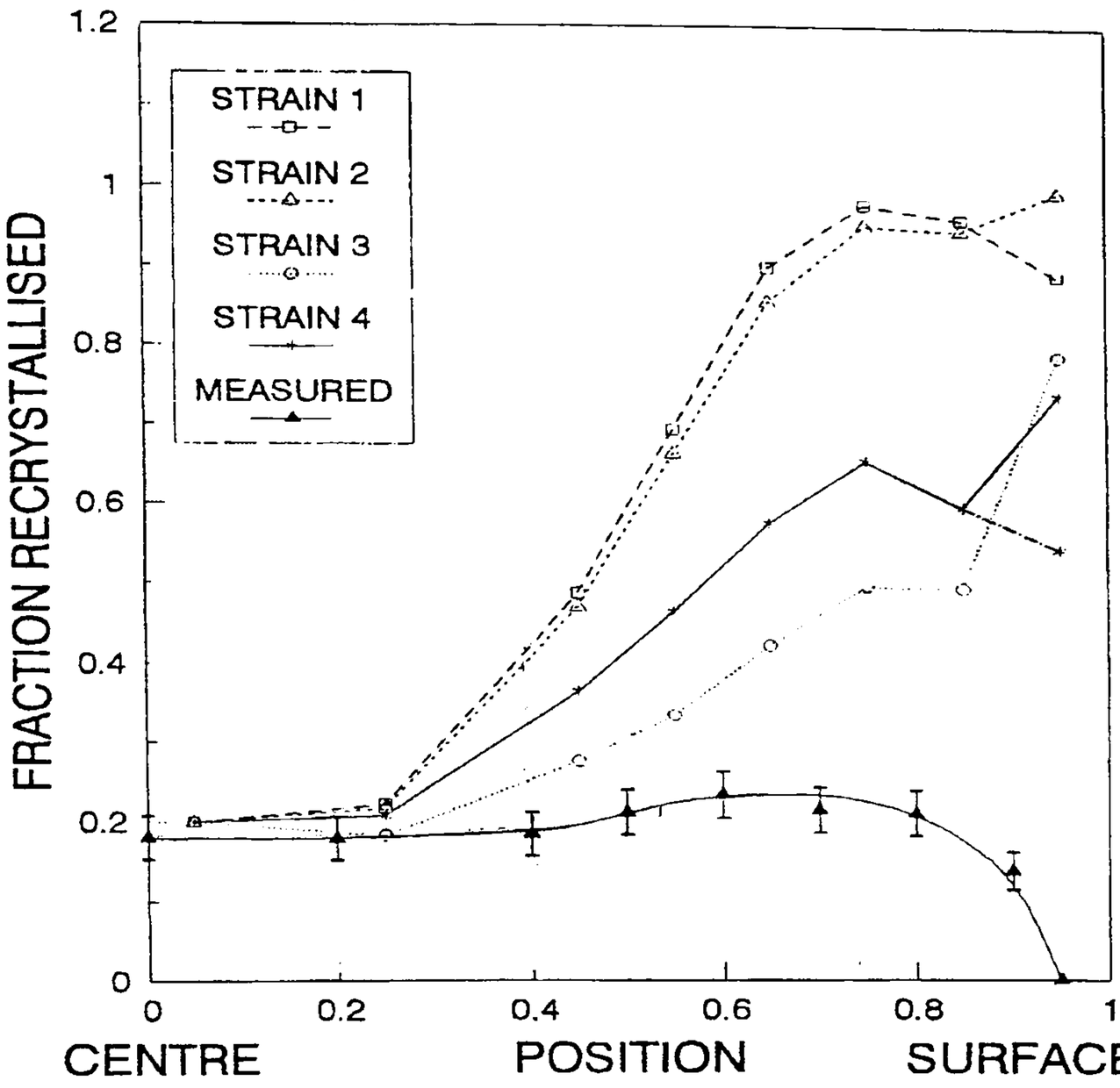

Fig.2-4 Comparison between the predicted and measured gradients in fraction recrystallised (after McLaren 1994)

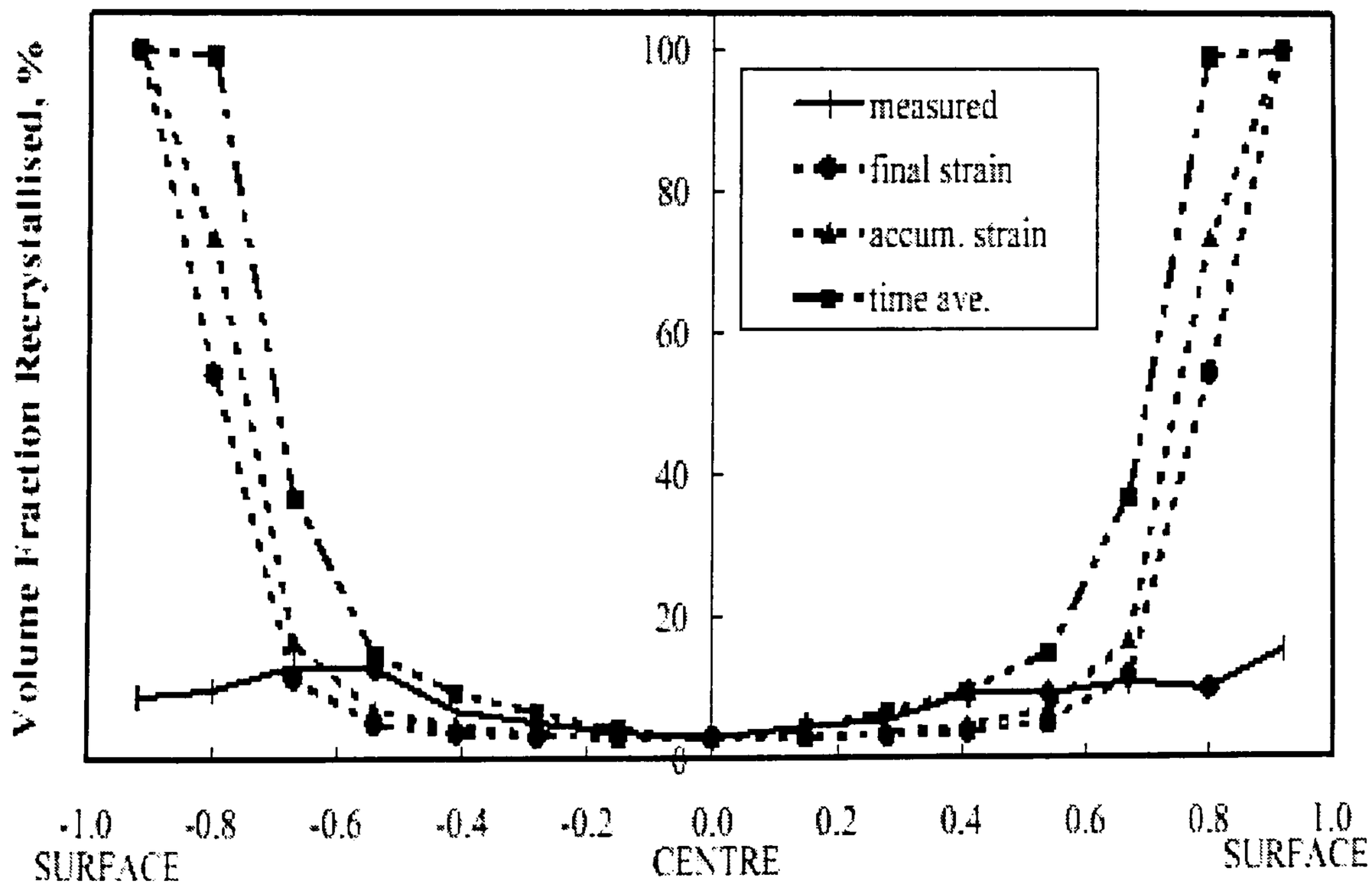

Fig.2-5 Comparison between the measured and predicted microstructural gradients (after Dauda & McLaren 1999)

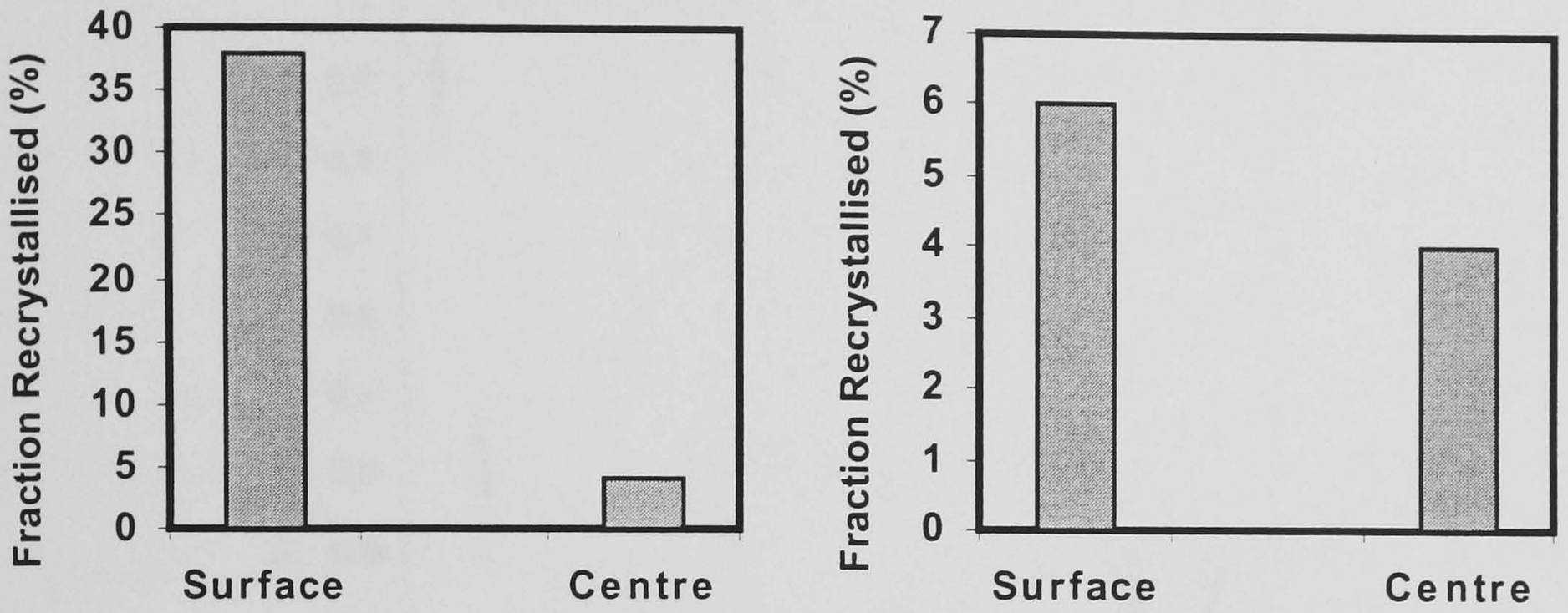

(a) (b)

Fig.2-6 Comparison of fraction recrystallised (a) 4.45% Mg alloy (b) 1% Mg alloy (After Yiu et al 1990)

When modelling multipass hot flat rolling, Brand et al predicted the grain size evolution for AA2024 during a 6-pass rolling schedule (Brand et al 1996). Their method to deal with the combination between FEM and empirical models seems efficient. But regretfully, they did not give the predicted distribution of the fraction recrystallised or any measured data on grain size or the fraction recrystallised. Their results show a small gradient region near the surface where the grain is coarser than at the centre. Their conclusions were that " the kinetics for static recrystallisation is not evaluated exactly, the onset of SRX is calculated to occur too early in the multistage rolling process". Most recently, Mirza et al reported a very small prediction of the fraction recrystallised at the surface and relative high prediction at the centre for a 17-pass industrial schedule for AA3104 using two different approaches (Mirza et al 2001). No comparison with the measurement was presented in their work. The above two modelling results are unacceptable. The present authors have discussed this problem with several researchers connected with a large international aluminium company who have access to a considerable amount of micrographs. None of their micrographs support the above modelling results.

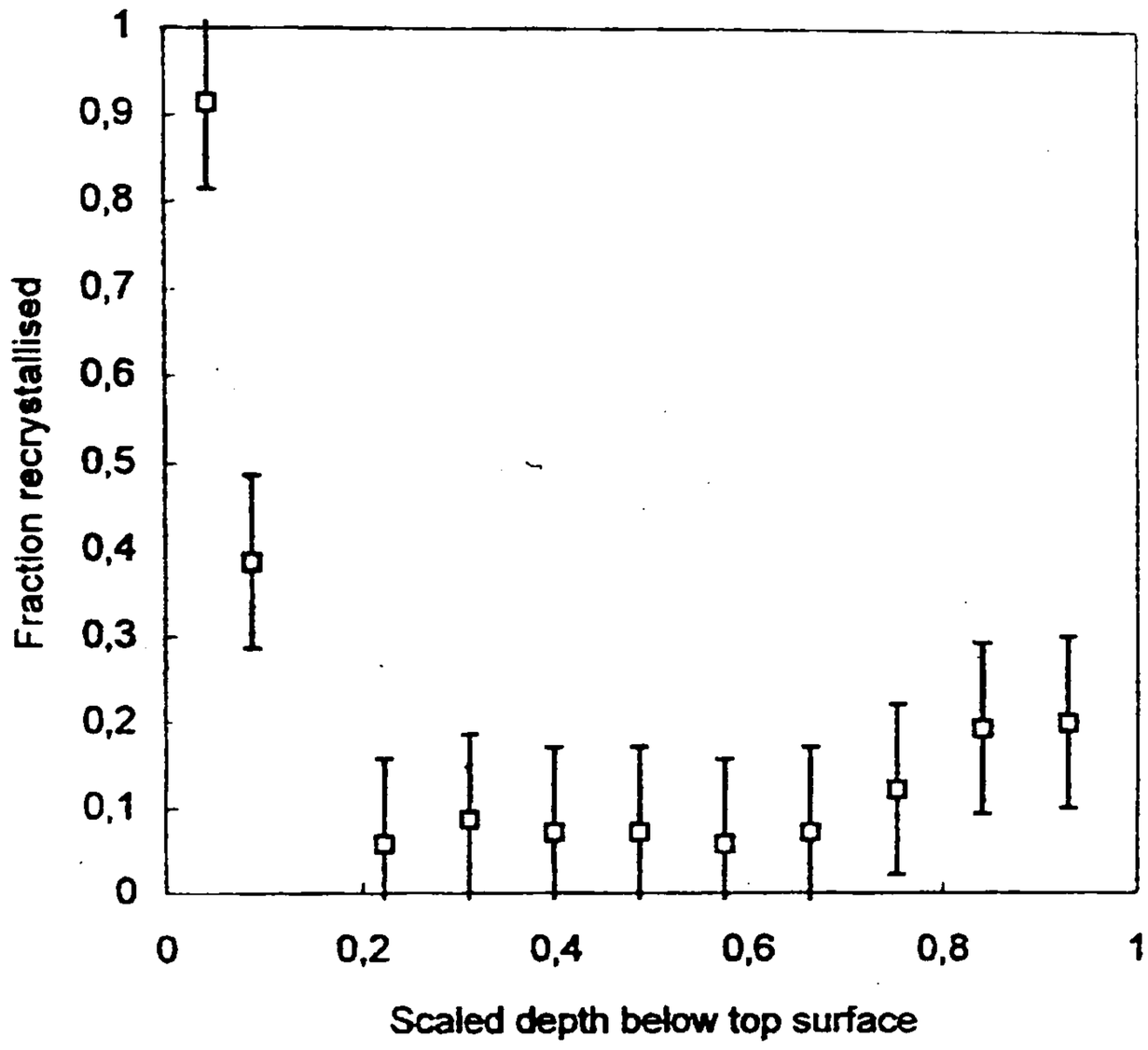

Fig.2-7 Measured Fraction recrystallised after 8 passes as function of depth below the top surface (after Winden 1999)

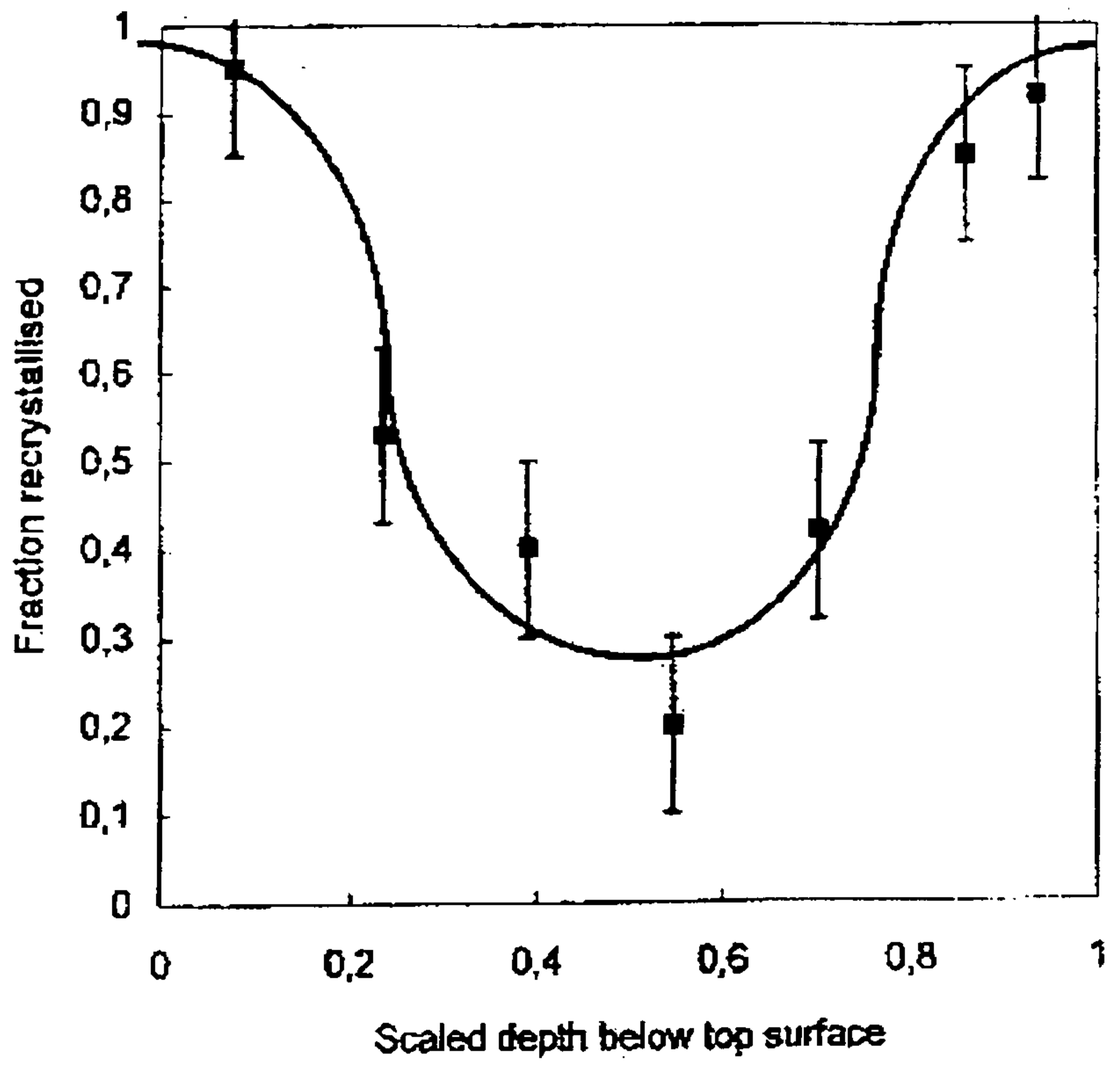

Fig.2-8 Measured Fraction recrystallised after 11 passes as function of depth below the top surface (after Winden 1999)

In contrast, Winden's laboratory measurement for this alloy in a 14-pass rolling schedule show that the maximum fraction recrystallised is at the surface, see Fig.2-7 and Fig.2-8 (Winden 1999). Wells et al measured a slightly finer grain size at the surface than at the centre after 3-pass hot tandem rolling of AA5182, see Fig.2-9, and there is an obvious difference in the distribution of the predicted recrystallised grain size through the thickness, see Fig.2-10 (Wells et al 1998). We can conclude from Fig.2-9 that the grain size is not wholly dependent on the variation of the fraction recrystallised because the gradient of grain size is much lower than the gradient of fraction recrystallised. Black et al's micrographs provide direct metallurgical evidence that rapid recrystallisation occurs at the surface in laboratory rolling, see Fig.2-11 (Black et al 2001). The alloy used in Black et al's laboratory experiments is Al-1%Mn alloy. The first micrograph was obtained by a 30% pass followed by a further 40% pass in the same direction. The second micrograph was obtained by 30% forward rolling followed by 40% reverse rolling.

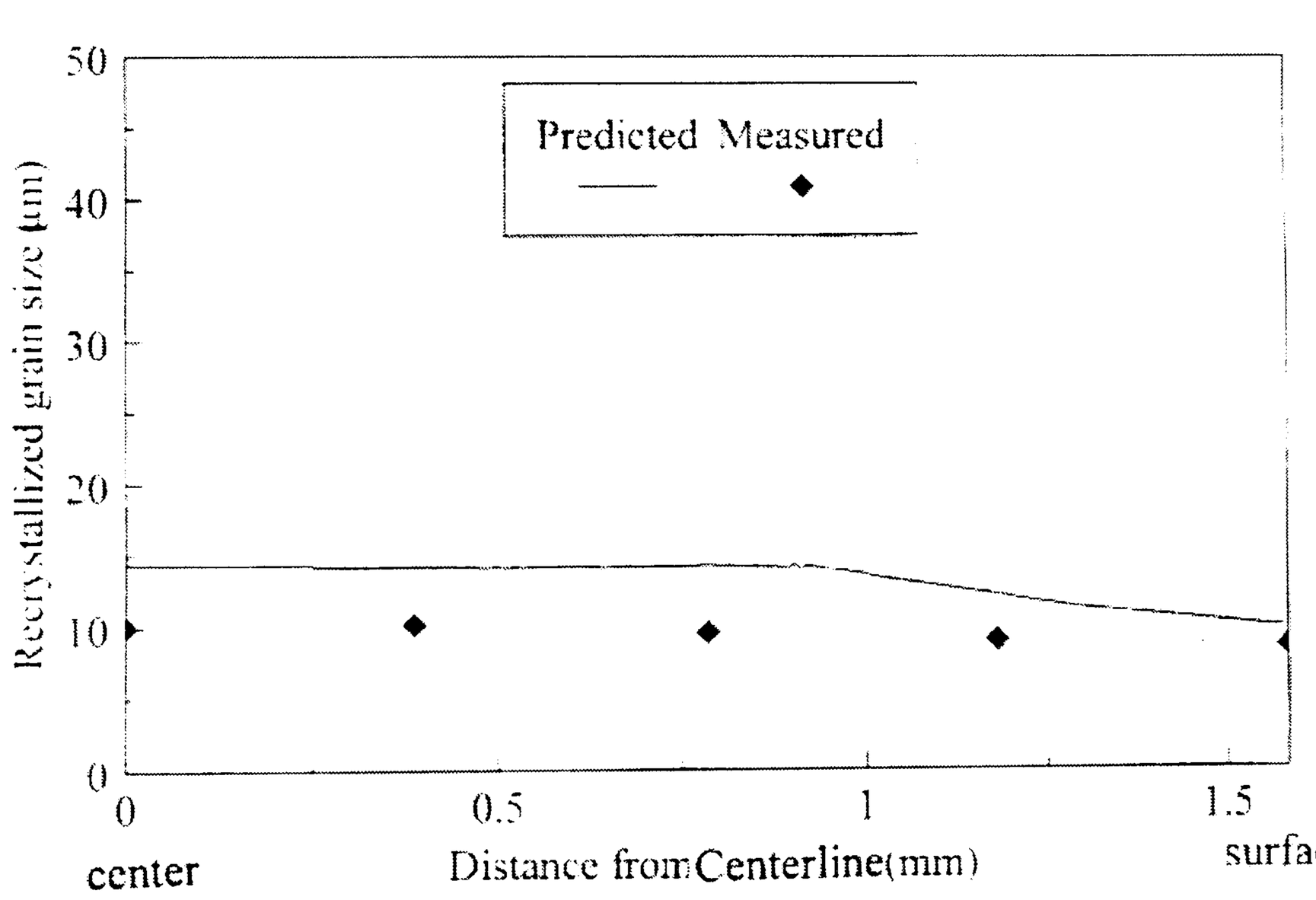

Fig.2-9 Comparison of model-predicted and experimental measurements of grain size in the strip after hot rolling for AA5182 (After Wells et al 1998)

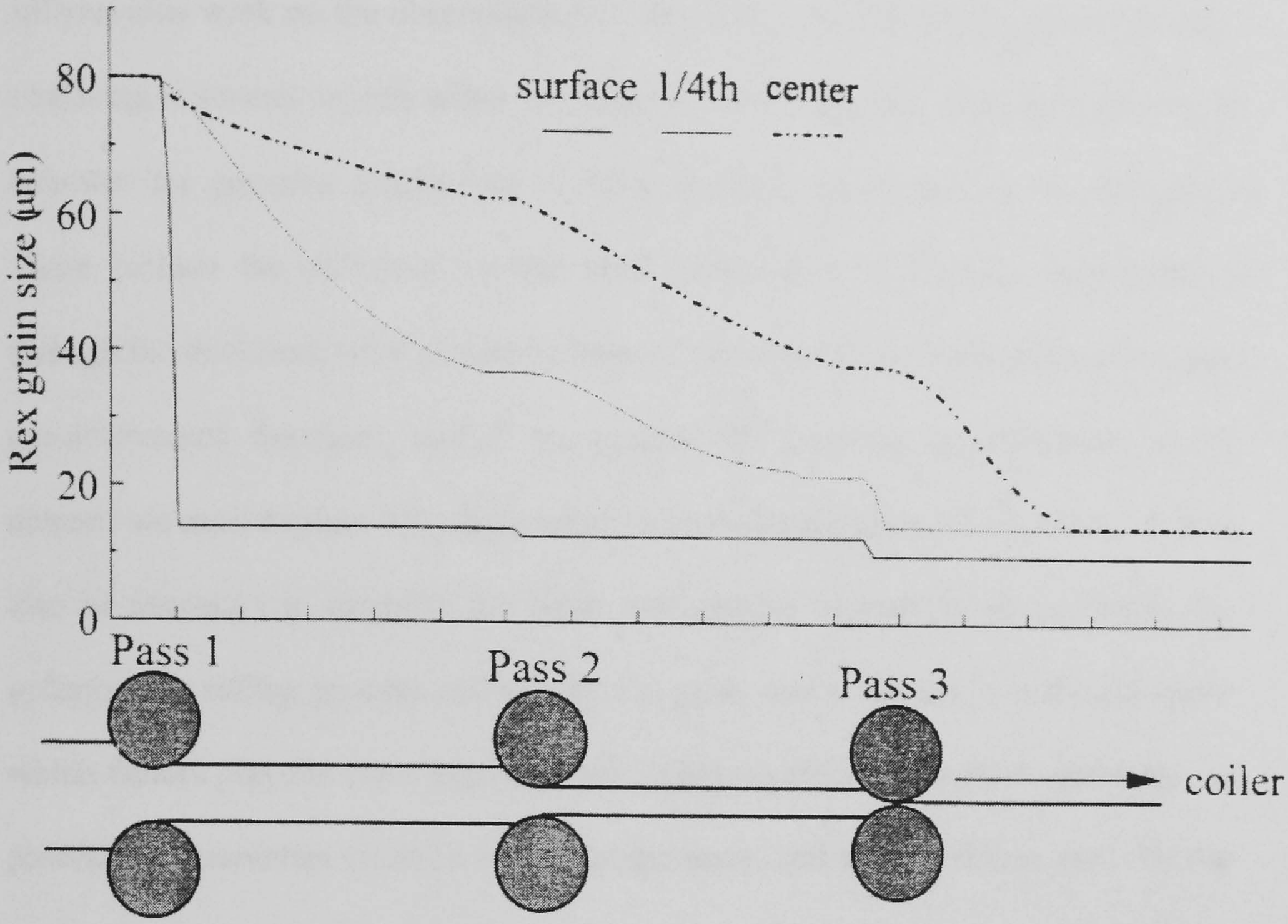

Fig.2-10 Model predicted average grain size throughout the hot tandem mill for AA5182 (after Wells et al 1999)

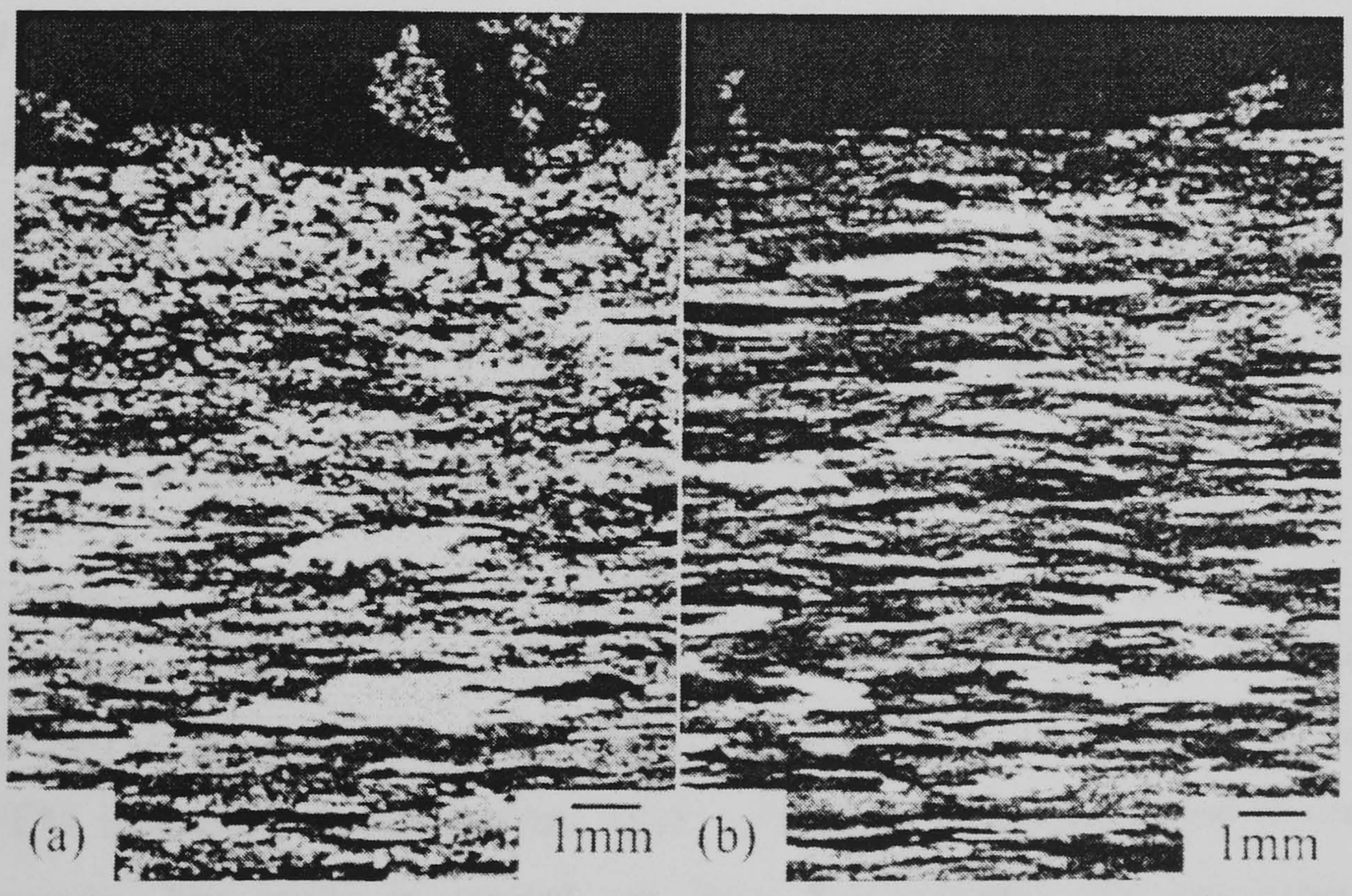

Fig.2-11 Micrographs showing material half thickness in ND-RD plane for (a) 20/40FF and (b) 30/40FR specimens annealed for 10s (after Black et al 2001)

All previous work on the observation and modelling of SRX has proved to be very confusing in several aspects either for single pass rolling or for multi-pass rolling. It indicates the complex mechanism of SRX. Several critical factors are unknown. These include the definition of the ideal distribution of fraction recrystallised through the thickness, what should be form of distribution (i.e homogenous or some pre-determined function), and if we assume all previous measurements to be correct, we must explain why these controversial distributions are necessary. It will also be necessary to establish the basic mechanisms behind the phenomenon. To optimise the rolling process and control the grain size evolution, we should know which factors play the most important role: alloying element, or stock geometry, or processing parameters (such as rolling temperature, roll speed, friction etc.). Of the testing methods available, it will be necessary to define which test is most suitable to satisfy the basic physical premises such that empirical models similar to equation (1) and (2) may be more meaningfully interpreted. The evidence presented would suggest that laboratory rolling would appear to be the preferred test at the present time. However, before commencing modelling by numerical methods, these questions must be clearly answered; otherwise any work would be questionable. Some of these points are covered in this thesis; others remain unsettled.

From Fig.2-4 to Fig.2-6, one conclusion can certainly be drawn: the fraction recrystallised is overpredicted at the surface region after a single pass deformation when FEM is applied. In the present work, new methods are proposed to correct this anomaly. The study is carried out from four aspects: the calculation of

equivalent strain; the calculation of Z; averaging Z and the application of different empirical models.

Coupling probabilistic cellular automaton with crystal plasticity FEM for simulating primary static recrystallisation have been reported by Rabbe and Becker (2000). The coupling between two models consists of: "extracting and translating the microstructure and stored energy data predicted by the FEA into the cellular automaton model; mapping these data on the quadratic cellular automaton in terms of the derived cell size, maximum driving force, and maximum grain boundary mobility occurring in the region, and establishing an adequate nucleation criterion, which makes use of these data. Davies(2000) and Aretz et al (2000) combined the modified cellular automaton with normal FEM to predict the nucleation and grain growth during static recrystallisation. The cellular automaton was not fully integrated into FEM. Some elements are picked out of the workpiece mesh. If the elements leave the deformation zone below the rolls, the FE simulation will be stopped and the resulting data (dislocation density) transferred to the cellular automaton simulation.

Combining the physical model described in section 2.3.3 with FEM to predict SRX has not been reported. These approaches are not so complicated as cellular automaton in terms of programming and better than using the empirical model from the point of view of metallurgy. However, this approach requires the predictions of ρ_i, δ and θ. As discussed before, no successful examples have been given for the simulation of subgrain size and misorientation. After solving these two problems, it would be possible to employ the physical model.

2.5 Design of hot rolling pass schedule

Designing a rational pass schedule is the most effective way to control the final product qualities. However, it is very difficult to obtain any information about the

rolling pass schedule from the aluminium industry because of commercial sensitivity. But, it is relatively easy to find the published pass schedules for steels in the literature (Wehage et al 1998b, Mäntylä et al 1992, Svietlichnyj and Pietrzyk 1999).

According to different production requirements and applications, the process of aluminium hot strip rolling is categorised into five main processes (Barnes et al 1996): the twin roll caster routine, the process of thin slab casting followed by rolling on a hot tandem finishing mill, reversing roughing mill which performs both roughing and finishing duties, the hot reversing roughing mill coupled with a reversing warm finishing mill, and the conventional hot rolling process: reversing roughing mill followed by a continuous multi-stand mill. The scheduling strategy for each process varies considerably.

Determining the number of pass, controlling temperature changes and product shape, allocating the amount of reduction and computing roll load and torque are the major contents in the design of pass schedule. The philosophy of scheduling is to maximise the output, minimise the power demand, achieve the narrowest tolerances for thickness, width, flatness and profile and run the mill with the least possible wear. Structure and properties of the material should also be considered since whatever the final form of the product, the hot rolled structure strongly influences the final properties.

There are two modes of designing pass schedule: a forward strategy and a reverse strategy. The selection depends on whether the required initial values of thickness, temperature and width are given directly or whether one of them has to be determined iteratively (Czlapinski et al 1989). For the design of an initial pass schedule, the forward scheduling strategy is usually adopted.

Models in the pass schedule design involve: thermal model, rolling force and roll torque model, profile model, and microstructure model. It is of special importance to calculate the exact temperature changes because it has the major impact on the calculation of the roll force and power and considerably influences the structure of finished product. The adopted temperature model varies with designer and always need to be tuned with the industrial measured data.

Accurate prediction of the rolling force is of paramount importance in the rolling industry. The most commonly adopted rolling force models are those due to Sim's, Orowan and Pascoe's and Ekelund's equation. Their comparisons have also been given in the literature (Larke 1957). Generally, the more accurate of the predicted rolling load, the less dependence on the control system, the less investment is required. The rolling force model for hot rolling is usually written:

$$F = \sigma^* l W_2 Q_F \tag{2-50}$$

where σ^* is the modified plane strain yield stress, l is the roll-strip contact length, W_2 is the strip width after the roll gap, Q_F is the factor to account for pass geometry and frictional conditions.

The product profile is determined by the profile of the flattened roll, which can be controlled by spray cooling (Atack et al 1996) roll camber, thermal camber and roll bending. To cope with the problem of strain accumulation and to control the microstructure evolution, static recrystallisation must be considered.

Chapter 3 FEM Programs and formulation

3.1 FEM programs

All simulations in the present thesis are conducted by FORGE2® and FORGE3®, which are two software packages developed by TRANSVALOR, a French company. Only those theories and analysis techniques, which are adopted by FORGE3® and related to the work in the following chapters, are taken from the literature (Chenot et al 1996 and 1999, TRANSVALOR 2001) and briefly introduced in this chapter.

FORGE2® is dedicated to simulate the hot, warm and cold axisymmetric and plane strain bulk deformation processes, such as forging, rolling and extrusion. It has three databases: material database, process condition database and press database. Several alloys have been added to the material database. It can analyse the process with multiple deformable dies. The latest version is v2.9.4.

FORGE3® predicts material flow for 3D bulk metal forming processes. A unique robust automatic remeshing technique enables the simulation of very complex parts. The program is also written to enable multi-processor computers to be used. This significantly reduces analysis time.

3.2 Constitutive equation

For hot rolling, the elastic effect can be neglected, the most economical laws are purely viscoplastic approximations. The 3-D isotropic viscoplastic Norton-Hoff law is written:

$$\mathbf{s} = 2K\left(\sqrt{3}\dot{\bar{\varepsilon}}\right)^{m-1}\dot{\boldsymbol{\varepsilon}} \tag{3-1}$$

$\dot{\bar{\varepsilon}}$ is expressed in term of the strain rate tensor $\dot{\boldsymbol{\varepsilon}}$:

$$\dot{\bar{\varepsilon}} = \left(2/3 \sum_{i,j} \dot{\varepsilon}_{ij}^2 \right)^{1/2} \tag{3-2}$$

K is the material consistency, a function of temperature T, and equivalent strain $\bar{\varepsilon}$

$$K = K_0 \left(\varepsilon_0 + \bar{\varepsilon} \right)^n \exp(\beta' / T) \tag{3-3}$$

where n and β' are constants, and m in equation (3-1) is the strain rate sensitivity index, which ranges between 0.1 and 0.2 for ordinary metals, and between 0.5 and 0.7 for superplastic metals. Dense materials show a negligible volume change, which results in the incompressibility constraint:

$$div(\mathbf{V}) = 0 \tag{3-4}$$

There is another viscoplastic flow stress law—the hyperbolic sine function, which is usually used to describe the flow stress behaviour at elevated temperatures,

$$\bar{\sigma} = \frac{1}{\alpha} Ln \left\{ \left(\frac{Z}{A} \right)^{1/n} + \sqrt{\left(\frac{Z}{A} \right)^{2/n} + 1} \right\} \tag{3-5}$$

A, α, n are constants. Their physical interpretations are given in the literature (Sheppard and Jackson 1997). For various alloys, these constants are listed in the appendix 2.

In FORGE2® and FORGE3®, the default constitutive equation is the Norton-Hoff law. The hyperbolic sine function is incorporated into these two programs by programming the user subroutine.

3.3 Friction model

Three kinds of friction law are available in the FORGE2/3® codes; Tresca friction, Viscoplastic friction and Coulomb friction. The Tresca friction law is written in the following form:

$$\tau = -m\frac{\bar{\sigma}}{\sqrt{3}}\frac{\Delta \mathbf{V}}{\Delta V} \tag{3-6}$$

where $\bar{\sigma}$ represents the yield stress, $\bar{\sigma}/\sqrt{3}$ is usually termed the shear strength, m is commonly referred to as a friction factor, ΔV is the velocity difference at the interface. The Tresca law treats the interface friction as pressure independent and relates the friction stress directly to the yield strength of the deformed material. When m=1, sticking friction occurs. The range of m is $0 \le m \le 1$.

Viscoplastic friction law arises from the consideration of a thin interface layer of a viscoplastic lubricant between the workpiece and tool, as shown in Fig.3-1.

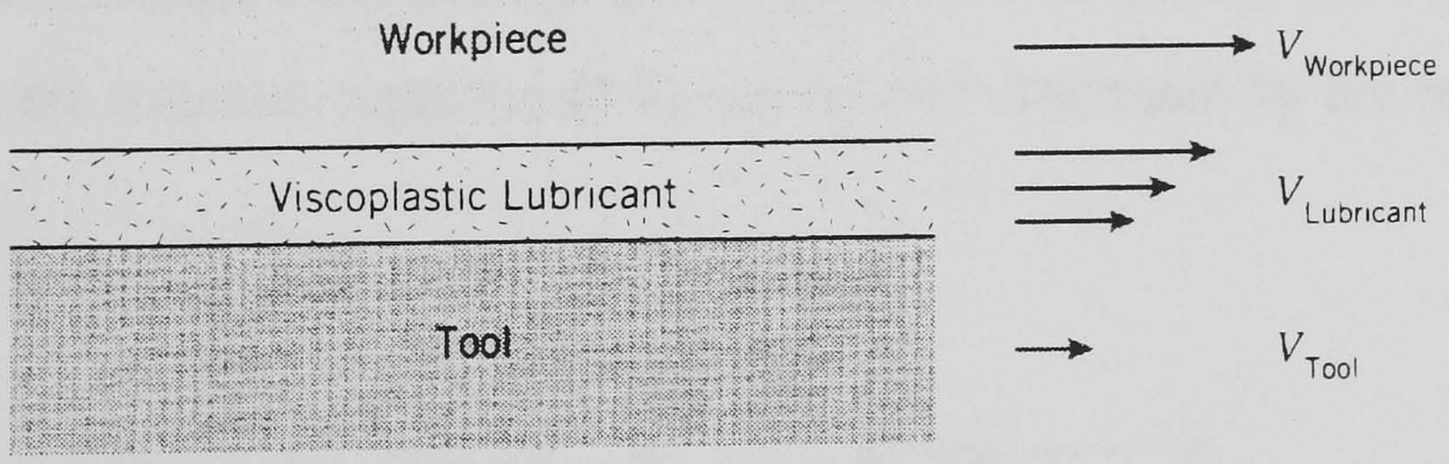

Fig.3-1 Conceptual view of viscoplastic friction condition
(after Wagoner and Chenot 1997)

The Viscoplastic friction law is written in the following form:

$$\tau = -\alpha * K * \Delta V^{\,p-1} * \Delta \mathbf{V} \tag{3-7}$$

where α is a Viscoplastic friction coefficient and $0 \le \alpha \le 1$, which is a function of the normal stress. That means α could vary with thickness reduction in rolling. K is the consistency of the material, which is defined in equation (3-3). P is the sensitivity parameter to the sliding velocity. P is usually chosen as the same value as the strain rate sensitivity index in equation (3-1). When p=0, equation (3-7) turns into equation (3-6). Therefore, for the same simulation model, the value of α must be lower than the value of m in equation (3-6).

The modified Coulomb friction law can be written as:

$$\tau = \mu\sigma_n \frac{\Delta \mathbf{V}}{\Delta V} \qquad \text{if } \mu\sigma_n \prec \frac{\bar{\sigma}}{\sqrt{3}}$$

and:

$$\tau = m\frac{\bar{\sigma}}{\sqrt{3}} \frac{\Delta \mathbf{V}}{\Delta V} \qquad \text{if } \mu\sigma_n \succ m\frac{\bar{\sigma}}{\sqrt{3}} \tag{3-8}$$

with this relationship, the friction shear stress is equal to the normal stress σ_n multiplied by the friction coefficient μ or to a fraction of the maximum shear stress sustainable by the material. Equation (3-8) can be well illustrated by the following figure.

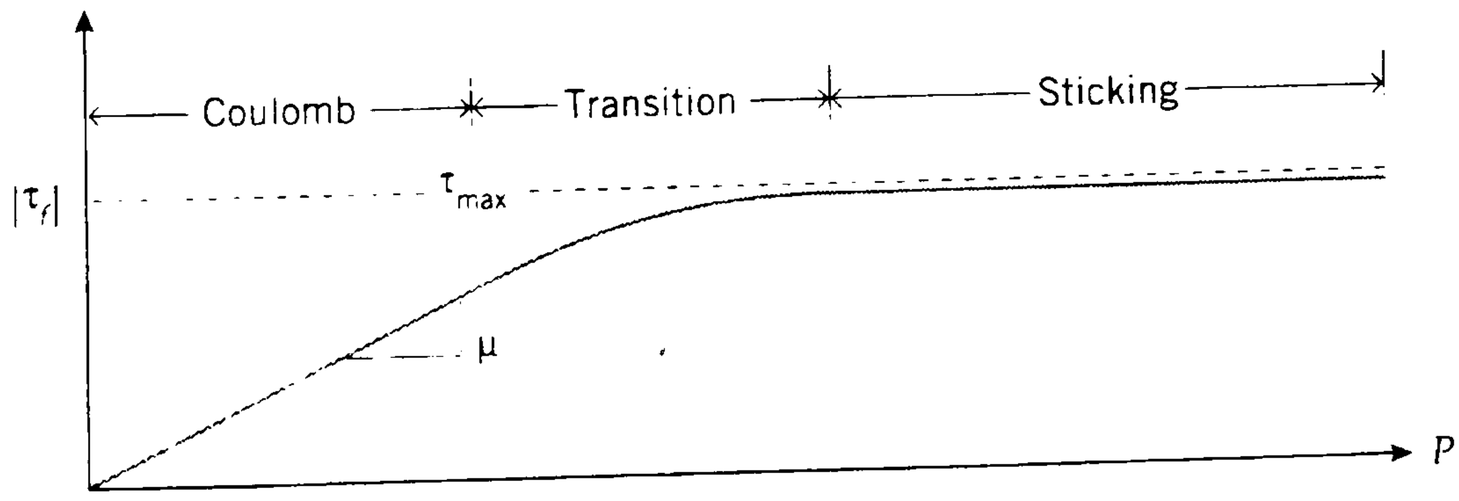

Fig.3-2 Conceptual view of the modified Coulomb friction law

(after Wagoner and Chenot 1997)

For convenient, α , μ and m are all called as friction coefficient throughout the present thesis.

From the above equations, it is clear that each equation includes a term ΔV , the velocity difference between tool and workpiece. When ΔV approaches zero, certain problems occur. To solve these convergence problems in such cases, these friction laws are regularised, i.e. written as follows:

$$\tau = -m\frac{\overline{\sigma}}{\sqrt{3}}\frac{\Delta \mathbf{V}}{\sqrt{\Delta V^2 + \Delta V_0^2}} \tag{3-9}$$

The regularisation sliding velocity ΔV_0 has a very small value.

3.4 Thermal analysis

The classical heat equation is written

$$\rho c\frac{dT}{dt} = \mathrm{div}(k\mathbf{grad}(T)) + \dot{q}_v \tag{3-10}$$

The Norton-Hoff viscoplastic heat dissipation $\dot{q}_v$ is written as:

$$\dot{q}_v = fK(\sqrt{3}\dot{\bar{\varepsilon}})^{m+1} \tag{3-11}$$

The f factor takes into account the fraction of energy which is converted into heat, it ranges generally between 0.9 and 1.0. f=0.95 is used throughout the present thesis.

On the free surface, radiation is modelled by:

$$-k\frac{\partial T}{\partial n}=\varepsilon_r\sigma_r\left(T^4-T_0^4\right) \tag{3-12}$$

On the surface of contact with the tools, conduction with the tool and surface dissipation due to friction must be taken into account:

$$-k\frac{\partial T}{\partial n}=h_{cd}\left(T-T_{tool}\right)+\frac{b^*}{b^*+b^*_{tool}}\alpha_f K\left|\Delta\mathbf{V}\right|^{p+1} \tag{3-13}$$

3.5 Finite element approximation

3.5.1 Finite element discretisation

Using isotropic elements, the velocity field is discretised with the help of the nodal velocity vectors $\mathbf{V}_n$, shape functions N_n and local co-ordinate vector ξ as:

$$\mathbf{v}=\sum_n \mathbf{V}_n \mathrm{N}_n(\xi) \tag{3-14}$$

The mapping with the physical space is defined by:

$$\mathbf{x}=\sum_n \mathbf{X}_n N_n(\xi) \tag{3-15}$$

and the strain rate tensor is computed with the help of the **B** linear operator:

$$\dot{\boldsymbol{\varepsilon}}=\sum_n \mathbf{V}_n\mathbf{B}_n \tag{3-16}$$

The pressure field is discretised in term of nodal pressure $\mathbf{P}_m$, with compatible shape functions M_m:

$$p = \sum_m \mathbf{P}_m M_m(\xi) \tag{3-17}$$

The discretised mixed formulation for viscoplastic material gives the set of nonlinear equations:

$$\mathbf{R}_n^V = \int_\Omega 2\mathbf{K}\left(\sqrt{3}\dot{\bar{\varepsilon}}\right)^{m-1} \dot{\boldsymbol{\varepsilon}} : \mathbf{B}_n dV + \int_{\partial\Omega_c} \alpha_f K |\mathbf{v}_s|^{p-1} \mathbf{v}_s N_n dS - \int_\Omega p tr(\mathbf{B}_n) dV = 0 \tag{3-18}$$

$$\mathbf{R}_m^p = \int_\Omega \mathbf{M}_m div(\mathbf{v}) dV = 0 \tag{3-19}$$

which takes the symbolic form :

$$\mathbf{R}(\mathbf{X}, \bar{\varepsilon}, \mathbf{V}, \mathbf{P}) = 0 \tag{3-20}$$

The time evolution of co-ordinate vectors and equivalent strain is governed by:

$$\frac{d\mathbf{X}}{dt} = \mathbf{V} \tag{3-21}$$

$$\frac{d\bar{\varepsilon}}{dt} = \dot{\bar{\varepsilon}} \tag{3-22}$$

3.5.2 Increment approach

The nodal update can be performed with the Euler explicit scheme. If $\mathbf{X}_n^t$ is the co-ordinate vector of node number n at time t, with velocity vector $\mathbf{V}_n^t$; at time $t + \Delta t$ the new co-ordinate vector will be:

$$\mathbf{X}_n^{t+\Delta t} = \mathbf{X}_n^t + \Delta t \mathbf{V}_n^t \tag{3-23}$$

A second order scheme was shown to improve the accuracy, especially regarding the volume conservation of the part, with a Runge--Kutta method or the semi-implicit scheme:

$$\mathbf{X}_n^{t+\Delta t} = \mathbf{X}_n^t + \frac{1}{2}\Delta t\left(\mathbf{V}_n^t + \mathbf{V}_n^{t+\Delta t}\right) \tag{3-24}$$

3.5.3 Approach of the coupled thermal and mechanical problem

The temperature field is discretised with the same elements as for the velocity field according to:

$$T = \sum_n T_n N_n(\xi) = \mathbf{T}\cdot\mathbf{N} \tag{3-25}$$

The classical semi-discretised form is easily obtained from equation:

$$\mathbf{C}\cdot\frac{d\mathbf{T}}{dt} + \mathbf{H}\cdot\mathbf{T} + \mathbf{F} = 0 \tag{3-26}$$

C and **H** are computed by:

$$C_{ij} = \int_\Omega \rho c N_i N_j dV \tag{3-27}$$

and

$$H_{ij} = \int_\Omega k\,\mathbf{grad}(N_i)\cdot\mathbf{grad}(N_j)dV \tag{3-28}$$

while the **F** vector contains the viscoplastic heat dissipation and boundary conditions. The temperature field can be integrated with a second order scheme where:

$$\mathbf{T} = a\mathbf{T}^{t-\Delta t} - (1.5 - 2a - g)\mathbf{T}^{t} + (a - 0.5 + g)\mathbf{T}^{t+\Delta t} \tag{3-29}$$

$$\frac{d\mathbf{T}}{dt} = (1-g)\frac{\mathbf{T}^{t} - \mathbf{T}^{t-\Delta t}}{\Delta t} + g\frac{\mathbf{T}^{t+\Delta t} - \mathbf{T}^{t}}{\Delta t} \tag{3-30}$$

$$\mathbf{C} = (0.5 - g)\mathbf{C}^{t-\Delta t} + (0.5 + g)\mathbf{C}^{t} \tag{3-31}$$

in the Dupont scheme, a=0.25 and g=1.

3.6 Meshing and remeshing

During the simulation of the forging and rolling process, which involve large or very large deformation, some elements soon become very distorted and are not appropriate for further computation. It is very often necessary to regenerate the mesh several times in order to complete the simulation. For very complicated industrial parts, tetrahedral elements seem more convenient for automatic meshing and remeshing. The 5 node tetrahedral mini element for the velocity, with linear continuous pressure is shown in Fig.3-3.

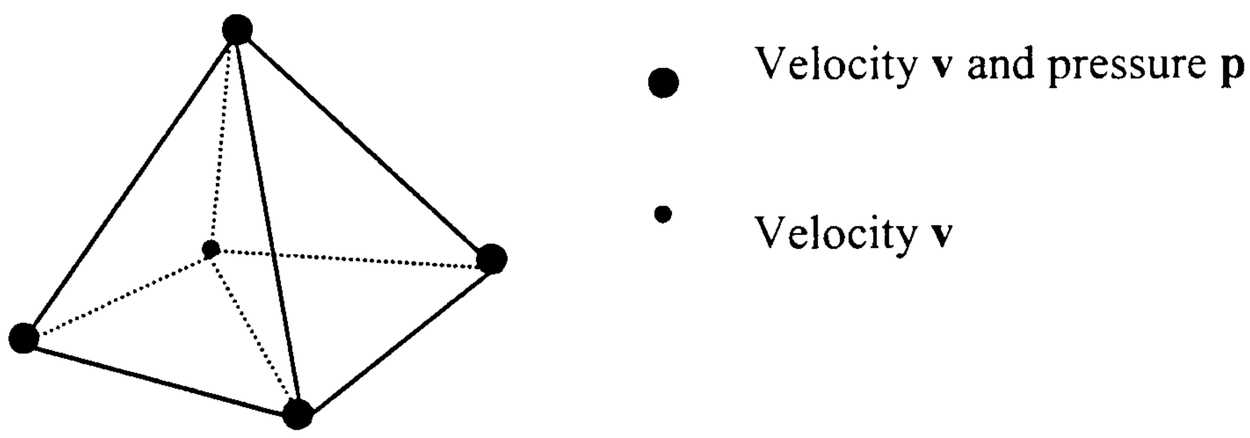

Fig.3-3 Finite element interpolation in a tetrahedron

The remeshing module must be activated when one of the following conditions is reached: (a) one element becomes too distorted, due to internal shear; (b) the element sides of the mesh of the workpiece, which are located on the contact surface, are not small enough to follow accurately the local geometry of the tool.

Chapter 4 Simulation of 3-D hot breakdown rolling

4.1 Comparison between the Norton-Hoff law and the hyperbolic sine function

Flow stress functions may be divided into a number of groups differing type and taking into account the parameters describing initial conditions and the development of the material from the initial state (Grosman 1997). As described in Chapter 3, two flow stress functions: the Norton-Hoff law and the hyperbolic sine function, are adopted to relate the viscoplastic material behaviour for aluminium alloys under hot work conditions in the present thesis. Although several workers have proposed some more complex and advanced constitutive equations in recent years (Gelin et al 1993, Shi et al 1997, Puchi et al 1998), the major aluminium alloys that are studied in the present work: AA3003 and AA1100 have not been represented by these models. In contrast, the hyperbolic sine function has been applied to describe the behaviour of a great number of aluminium alloys (Sheppard et al 1997).

Dashwood et al.(1996) have simply referred to the difference between these two flow stress functions for AA7075. However, their comparison was not thorough. Therefore, it is still necessary to give more details about their difference under different temperature and strain rate conditions, especially their influence on the computed FEA results. Since the only available experimental data available to the present author is 4%Cu binary 2014 alloy (see appendix 4), the comparison is made for this alloy first. The comparison for AA3003 is followed.

Fig4-1 indicates the correlationship among the regressed Norton-Hoff law, the regressed hyperbolic sine function, and the measured flow stress obtained from the literature. The regressed Norton-Hoff equation for 4%Cu binary 2014 alloy is written

$$\bar{\sigma} = \sqrt{3}^{1.1772} * 875.71 * (\varepsilon + \varepsilon_0)^0 * \exp(2607.937/T) * \dot{\bar{\varepsilon}}^{0.177206} \quad \text{(KPa)} \qquad (4\text{-}1)$$

The regressed hyperbolic sine function for 4%Cu binary 2014 alloy is given in the appendix 3.

It is clear from Fig.4-1 that the hyperbolic sine function gives a better description for actual stress than the Norton-Hoff law does. The correlation coefficient of the hyperbolic sine function is nearly 1.0. Therefore, we have sufficient confidence to assume that, the hyper sine function can truly relate the flow stress with strain rate and temperature during steady state deformation under high working conditions.

Because the flow stress behaviour for most aluminium alloys were expressed by the hyperbolic sine function in the past, in order to use the Norton-Hoff law in FORGE2/3®, conversion from the hyperbolic sine function to the Norton-Hoff law is inevitable. How much accuracy is lost during this conversion is a common concern for each analyst. In the past the necessity for such a transformation was not occurred. Fig.4-1(c) compares the correlationship between the hyperbolic sine function and the Norton-Hoff law which is regressed from the hyperbolic sine function. The correlation coefficient in Fig.4-1 (c) equals the correlation coefficient in Fig.4-1 (a). That means the Norton-Hoff law regressed from the existing hyperbolic sine function has the same accuracy as the Norton-Hoff law regressed from experimental data. This discovery is of importance for the conversion between these two flow stress functions.

Curves of the flow stress with temperature under different equivalent strain rates for these two flow stress functions are shown in Fig.4-2. We can see that, there are significant differences between two curves in the low temperature range (lower than 573K). The difference decreases with increase of temperature. The Norton-Hoff law significantly over-predicts the flow stress at low temperatures, and slightly under-

predicts the flow stress at high temperature. As the equivalent strain rate increases, the difference expands. It is noteworthy that, no measurement was carried out for temperatures lower than 573K (see appendix 4). The correlationship coefficient—0.985 between the Norton-Hoff law and the actual flow stress, shown in Fig.4-1 (a), is only valid when conditions fall within the measurement range. When predicting the flow stress for a condition outside the valid range, the deviation from the true situation could be very large, as shown in Fig.4-2.

The same comparison is conducted for AA3003, and shown in Fig.4-4 and Fig.4-5. The regressed Norton-Hoff equation for this alloy is written

$$\overline{\sigma} = \sqrt{3}^{1.1262} * 777.67 * (\varepsilon + \varepsilon_0)^0 * \exp(2194.284/T) * \dot{\bar{\varepsilon}}^{0.0.1262} \quad \text{(KPa)} \qquad (4\text{-}2)$$

From Fig.4-4 (a), it is apparent that, these two equations correspond very well in whole temperature range. Fig.4-4 shows similar feature as in Fig.4-2.

Fig.4-6 shows the application of two flow stress functions into FEM for the plane strain rolling of AA3003. The rolling parameters, shown in Table 2, were provided by an aluminium company in Italy.

Table 2 Rolling pass schedule

Entry thickness	Exit thickness	Rolling temperature	Roll speed	Roll radius	Measured pressure
30mm	15mm	450^0C	80 rpm	495mm	0.755 ton/mm

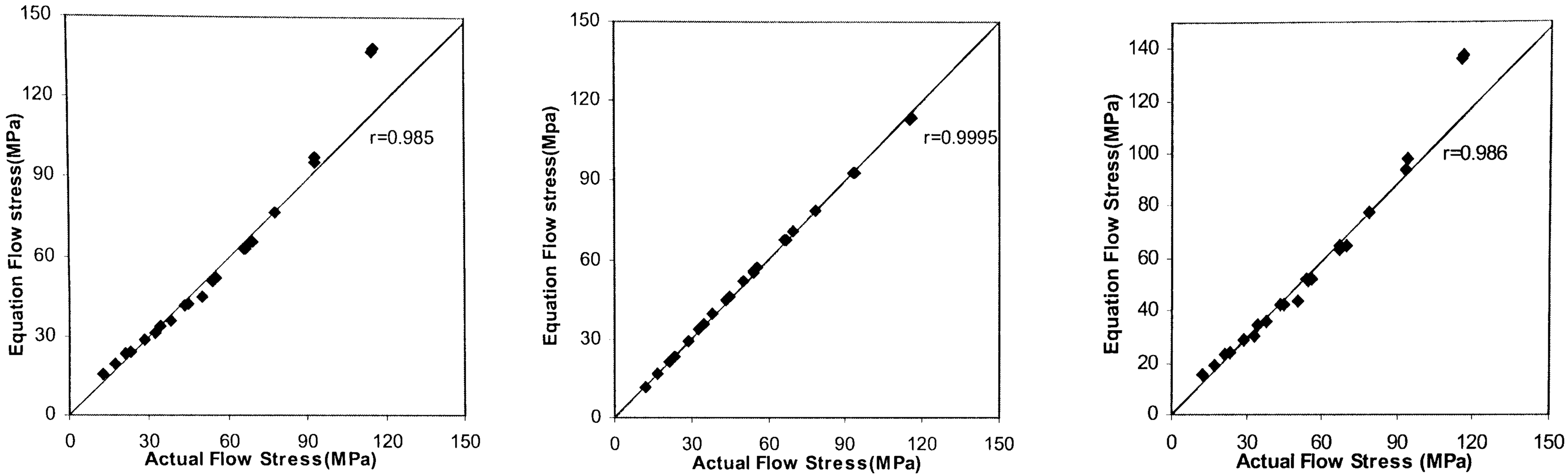

(a) (b) (c)

Fig.4-1 Correlation coefficients for various flow stress functions. (a) the Norton-Hoff law regressed from the experimental data; (b) the hyperbolic sine function regressed from the experimental data (c) the Norton-Hoff law regressed from the hyperbolic sine function. (For 4%Cu binary AA2014)

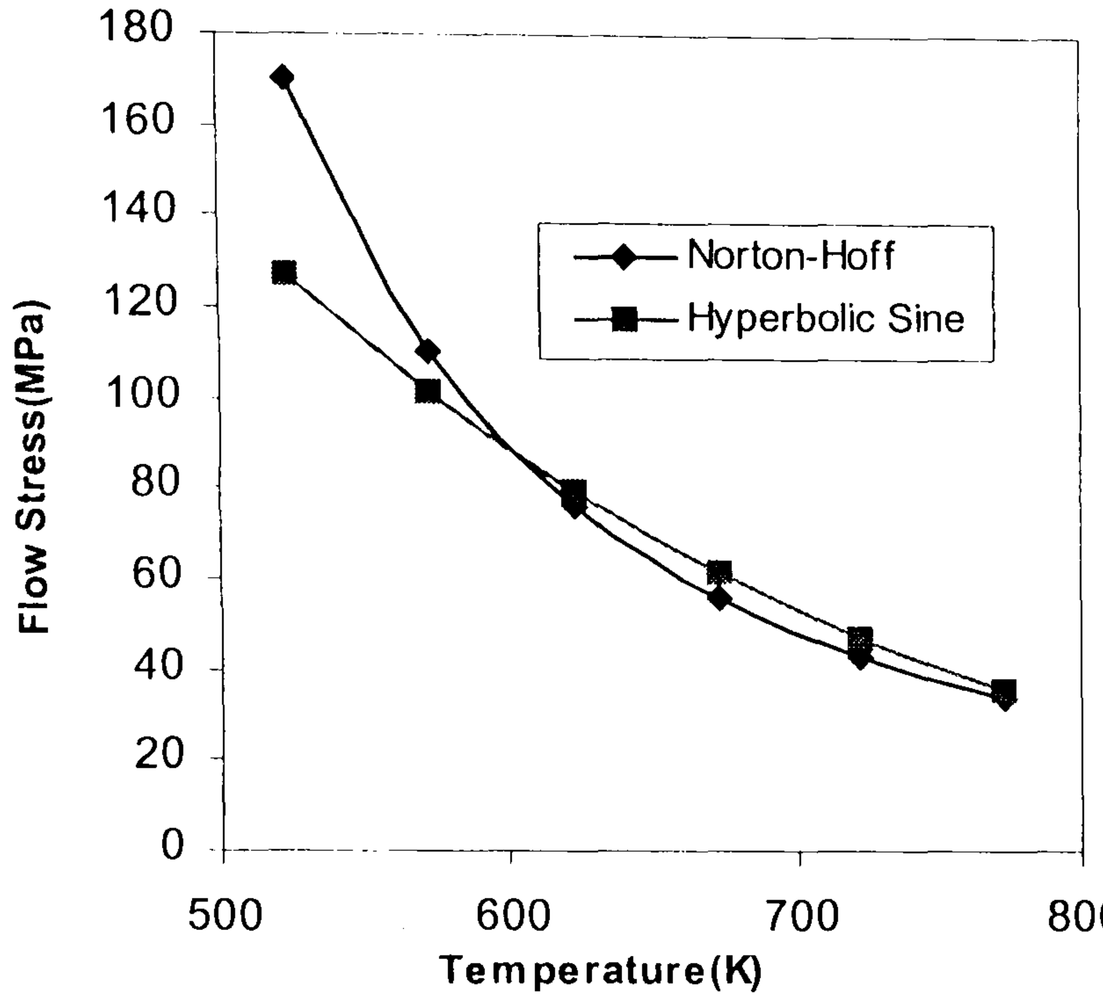

(a)

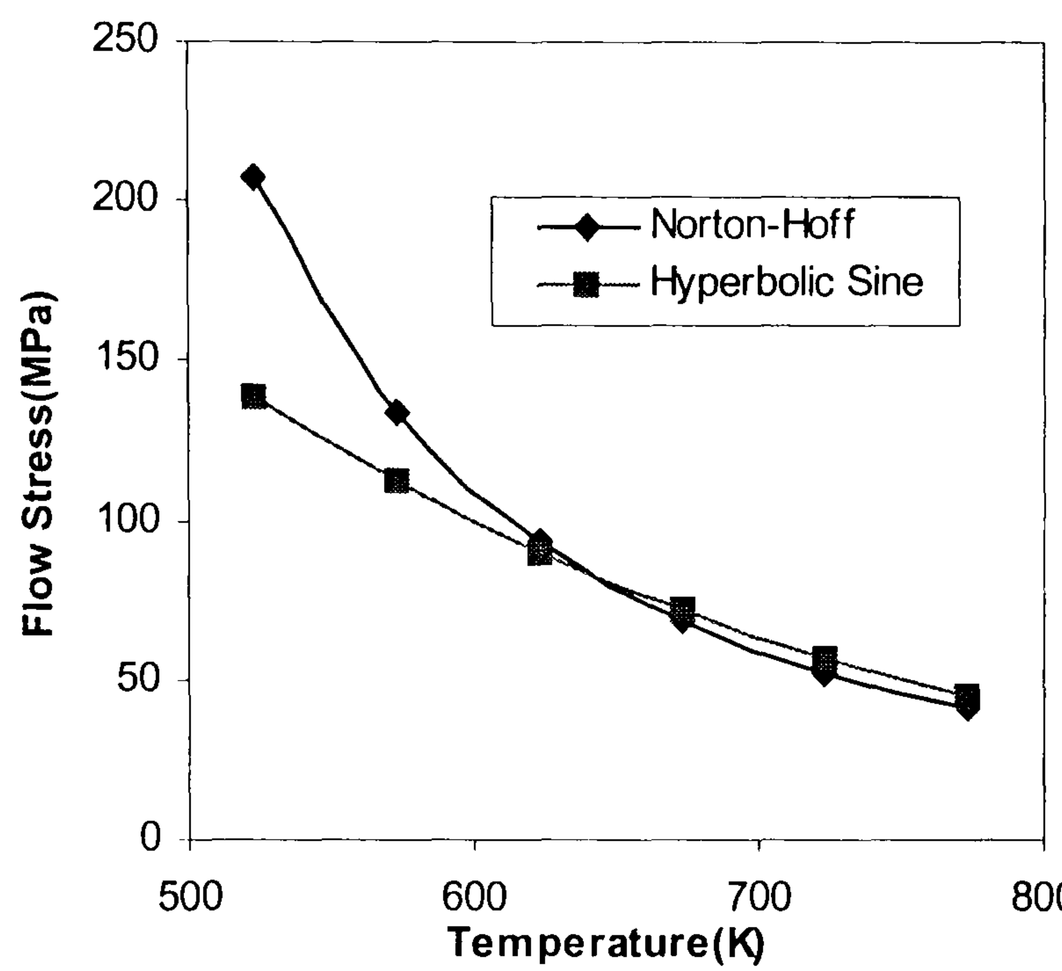

(b)

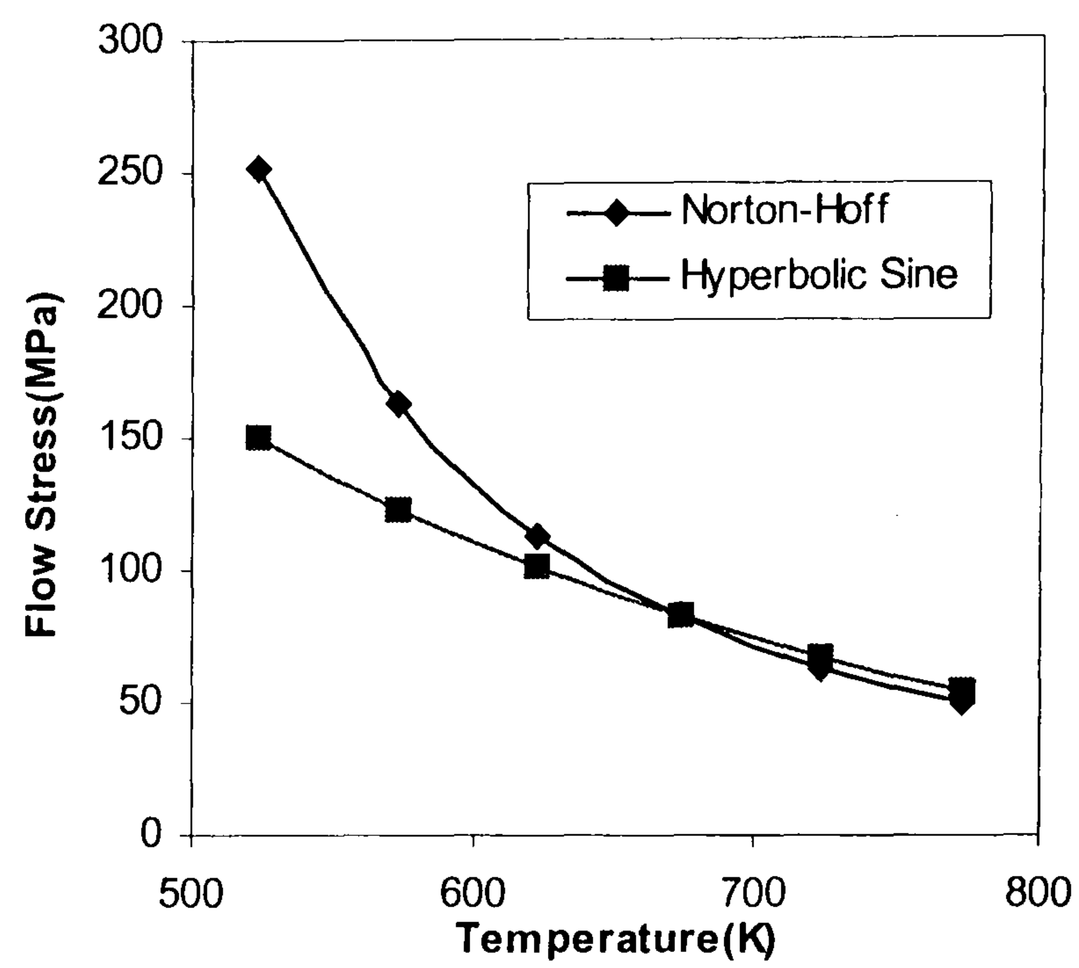

(c)

Fig. 4-2 Comparison of flow stress vs. temperature for 4%Cu binary AA2014. (a) $\dot{\bar{\varepsilon}}$=5; (b) $\dot{\bar{\varepsilon}}$=15; (c) $\dot{\bar{\varepsilon}}$=45.

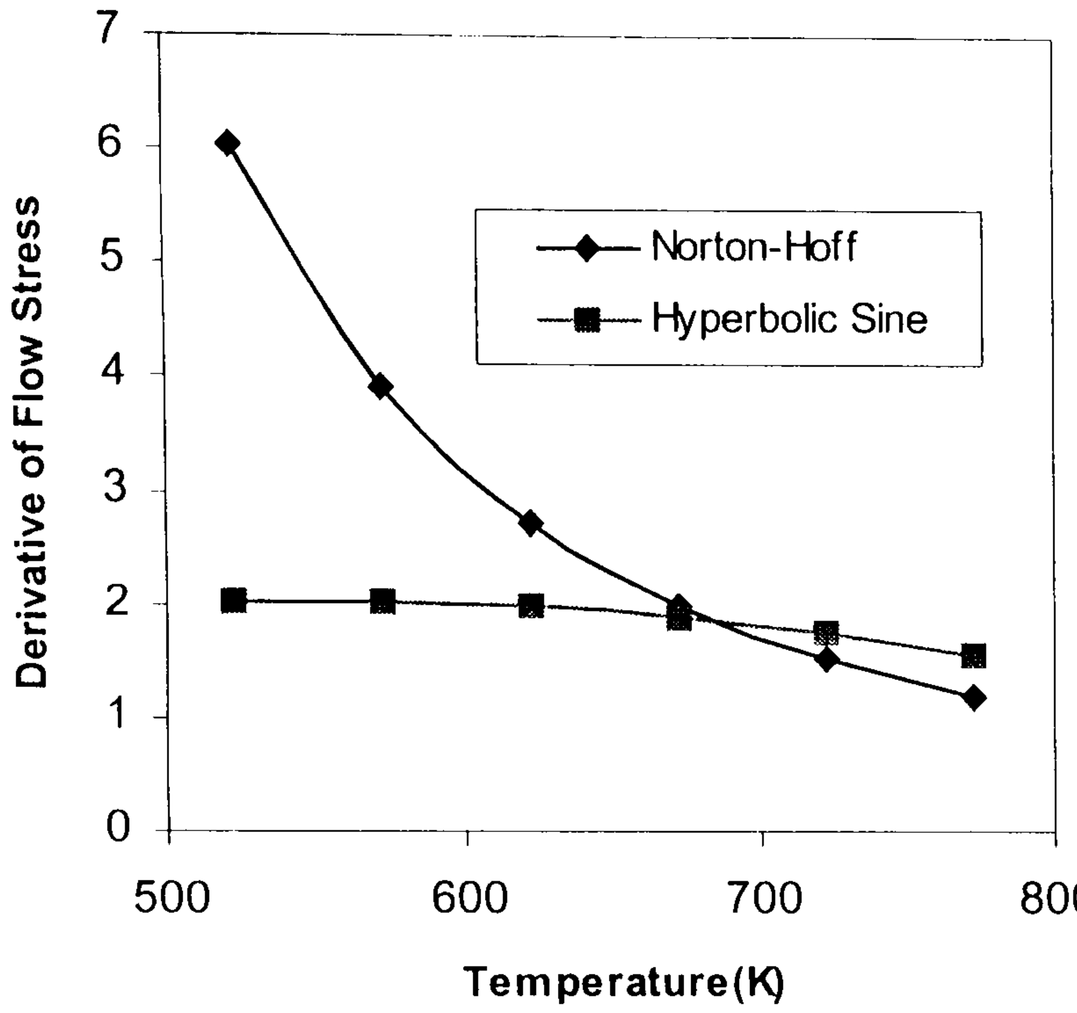

(a)

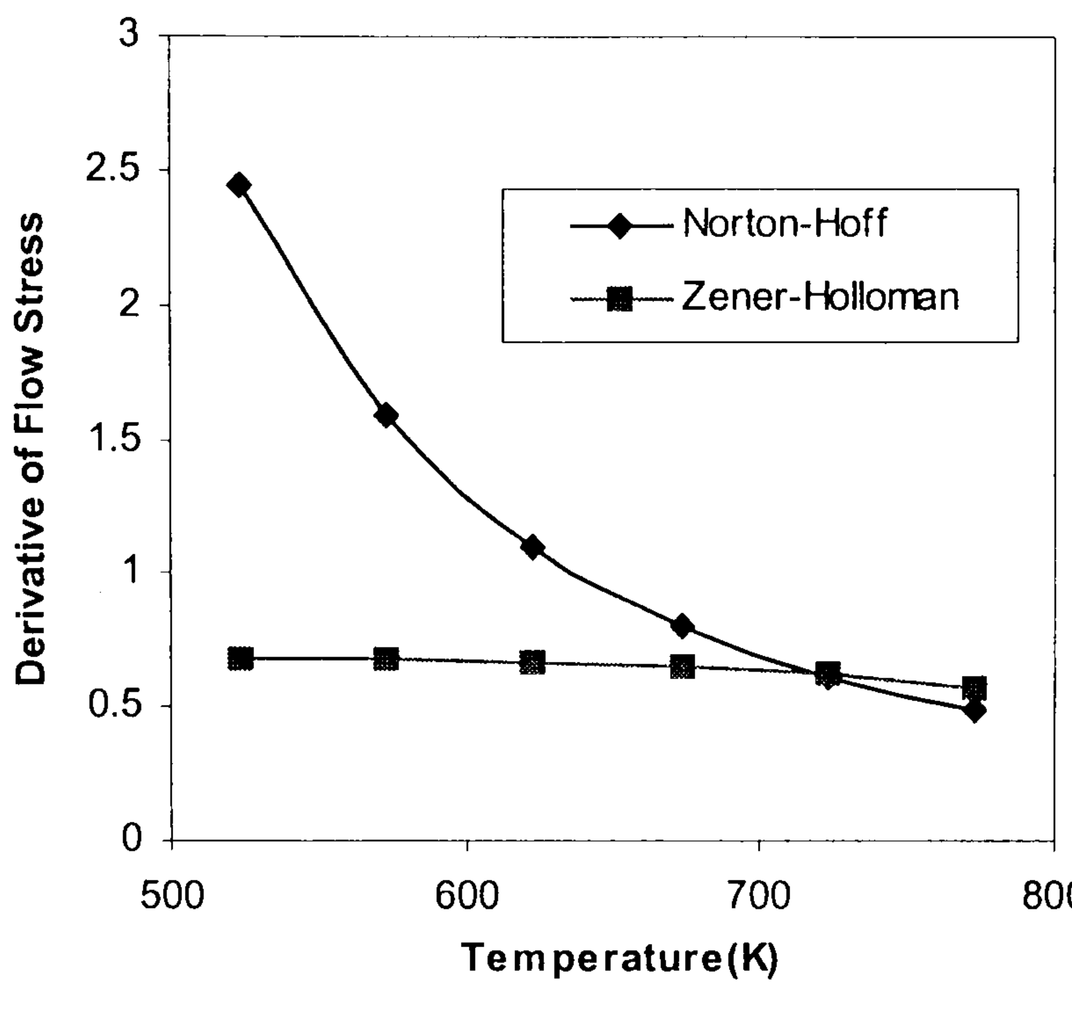

(b)

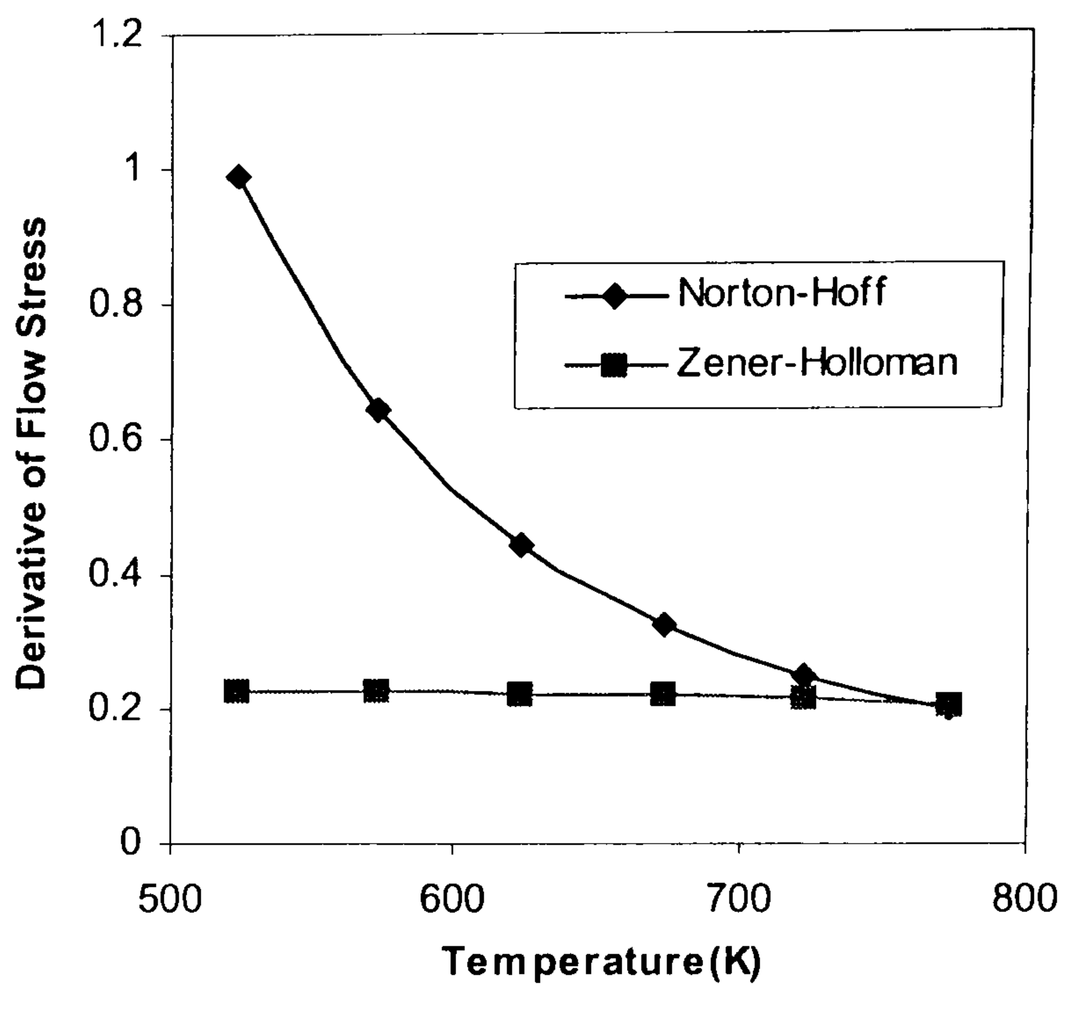

(c)

Fig.4-3 Comparison of the derivative of flow stress vs. temperature for 4%Cu binary AA2014 (a) $\dot{\bar{\varepsilon}}$=5; (b) $\dot{\bar{\varepsilon}}$=15; (c) $\dot{\bar{\varepsilon}}$=45.

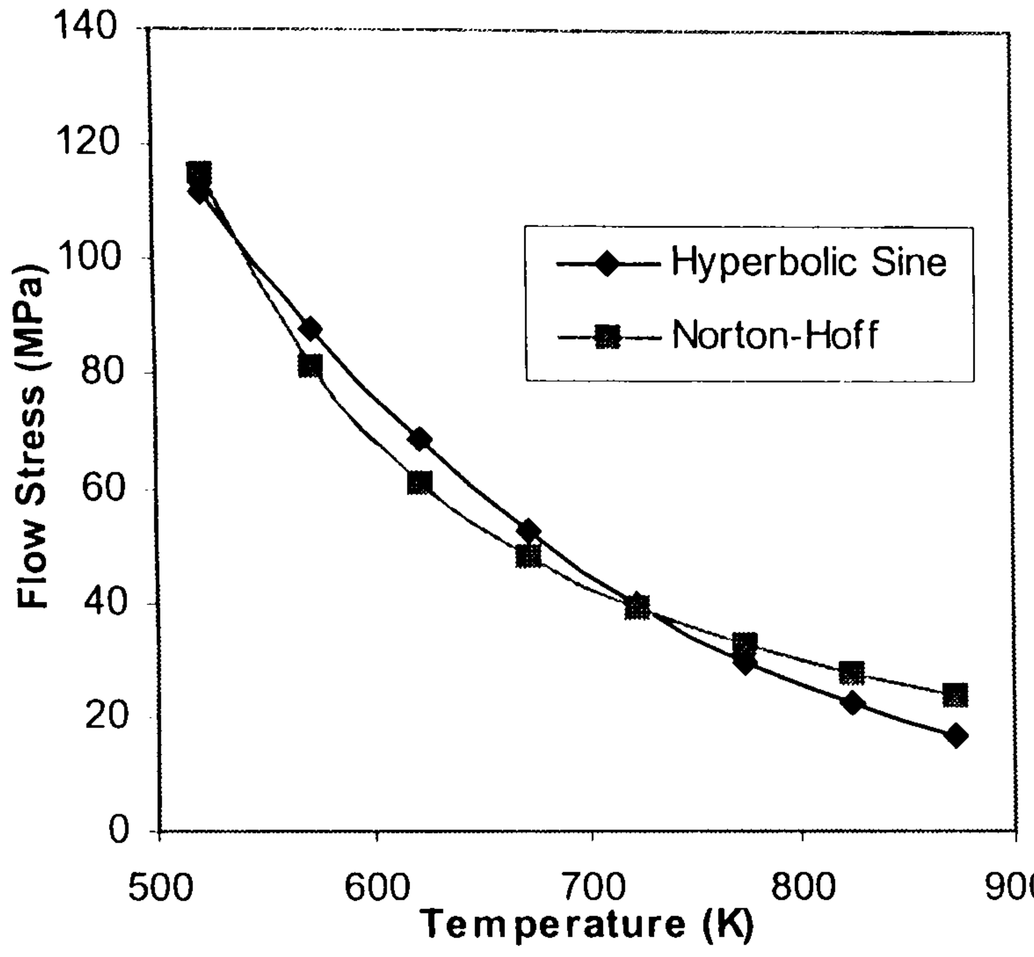

(a)

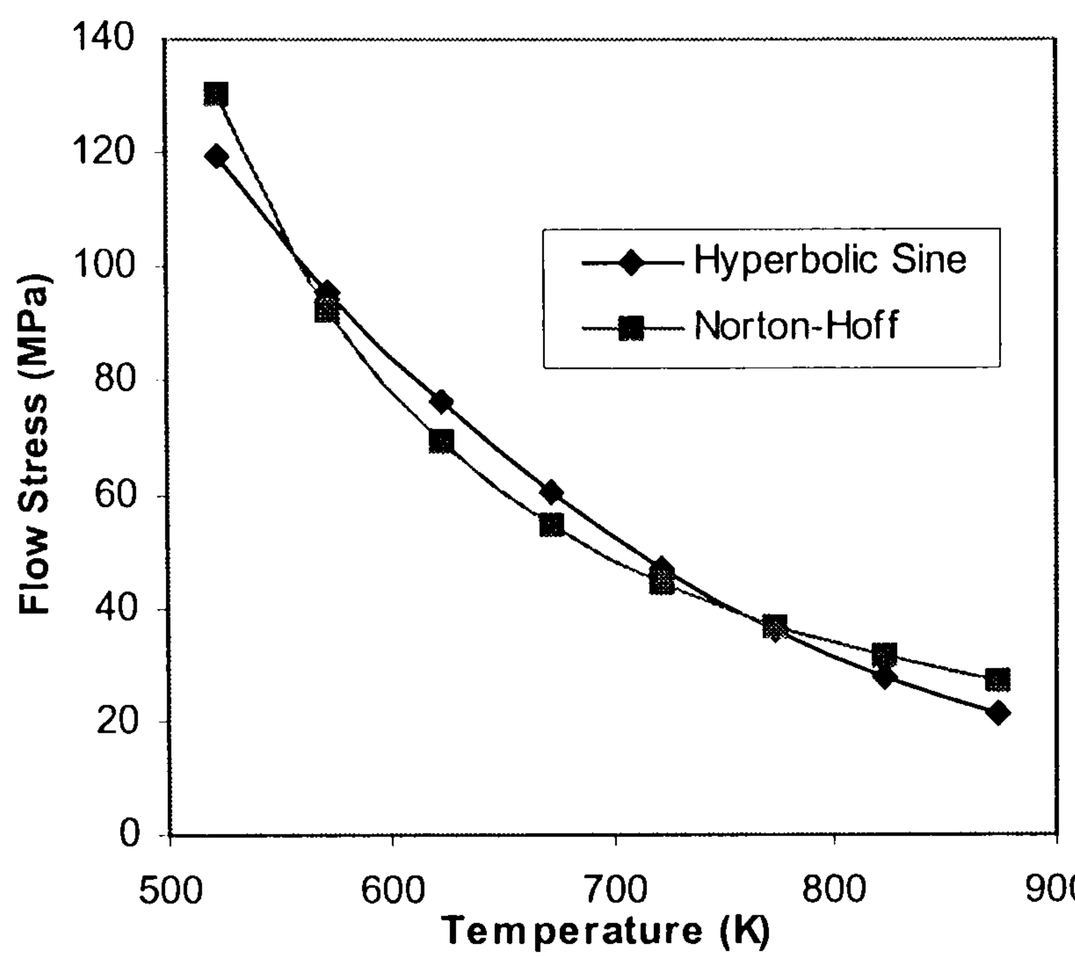

(b)

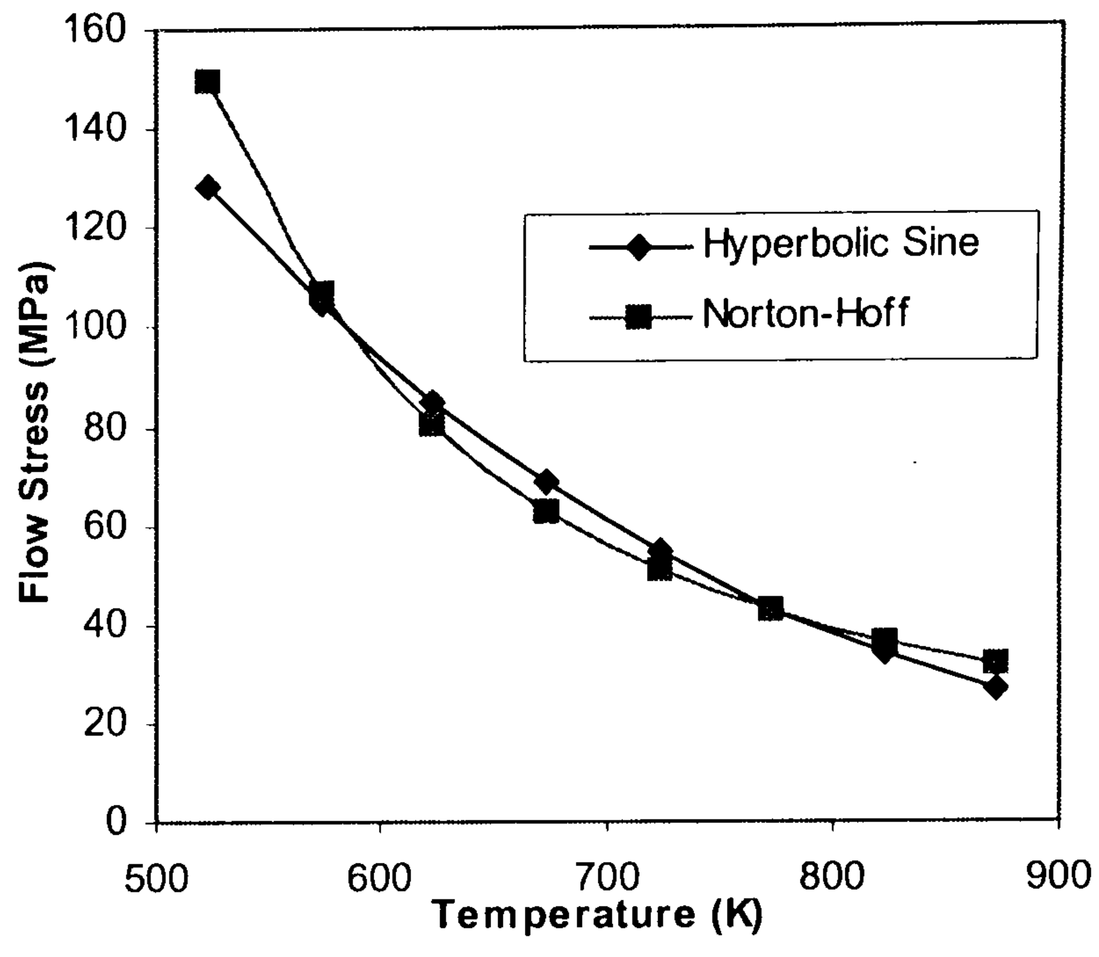

(c)

Fig. 4-4 Comparison of flow stress vs. temperature curve for AA3003. (a) $\dot{\bar{\varepsilon}}$=5; (b) $\dot{\bar{\varepsilon}}$=15; (c) $\dot{\bar{\varepsilon}}$=50.

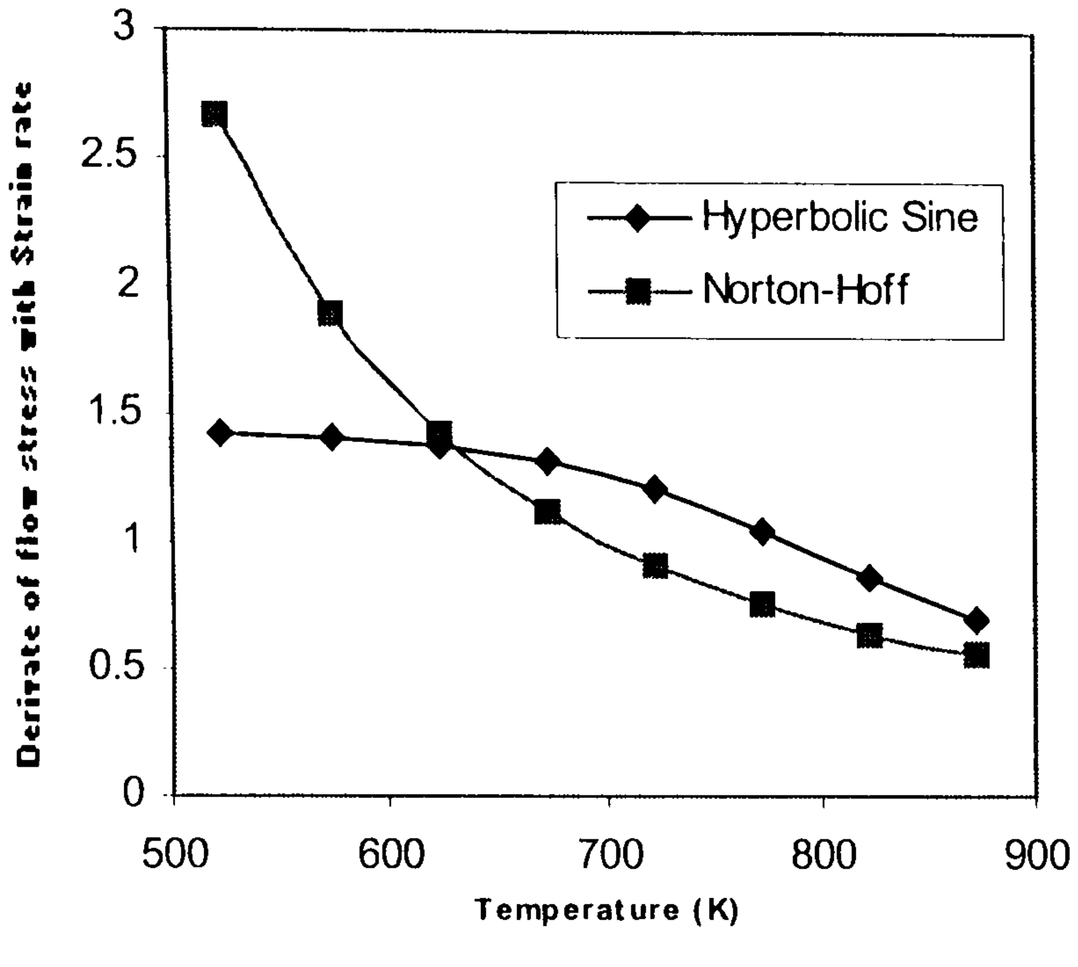

(a)

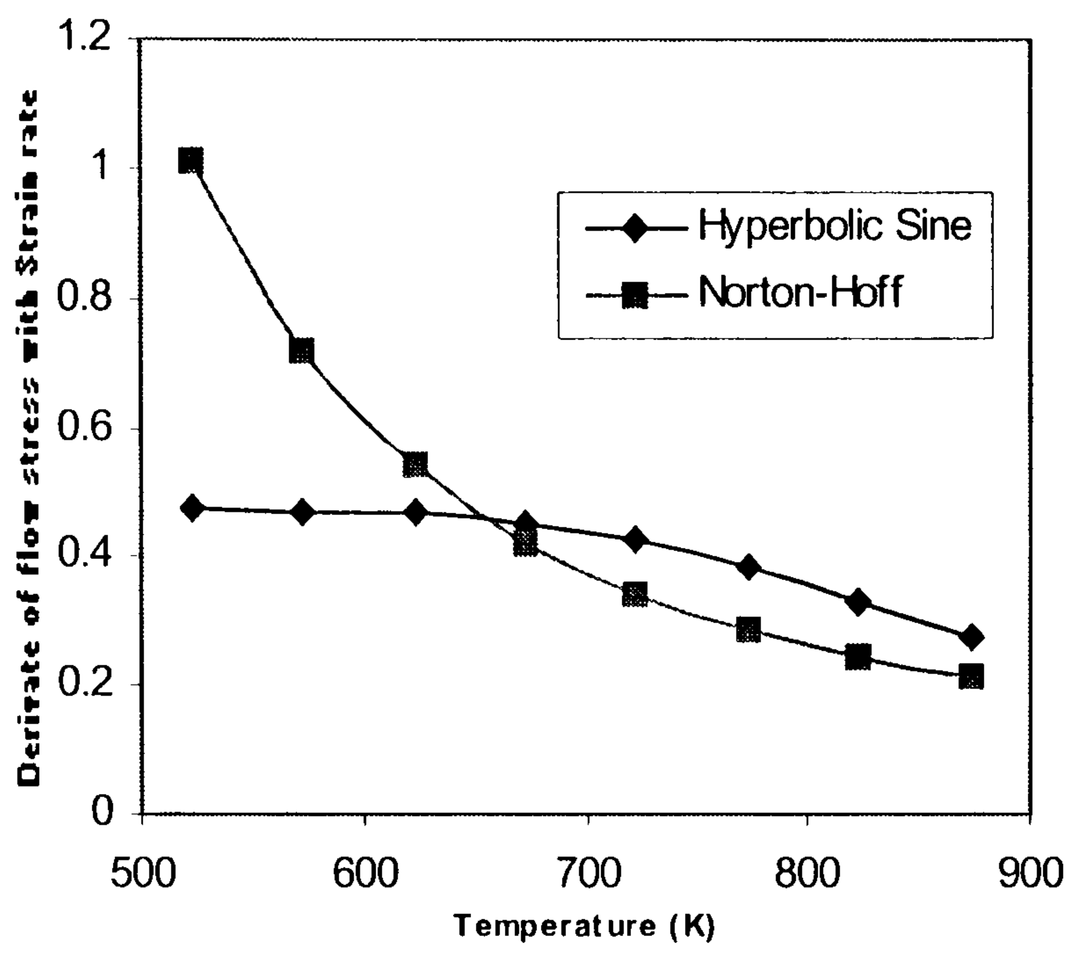

(b)

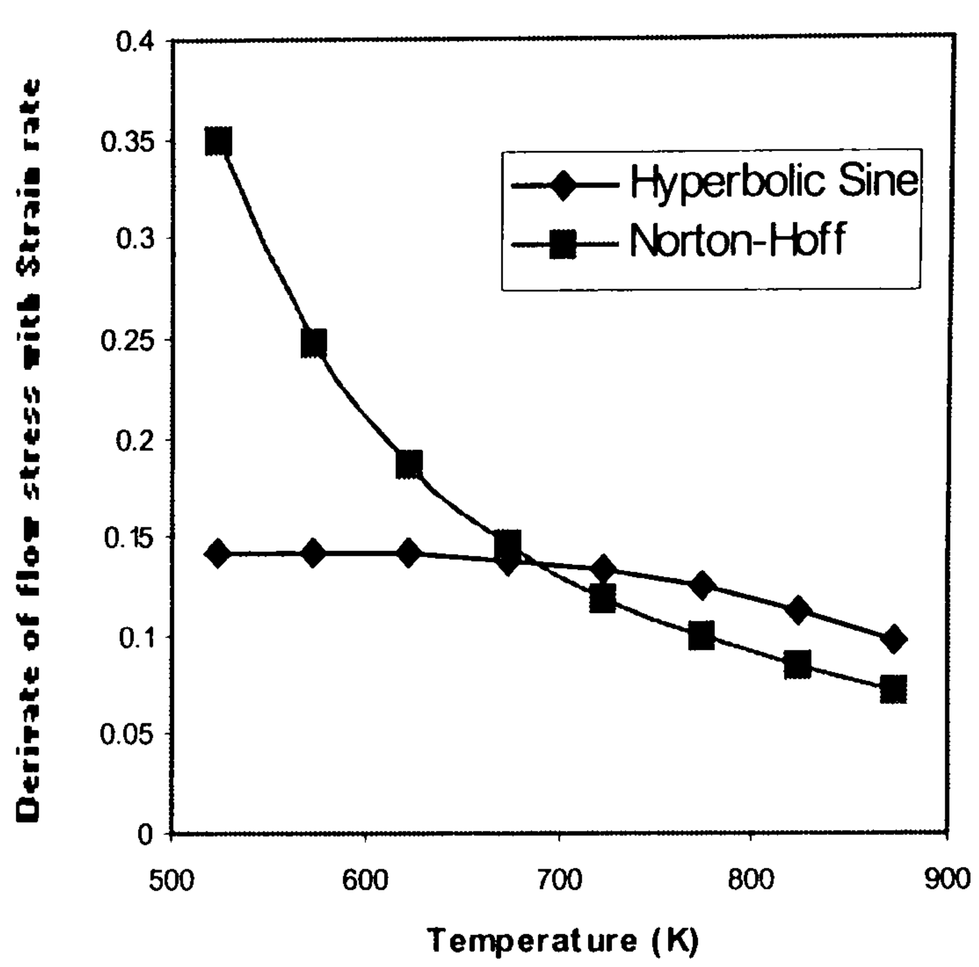

(c)

Fig.4-5 Comparison of the derivative of flow stress vs. temperature for AA3003 (a) $\dot{\bar{\varepsilon}}$=5; (b) $\dot{\bar{\varepsilon}}$=15; (c) $\dot{\bar{\varepsilon}}$=50.

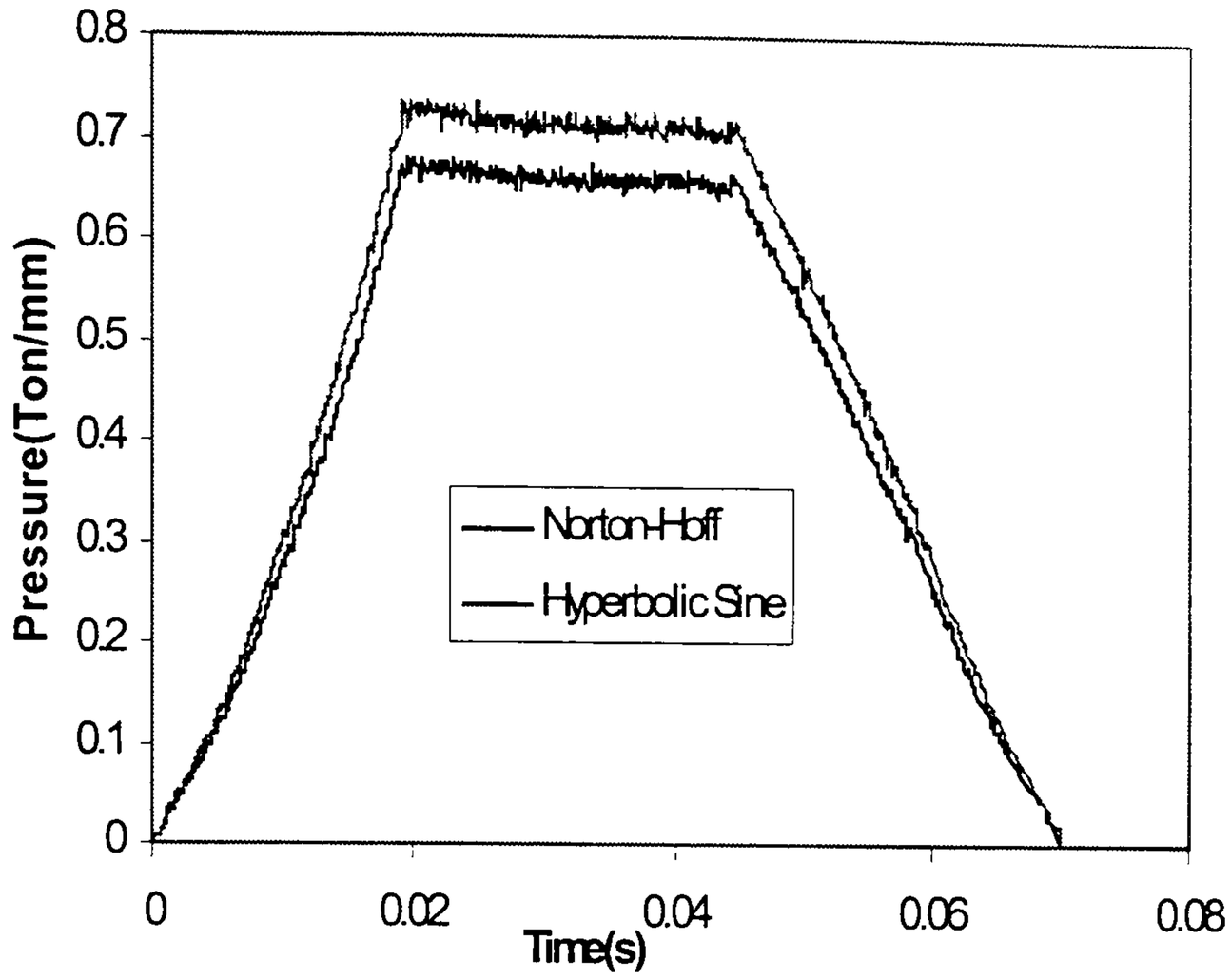

Fig.4-6 Comparison of the computed pressure by two different flow stress functions regressed from the experimental data

It is clear from Fig.4-6 (a) that, the two functions give identical curve shape. They reach the steady state regime and leave the roll gap at the same time. The measured rolling pressure in the steady state regime is 0.755ton/mm. The computed pressure by the hyperbolic sine function is 0.718 ton/mm. The relative error between the measured pressure and the computed pressure is 4.91%. For the model with Norton-Hoff law, the computed pressure is 0.663 ton/mm; the relative error is 12.2%. It is not surprising that the hyper sine function gives a better prediction than the Norton-Hoff does. The problem is that, the difference between two equations seems a little large. Since at the nominal rolling temperature 425^{0}C (698K), two functions correspond very well (see Fig.4-2), the difference should not be so large. The reason could be attributed to the derivative of the flow stress vs. strain rate.

To have a clear understanding of how flow stress function affects the computed results, it would be useful to briefly review the fundamental formulae of the rigid-viscoplastic finite element method (Kobayashi et al 1989).

For rigid-viscoplastic materials, the following functional exists:

$$\pi = \int_V E(\dot{\varepsilon}_{ij})dV - \int_{S_F} F_i u_i dS \tag{4-3}$$

The first order of variation of above functional is:

$$\delta\pi = \int_V \bar{\sigma}\delta\dot{\bar{\varepsilon}}dV - \int_{S_F} F_i \delta u_i dS = 0 \tag{4-4}$$

Where $\bar{\sigma} = \bar{\sigma}(\bar{\varepsilon}, \dot{\bar{\varepsilon}})$. The incompressibility constraint on admissible velocity fields in Equation (4-3) is removed by using the penalised form of the incompressibility as

$$\delta\pi = \int_V \bar{\sigma}\delta\dot{\bar{\varepsilon}}dV + K\int_V \dot{\varepsilon}_V \delta\dot{\varepsilon}_V dV - \int_{S_F} F_i \delta u_i dS = 0 \tag{4-5}$$

From arbitrariness of δV_I, a set of algebraic equations (stiffness equations) are obtained as

$$\frac{\partial\pi}{\partial u_I} = \sum_j \left(\frac{\partial\pi}{\partial u_I}\right)_{(j)} = 0 \tag{4-6}$$

Linearising Equation (4-5) by Taylor expansion near an assumed solution point $\mathbf{V} = \mathbf{V}_0$, namely

$$\left[\frac{\partial\pi}{\partial u_I}\right]_{V=V_0} + \left[\frac{\partial^2\pi}{\partial u_I \partial u_J}\right]_{u=u_0} \Delta u_J = 0 \tag{4-7}$$

The first term of Equation (4-6) are expressed as

$$\frac{\partial \pi}{\partial u_I} = \int_V \frac{\overline{\sigma}}{\dot{\overline{\varepsilon}}} P_{IJ} V_J dV + \int_V K C_J V_J C_I dV - \int_{S_F} F_j N_{jI} dS \tag{4-8}$$

The second derivatives of π are expressed as

$$\frac{\partial^2 \pi}{\partial u_I \partial u_J} = \int_V \frac{\overline{\sigma}}{\dot{\overline{\varepsilon}}} P_{IJ} dV + \int_V \left(\frac{1}{\dot{\overline{\varepsilon}}} \frac{\partial \overline{\sigma}}{\partial \dot{\overline{\varepsilon}}} - \frac{\overline{\sigma}}{\dot{\overline{\varepsilon}}^2} \right) \frac{1}{\dot{\overline{\varepsilon}}} P_{IK} V_K V_M P_{MJ} dV + \int_V K C_J C_I dV \tag{4-9}$$

The term $\overline{\sigma}$ and $\frac{\partial \overline{\sigma}}{\partial \dot{\overline{\varepsilon}}}$ are involved in equation (4-9). The influence of different flow stress functions on the computed results is thus introduced into FEM.

For the hyperbolic sine function, the derivative of the flow stress with the equivalent strain rate is obtained as

$$\frac{d\overline{\sigma}}{d\dot{\overline{\varepsilon}}} = \exp\left(\frac{\Delta H}{RT}\right) \cdot \frac{1}{\alpha \cdot n \cdot A \cdot [\sinh(\alpha \overline{\sigma})]^{n-1} \cdot \cosh(\alpha \overline{\sigma})} = \frac{\tanh(\alpha \overline{\sigma})}{\alpha \cdot n \cdot \dot{\overline{\varepsilon}}} \tag{4-10}$$

and for the Norton-Hoff law exists

$$\frac{d\overline{\sigma}}{d\dot{\overline{\varepsilon}}} = \overline{\sigma} \cdot m / \dot{\overline{\varepsilon}} \tag{4-11}.$$

Fig.4-3 compares the difference between equation (4-10) and equation (4-11) under different temperature and strain rate conditions. There is considerable difference when the temperature is lower than 300^0C (573K). As the equivalent strain rate increases, the difference rises from 200% to approximately 400%. When experimental data is correlated by either the Norton Hoff law or the hyperbolic sine function, the confidence level is usually higher than 95%. That means a very good

regression for the flow stress, but not for the derivative of the flow stress with the equivalent strain rate. Even if two flow stress functions have the same regression accuracy for the actual flow stress, it can not be assured that the same value of the derivative of flow stress with equivalent strain rate, which definitely contributes somewhat extent to the finite element analysis results. A quantitative description of this contribution could be very difficult due to the complex formulae in FEM.

One interesting feature in Fig.4-3 is that, the curve given by the hyperbolic sine function varies little with change of temperature, especially when strain rate is at a high value. Temperature affects the derivative of the flow stress with strain rate in a very complicated way, since both the numerator and the denominator in equation (4-10) involve the temperature T. If we take a look at Fig.4-5, the curve given by the hyperbolic sine function varies considerably with temperature change, but still much less than the variation of the curve given by the Norton-Hoff law. That means the derivative of the flow stress with strain rate is sensitive to materials.

The temperature distributions in the roll gap obtained by using these two constitutive laws are shown in Fig.4-7 and Fig.4-8. The temperature rise obtained by the hyperbolic sine function is little larger than the model given by the Norton-Hoff law. This is a reasonable result, because the load computed by the hyperbolic sine function is higher than the load obtained by using the Norton-Hoff law. Hence, more heat is expected to be generated.

It is strongly advised that the reader should read appendix 9 before going through the following sections. In appendix 9, some important aspects related with the selection of the constitutive equation in the present thesis are explained. This explaination would be helpful for the reader to understand the work in the following chapters.

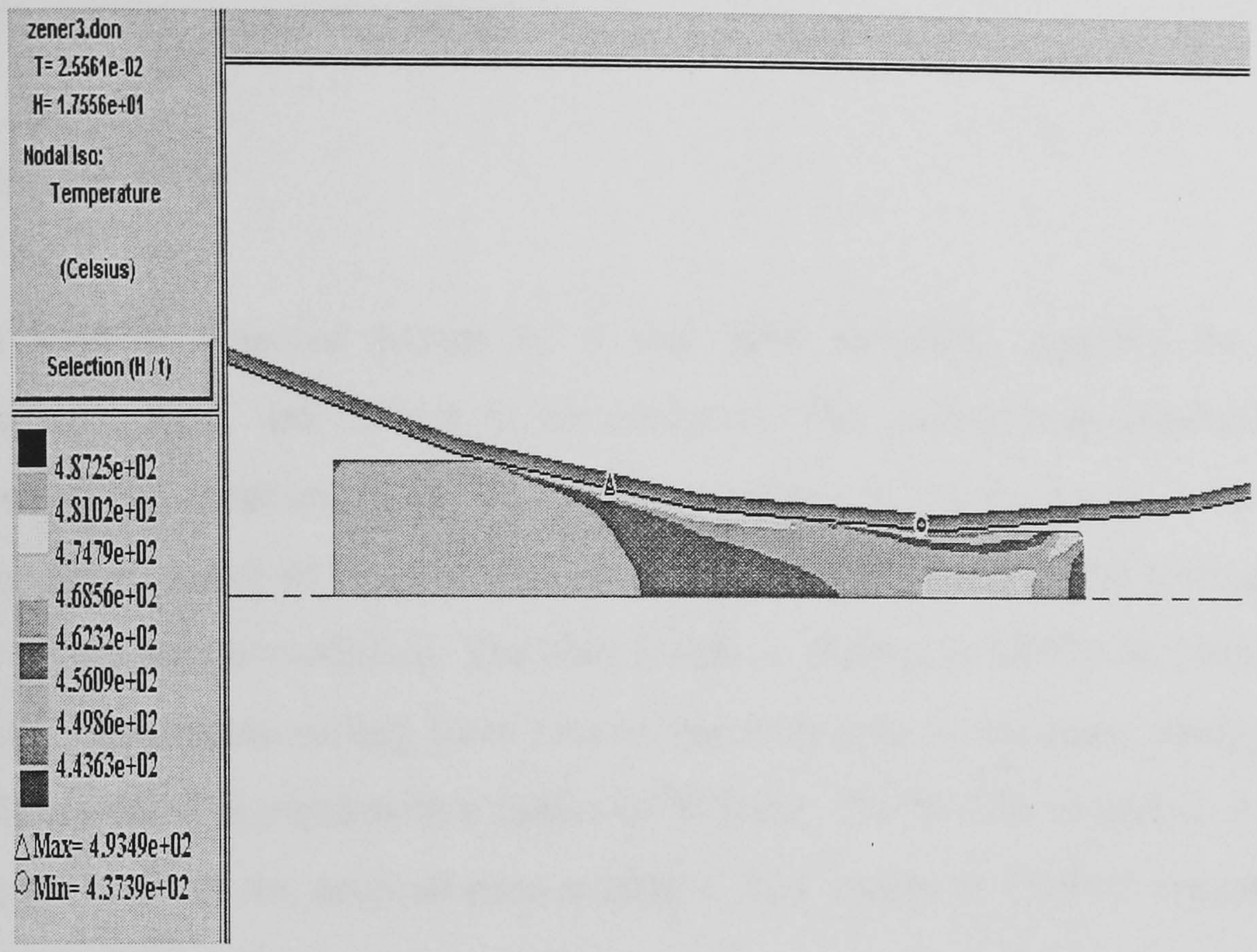

Fig.4-7 Temperature distribution computed by the hyperbolic sine function

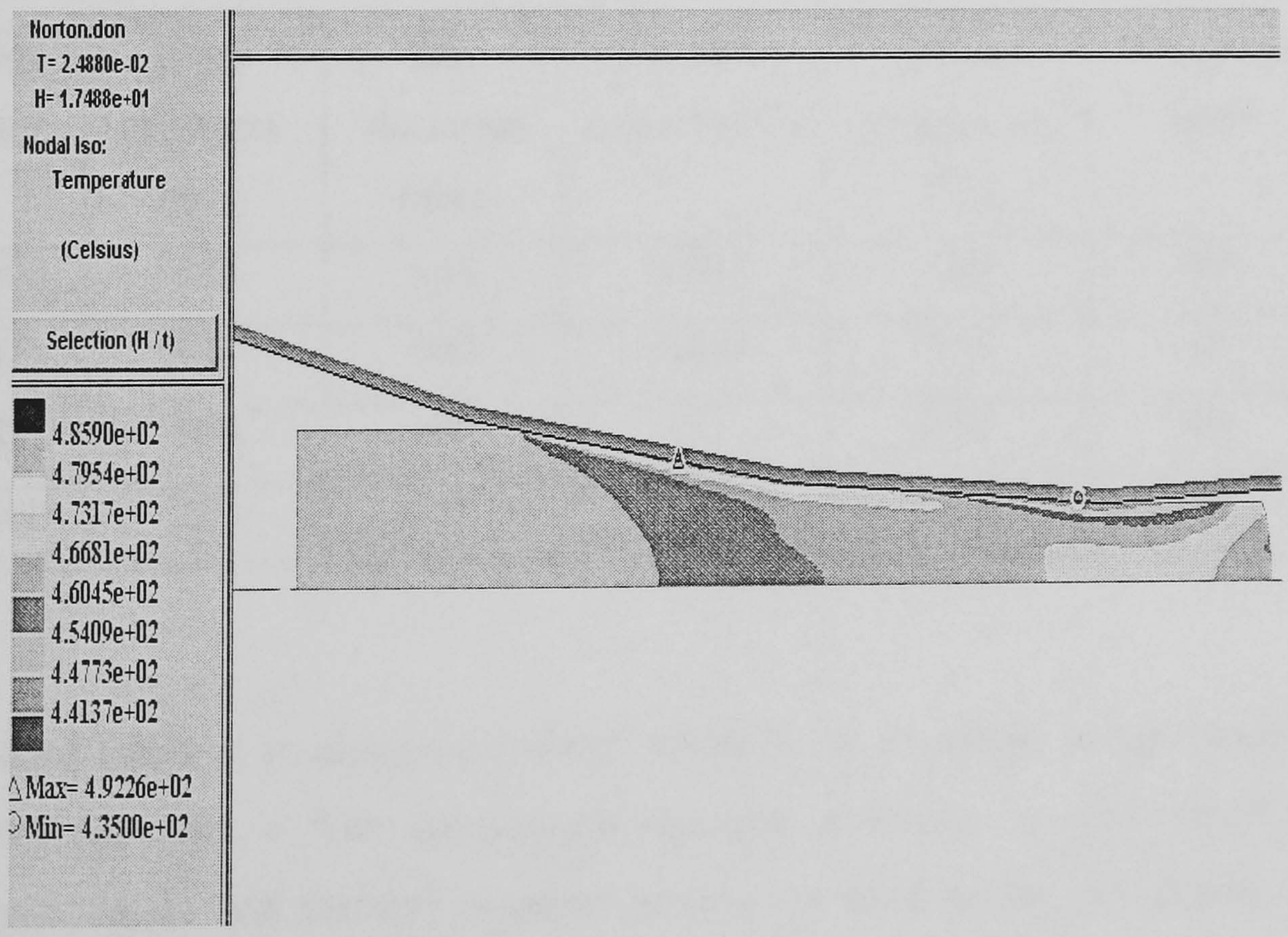

Fig.4-8 Temperature distribution computed by the Norton-Hoff law

4.2 Rolling force and roll torque

4.2.1 Rolling force

In this section, selected passes of a real pass schedule supplied by M.P.C. Laminazione, Italy, are chosen to be analysed. The rolling was conducted in a single stand hot reversing mill. The rolling parameters are shown in Table 3. The FEM model is shown as Fig 4-9. Due to the symmetric nature of flat rolling, only a quarter of the slab is modelled. The slab length is chosen as 1000mm, long enough to obtain a reasonable rolling force record, short enough to minimise analysis time. The roll is treated as rigid with a radius of 495mm. The widths of pass 2, 3, and 10 are not provided in the original pass schedule. The values in Table 2 are calculated by the spread formulae.

Table 3. Rolling pass parameters

Pass No.	Width (mm)	Entry thickness (mm)	Exit thickness (mm)	Thickness reduction(%)	Average temperature (^{0}C)	Roll speed (rpm)
1	1800	580	540	6.897	560	40
2	1814	540	500	7.407	555	40
3	1832	500	460	8	550	40
10	1860	220	180	18.1	515^{0}C	55

The deformed material is aluminium alloy AA3003. Its chemical composition is given in the appendix 4. The constitutive equation is shown in equation (4-2). Material mechanical and thermal property parameters used in the simulation are given in Table 4. The measured roll force and torque are shown in Table 5.

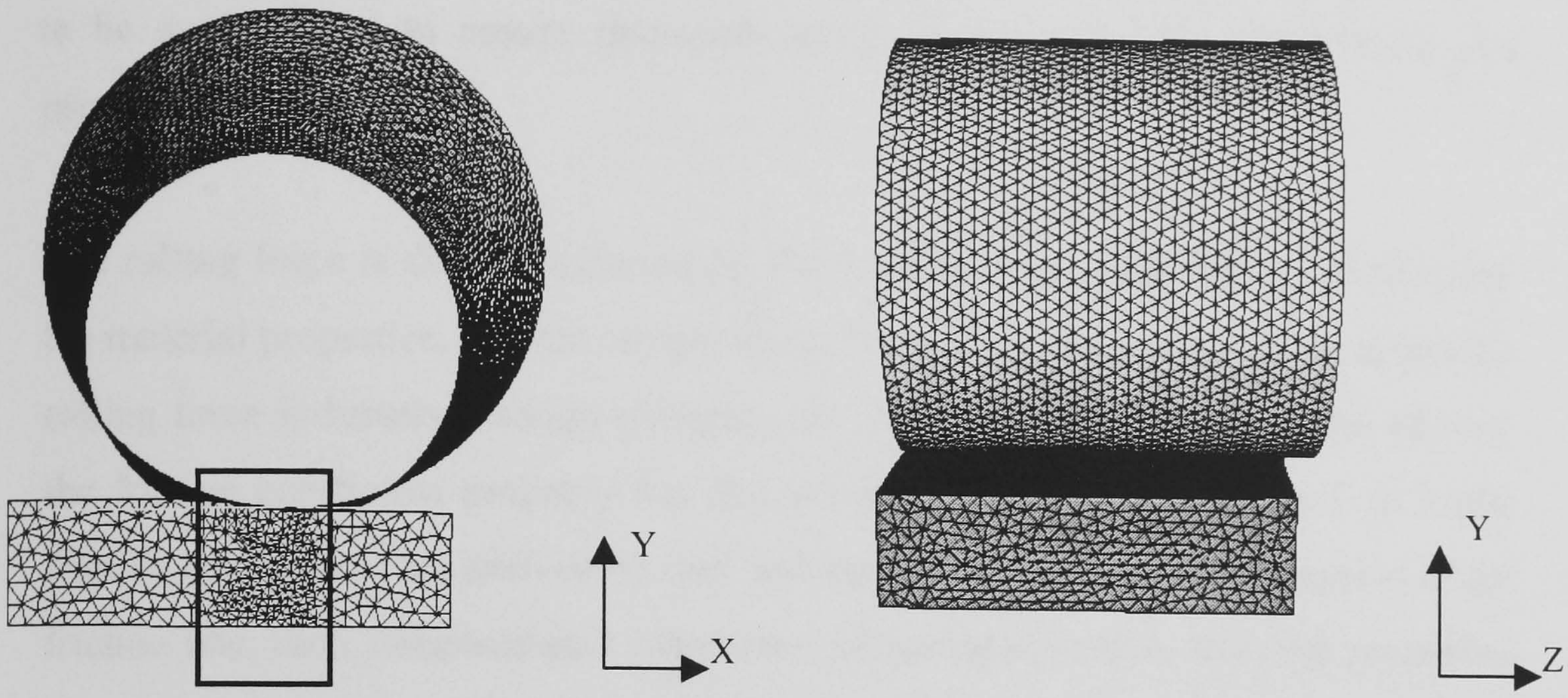

Fig. 4-9 The FEA model

Table 4. Physical properties of slabs used in the finite element model

Heat capacity ($J.Kg^{-1}.K^{-1}$)	Conductivity ($W.m^{-1}.K^{-1}$)	Heat transfer ($W.m^{-2}.K^{-1}$)	Possion Ratio	Density ($Kg.m^{-3}$)
960	198	30000	0.33	2730

Table 5. The measured roll force and torque

Pass No.	Measured Force(MN)	Measured Torque(MN-m.)
1	8.11	1.46
2	8.36	1.49
3	8.61	1.52
10	9.12	1.35

Accurate information about the rolling force is essential when designing a rolling pass schedule. The rolling force directly determines the thickness precision of rolled products. The rolling force is also the basis for computing the rolling torque. The accurate prediction of both of these parameters is imperative if mill breakdowns are

to be avoided and to ensure maximum productivity in terms of geometric and property requirements.

The rolling force is directly affected by the contact length, the friction coefficient, the material properties, and the temperature. The roll radius and reduction affect the rolling force indirectly through changing the contact length. Among these factors, the friction coefficient probably has the greatest influence. For passes 1 to 3, the friction coefficients are derived by trial and error by FEA. With the exception of the friction law, each computational parameter, including the mesh, material properties etc., are held constant. The derived friction coefficients are 0.7, 0.6 and 0.35 for Coulomb friction law, Tresca friction law and Viscoplastic friction law respectively.

It is clear that the friction coefficient is not the same for the same rolling condition for different friction laws in FORGE3. A lower value of friction coefficient is obtained for the Viscoplastic law than the other two friction laws. This is inevitable since the definition assumes that there is a continuous lubricant film within the roll gap, which is viscoplastic and is directly related to the material properties. Since the difference of thickness reduction for passes 1 to 3 is small, identical friction coefficients have been derived for coulomb and Tresca friction.

The computed rolling load for pass 1 as the material traverses the roll gap is shown in Fig. 4-10. As expected the rolling force increases gradually when the slab feeds into the mill gap and reaches a relatively steady value when the deformation is in the steady state regime. Since only a quarter slab is modelled, the actual rolling force equals twice the average value in the steady state deformation shown in Fig. 4-10.

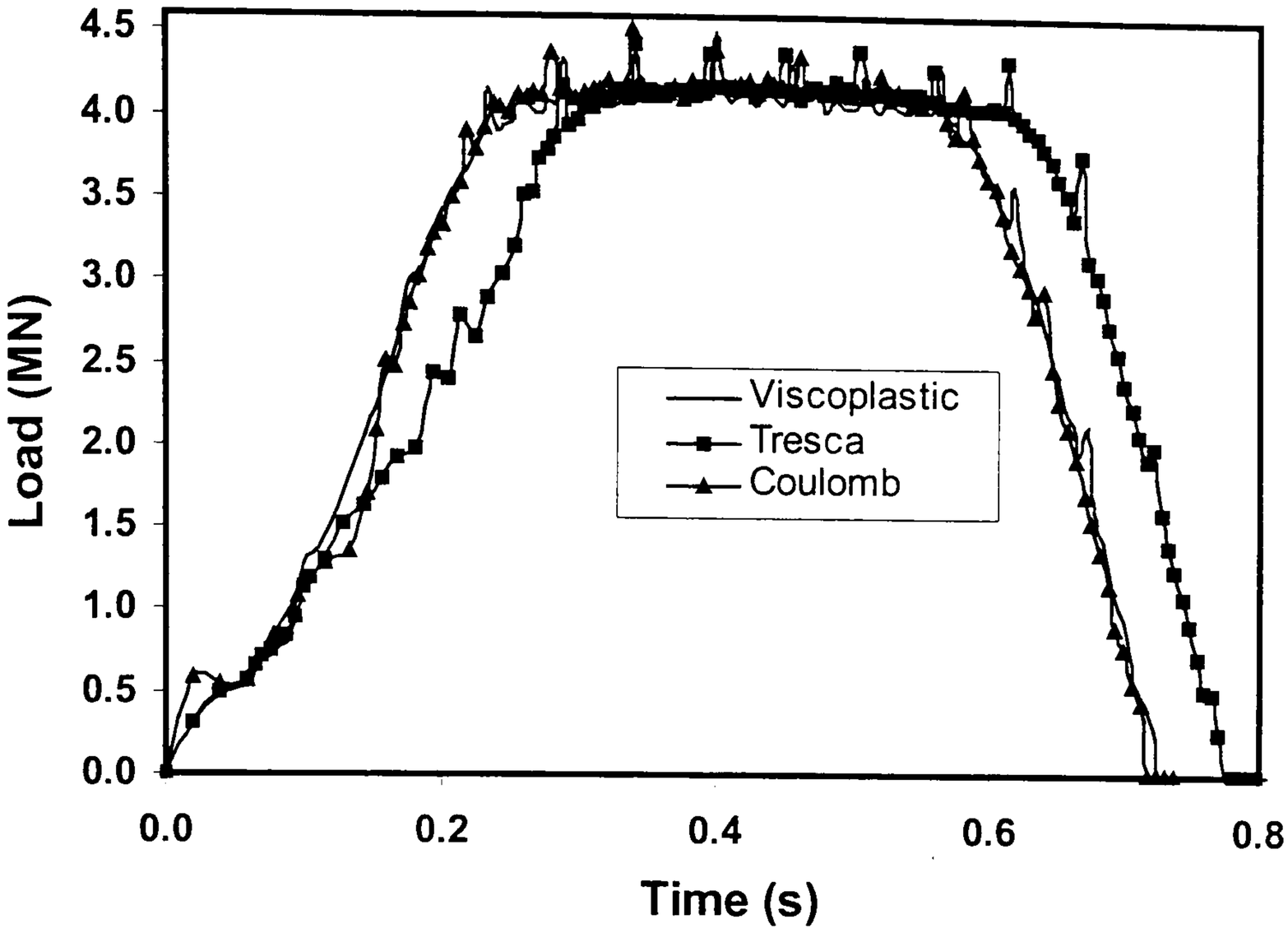

Fig.4-10 Comparison of the rolling load between the computed and the measured for pass 1

For the viscoplastic friction law, the calculated rolling force is 4.12*2=8.24 MN. The relative error compared with the measured rolling force 8.11 MN is 1.6%. The error for the Tresca friction law and the Coulomb friction law are 1.1% and 3.3% respectively. The curves of Coulomb and Viscoplastic show nearly identical shapes, the same time to reach the steady state and same time to leave the roll gap. The curve for Tresca friction differs in shape. It needs greater time before reaching the steady state, and therefore the time leaving the roll gap is greater than other two friction laws. This phenomenon is of course due to the varying slip predicted by each friction mode. The common factor is that all friction modes give approximately the same averaged load in the steady state. Generally consideration of predicted rolling load value and the curve shape suggest that the Viscoplastic friction law gives a slightly better prediction than the other two friction laws. We may therefore adopt the Viscoplastic friction law and investigate pass 10.

For pass 10, the analysis shows that when the friction coefficient is chosen as 0.35, the computed rolling load agrees well with the measured load. The computed

rolling load is 4.54*2=9.08 MN. The relative error compared with the measured load is 4.4%. One point, which should be noted, is that this is a larger reduction than for pass 1, but nevertheless the friction coefficient is same. This phenomenon we may be attributed to the higher rolling speed and lower temperature compared with the first three passes. According to Lenard's study on hot rolling of commercially pure aluminium, the friction coefficient falls as the rolling speed increases and increases when the reduction is increased (Lenard et al 1999). In pass 10, the effect of low temperature and high rolling speed balance the effect of high reduction, which may explain the calculation of the same friction coefficient. The comparison of the measured and computed rolling load is illustrated in Fig.4-11. It is obvious that FEA gives excellent prediction.

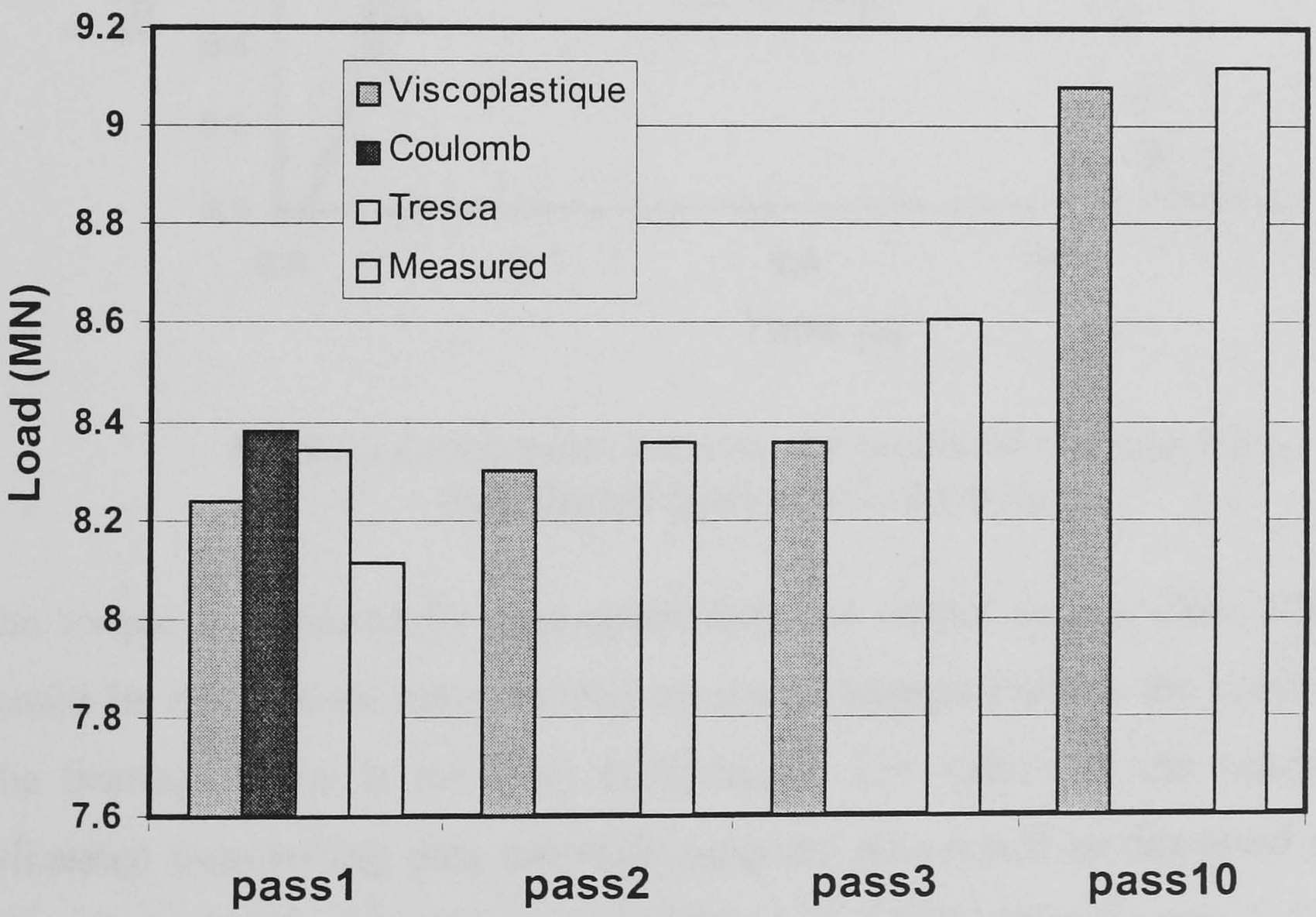

Fig.4-11 Comparison between the predicted and the measured rolling loads

4.2.2 Torque

Perhaps the most important feature when designing the pass schedule is the calculation of energy requirement. An underpowered unit is the most obvious risk

since this will lead to a reduction in productivity due to stalling. Thus we must ensure that the motor is more than adequate for any immediate or future workloads. In the present work, the calculated torque for various friction laws for pass 1 are shown in Fig.4-12.

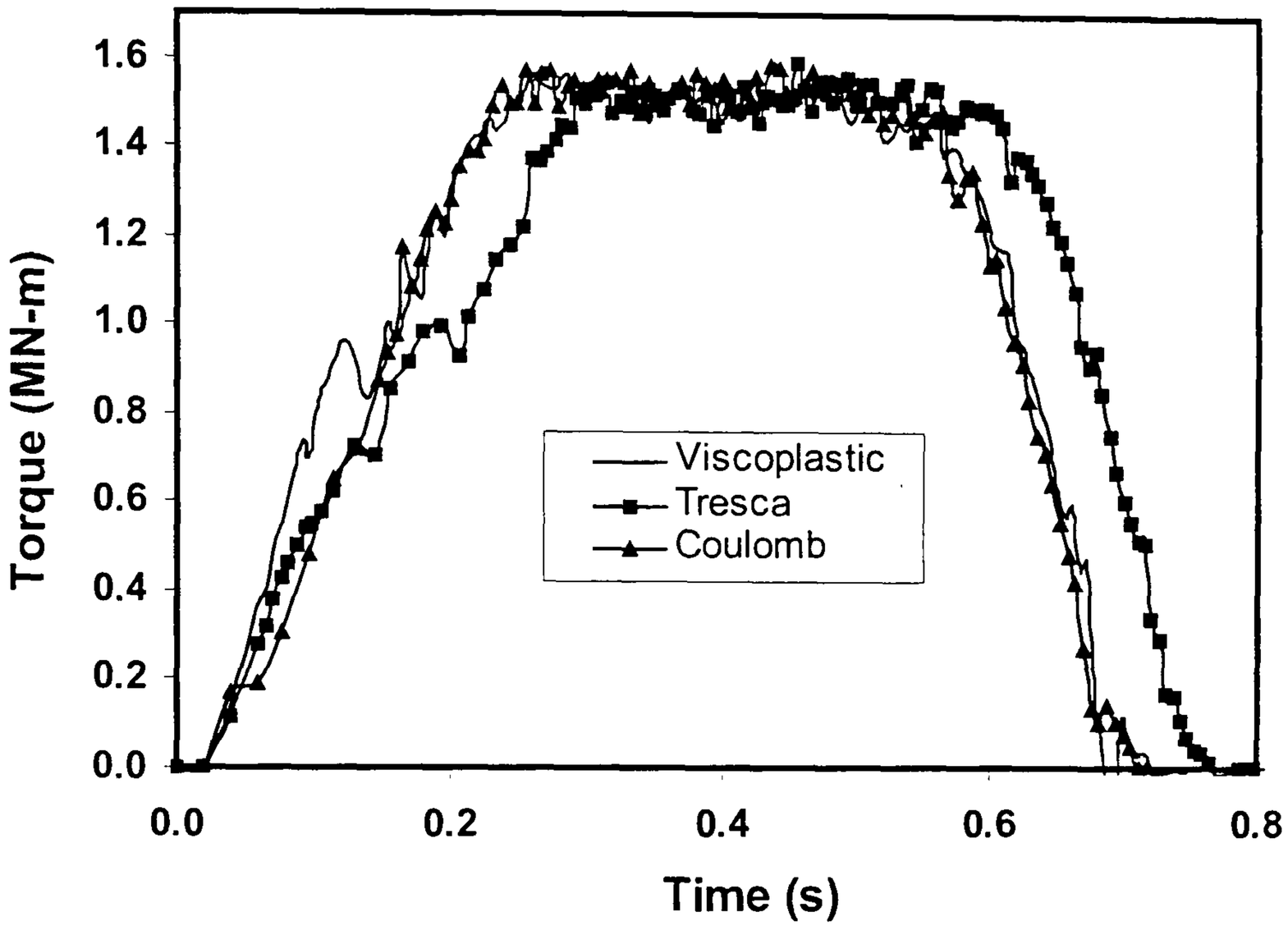

Fig.4-12 Comparison between the predicted rolling torques by different friction laws for pass 1.

The torque is obtained by post processing the output results from FORGE3. It should be emphasised here that the measured torques include the bearing torque. The bearing torque is not easy to measure. The values of the bearing torque calculated from rolling pass schedule program, which will be discussed in chapter 6, are 0.084MN-m, 0.083MN-m, 0.082MN-m and 0.06MNm for pass 1, 2, 3 and 10 respectively. Therefore, the rolling torques are 1.38MN-m, 1.41MN-m, 1.44MN-m and 1.29MN-m respectively (shown in Fig.4-13). The computed error of the rolling torque for the pass 1, 2, 3 and 10 are 9.4%, 7.8%, 6.9% and 14% respectively when Viscoplastic friction is employed. The computed rolling torque is ,under all conditions, slightly greater than the measured value. So there is no risk of designing an underpowered unit. The torques calculated for pass 10 and the initial passes

would appear to be of good accuracy. In the practical rolling process, motors usually are able to sustain a certain amount of overload, and there are many interrelated factors, nevertheless it is necessary to pursue high computation accuracy to ensure that capital costs of the motor and drive chain are minimised.

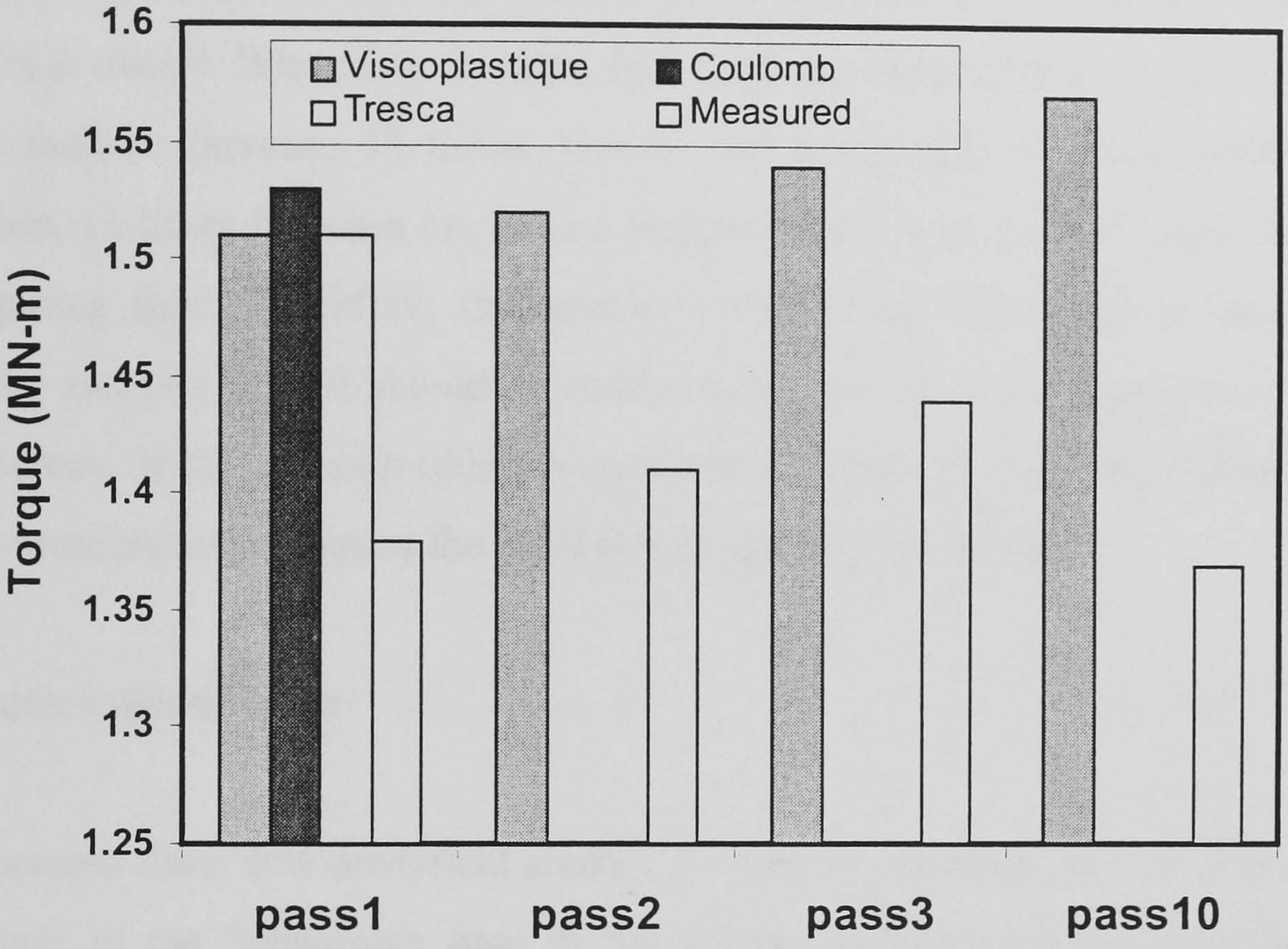

Fig.4-13 Comparison between the predicted torques and the measured values for different passes

Table 6 The influence of element size on the computed results

H/a	Total element number	Computed load(MN)	Computed torque(MN-m)
3	3349	4.25	15.6
4	7661	4.15	15.2
5	13905	4.13	15.2
6	44998	4.13	15.1

In table 6, all analyses are carried out by using the viscoplastic fraction law with a friction coefficient of 0.35 for pass 1. The ratio of H/a is the value of slab thickness

of the simulation model over the characteristic element size. The increase of the ratio H/a means that the element size decreases and more elements are used. As we can see, when H/a is greater than 4, there is almost no difference among the computed loads and torques. The computing precision improves no more. That also means that the searched friction coefficient is independent of the mesh density when H/a is over 4. When H/a doubles, for example changing from 3 to 6, the total element number increase 13 times. Due to the complexity of three-dimensional simulation, 13 times increase in element number leads to at least 30 times increase in computing time. Therefore, the search of the critical H/a value is crucial for saving the analysis time. It should be emphasised here that the optimal value of H/a could increase if the research object is pressure distribution along the contact since it needs more nodes to display the local deformation information.

4.3 Pressure distribution

At the present time, few analytical studies have been presented on the distribution of pressure in the breakdown pass in hot rolling using numerical methods. The curves of pressure distribution in the roll gap for pass 1 and the pass 10 are shown in Fig4-14. The maximum pressure occurs close to the point of entry; after which the pressure drops gradually. This is in contrast to the pressure peak near the centre line for strip rolling. This conclusion coincides with Macgregor and Palme's (1951) observation and the computed normal pressure curve of Chen et al. (1992) by using explicit dynamic relaxation model.

Although the reduction of the pass 10 is about twice that of pass 1, the peak pressure value of pass 10 is lower than the peak pressure value of pass 1(see Fig.4-14). This phenomenon was also observed in Macgregor and Palme' (1951) experiment. The maximum pressure in pass 1 is about 45 MPa. The yield strength under the current deformation condition is about 19 MPa. Peak pressure is thus much higher than yield strength. That is what Orowan called the "peening effect".

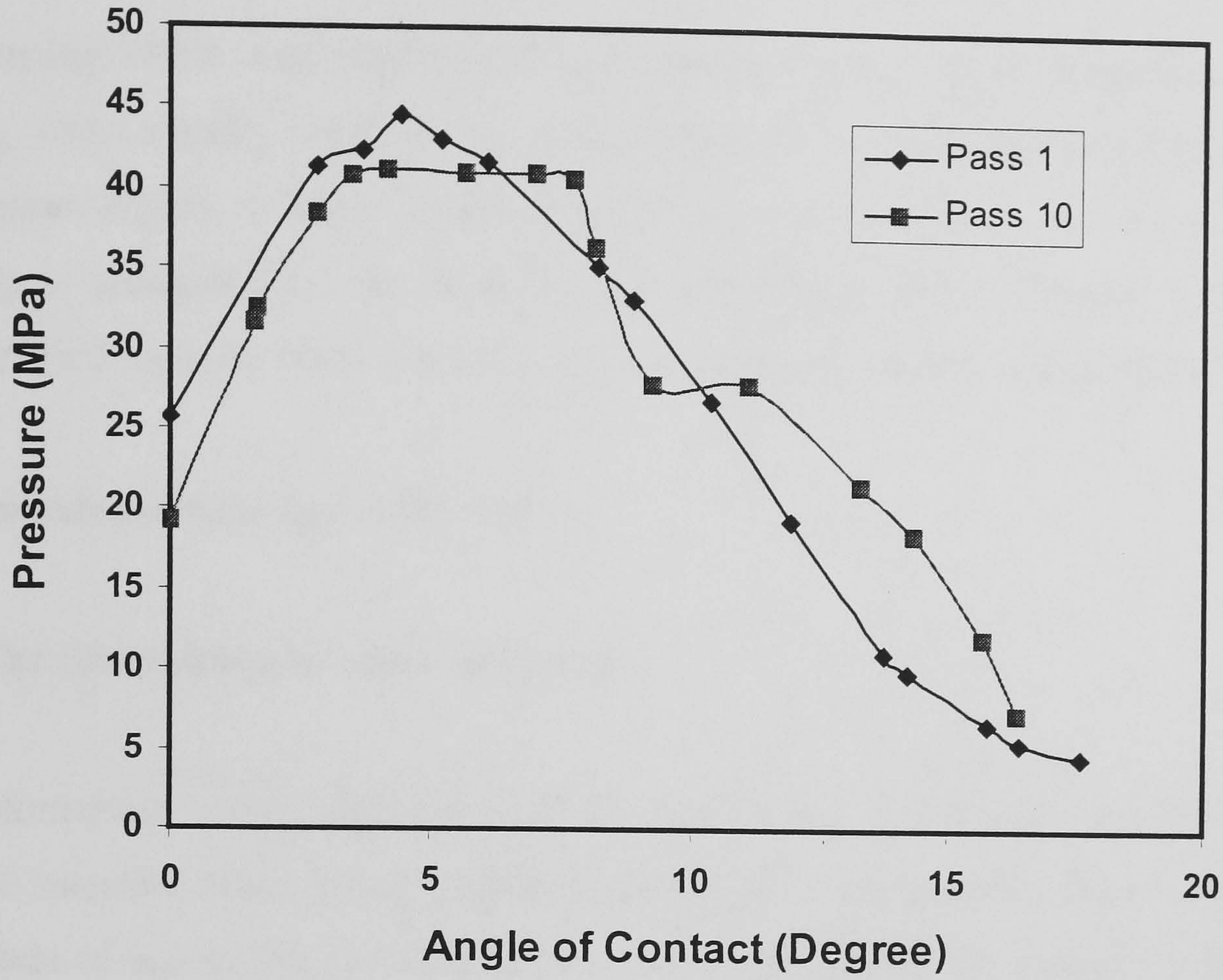

Fig. 4-14 Distribution of pressure in the contact plane between Roll and slab

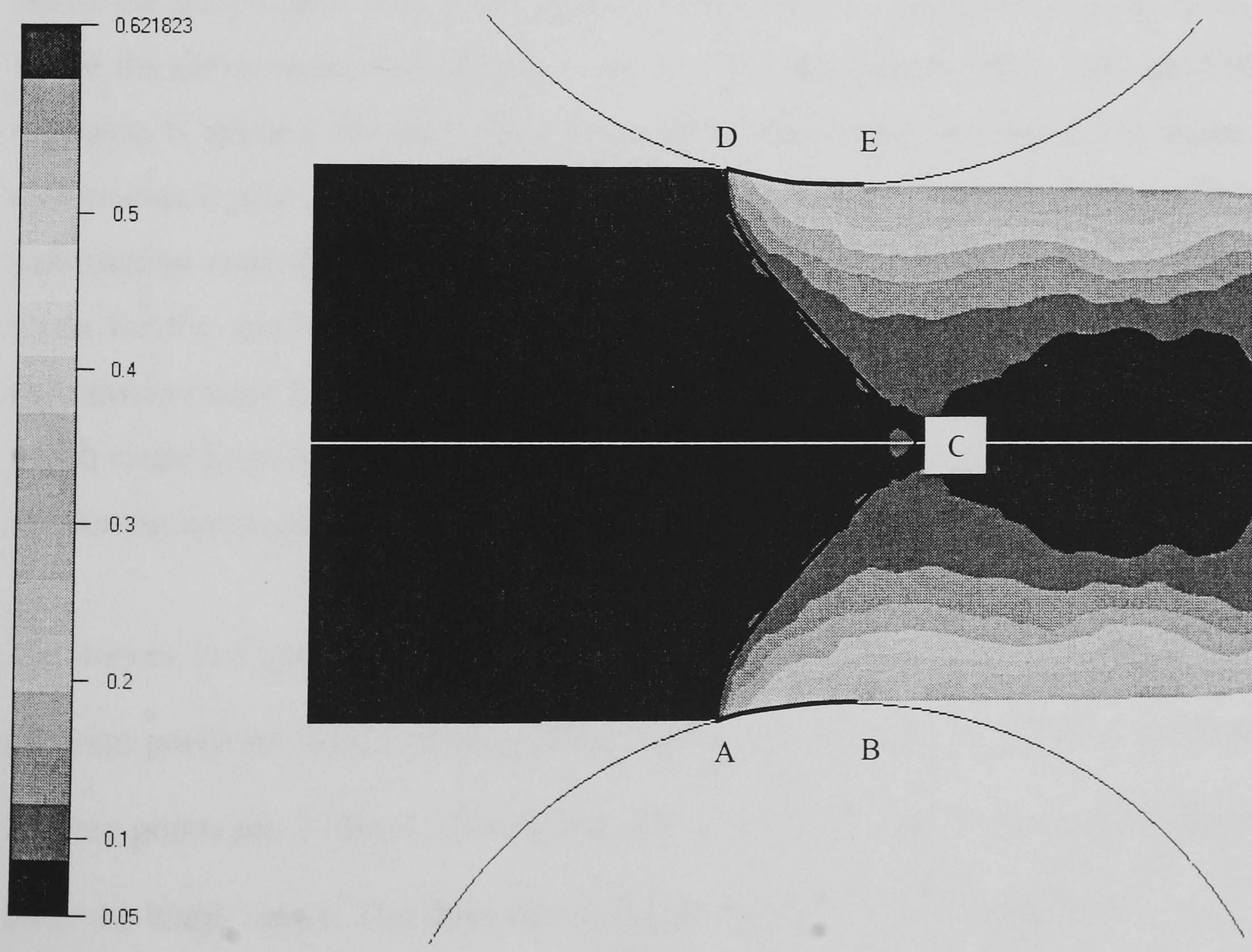

Fig.4-15 Illustrationof the contact length and the division between elastic region and plastic region

The peening effect was also found in Macgregor and Palme' experiment. The peening effect usually occurs in the early passes of the breakdown rolling, where the contact length is many times smaller than the slab thickness. Near entry, yielding is restrained by the adjacent and underlying elastic regions. V-shaped elastic region presents under a portion of the contact arc (shown in Fig.4-15).

4.4 Equivalent strain and stress state

4.4.1 The distribution of equivalent strain

The deformation mainly concentrates within the region of half thickness below the roll/slab interface when a small reduction (<10%) is applied (see Fig. 4-16). The magnitude of equivalent strain in the slab centre is about 0.08 indicating that the steady state deformation is not achieved in the slab centre. The curve of pass 3 shows the same shape. This is a common phenomenon in industrial roughing rolling where the deformation can not penetrate into the slab centre. When 18% (pass10) reduction is applied, the equivalent strain at the slab centre increases. The highest deformation region is still concentrated near the interface of roll and slab but a large deformation zone gradually expands into the slab centre. For pass 1, the equivalent strain for the whole deformation zone is less than 0.25. For pass 10, the whole deformation zone has an equivalent strain value over 0.25. There are two factors, which cause large deformation in pass 10. One is large reduction and another is the thinner thickness compared with the thickness in pass 1.

The curves in Fig.4-17 show the variation of equivalent strain with time at three different positions from entering the roll gap to leaving the roll gap. The positions of three points are 270mm, 130mm and 30mm below the surface at a plane 30mm away the width centre. The three curves further verify the above conclusion.

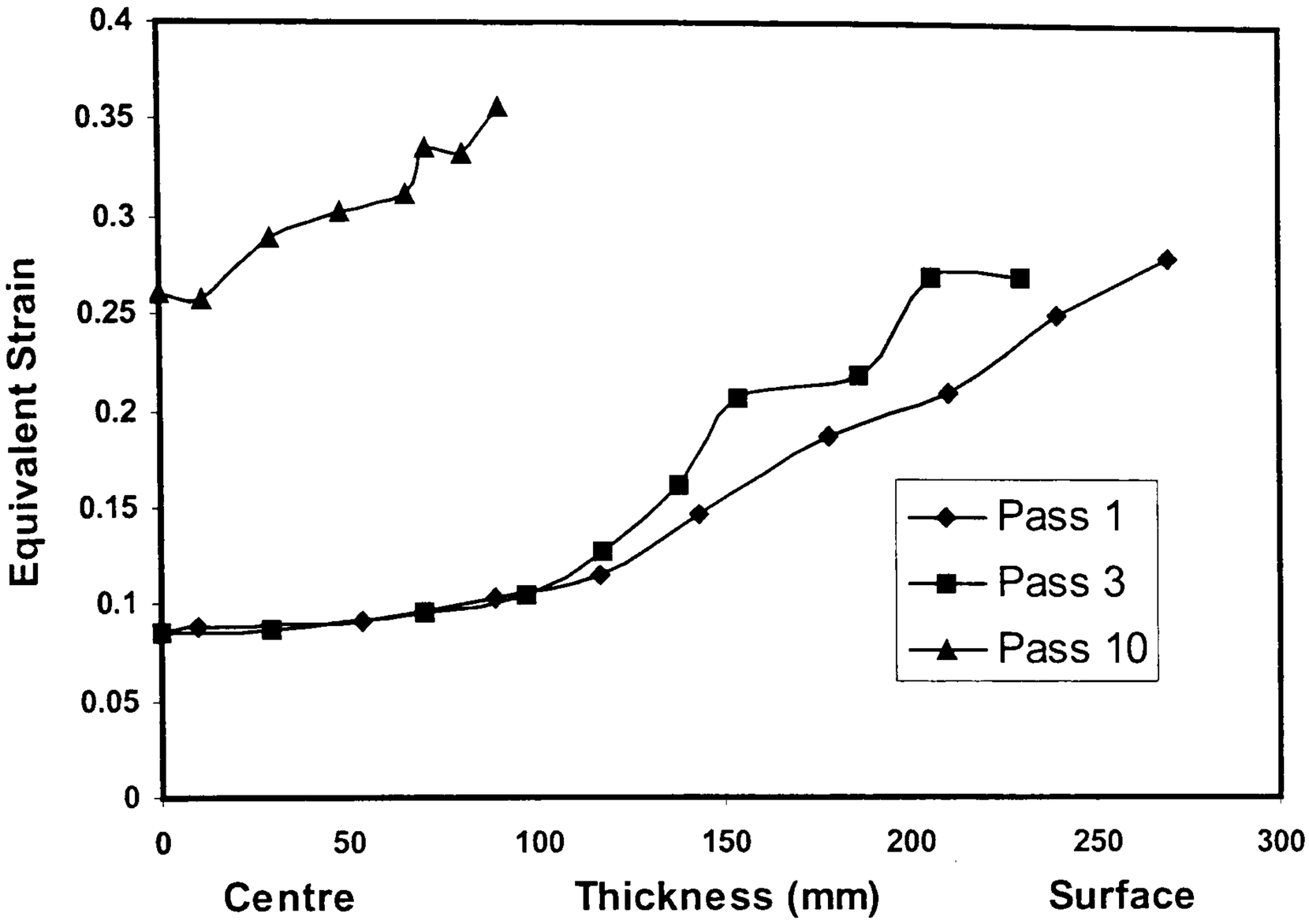

Fig. 4-16 Distribution of equivalent strain through the thickness

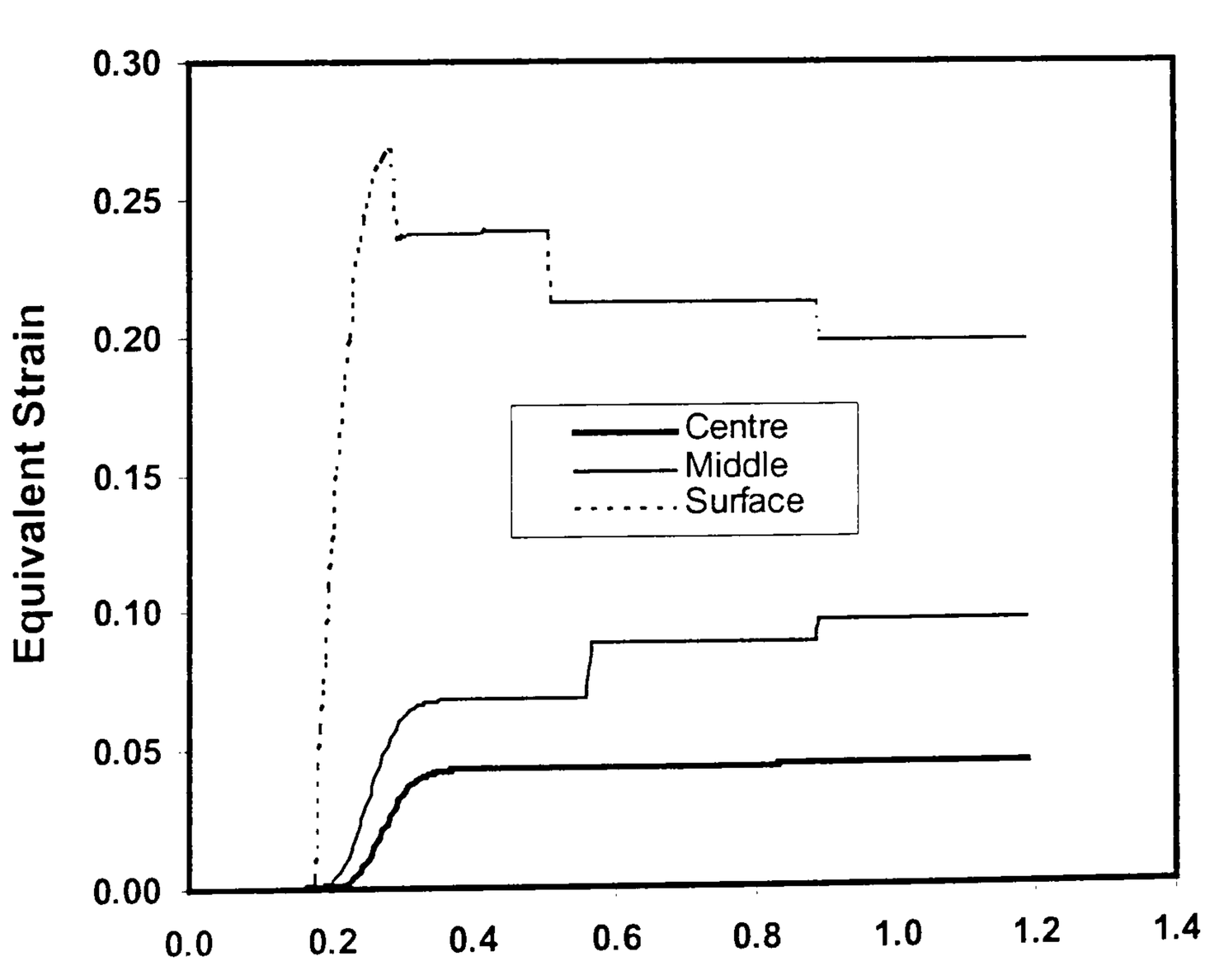

Fig.4-17 Equivalent strain/time curves for different points of pass 1

4.4.2 Stress state

There are two-dimensional tensile stresses, along the rolling direction and along the width, in the slab centre in the roll gap for pass 1 (see Fig. 4-18). Two-dimensional tensile stresses are undesirable because they tend to cause microcracks if the slab quality is not excellent. The stress through the thickness is compressive stress. This phenomenon is a feature of all rolling operations. The combined effect of three stress components is shown as the curve of pressure in Fig.4-18.The pressure is defined as $(\sigma_x + \sigma_y + \sigma_z)/3$, the hydrostatic stress. In many fracture criteria, this hydrostatic stress is regarded as having a direct link with crack generation and plays an important role in causing cracks (Kim et al 1995). The compressive hydrostatic stress improves the plasticity and hence reduces the possibility of crack, and the tensile hydrostatic stress increases the possibility of crack

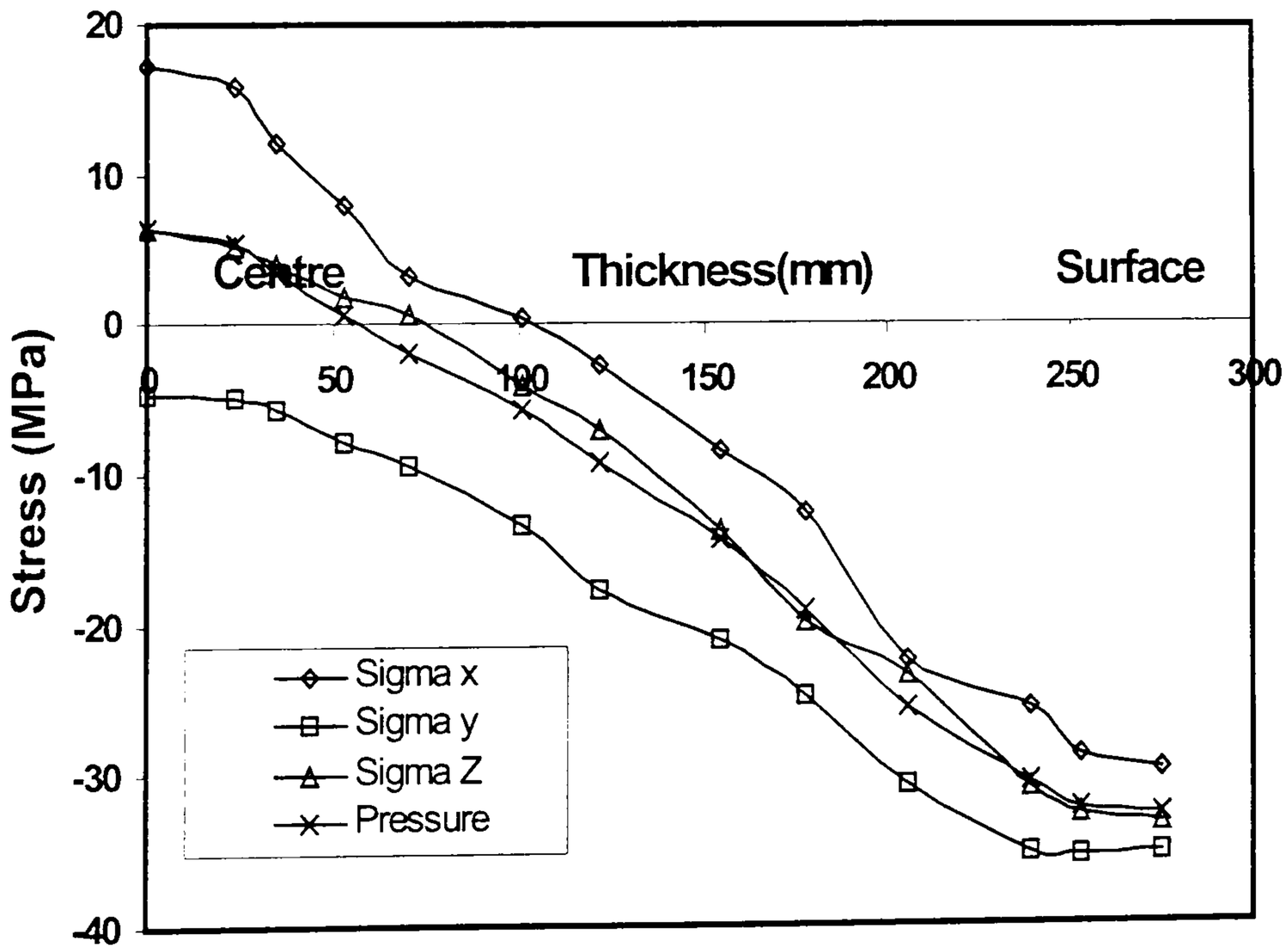

Fig.4-18 Stress distribution in the roll gap during the steady state for the pass 1

4.5 The temperature variation during and after hot rolling

Due to the limitation of equipment in the laboratory, there are severe differences between laboratory rolling and industrial rolling under some rolling conditions, such as the ratio of roll radius to the slab thickness, friction and cooling system. The ratio of roll radius to the slab thickness has a significant influence on the temperature profile through the thickness in the roll gap, and on the determination of spread. Presently, there appears to be no published literature reporting the comparison of the temperature distribution between different rolling conditions.

All these aspects will be discussed in this section. The role of FEM is highlighted. The research works on the heat transfer coefficient in the rolling of aluminium alloys are reviewed since it is the major factor affecting the FEA accuracy of temperature. Knowledge of temperature changes in different slab positions after several passes will be helpful by offering the designer of rolling pass schedule a unique chance to understand rolling processes, and therefore to control the rolling process. In the following parts, a three-pass laboratory rolling schedule and a two-pass commercial rolling schedule are simulated. FEM gives an excellent agreement with the recorded temperature changes.

4.5.1 The finite difference (FD)

The theories of the analytical approach and the FEM have been discussed before. Here, only the method adopted by Sheppard and Wright (1980) is chosen as a representative for the FD. The theory of this method is briefly revisited.

Applying the explicit finite difference equation to the general heat transfer equation and ignoring the material flow in the lateral direction (z), we obtain:

$$K\frac{\partial^2 T}{\partial x}+K\frac{\partial^2 T}{\partial y}-\rho C\frac{\partial T}{\partial t}+q=0 \qquad (4\text{-}12)$$

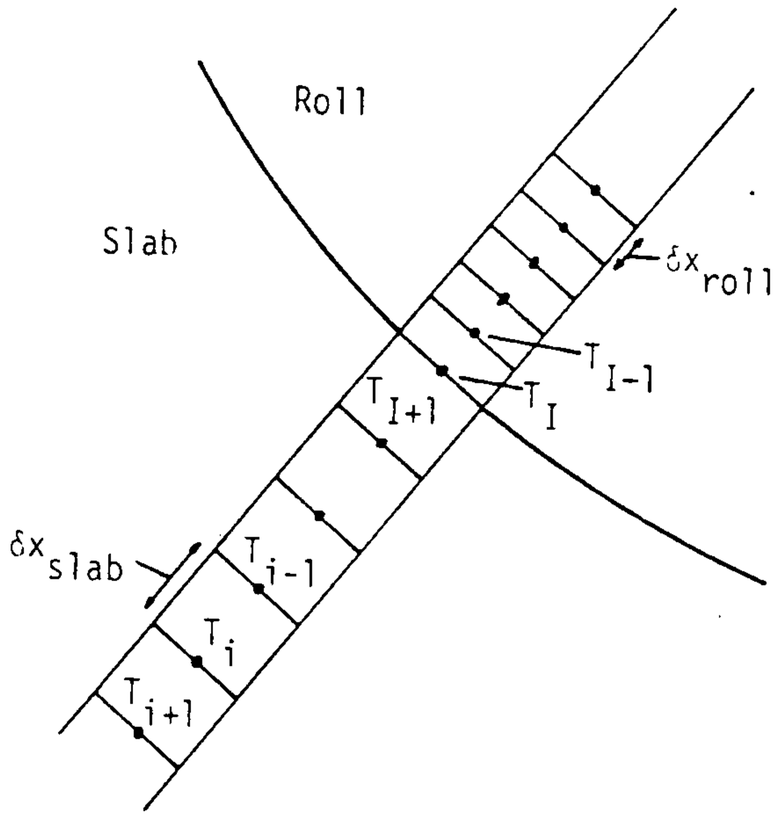

(a)

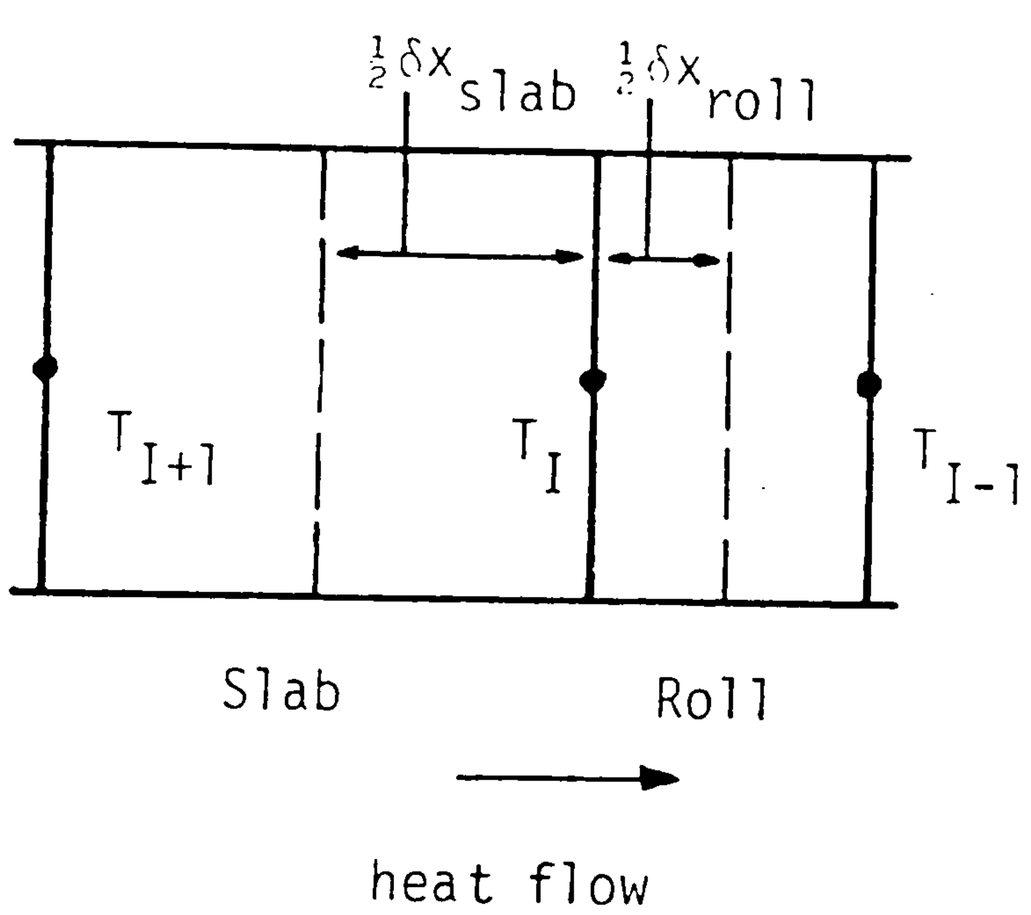

(b)

Fig.4-19 Arrangement of elements across the roll and slab
(a) and the surface region (b)

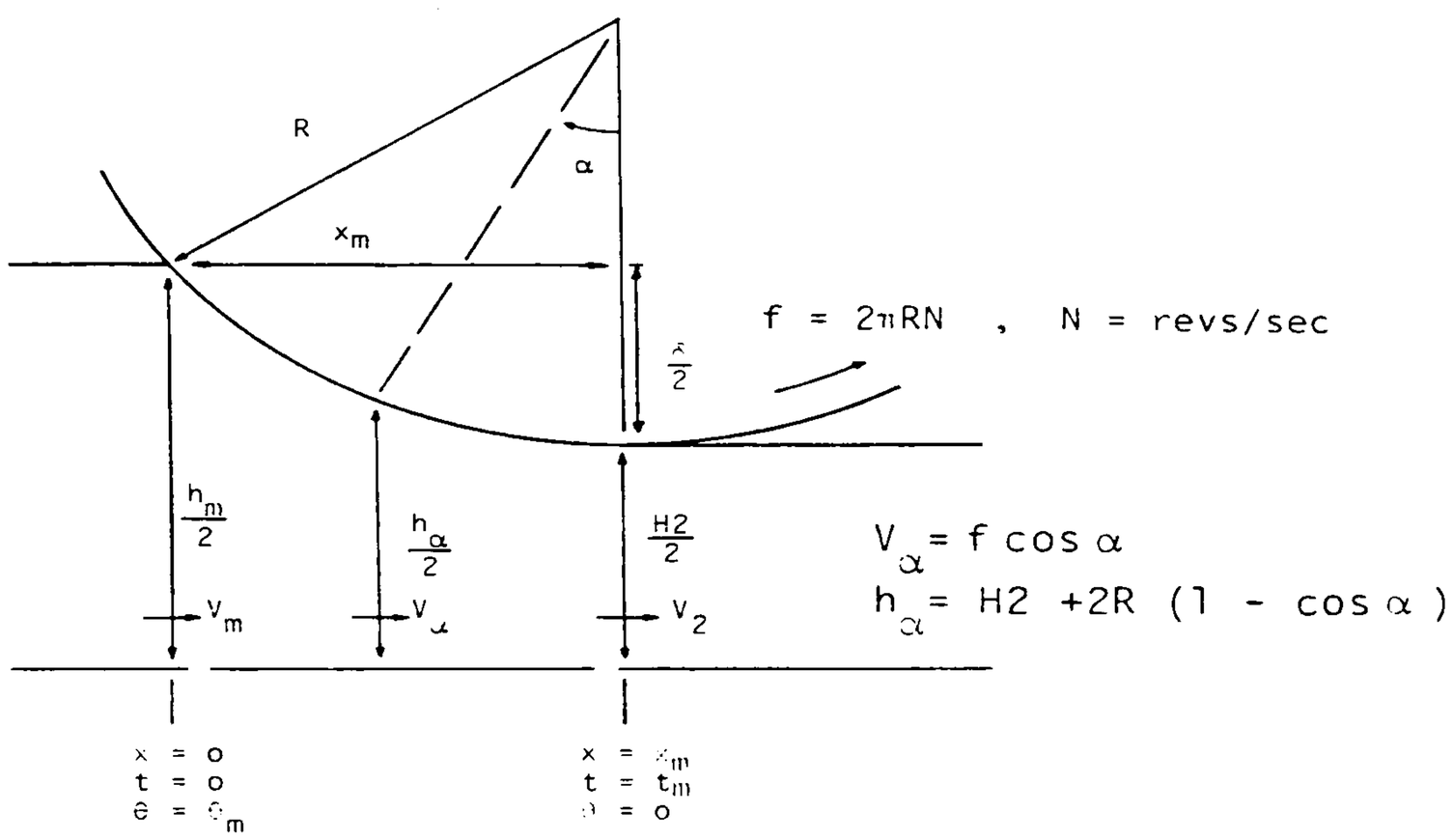

Fig. 4-20 Roll gap geometry and nomenclature

Further assuming that heat flow is predominantly towards the rolls and using the nomenclature of Fig. 4-19 and 4-20, we obtain:

$$T_i(t+\Delta t) = \frac{\alpha \Delta t}{(\delta x)^2}\left[T_{i-1}(t) + T_{i+1}(t)\right] + q\frac{\alpha \Delta t}{K} + T_i(t)\left[1 - \frac{2\alpha \Delta t}{(\delta x)^2}\right] \qquad (4\text{-}13)$$

using the same calculation time increment Δt for the slab and roll, the heat balance at the interface gives an interface temperature T_I in the equation:

$$T_I(t+\Delta t) = T_I(t) + \frac{2M^*(1+r)}{r}\left\{T_{I-1}(t) - T_I(t) + r\left[T_{I+1}(t) - T_I(t)\right]\right\} \qquad (4\text{-}14)$$

where:

$$r = \frac{K_{slab}(\delta x)_{roll}}{K_{roll}(\delta x)_{slab}} \qquad (4\text{-}15)$$

$$M^* = \frac{2(\Delta t)}{(\delta x)^2} \qquad (4\text{-}16)$$

Friction at the roll-slab interface will cause a temperature rise locally near the interface. Assuming that the heat is generated only at the interface, and that sticking friction prevails, the temperature rise is given as:

$$\Delta T = \frac{2\tau(\Delta V)(\Delta t)}{(\rho C \delta x)_{roll} + (\rho C \delta x)_{slab}} \tag{4-17}$$

The tangential relative velocity between the slab and the roll is given by:

$$\Delta V = f \frac{1 - h_\alpha \cos\alpha}{h_\theta \cos\theta} \tag{4-18}$$

The time of contact between any element in the slab and the roll is calculated by:

$$t = \frac{R}{V_\alpha h_\alpha}\left[(h_2 + 2R)\sin\theta_m - R\theta_m - \frac{R\sin 2\theta_m}{2}\right] \tag{4-19}$$

where θ_m is defined as:

$$\theta_m = \sin^{-1}\left[\frac{\sqrt{R\delta - \delta^2/4}}{R}\right] \tag{4-20}$$

The heat generation per unit volume, q, is determined from the known stress-strain behaviour of the alloys:

$$q = \frac{\eta\sigma_s}{t'}\ln\left[\frac{h_1}{h_2}\right] \tag{4-21}$$

where η is the fraction of work turned into heat.

4.5.2 Single pass laboratory rolling

Fig.4-21 to Fig.4-25 show the calculated results for a laboratory hot rolling pass. The material rolled is commercial purity aluminium. Details of the experimental program were given in Wright's thesis (1978). Briefly, the slab size is 30mm in length (rolling direction), 25mm in width and 25mm in thickness. The exit thickness is 17.5mm, resulting in a 30% thickness reduction. The nominal rolling temperature is 500^0C, and the roll diameter is 250mm. The average characteristic element size is 1.2mm for the laboratory simulation. The comparison between the measured temperature data and the calculated curves is shown in Fig.4-21.

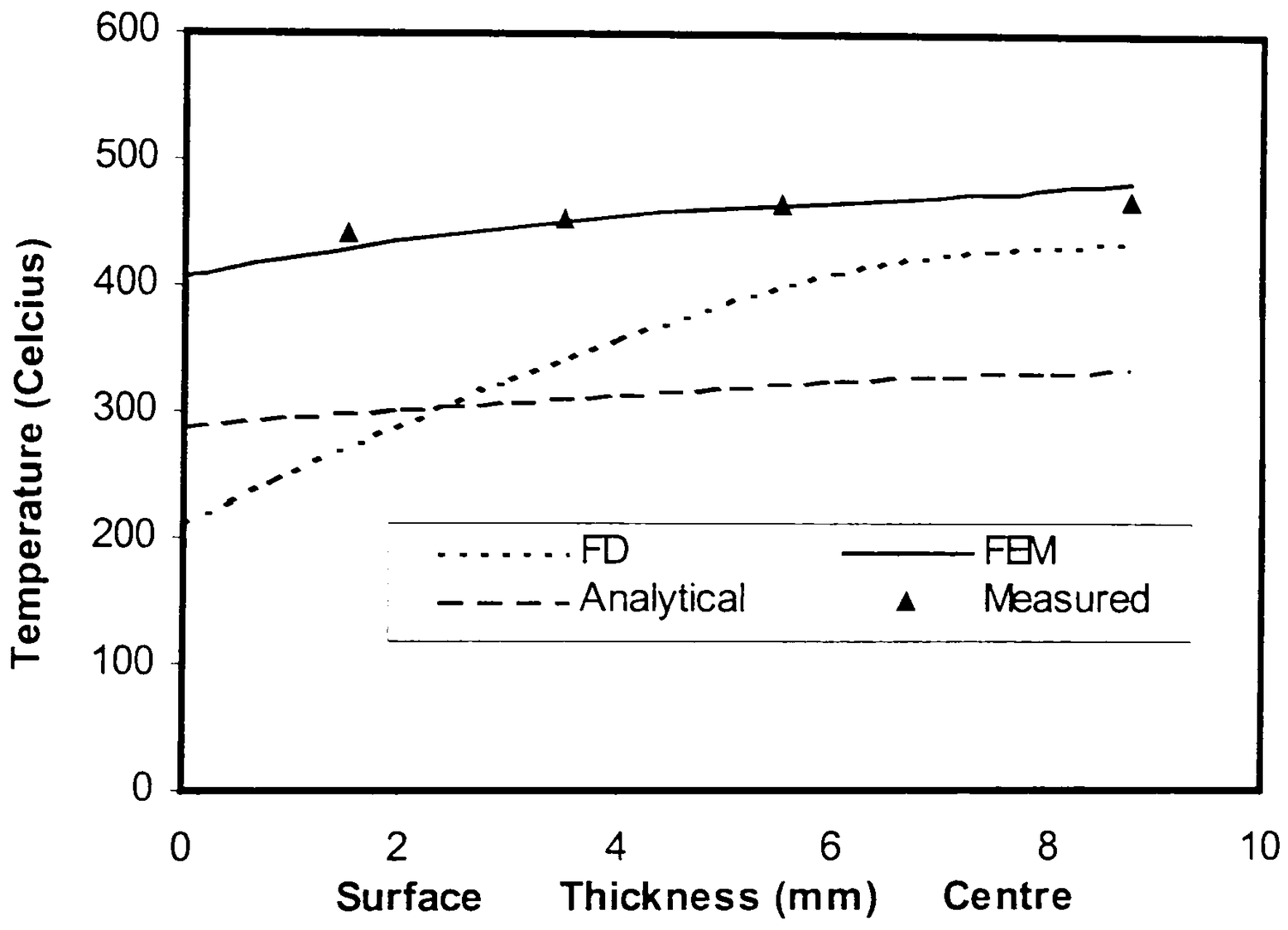

Fig.4-21 Comparison of temperature distribution through thickness for a laboratory slab rolling pass

From fig.4-21, we can see that, the curve predicted by FEM is much better than the curves given by the analytical approach and FD, especially in the region near the surface. From the point of view of the curve shape, all three methods give the same trend. The analytical approach gives a small temperature variation from the slab

surface to the slab centre, and the curve is much smoother than FD and FEM. This is not surprising since this method does not consider the heat generation caused by plastic deformation and friction work, and heat loss by radiation and convection. The thickness reduction in the current slab rolling pass is up to 30%. The effect of heat generation by plastic deformation at such a large deformation is expected to be very large and will change the temperature distribution greatly. When this effect is taken into account in the FD, the calculated accuracy improves greatly, especially in the centre region, where more heat is generated by plastic deformation. But the predicted temperature distribution is even worse than that provided by the analytical approach near the surface region.

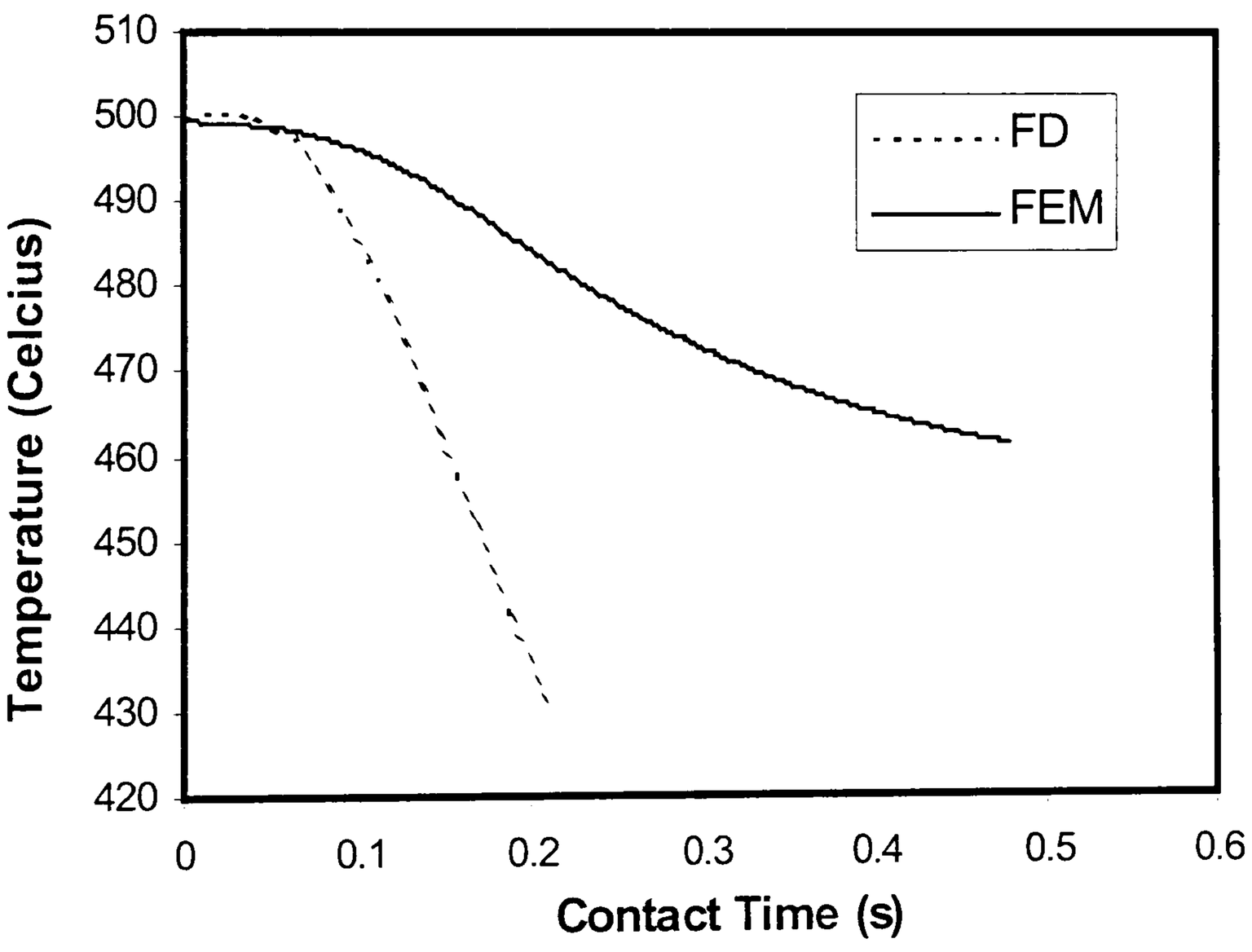

Fig.4-22 Comparison of temperature evolution through roll gap computed by FD and FEM for a laboratory slab rolling pass

The centre temperature profiles calculated by the FEM and FD are shown in Fig.4-22. The contact time given by the FEM is about twice that given by the FD. One possible reason is that the influence of width spread is ignored in the FD. Metal flowing to the lateral side will increase the contact time by increasing the contact area with the rolls. Since the ratio of width to height of the current pass is 1.0, this is

a strong three-dimensional deformation. The width spread is significant. The computed transverse section predicted by FEM is shown in Fig.4-23. It should be noted that Fig.4-23 shows only a quarter of the actual section. It can be seen that there is intensive lateral deformation, causing non-uniform spread behaviour.

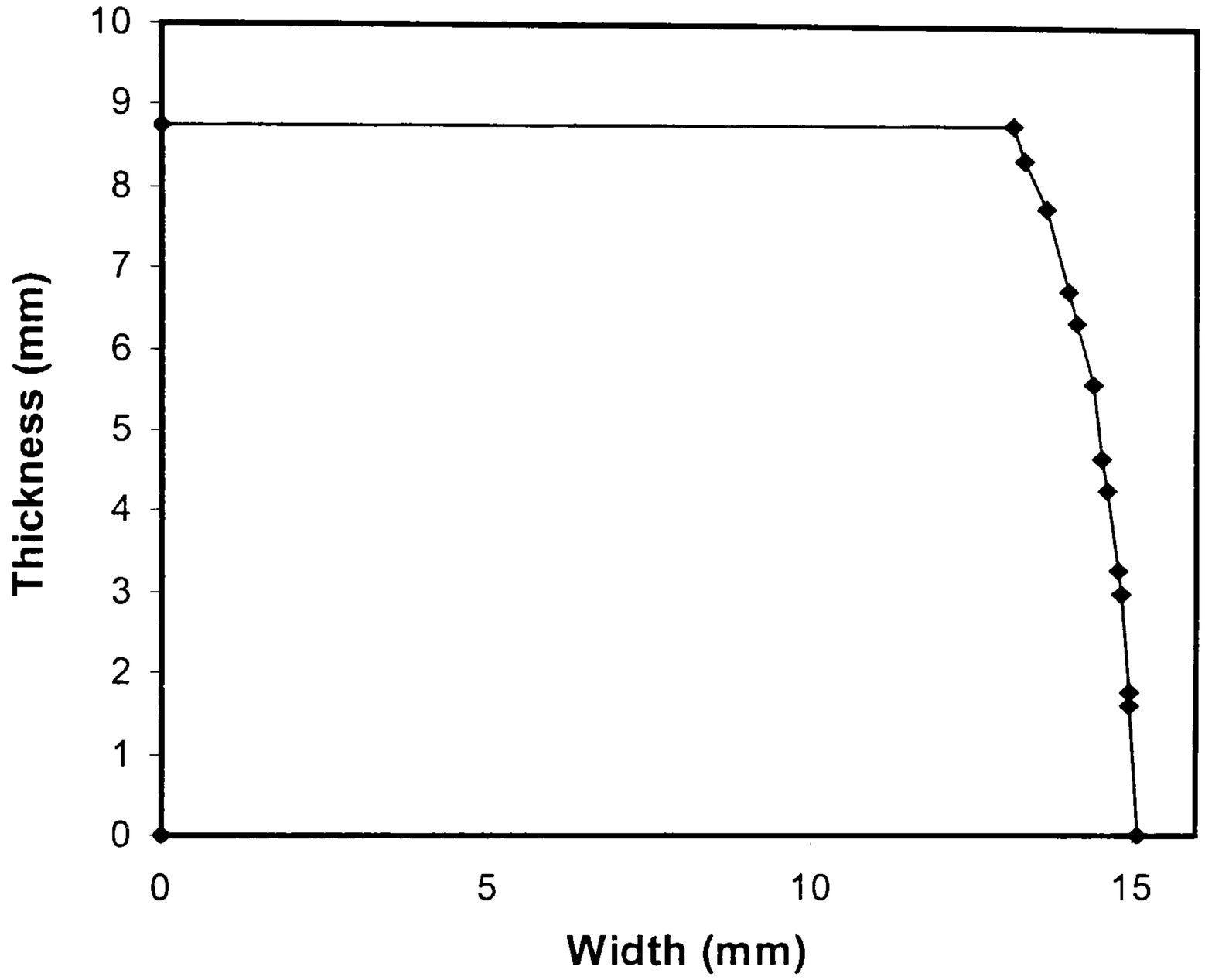

Fig.4-23 The transverse section of the deformed slab (a

Another possible reason is due to the assumption of uniform strain-rate distribution through the thickness adopted by the FD. In a process where high friction predominates (sticking friction was obtained in experiments by using a cleaning roll and an absence of lubricant), the difference of strain rate from slab surface to slab centre is significant. Therefore, the assumption of uniform strain rate is not appropriate. From Fig.4-22, we can also see that the curve given by the FD drops quickly, while the curve given by FEM drops slowly. The temperature difference between FD and FEM increases with time.

Previous work has shown that the heat transfer coefficient plays an important role on the determination of the computed temperature by FEM. Very few experiments have been carried out to determine the heat transfer coefficient across the roll gap in the hot rolling of aluminium alloys, whereas the heat transfer coefficient in the hot rolling of steels reported by several workers (Semiatin et al. 1987, Smelser et al. 1987) has shown large differences.

In addition to the experimental method (Attack, Round, and Wright 1988), inverse analysis by FEM is another way to ascertain the heat transfer coefficient. When using this method, FEA is run iteratively until the computed temperature histories match the measured values satisfactorily. The reported values of heat transfer coefficient show great differences from 10,000 to 400,000 $Wm^{-2}K^{-1}$ by this method (Chen et al. 1992, Lenard and Pietrzyk 1992, Well et al 1998, Mirza et al 2001). These differences may be attributed to the varying thickness of surface roughness of the roll and strip, the thickness reduction (which influences the pressure and hence the true contact area), and finally the thickness of the lubricant layer, this last factor alters the heat transfer characteristics across the interface.

The influence of heat transfer coefficient on the computed temperature in the present work is shown in Fig.4-24 and Fig.4-25. Considering curves in both Fig.4-24 and Fig.4-25, a heat transfer coefficient of 14000 $Wm^{-2}K^{-1}$ gives good prediction for both the surface point and the centre point. At the instant of time equalling 2s, the temperature differences between the curve given by 13000 $Wm^{-2}K^{-1}$ and the curve given by 15000 $Wm^{-2}K^{-1}$ in Fig 4-24 are 3^0C and 4^0C respectively. It is interesting to observe that in Fig.4-25, there is a small temperature rise at the surface point after the slab leaves the roll gap. This re-heating phenomenon can be attributed to the equalisation of temperature throughout the slab after the severe chilling of the rolls has governed the distribution when the material is in the roll gap. Fig.4-25 also clearly indicates a great temperature drop even in the slab centre. This is mainly caused by the chilling effect of the roll, even though 30%

deformation is expected to generate a considerable amount of heat. The reason is the thermal mass of the studied slab is less than 10% of the thermal mass of the rolls. The chilling effect penetrates into the slab centre, leading to considerable temperature drops in the centre region. The chilling effect on the surface of the slab can cause a substantial transverse gradient in the flow stress of the material, which influences the deformation and the roll forces. The temperature variation will result in differences in recrystallisation behaviour and in subgrain and grain sizes. Significant differences in temperature profiles at the slab centre and at the slab surface in the roll gap found in the present study confirm the necessity of employing a thermomechanical coupled model to simulate the hot rolling process, since the deformation at different temperatures may lead to a significant variation in the flow stress and in the microstructure development.

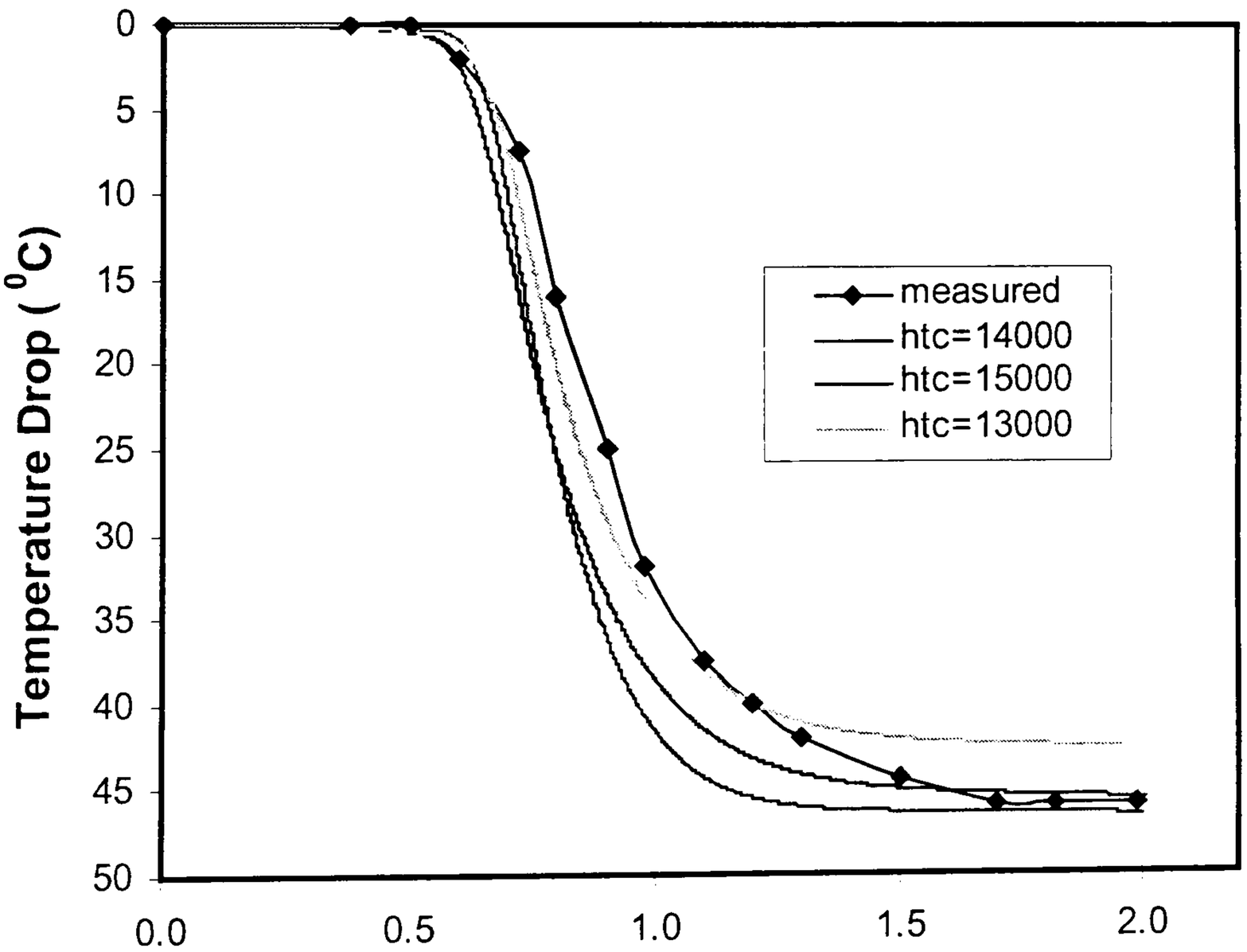

Fig.4-24 Comparison of computed and measured temperature history for a point at slab centre

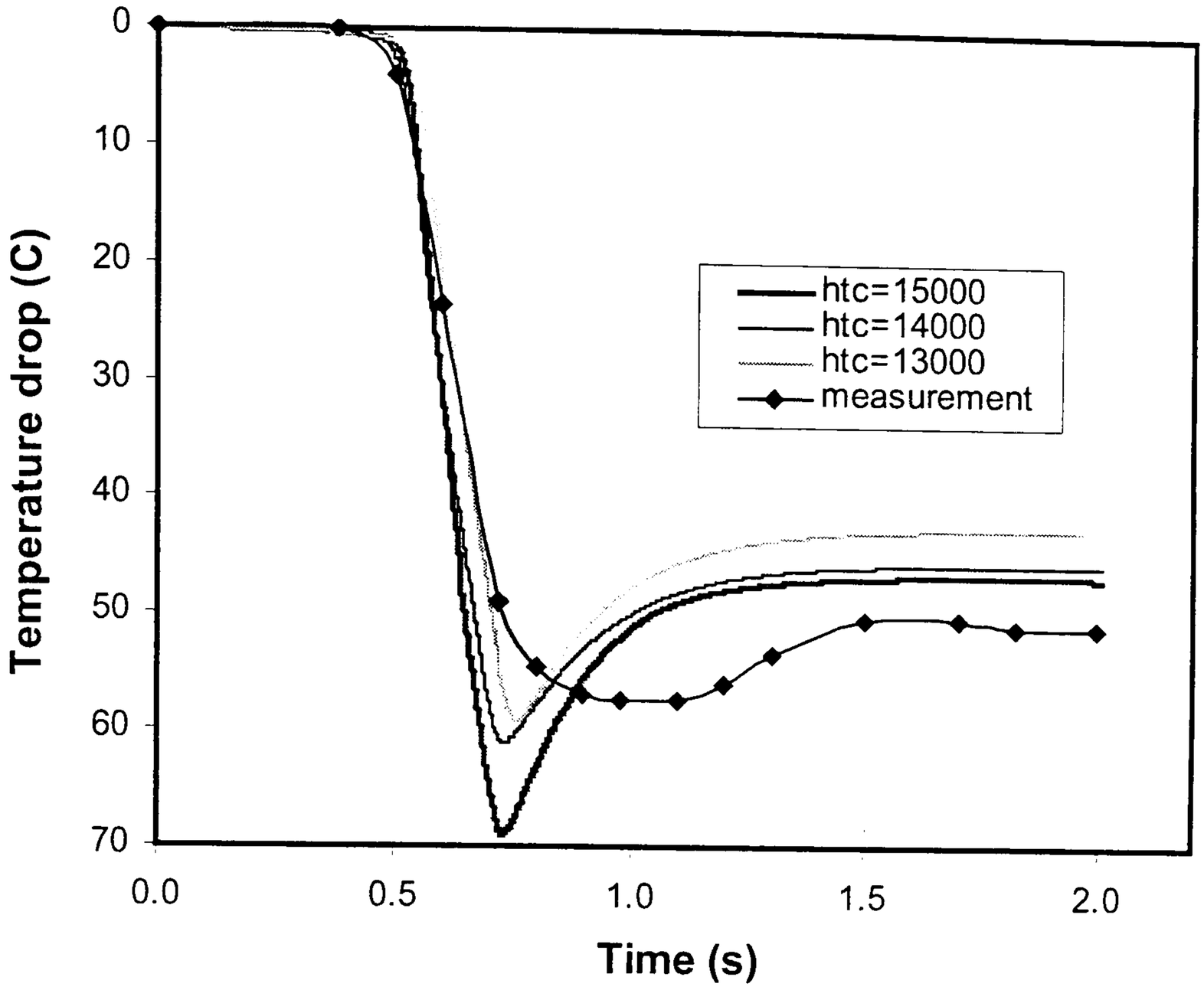

Fig.4-25 Comparison of computed and measured temperature history for a point 2.5 mm below slab surface

4.5.3 Single pass industrial rolling

In industrial rolling, especially in the early passes, the thermal mass of the slab is usually of the same order as the roll, and the thickness reduction is often less than 10%. These conditions will essentially cause a different temperature distribution in the slab to that encountered in the laboratory. The temperature distribution is calculated here for an actual pass schedule. Laminazione Sottile SA, Caserta, Italy, supplied the experimental results. Rolling was conducted in a single stand hot reversing mill. The material rolled is AA3003. The inlet slab thickness is 580 mm and the exit thickness is 540 mm. The rolling was carried out at 560^0C. The roll diameter is 990mm and surface speed is 2.073 m/s. Two remeshing boxes were adopted and the second box is located in the first box. The characteristic element size outside the remeshing box is 30mm, the element size in the first remeshing box

is 15mm, the element size in the second remeshing box is 8mm. Computed results are shown from Fig.4-26 to Fig.4-29.

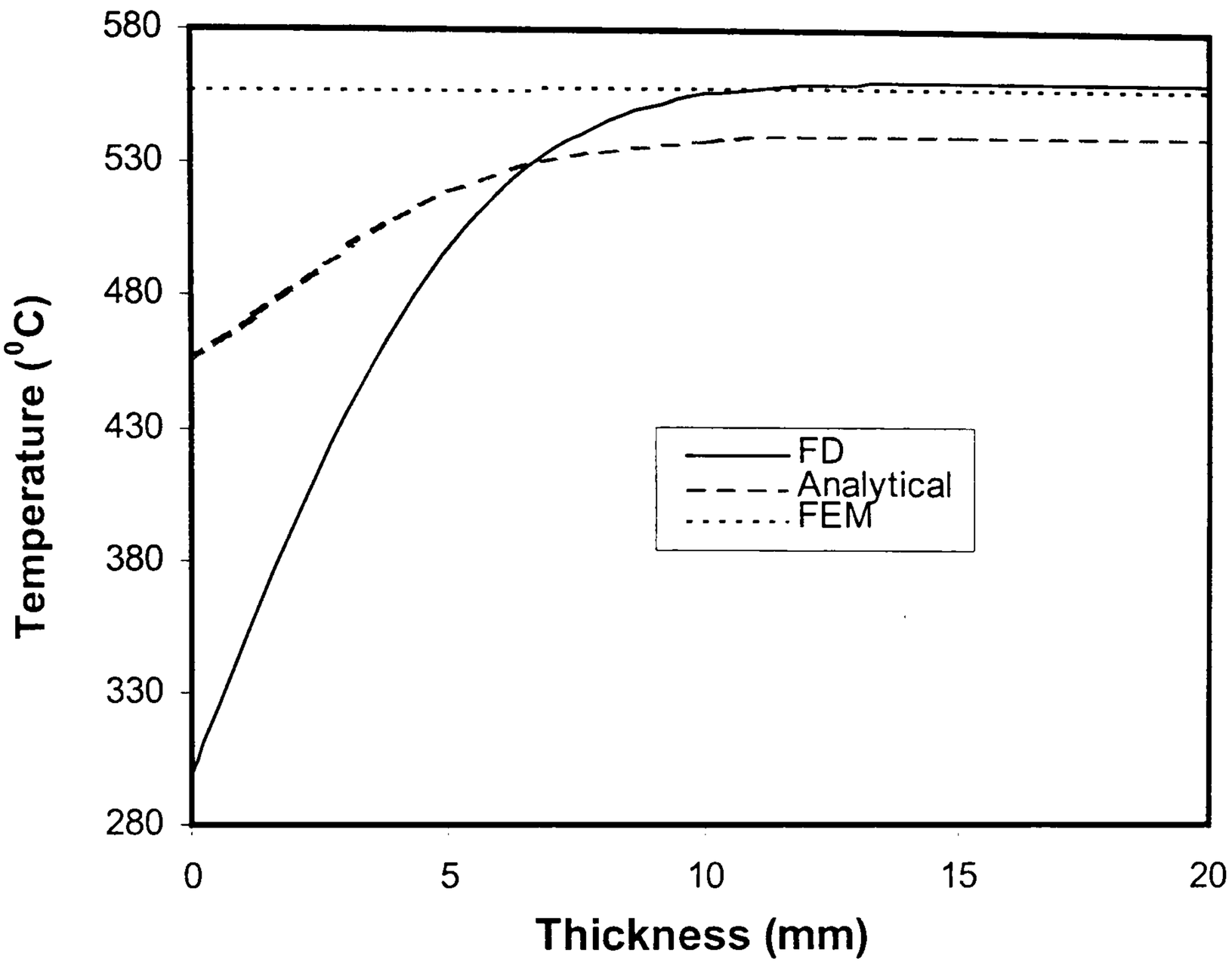

Fig.4-26 Comparison of temperature distribution along thickness of slab for a industrial rolling pass

Fig.4-26 shows the temperature variation in the region 20mm below the slab/roll interface. After 20mm, there is no temperature change for all three approaches. The differences among the three different methods appear within the first 10mm. FD gives the lowest surface temperature, followed by the analytical approach, and FEM predicts nearly constant temperature distribution from slab surface to the slab centre. The temperature drop at the surface is 2^0C. The curves show the same trend as they do in Fig.4-21. FD provides identical prediction as FEM does at 10 mm below the surface. The temperature difference between the FEM and the analytical approach is 20^0C after a depth of 20mm below the surface. The reason for the small temperature variation along the slab thickness may be attributed to the distribution of equivalent strain.

From Fig.4-27, we can see that deformation is mainly concentrated near the interface and there is very little deformation in the centre region. This is a common phenomenon in industrial roughing rolling where the deformation cannot penetrate into slab centre. A consequence of this kind of strain distribution is that much more plastic deformation energy is converted into heat in the surface region than in the centre region. Adding to the effect of friction in the interface region, all this generated heat compensates the heat loss into the roll, resulting in little temperature change in the surface, as shown by the FEM curve in Fig.4-26.

There could be some errors of the computed temperature distribution for the first 8mm below the surface. This is because the slab is so large it is very difficult to use an element with a characteristic size less than 10mm. In the present simulation, the minimum element size is 8mm in the roll gap and 30mm outside the roll gap. Another possible reason, which can cause computation error, is the heat transfer coefficient. In this case, the heat transfer coefficient is 30000 $Wm^{-2}K^{-1}$. Because no measurement of temperature distribution along the thickness was performed, it is very difficult to give an accurate value. However, the heat transfer coefficient adopted by Wells et al (1998) is an order of magnitude larger than the above value. When a heat transfer coefficient of 300,000 $Wm^{-2}K^{-1}$ was applied into the same FE model described above, it was found that nearly the same temperature drop, 2.4^0C, is observed. That means the mesh size is the major source error. Hence, a third remeshing box with an element size of 4mm was added to refine the elements below the surface. For the heat transfer coefficient of 30,000 $Wm^{-2}K^{-1}$, the predicted temperature drop is 4.8^0C on the surface just after the slab leaves the roll gap. This value agrees very well with the measured surface temperature drop (5^0C) using a non-contact pyrometer. Therefore, one conclusion can be drawn that the element size is the dominant factor determining the predicted surface temperature in the finite element computation.

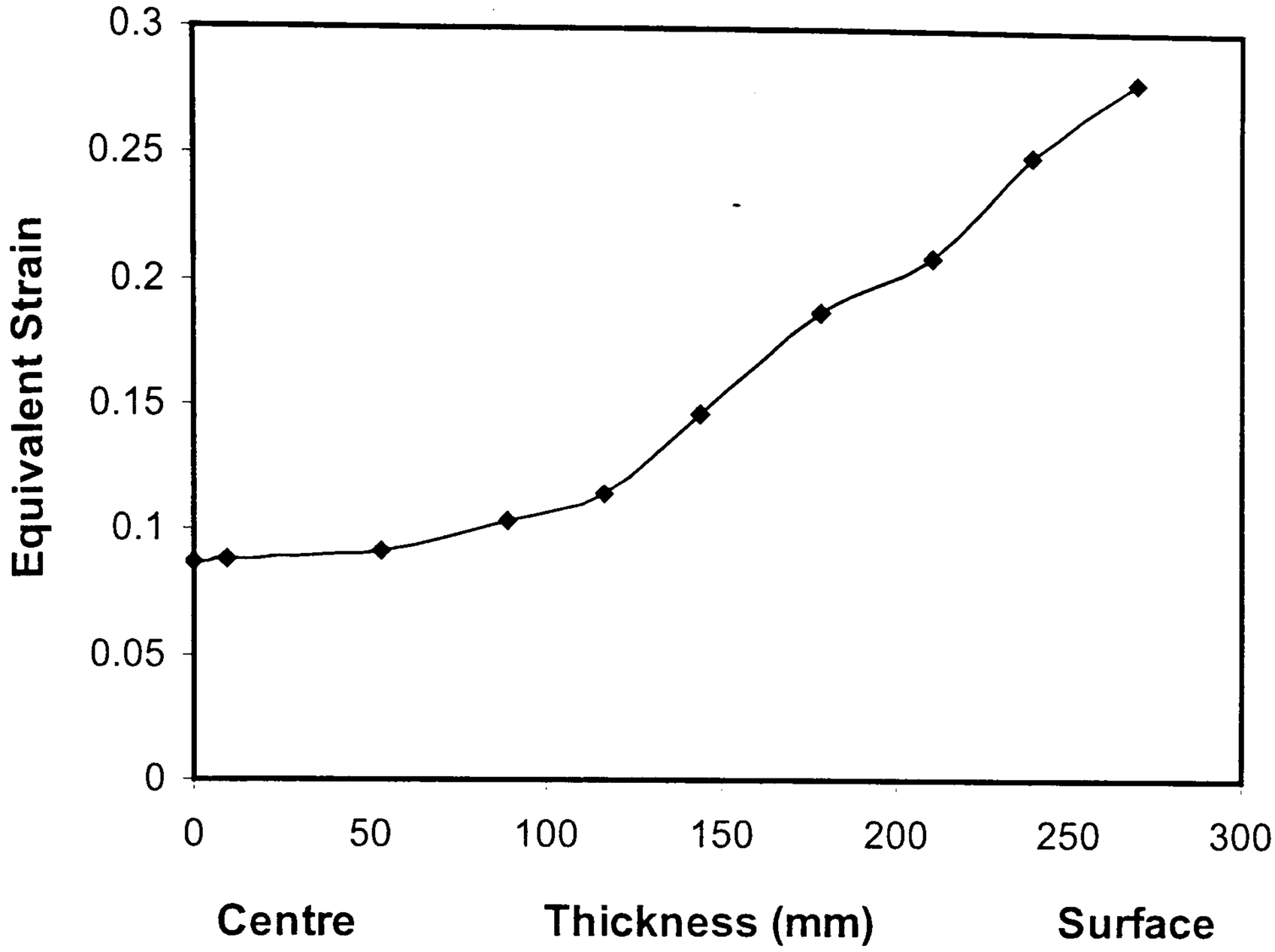

Fig.4-27 The distribution of equivalent strain through the thickness for the industrial breakdown pass

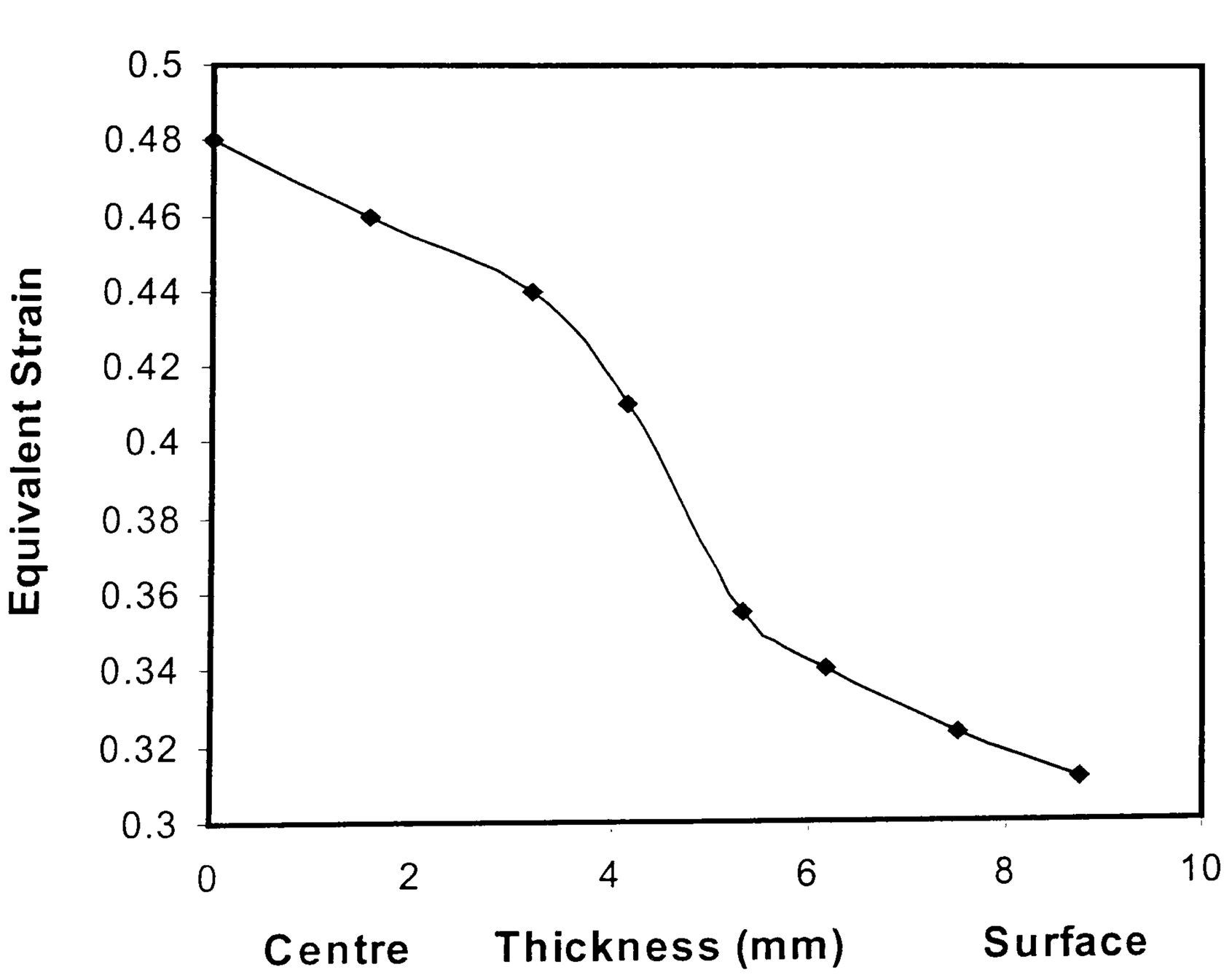

Fig.4-28 The distribution of equivalent strain through the thickness for the laboratory breakdown pass

In Fig.4-28, the maximum deformation is in the slab centre, indicating a completely reverse curve shape to the curve in Fig.4-27. From Fig.4-29, it is apparent that there is very little temperature rise in the slab centre as slab goes through the roll gap. This is a completely different temperature variation history to the slab in laboratory rolling experiments. In laboratory rolling, even in the slab centre, there is a temperature drop of approximately 45^0C, caused by the large chilling effect of the roll. Such a significant difference between industrial rolling and laboratory rolling will certainly cause quite a different microstructure development. Therefore, conclusions drawn from laboratory rolling experiments should be treated with considerable caution when applied to industrial rolling.

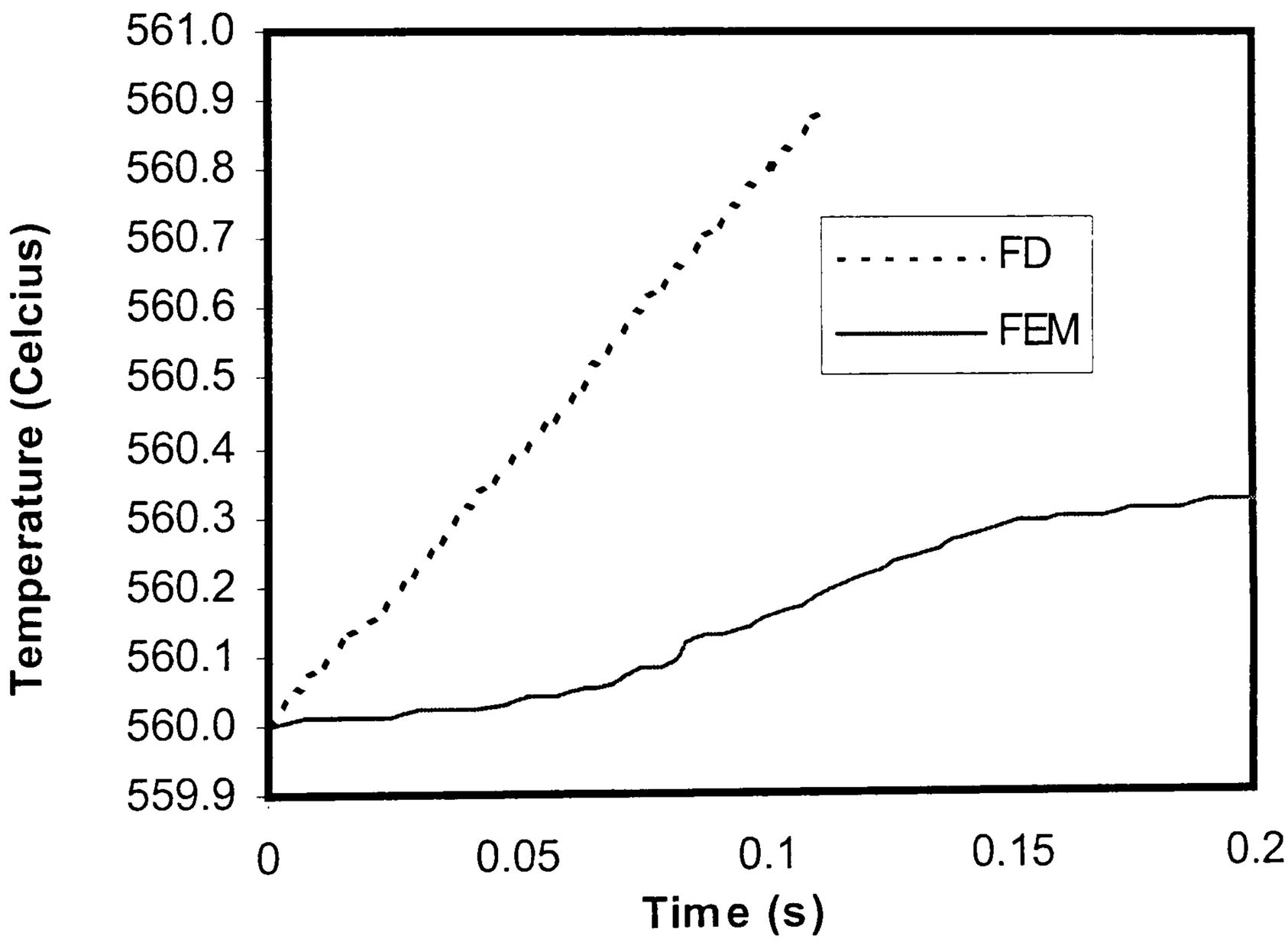

Fig.4-29 Comparison of temperature evolution through roll gap computed by FD and FEM for an industrial rolling pass

In order to minimise this striking difference between laboratory and industrial rolling, some new experimental techniques should be built into any laboratory study. A new rolling technique—SMART has been proposed by Winden (1999) to

fulfil a reasonable temperature control for a 14-pass rolling schedule in a laboratory mill. Another laboratory study of hot rolling can be performed by Channel Die Hot Compression (Maurice and Driver 1994).

4.5.4 Two-pass industrial rolling

For most aluminium alloys, static recrystallisation may intervene during the interpass time if sufficient deformation at specific temperatures has been applied in previous deformations. Temperature has the most important influence on the recrystallisation behaviour. Temperature change in the slab during the interpass time is caused by the radiation and convection with surrounding air, and conduction with runout tables. The conduction with runout tables will cause non-symmetric temperature distribution between slab surface and slab bottom. This effect is ignored in order to shorten analysis time by using only a quarter of a complete slab.

To study the temperature difference between the slab head and slab rear during rolling and during dwell time between passes, the temperature changes of some points are traced. Their positions within slab are shown in Fig.4-30, in which X represents the rolling direction, Y represents the thickness direction and Z represents the width direction. The slab is 5 meters long. Other rolling parameters are the same as described in Table 3.

Curves of temperature vs. time for these points are given in Fig.4-31. The interpass air cooling time is of 20 seconds. For point 4, contrary to expectations, the temperature rises slightly, even after about 46 seconds. Temperature drops for point 3, 8, 9 and 10 are 3, 4, 5, 5 degrees respectively at the end of the first air cooling phase, and 6,7,9 and 10 degrees respectively at the end of the second air cooling phase. At the end of the second air cooling phase, point 9 and point 10 experience nearly the same time exposure in air, therefore the difference is very small. The

measured temperature drop by radiation pyrometer is approximately 5^0C after each pass.

It should be noted that since pass 1 and pass 2 were performed on the same mill and have similar reductions, the heat transfer coefficient is chosen the same as in section 4.5.3, 30000 $Wm^{-2}K^{-1}$.

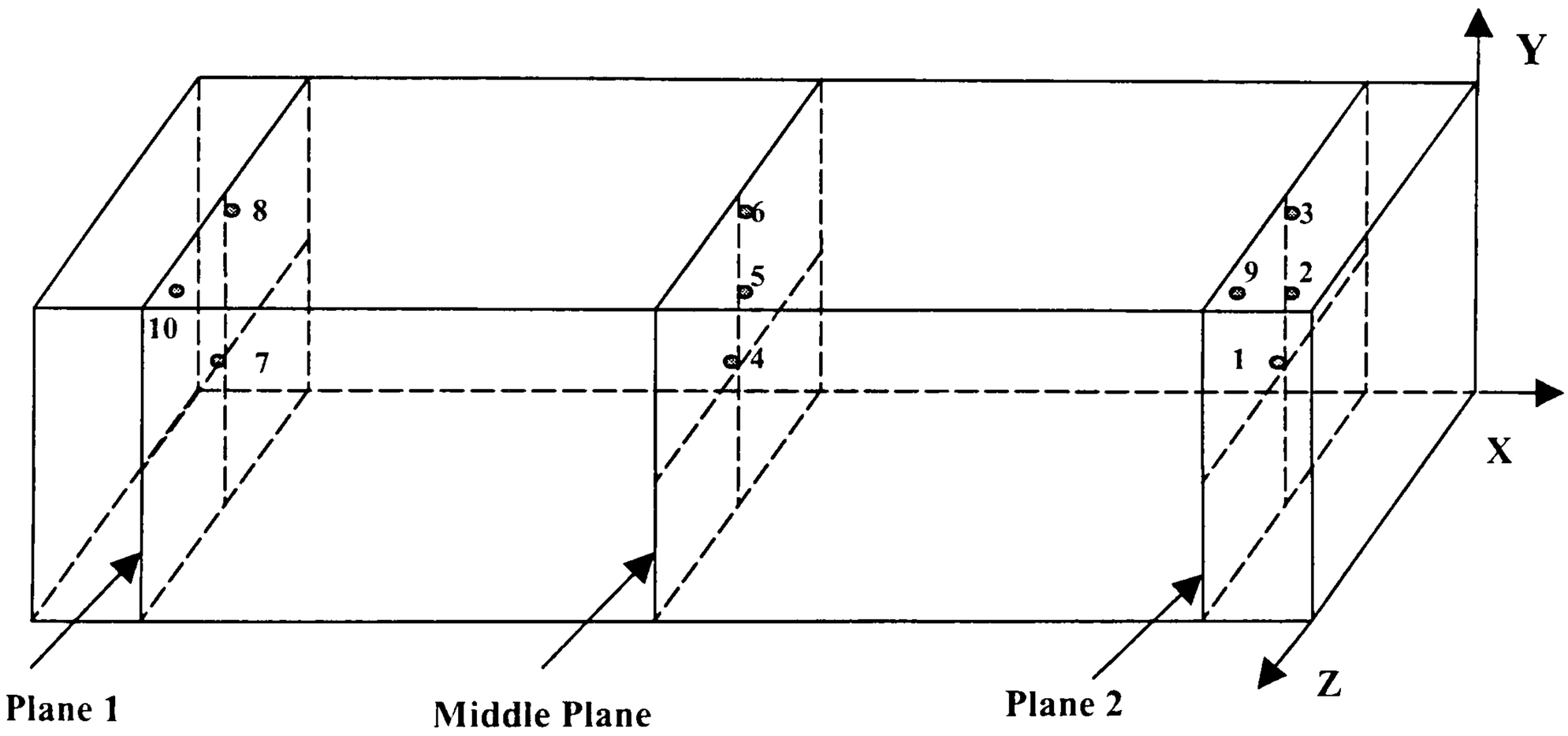

Fig.4-30 Illustration of trace point in slab

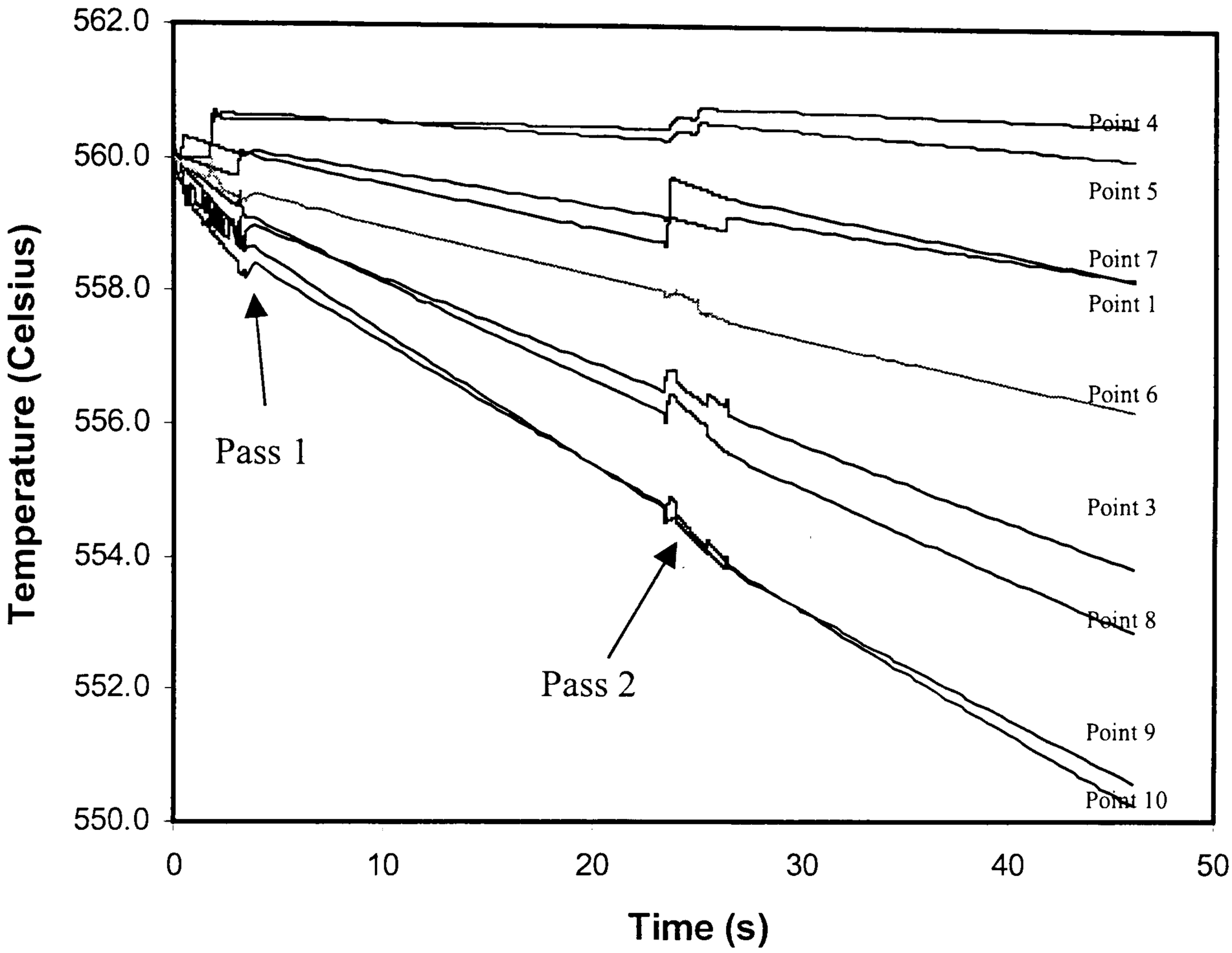

Fig 4-31 Temperature history for different points of the industrial rolling

4.5.5 Three-pass laboratory rolling

This is a three-pass rolling schedule. The details of the experimental program, equipment and materials are given in Raghunathan's thesis (1986). Briefly, the material is AA5056, with a size of 200mm in length, 70mm in width and 45 mm in thickness. The recorded temperature histories, at positions of 3.5mm below slab surface (called the surface point here) and at 22.5mm below the slab surface (called the centre point here) within the symmetrical plane along the width, were taken to compare with the computed results. Slab temperature after leaving the heating

furnace is 456^{0}C. The thickness reduction of each pass is 5.5mm. The roll surface speed is 220mm/s.

Three-dimensional finite element analyses were run from the initial air cooling phase due to transfer before the first pass, to the air cooling phase after the third pass. There are four cooling phases and three deformation phases. The computed temperature curves are shown in Fig.4-32 and Fig. 4-33. Since the rolling were conducted on the same mill as described in section 4.5.2, the heat transfer coefficient is chosen as 14000 $Wm^{-2}K^{-1}$ for all simulation.

Fig.4-32 and Fig.4-33 indicate that the slab temperature drops continuously and the rate of temperature drop is higher in the first air cooling phase than in the latter cooling phases. In each pass, the slab surface loses more temperature (38^{0}C) than the slab centre (15^{0}C). These temperature drops remain almost constant in all the passes. This is because the rolls are at the room temperature all the time and the heating effect of the slab on the rolls does not change the roll temperature apparently. The trace of each point contains three spikes. The rise in the temperature corresponding to these spikes increases with a decrease in the entry temperature (fig.4-32). With a decrease of entry temperature for the same thickness reduction, the deformation energy input increases and thus the temperature rises. It has also been observed that this temperature rise decreases near the slab surface. Near the surface, the roll quenching effect more than compensates for the heat generation due to deformation and friction. Thus, for the material near the surface, the thermal history consists of two stages, an initial heat loss due to roll quenching followed by a quick rise in the temperature to an equilibrium value by the heat gain from the hot interior. Outside the roll gap during the interpass period, there is not much variation in the temperature from the centre to the surface because of the high conductivity of aluminium alloys.

When comparing the measured curves with the computed curves (see Fig.4-32 and Fig.4-33), the first impression is that FEM gives a better prediction of temperature variation for the centre point than for the surface point in terms of the time that spikes occur and the value of spikes. Both predictions agree well with the recorded profiles. The predicted times at which the spikes of surface point occur are all about 2-3 seconds in delay after the measured time, while the predicted times of spike for the centre point match very well with the measured values. The reason is that the interpass time used in comparison is taken from the curve of the centre point. The magnitude of temperature drop for both points at each pass is accurately predicted. The computed rate of temperature drop during interpass cooling is nearly identical to the measured rate. Only the effect of radiation and convection with the surrounding ambient air is included in the FEA simulation during the cooling computation.

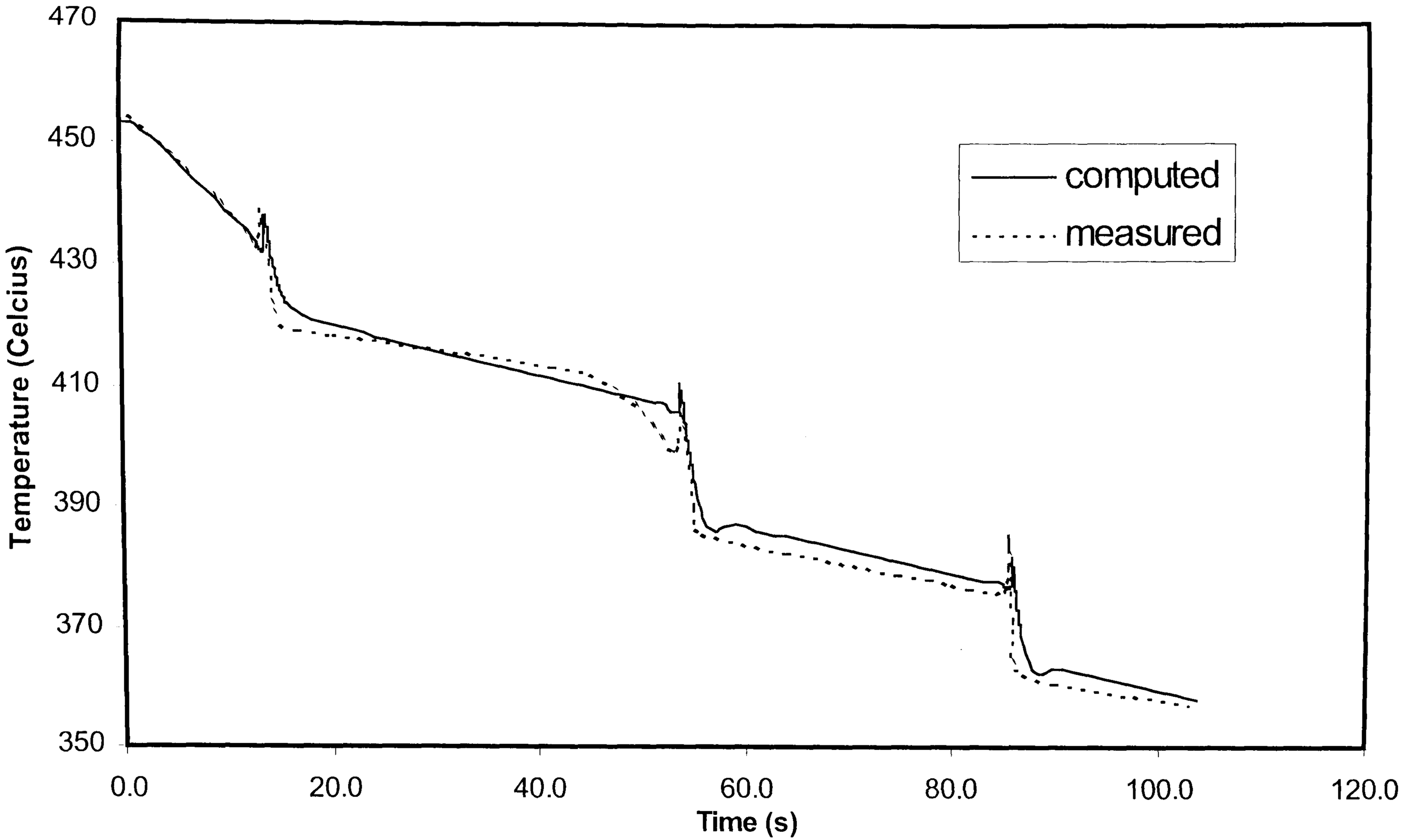

Fig.4-32 Comparison of temperature history of centre point

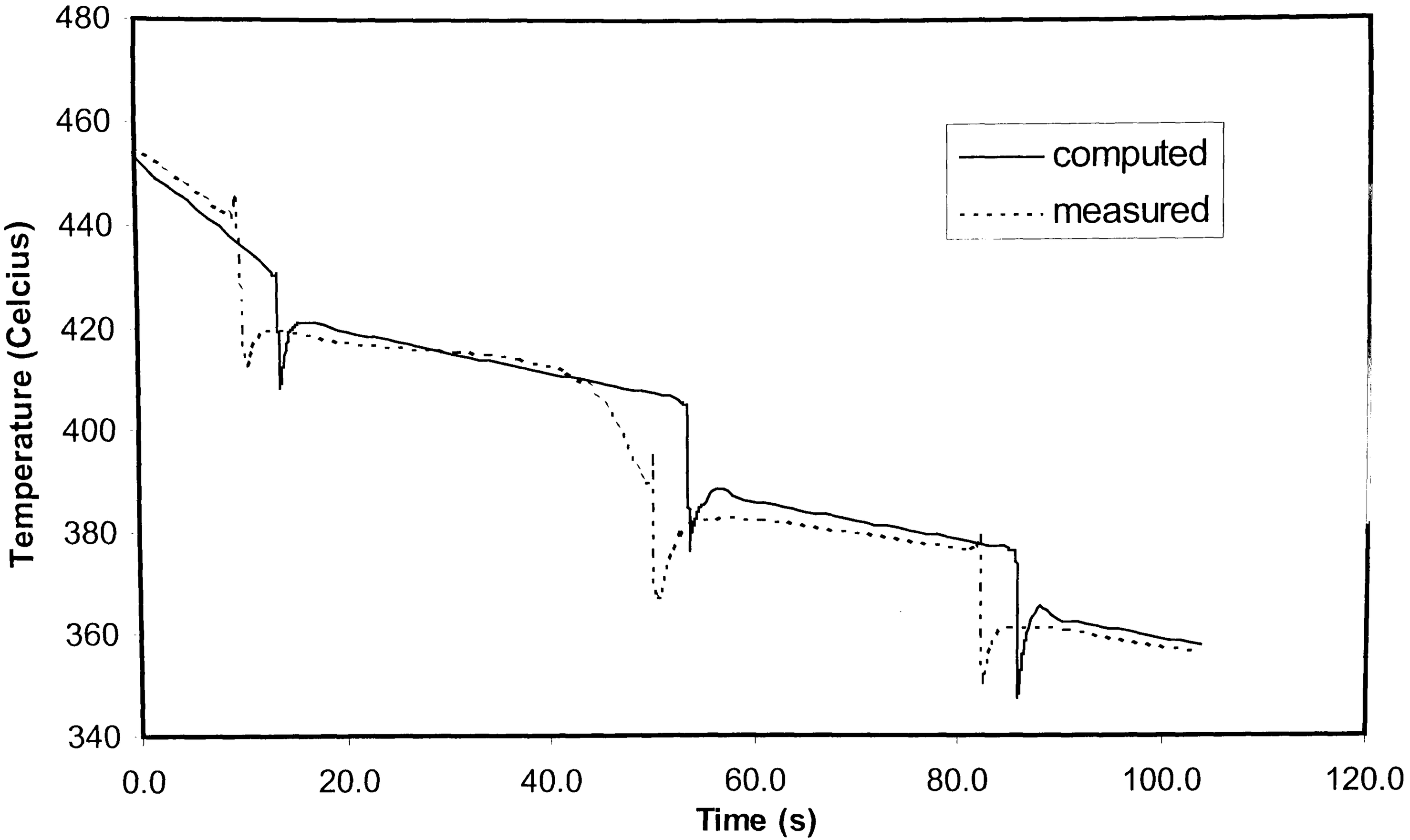

Fig.4-33 Comparison of temperature history of surface point

4.6 Lateral deformation

In this section, slabs with various initial lateral profiles rolled in both laboratory and industrial circumferences, either single pass or two successive passes, will be studied and compared with measured data in the literature (Wright 1978). The validities of various existing formulae on the prediction of spread under experimental and industrial conditions are compared. The difference of lateral deformation behavior under both laboratory and industrial rolling conditions is highlighted and discussed. The Taguchi method is applied to study the influence of various factors on the spread. Finally, a new formula is derived from a large amount of mixed data sets.

4.6.1 Source of experimental data and the analysis model

Four aluminium alloys are considered. Their chemical compositions are shown in appendix 5. The rolling pass schedules adopted in the simulation are shown in Table 7. All the experimental data are extracted from Wright's thesis (1978). The measured profile are given in the appendix 6. For the rolling of slab D8A, the experiment was conducted in the laboratory. The measurement of width was made by micrometer giving readings accurate to within 0.01 mm. The rolling of AA5051 and AA7075 were carried out at the Kitts Green works of Alcan Booth Sheet Ltd (now Alcoa Aluminium). The profile of each slab was measured before and after each normal pass with a hand held profile follower using pins of 7.5 mm diameter. The measurement error of this method is ± 0.1 mm; an order of magnitude less accurate than for the laboratory measurements. The top widths of slabs KG3 and KG7 were measured by photographing the slab with a specially marked rule held on its surface. The measurement error is ± 4 mm, less than 0.3% compared with the whole width. The top widths of KG13A, KG13B and KG13C were measured by employing a large hand held 'vernier' which lay across the slab surface allowing the measurements to within ± 1 mm. Experimental details for 3003 were supplied in

the form of a 19 pass schedule by Lamanazione Sottile, Caserta, Italy. This schedule gave details of roll load and torque, but measurements of spread and edge profile were not supplied.

To describe the simulation results clearly, some geometrical terms are defined according to Fig.4-34. Only a quarter of the real slab is simulated. The plane EFGH and FDCG are symmetry planes. X represents the rolling direction, Y represents thickness, and Z represents the width direction. The variation of edge AD is the principal objective studied in the present paper. Ideally, the edge should be straight, but usually a convex or concave shape is observed. Throughout this section, only this curve is used to represent the edge profile. Point A is defined as the surface point, point D is the center point. The curve AE is the leading edge.

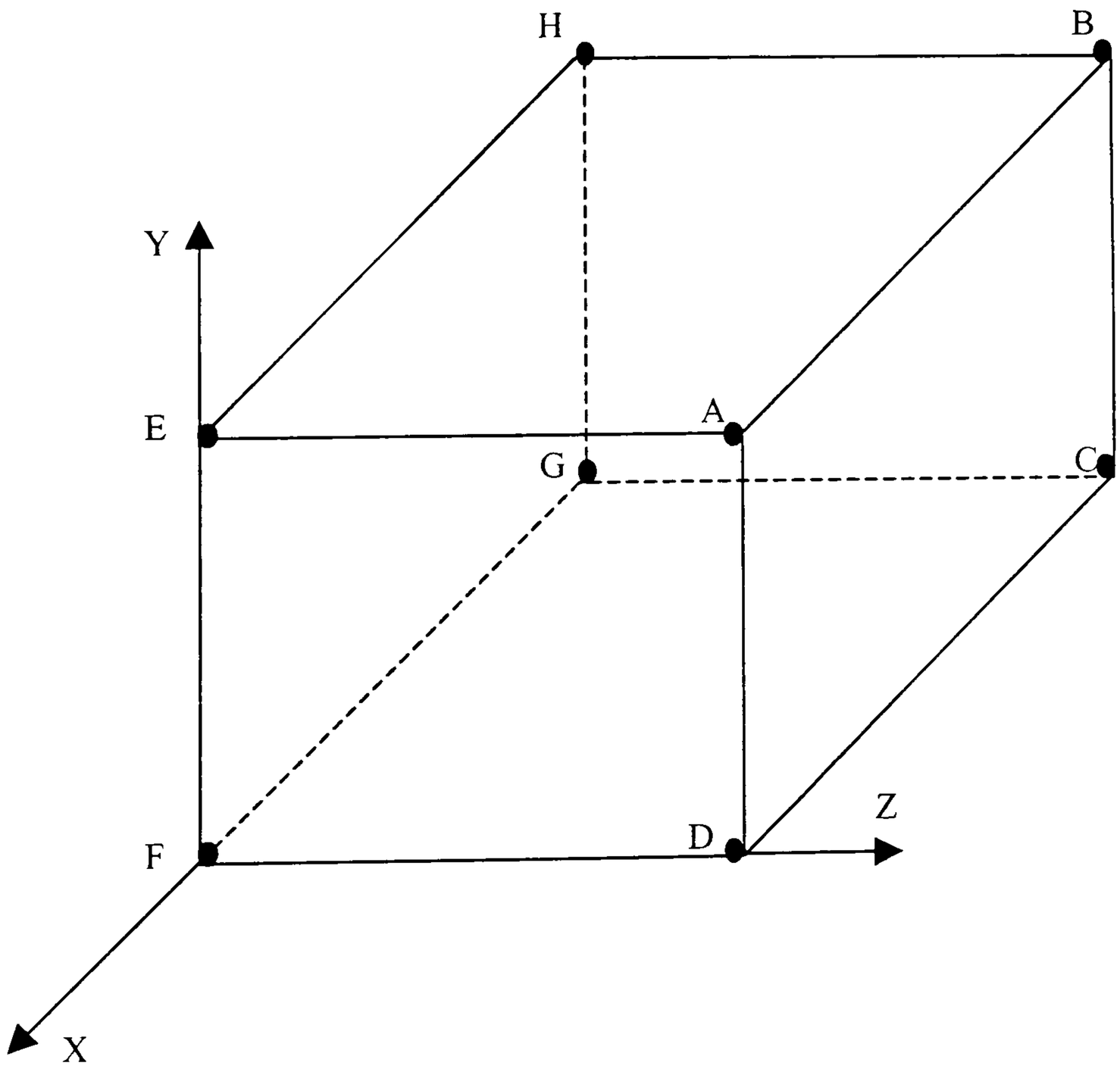

Fig 4-34 Schematic slab geometry for FEM

Table 7 Rolling pass schedules used in simulation

Material	AA1100	AA1100	AA1100	AA5051	AA5051	AA7075	AA7075	AA3003
Code	D8A-1	D8A-2	D8A	KG3	KG7	KG13A	KG13B	AA3003
Roll Speed(rpm)	11.5	11.5	11.5	40	40	40	40	48
Roll diameter(mm)	250	250	250	678	678	678	678	990
EntryThickness(mm)	25	22.5	25	228	286	316	300	580
Exit thickness(mm)	22.5	17.5	17.5	206	253.4	300	275	540
Temperature (^{0}C)	500	500	500	445	445	380	380	560
Edge Profile	Straight	Convex	Straight	Concave	Convex	Convex	Convex	Straight
$\sqrt{R\delta}/H_1$	0.707	1.11	1.22	0.38	0.36	0.233	0.31	0.24
Description	Labor-atory	Labor-atory	Labor-atory	Indus-trial	Indus-trial	Indus-trial	Indus-trial	Indus-trial

Note:

D8A is taken from D.S. Wright's laboratory experiments (Wright 1978)

KG3, KG7, KG13A, KG13B are industrial experiments conducted by D.S. Wright in Kitts Green works (Wright 1978)

AA3003 is taken from the practical industrial rolling pass schedule from Lamanazione Sottile, Caserta, Italy.

4.6.2 Computed results

The predicted edge profile for AA3003 is shown in Fig.4-35. This pass is the first pass of a 19-pass schedule. The friction coefficient 0.6 was obtained by the method of inverse analysis, which has been discussed in section 4.2. A sticking friction condition with friction factor of 0.95 illustrates the effect of friction coefficient on the spread. The edge profile is assumed straight before entering the breakdown pass. It should be noted that the starting point of measurement along the thickness is on the surface, corresponding to point A in Fig.4-34. It is obvious that after the breakdown pass, the straight edge line turns into a concave profile. The reason will be explained in the next section.

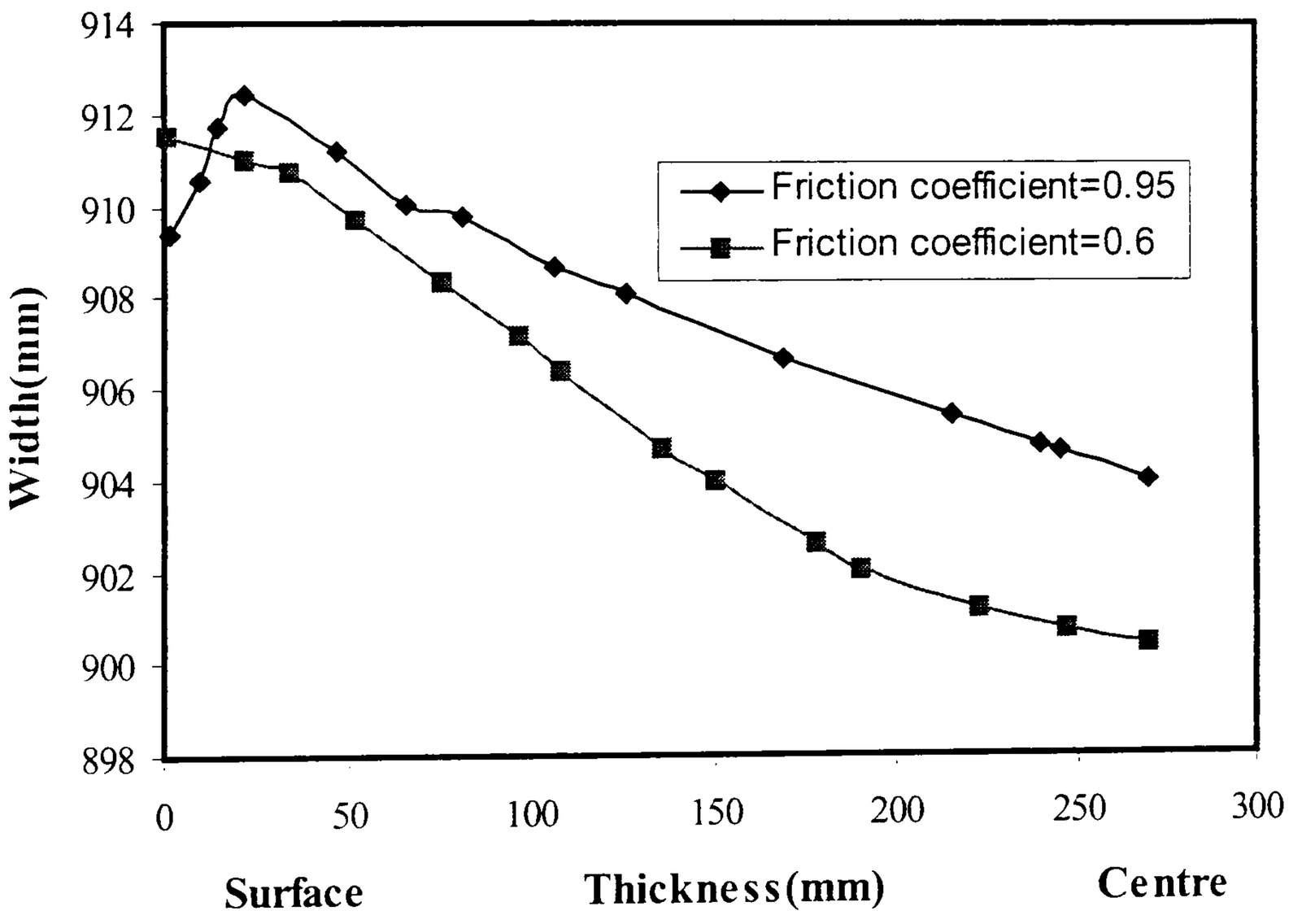

Fig.4-35 Predicted edge profiles of a slab with an initially straight profile for the industrial rolling of AA3003

It also can be seen that, from Fig.4-35, there is more increase in surface width for the lower friction coefficient than for the larger friction coefficient. Two mechanisms have been used to explain the widening of the slab contact face. The

first is termed 'side-fold', occurring by the transfer of material from side faces and being folded to form a new interface (Sheppard and Wright 1981). Another mechanism is by the billet slipping across the rolls during rolling. Obviously, the second mechanism operates in this case. However, for sticking friction, there is a very strong trend of the occurrence of the side-fold.

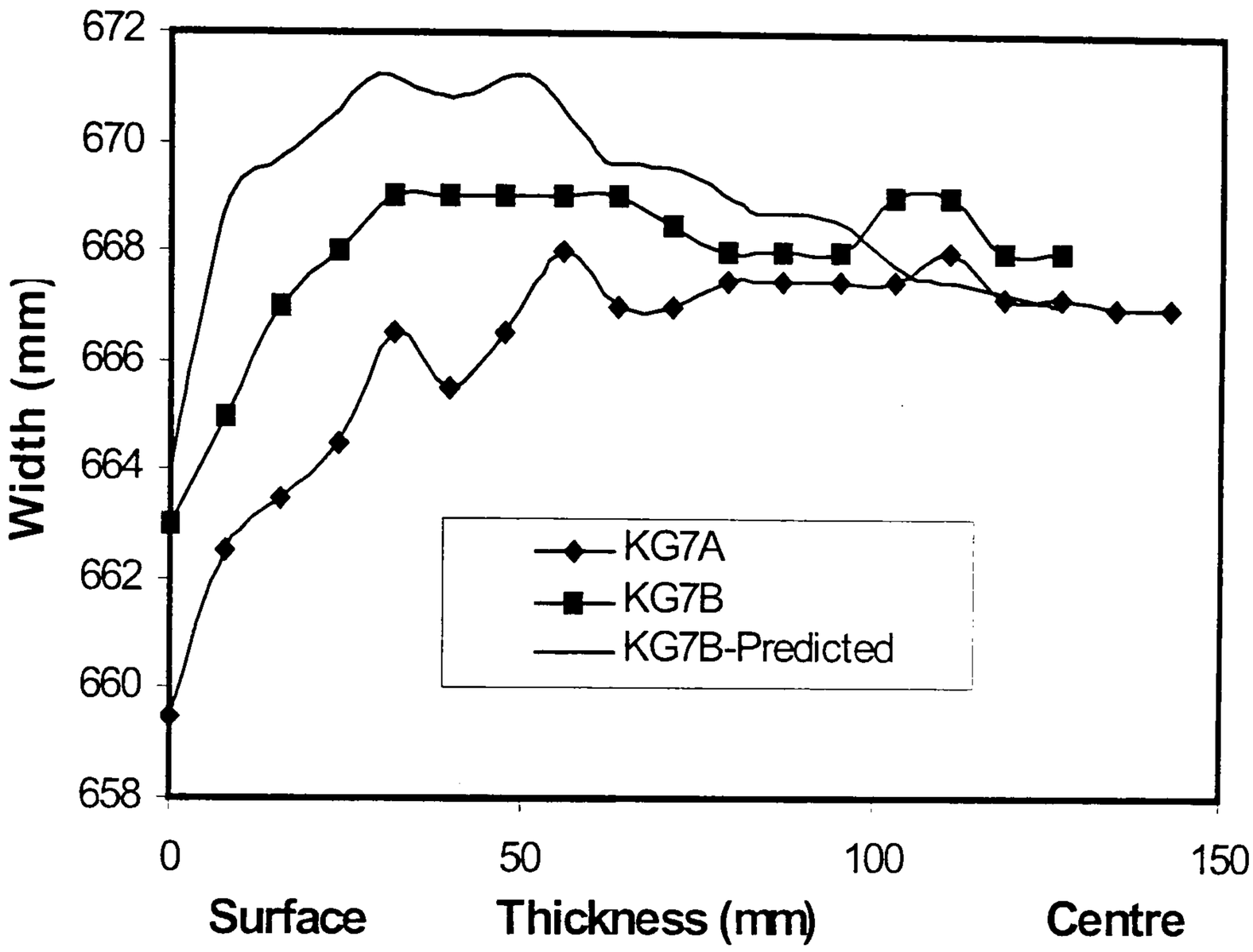

Fig.4-36 Changes of lateral profile of a slab with initially concave edge shape (KG7A is the initial profile and KG7B is the measured profile after deformation)

Fig.4-36 shows the change of an initially convex edge profile before and after a breakdown pass. The initially convex profile is inherited from the preceding "broadside" rolling. The width differences between the surface point and the center point of the curves for KG7A, KG7B and KG7B-Predicted are 7.5mm, 5mm and 2.5mm respectively. This indicates that the width difference between the surface and the center decreases. The deformation tends to reduce the extent of convex profile. If the deformation continues, a concave profile will inevitably be produced. Fig.4-37 shows an actual profile when rolling an AA5051 plate of 35mm final thickness. There is an obvious concavity.

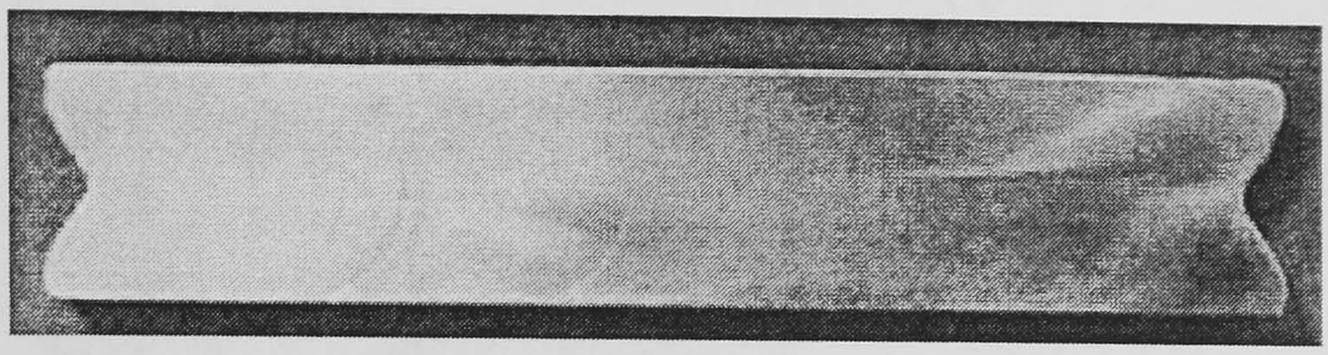

Fig.4-37 Profile of actual rolled product

The change of an initially convcave edge profile before and after a breakdown pass is shown in Fig.4-38. The curve KG3A represents the initial edge profile. KG3B is the measured profile after deformation. It is clear that, the extent of concavity increases and the computed profile matches very well with the measured curve.

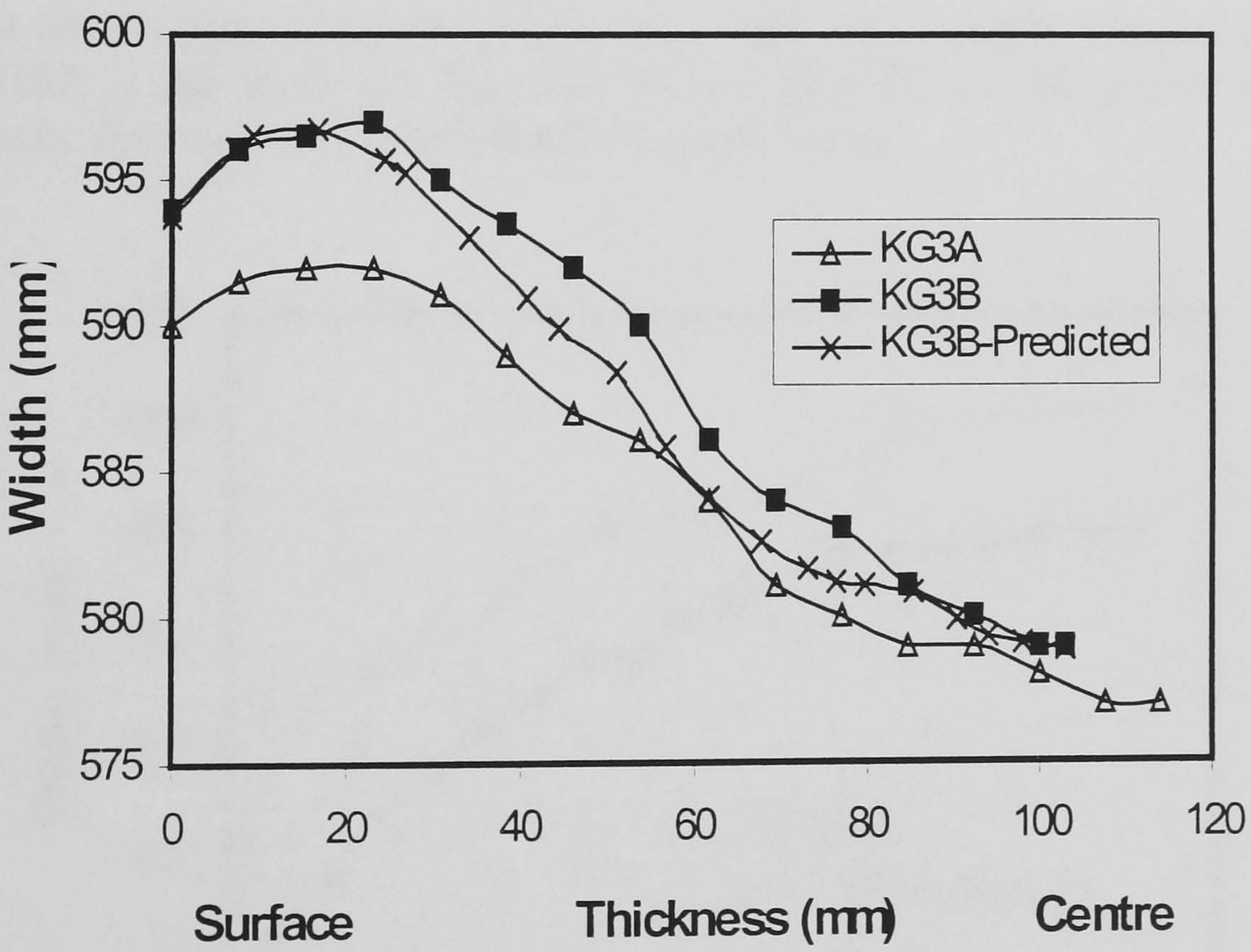

Fig.4-38 Lateral profile of a slab with initially curved edge shape obtained by broadside rolling (KG3A is the initial profile, KG3B is the measured profile after deformation)

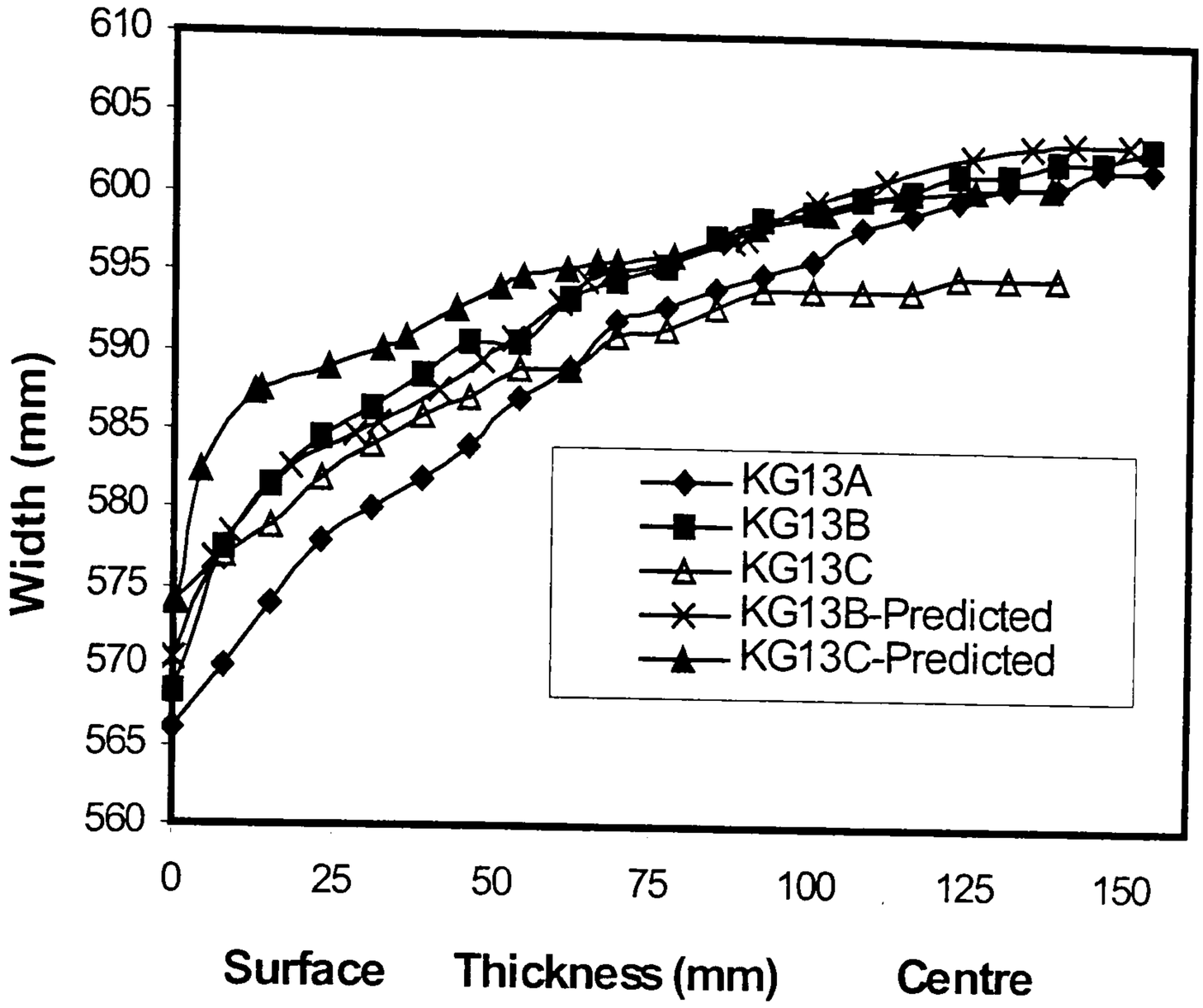

Fig.4-39 Changes of lateral profile of a slab with initially convex edge shape (KG13A is the initial profile, KG13B and KG13C are the measured profiles after the first and second deformation respectively)

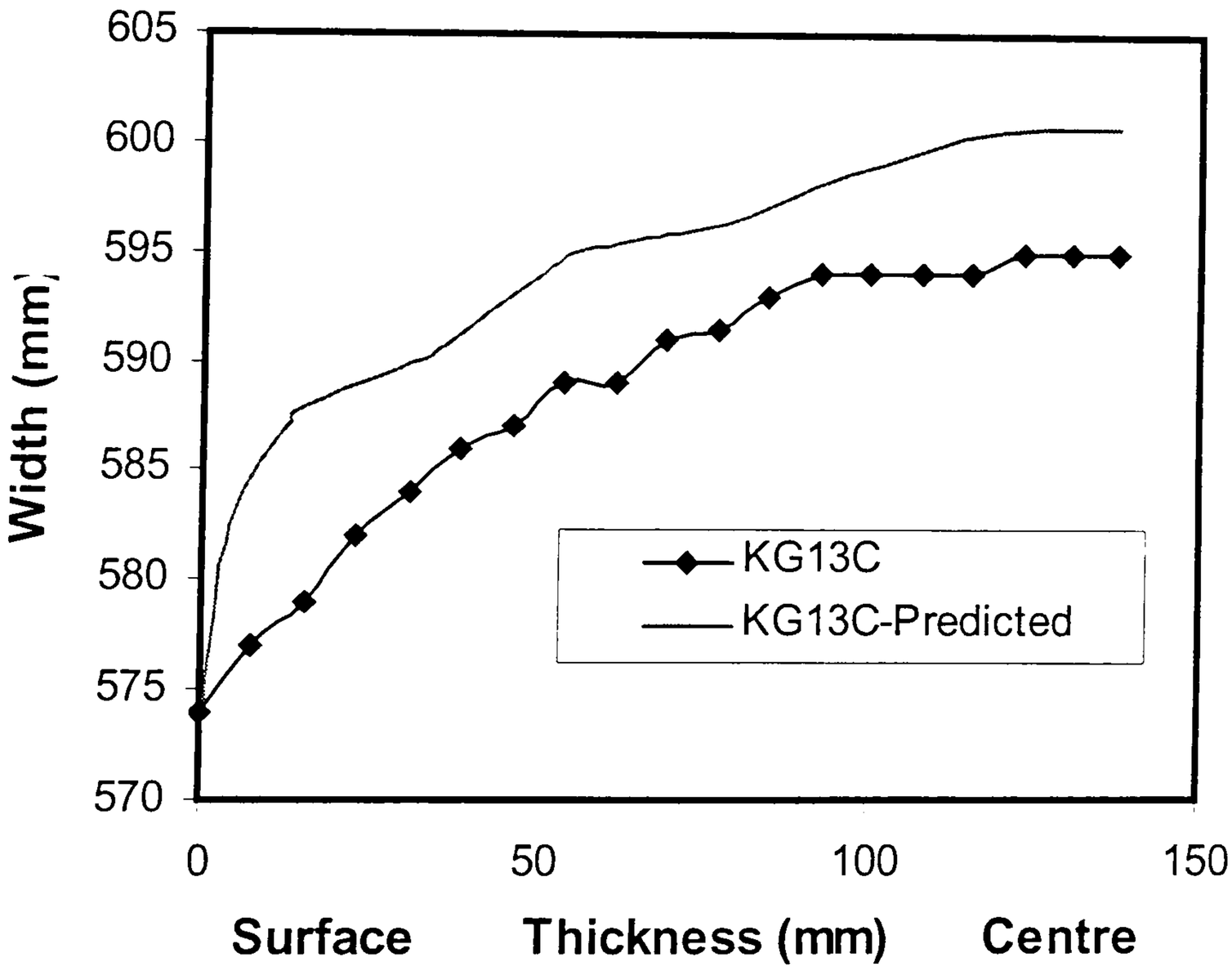

Fig.4-40 Comparison of the predicted and the measured profile for KG13C (KG13C is the measured profile after two pass deformation)

Fig.4-39 shows the changes of an initially convex profile (KG13A) after two-pass deformation. After approximately 5% thickness reduction, the curve KG13B is measured, following another 8.3% reduction, the curve KG13C is obtained. The fit between the curve KG13B-Predicted and KG13B is much better than the fit between the curve KG13C-Predicted and KG13C. In Fig.4-40, the FEM model is shown to fit very well at the interface width and appears to overpredict the width for the data from KG13C. However, the measured width at the slab centre for KG13C is even smaller than that for KG13B, the only reasonable explanation is that there was a measurement error at the slab centre for KG13C. We can see that, from Fig.4-39, the faces of the slab which are in contact with the rolls increase significantly in width, the extent of bulge in the slab center decreases. The increase of interface width appears to originate mainly from the billet slipping. If the slab is further rolled, side fold will dominate, (see the predicted curve in Fig.4-40).

A careful measured lateral profile from laboratory rolling is shown in Fig.4-41. The maximum measurement error is 0.01mm. The curves of D8A, D8A-1 and D8A-2 are all predicted profile. The curve D8A represents the edge profile after a single pass rolling of an initially straight edge. The total reduction (30%) of D8A-1 and D8A-2 is equivalent to the reduction of D8A. The relative thickness reduction for D8A-1 is 10%. The following relative thickness reduction is 22.2% for D8A-2. The measured edge profile after 30% single pass reduction is labeled as the "measured". It is obvious, the curve D8A matches very well with the measured curve. The curve D8A-1, obtained after slight deformation, shows little shape change in the center region, and slight more increase in surface width. This increase is caused by the effect of sidefold, since sticking friction is applied in the simulation. It is interesting to note that, the curve D8A-2 exhibits a "large" difference with the measured curve. This phenomenon was also discovered in the literature (Wright 1978). The interpretation can be attributed to several factors, and will be discussed in the following section.

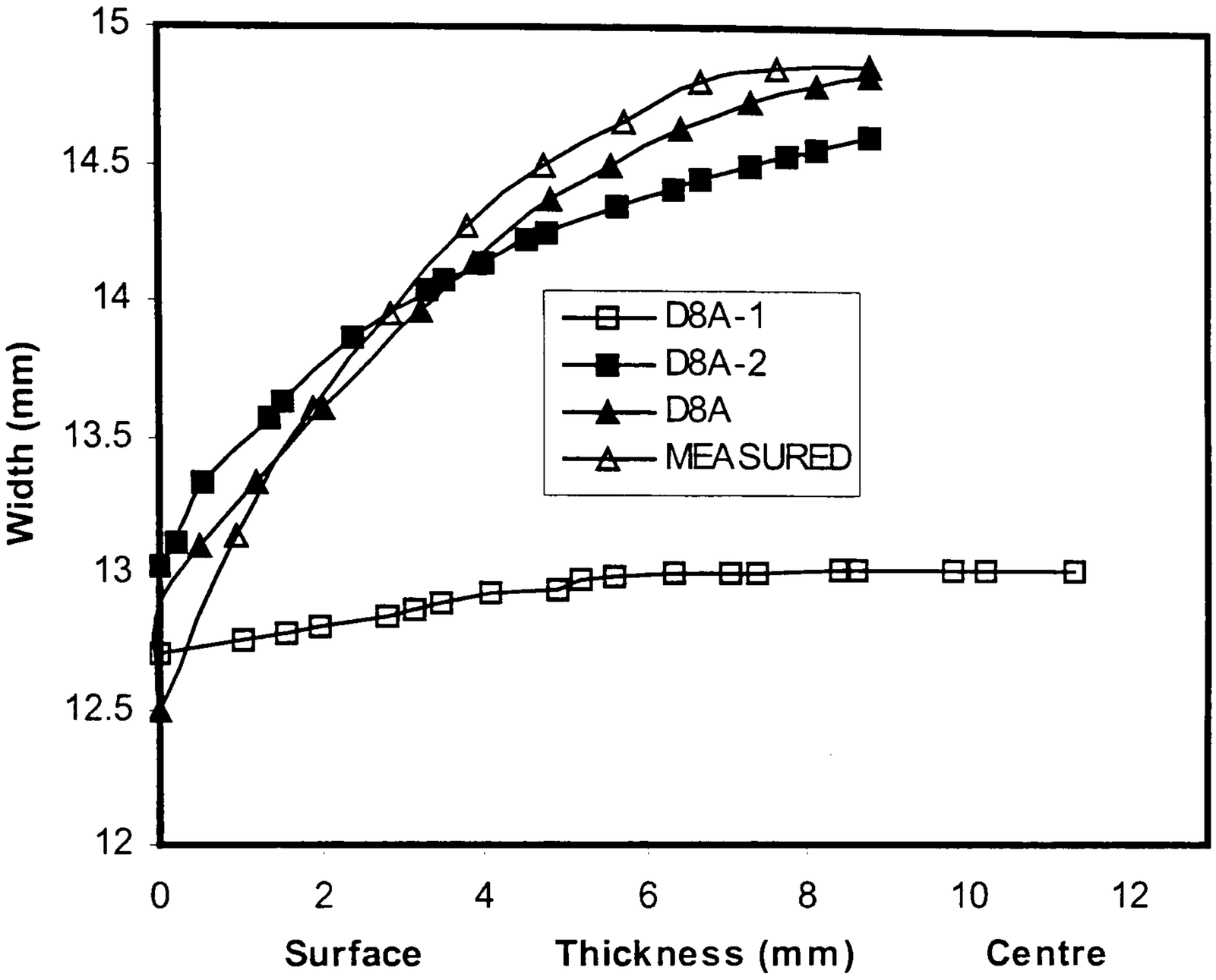

Fig. 4-41 Comparison of lateral profile between one single pass and two successive passes (D8A-1 is predicted after 10% relative reduction from an initial straight profile, D8A-2 is predicted after 22.2% relative reduction from D8A-1, and D8A is obtained by 30% relative reduction from an initial straight profile)

Prior to discussing the computed results, it would be useful to revisit the existing conclusions drawn on spread during hot flat rolling. The lateral spread increases with

- A decrease in the width/ thickness ratio of the slab
- An increase in the roll radius/ initial thickness ratio
- An increase in the reduction
- An increase in the entry temperature
- Other factors such as the interface friction, roll speed, and the material flow stress exert minor influence on the spread.

4.6.3 The effect of friction on the spread

Fig.4-35 indicates the influence of friction coefficient on the edge profile. In contrast to previous conclusions, the lateral shape is sensitive to the friction coefficient. When the friction coefficient varies, there is an obvious response to the profile. Since friction causes inhomogenous deformation in the slab, the smaller the friction coefficient, the more homogenous is the deformation in the slab. That is why the spread obtained when a low friction coefficient obtains is larger than the width spread obtained by a high friction coefficient. It also means that the elongation increases with increase of friction coefficient. But how to explain the contradiction between the predicted results here and the previous experimental results? The contradiction arises from the difference of temperature distribution throughout the slab thickness between industrial and laboratory rolling conditions. Generally, there is a high temperature drop (up to 45 ^{0}C in the slab centre in the rolling of D8A) in the slab in laboratory rolling (see Fig.4-24). However, the temperature remains nearly constant in the slab centre in industrial practice even after two pass deformations and two air cooling periods (See Fig.4-31). The temperature drop after the first breakdown pass on the slab surface is also small, less than 5 degrees in industrial practice. This significant difference in temperature distribution will naturally cause a different gradient of flow stress along the slab thickness. The flow stress at the surface is much higher than that in the slab centre in laboratory rolling conditions. The material in the slab centre flows easily whenever the friction coefficient is high or low, leading to the previous conclusion that the interface friction exerts a minor effect on spread. In industrial circumstances, the gradient of the flow stress along the thickness is small because of the small temperature gradient, and the thickness reduction is normally less than 10% in those passes which are clearly three dimensional, resulting in a deformation concentration near the slab surface. The combined effects of these two factors ensure that the material flow at the surface is encouraged.

4.6.4 Successive reduction

It is unusual to find a large single pass reduction in early stages in industrial breakdown rolling. Therefore, it is of interest to know how a succession of small reductions compares with one equivalent large reduction, and how lateral profile develops. Comparing the curves D8A-2 and D8A presented in Fig.4-41, we can find that, for the curve D8A-2 which is the result of two successive reductions, the magnitude of outward spread at the slab centre is reduced, and the spread near the surface region is increased. This discovery is useful for the control of lateral profile by adjusting the amount of reductions for each pass. It also hints that, for a multipass schedule, the spread should be calculated pass by pass. There are several factors, which can account for the spread discrepancy. The first factor is the value of $\sqrt{R\delta}/H_1$ differs with each pass. For the curves D8A-1, D8A-2, and D8A, the values of $\sqrt{R\delta}/H_1$ are 5, 7.45 and 8.66 respectively. The second factor is the deformation concentration near the surface region due to the small reductions, leading to large spread in the surface. The third factor is the variation of the width/thickness ratio.

4.6.5 Prediction of slab shape

According to Wright's study (1978) based on the results from both laboratory and industrial experiments, when

$$\frac{\sqrt{R\delta}}{H1} < C \pm 0.06 \tag{4-22}$$

the lateral shape is concave. For laboratory experiments C=0.8 and for industrial rolling C=0.3-0.6. The computed values of $\sqrt{R\delta}/H_1$ for various rolling conditions are shown in Table 7. In all industrial rolling cases, the values of $\sqrt{R\delta}/H_1$ are less

than 0.4, and all show a tendency of concave profile. In all laboratory cases, except the D8A-1, equation (4-22) also gives an accurate prediction of shape changes.

Fig.4-42 shows the predicted shapes of the leading edge, which is obtained by two successive reductions of KG13A. It is clear that the material at the slab centre elongates more than the material at the slab edge region, and the length difference between the centre and the edge increases with pass number. This kind of shape is always observed in industrial roughing passes and perhaps illustrates that spread does indeed induce residual stresses since when insufficient material is in the roll gap each fibre is allowed to elongate freely.

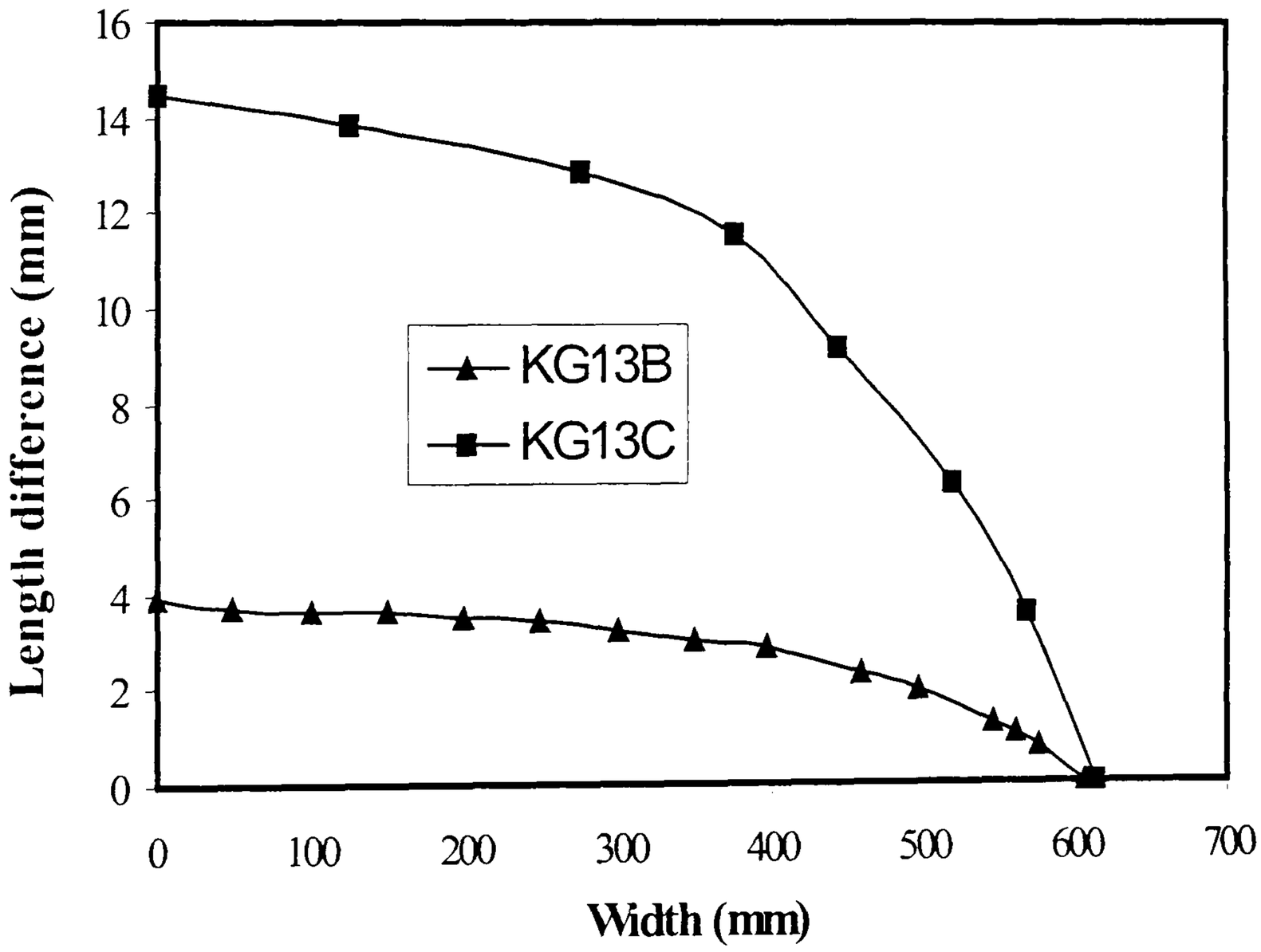

Fig.4-42 The shape of leading edge (KG13B is predicted after 5% reduction from KG13A and KG13C is obtained after further 8.3% reduction from KG13B)

4.6.6 Calculation of spread by different formulae

The comparison of the predicted and the measured spreads for the cases of D8A and AA3003 are listed in Table 8.

Table 8. Comparison of calculated spread

Formula	D8A	AA3003
Hill	0.37	0.00433
Helmi & Alexander	0.53	0.0135
Wusatowski	0.44	0.0012
Sparling	0.39	0.00007
Wright*	0.48	0.001
Raghunathan*	0.02	0.00014
Computed	0.478	0.17
Measured	0.487	

*: Spread is defined as:

$$S_W = \mathrm{Ln}(W_2 / W_1) / \mathrm{Ln}(H_1 / H_2)$$

The six formulae to be examined here are due to Hill, Wusatowski, Sparling, Helmi & Alexander, Sheppard and Wright, and Raghunathan & Sheppard. Each formula, except Raghunathan & Sheppard's, gives an acceptable prediction for laboratory rolling (D8A). Sheppard & Wright's formula gives the best prediction for this case. However, none of the existing formulae agrees with the predicted spread obtained by the FEM. They all significantly underestimate the maximum spread during the breakdown passes in the industrial data. The reasons that all formulae fail to predict the spread for industrial practice may arise from:

(1) Different slab geometry

For the rolling of AA3003, the ration W_1/H_1=3.1, R/H_1=0.853. The corresponding ranges of W_1/H_1 and R/H_1 for various formulae are shown in Table 9. The R/H_1 automatically included in the FEA is excluded in all formulae. The reason for this omission in laboratory data is presumably that rolling the thick, wide specimens would overload an experimental mill. This exclusion might be the cause of the considerable difference in the two calculations.

Table 9 The range of some geometric factors used in experiments

Formula	R/H	W/H
Helmi & Alexander	3.75-10	1-13
Wusatowski	3-5	0.5-30
Wright*	2.54-8.5	1-4
Raghunathan*	5-12.5	1-3

(2) Different rolling conditions

All the above formulae are constructed from data collected in single pass rolling of flat slabs in the laboratory. There is usually no rolling emulsion applied, which could lead to sticking friction at the roll surface. The surface is thus restrained from expanding in the width direction. In industrial rolling, there is some degree of lubrication. The surface can expand along the width direction. When the reduction is small, all deformation concentrates near the roll/slab interface, causing large spread on the top surface of slab.

Hill's formula was the only work in which the spread was derived by analytical analysis. It is analytically correct but grossly underestimates the spread. In addition to the geometrical factors, the influence of temperature and friction condition is included in Sheppard & Wright's formula for aluminium alloys. As reported in the

literature (Raghunathan and Sheppard 1989), for steels, the formula proposed by Helmi & Alexander superseded the formulae proposed by Wusatowski, Hill and Sparling. Table 8 validates this conclusion. The reasonable prediction for D8A given by Helmi & Alexander's formula indicates that the properties of the material would exert a minor effect on the spread. From the point of view of the theoretical consideration, Raghunathan & Sheppard's formula is advanced since it involves all major factors. However, the formula was built up only on the basis of AA5056 and AA5083 at the temperatures of 300^0C and 500^0C. The term of $Ln\frac{Z}{A}$ is adopted to consider the combined effect of roll speed, temperature and differing material behaviour. Although we would expect this to improve the prediction accuracy, the term greatly reduces the predicting capacity when the formula is applied to other alloys, which are not involved in the experiments. It indicates that more research is necessary in this area.

Most recently, Winden (1999) proposed a formula for industrial break down rolling where the experiments were carried out on a laboratory mill. The predicted spreads $S_{w'} = \frac{Ln(W_2/W_1)}{Ln(H_1/H_2)}$ by equation (2-10) for the D8A and the AA3003 are 0.16 and 0.19 respectively. It is clear that equation (2-10) fits very well with the AA3003, but provides a bad prediction for the D8A. That is not surprising since equation (2-10) only considers the second important influence factor, the reduction, but neglects the most important factor, the ration of initial width to the entry slab thickness. Hence the valid range is greatly reduced. The ranges of R/H and W/H where equation was regressed are 0.6-17 and 0.9-30 respectively.

4.6.7 Taguchi experimental design method

In this part, the Taguchi method is employed to find out the influence of each rolling parameter on the spread, to quantitatively estimate the relative contribution

of each control parameter and to express this contribution as a percentage. Quantifying the contribution as a percentage permits the engineer to gain insight into which control factors are the most important and which are less important. This kind of information can be very helpful for choosing the right variables to construct a new spread formula.

The Taguchi method was conceived and developed by Dr. Genichi Taguchi in Japan after World War II. It is considered as a highly effective method for the determination of optimal values for the various parameters involved in a given manufacturing system and has been successfully used in many industries. The application of this method in the rolling industry is few (Tseng et al 1996, Yoshimura et al 1995). The Taguchi method emphasises returning to the design stage after inspection since statistical quality can never fully compensate for bad design. It seeks to design a process that is insensitive or robust to causes of quality problems.

The Taguchi method adopts a set of standard orthogonal arrays (OA) to determine parameters configuration and analyse results. These kinds of arrays use a small number of experimental runs but obtains maximum information and have high reproducibility and reliability. The steps in applying the Taguchi method include:

- Determine the quality characteristics to be optimised
- Select control factors(parameters)
- Design the orthogonal array
- Conduct experiments according to the array
- Analyse the experimental data
- Determine the optimum parameter combination and quantify the contribution of each factor on the quality characteristics in percentage.

There are four approaches that have been devised to study specific experimental design space: Build-test-fix, one-factor-at-a-time experiments, full factorial

experiments, and orthogonal array experiments (fractional factorial). Build-test-fix is an ineffective and inefficient method that necessarily leads to long development times and is strongly dependent on the skill of the experimenter. It is impossible to find an optimum design using this method.

In one-factor-at-a-time experiments, the first factor is thoroughly studied under fixed conditions, and then moves to another factor until all factors are thoroughly studied. The drawbacks of this method are that it is not balanced and does not consider the interactions among factors.

The full factorial approach investigates all possible combination of all factor levels. The biggest weakness of this approach is that it requires too many experiments. For example, 8 factors at three levels, all possible combinations are 3^8(6561). The time and cost to conduct such a study is prohibitive.

Taguchi's OA is considered to be superior than the traditional factorial design method since:

- The factorial design experiment is not efficient in handling large number of factor variables.
- Taguchi's OA experiments, on a product design yield similar and consistent results, even though the experiment can be carried out by different experimenters.
- The OA table allows determination of the contribution, of each quality influencing factor.
- OA allows easy interpretation of experiments with a large number of factors.

A typical tabulation is shown in Table 10. In the array, there are four parameters A, B, C and D, each at three levels. There are 9 rows and each row represents a trial condition with factor levels indicated by the numbers in the row. The vertical

columns correspond to the factors specified in the study and each column contains three level 1, three level 2 and three level 3 conditions for the factor assigned to the column. This is called an $L_9(3^4)$. Usually, the orthogonal array is written as $L_A(B^C)$. A stands for the number of experimental runs. B stands for the number of levels for each factor. C is the number of factors. The total degree of freedom (DOF) equals A-1. In this array, the columns are mutually orthogonal. That is, for any pair of columns, all combinations of factor levels occur; and they occur an equal number of times. This characteristic is termed orthogonal.

Note that this design reduces 81 (3^4) configurations to 9 experimental evaluations. There are greater saving for larger arrays. For example, using an $L_{27}(3^{13})$ array, only 27 experiments are required instead of 1594323 (3^{13}). As a result, the development time and cost are largely reduced.

Table 10 An orthogonal array $L_9(3^4)$

Test number	Parameter A	Parameter B	Parameter C	Parameter D
1	1	1	1	1
2	1	2	2	2
3	1	3	3	3
4	2	1	2	3
5	2	2	3	1
6	2	3	1	2
7	3	1	3	2
8	3	2	1	3
9	3	3	2	1

As discussed before, there are several kinds of parameters that have influence on the spread. They are initial geometry parameters (width/thickness, length/thickness), deformation zone parameters (draft, the contact length), process

parameters (temperature, roll speed) and material parameters (component). Four variables, the ratio of initial width to the entry thickness (W_1/H_1), the ratio of roll radius to the entry thickness (R/H_1), the slab temperature (T), and the amount of reduction (ΔH%) that are easily controlled, are selected for the study. Each parameter has three values, also called three levels. These values are shown in table 11. For the ratio W_1/H_1, the values are 3, 6 and 10. For the ratio of R/H_1, the values are 1, 5 and 8. For the slab temperature, the values are 400^0C, 470^0C and 540^0C. For the reduction ΔH%, the values are 10%, 20% and 30%.

Table 11 Test parameters and their levels

Level	W_1/H_1	R/H_1	ΔH%	T(^{0}C)
1	3	1	10	400
2	6	5	20	470
3	10	8	30	540

Substituting corresponding parameter values to table 10, the experiment design is obtained and is shown in table 12. In this study, the entry slab thickness is fixed at 60mm.

Table12 Experimental design and results

Run No.	W_1/H_1	R/H_1	ΔH%	T(^{0}C)	Spread
1	3	1	10	400	0.124313
2	3	5	20	470	0.14199
3	3	8	30	540	0.2186
4	6	1	20	540	0.03117
5	6	5	30	400	0.055387
6	6	8	10	470	0.047248
7	10	1	30	470	0.02
8	10	5	10	540	0.016147
9	10	8	20	400	0.103962

With regard to the spread, there are two types of definition. One is defined as

$$S_w = \frac{Ln(W_2 / W_1)}{Ln(H_1 / H_2)} \tag{4-23}$$

Another definition is usually referred to the natural width strain

$$S_w = Ln(W_2 / W_1) \tag{4-24}$$

Equation (4-23) is first studied.

Results obtained from the orthogonal array are usually analysed to achieved the following objectives (William et al 1995):

- To estimate the contribution magnitude of each parameter on quality characterics.
- To gain the best or optimum condition for a process or a product, so those good quality characteristics can be sustained.
- To predict the response of the product design parameters under the optimum conditions.

The first objective is obtained through the analysis of variance (ANOVA). ANOVA uses the sum of squares to quantitatively examine the deviation of the control factor effect responses from the over all experimental mean response.

The optimum design is identified by investigating the average response of each parameter level in the OA experiments. For each level, the mean of quality charactertic response is calculated by

$$\bar{Y} = \frac{1}{n}\sum_{i=1}^{n} Y_i \tag{4-25}$$

n is the number of experiments that include the level. For example, The first level of the W_1/H_1 is included in the experimental run number 1, 2 and 3. The first level of the R/H_1 is included in the experimental run number 1, 4 and 7. In the array $L_9(3^4)$, n is a constant 3. So for the W_1/H_1 at level 1, the mean for spread is calculated by:

$$\begin{aligned}\bar{y} &= \frac{1}{3}(0.1243 + 0.141994 + 0.2186) \\ &= 0.161636\end{aligned} \tag{4-26}$$

The mean values at other levels of other factors for the spread can be calculated in the same way, and calculated results are shown in the Table 13 under the column $\bar{y}$.

In order to determine the optimal parameter design, the signal-to-noise (S/N) ratio is adopted. The S/N ratio can reflect both the average (mean) and the variation(scatter) of quality characterics under one trial condition. The S/N function is defined by

$$S/N = 10 * Log(MSD) \tag{4-27}$$

where the MSD stands for the mean square deviation. The purpose of using the constant 10 is to magnify the S/N value for easier analysis. In this investigation, the MSD is expressed as:

$$MSD = y_i^2 \tag{4-28}$$

The mean S/N ratio is expressed as:

$$\begin{aligned}\overline{S/N} &= \frac{1}{9}\sum_{i=1}^{9}(S/N)_i \\ &= -24.39119\end{aligned} \tag{4-29}$$

Table 13 Level average response analysis using S/N ratio

Variables	Level	Runs	y	$\bar{y}$	S/N	$\overline{S/N}$	$(S/N)^2$
		1	0.124313		-18.1097		327.9612
W_1/H_1	3	2	0.141994	0.161636	-16.9546	-16.0904	287.4584
		3	0.218601		-13.2069		174.4234
		4	0.03117		-30.1253		907.5346
	6	5	0.055387	0.044602	-25.1318	-27.2565	631.6076
		6	0.047248		-26.5124		702.908
		7	0.02		-33.9794		1154.6
	10	8	0.016147	0.046703	-35.838	-29.8266	1284.365
		9	0.103962		-19.6625		386.6134
		1	0.124313		-18.1097		327.9612
R/H_1	1	4	0.03117	0.058494	-30.1253	-27.4048	907.5346
		7	0.02		-33.9794		1154.6
		2	0.141994		-16.9546		287.4584
	5	5	0.055387	0.071176	-25.1318	-25.9748	631.6076
		8	0.016147		-35.838		1284.365
		3	0.218601		-13.2069		174.4234
	8	6	0.047248	0.12327	-26.5124	-19.7939	702.908
		9	0.103962		-19.6625		386.6134
		1	0.124313		-18.1097		327.9612
ΔH%	10	6	0.047248	0.062569	-26.5124	-26.8201	702.908
		8	0.016147		-35.838		1284.365
		2	0.141994		-16.9546		287.4584
	20	4	0.03117	0.092375	-30.1253	-22.2475	907.5346
		9	0.103962		-19.6625		386.6134
		3	0.218601		-13.2069		174.4234
	30	5	0.055387	0.097996	-25.1318	-24.106	631.6076
		7	0.02		-33.9794		1154.6
T.	400	1	0.124313		-18.1097		327.9612
		5	0.055387	0.094554	-25.1318	-20.968	631.6076
		9	0.103962		-19.6625		386.6134
							0
	470	2	0.141994		-16.9546		287.4584
		6	0.047248	0.069747	-26.5124	-25.8155	702.908
		7	0.02		-33.9794		1154.6
	540	3	0.218601		-13.2069		174.4234
		4	0.03117	0.088639	-30.1253	-26.3901	907.5346
		8	0.016147		-35.838		1284.365

The sum of the squares due to variation about the mean is:

$$SS = \sum_{i=1}^{9} \left(S/N_i - \overline{S/N} \right)^2 = 503.1005 \tag{4-30}$$

For the factor expressing the ratio of width to thickness, the sum of the squares due to variation about the mean is

$$SS_{W_1/H_1} = \sum_{j=1}^{3} M * (\overline{S/N}_{Wj} - \overline{S/N})^2 \tag{4-31}$$

Where M is the number of experiments at the level 1 of the ratio of width to thickness.

$$SS_{W_1/H_1} = 3*(\overline{S/N}_{W1} - \overline{S/N})^2 + 3*(\overline{S/N}_{W2} - \overline{S/N})^2 + 3*(\overline{S/N}_{W3} - \overline{S/N})^2 = 319.9713 \tag{4-32}$$

If this procedure is repeated for R/H_1, dH and T, the following is obtained:

$$SS_{R/H_1} = 98.173$$

$$SS_{\Delta H\%} = 31.729$$

$$SS_T = 53.227$$

These values represent a measure of the relative importance of each control factor in controlling the spread. The percentage contribution of the relative effect each factors has on the spread is shown in the following:

Factor W_1/H_1 : (319.9713/503.1)×100=63.59988%

Factor R/H_1 : (98.173/503.1)×100=19.51362%

Factor ΔH% (31.729/503.1)×100=6.30662%

Factor T: (53.227/503.1)×100=10.57987%

From table 14, it is clear that the factor W_1/H_1 has an overwhelming influence on the spread, the factor ΔH% has the minimum effect. Table 14 also implies that the factor of temperature should be included in spread formulae.

Table 14 Analysis of variance of spread defined by equation (4-23)

	DOF	SS	SS%
W_1/H_1	2	319.9713	63.59988
R/H_1	2	98.173119	19.51362
ΔH%	2	31.728658	6.30662
T	2	53.227398	10.57987
Total	8	503.1005	100

ΔH% having the minimum effect on the spread does not seems a reasonable conclusion. Most researchers could not accept it. But it does come from scientific analysis. This is due to the definition of the spread. All the above analyses are performed based on the equation (4-23), $S_w = \frac{Ln(W_2/W_1)}{Ln(H_1/H_2)}$. The effect of reduction on the spread is involved implicitly in the definition of spread through the introduction of the term $Ln(H_1/H_2)$.

If equation (4-24) is adopted, a differing analysis emerges. The obtained analysis of variance for the spread defined by equation (4-24) is shown in table 15.

Table 15 Analysis of variance of spread defined by equation (4-24)

	DOF	SS	SS%
W_1/H_1	2	321.04148	41.05
R/H_1	2	97.559536	12.474
ΔH%	2	309.42486	39.564
T	2	54.06191	6.912
Total	8	782.08778	100

Surprisingly, a totally different order is given except for the ratio of W_1/H_1 . W_1/H_1 has nearly the same effect as ΔH% on the spread, followed by R/H_1 and T. Considering this point, Winden's formula, which just considers the effect of reduction, is incorrect. It is clear the effect of T can be neglected to simplify the process of establishing a new formula.

From the aforementioned discussion, we can see that the Taguchi method is indeed helpful for gaining insight into the spread behaviour, and does provide useful guides for controlling the spread behaviour.

When applying the Taguchi method, two elements have significantly influence on the results. They are the choice of parameters and the value at each level. For the spread, the influencing parameters include: roll speed, roll temperature, friction coefficient, material resistance and the four parameters studied in the above sections. The reason for excluding the first four parameters are that they either have minor influence on the spread, or they are difficult to control. If all these parameters are chosen as parameters, an orthogonal array $L_{18}\left(3^8\right)$ will suit this task.

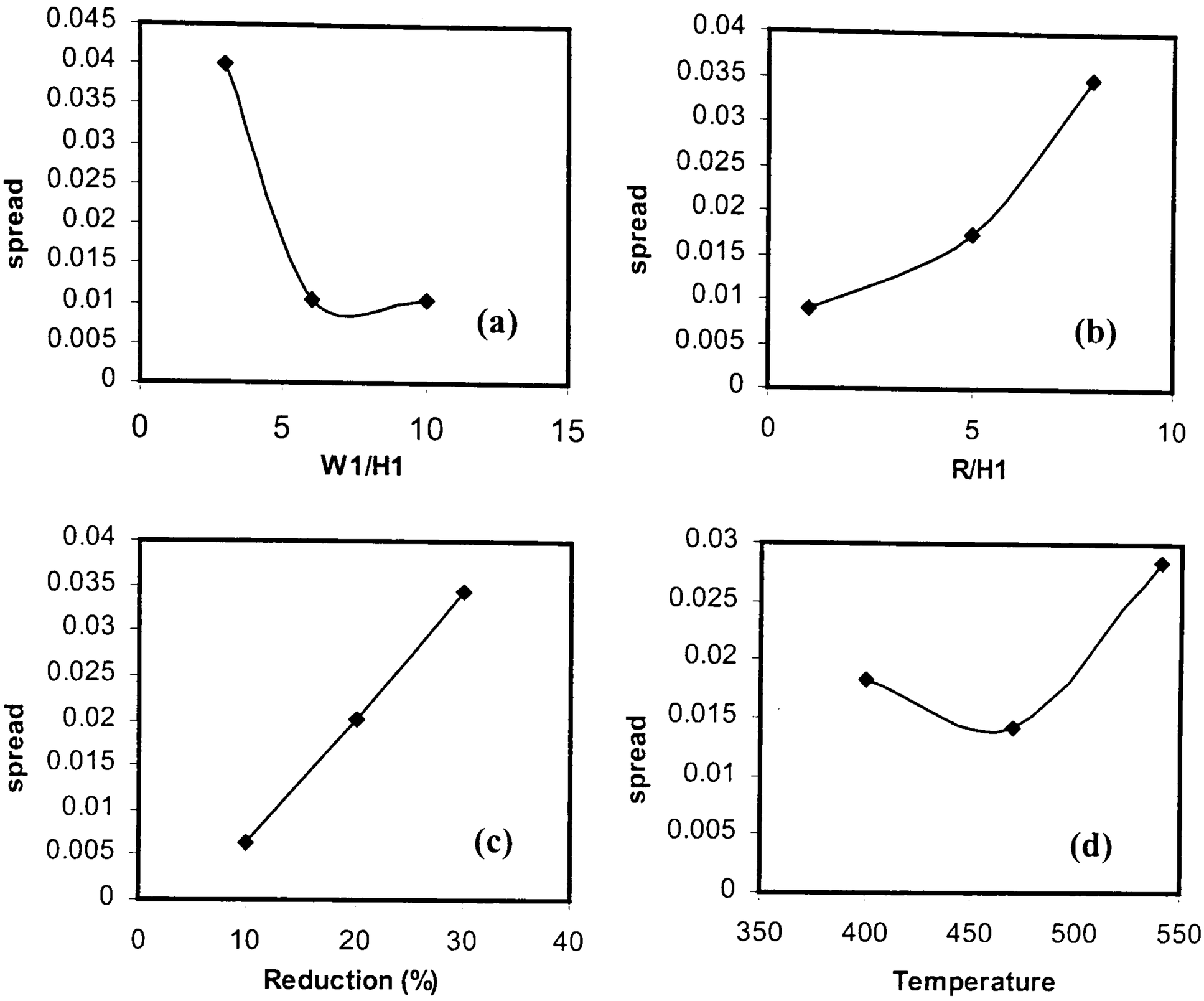

Fig.4-43 Plots of response of each parameter level on the spread defined by equation (4-24)

The average effect of each parameter level on the spread is shown in Fig.4-43. From Fig.4-43, it can be seen that:

(a) the spread coefficient increases with the decrease of W_1/H_1

(b) the spread coefficient increases as reduction $\Delta H\%$ increases

(c) the spread coefficient increases as R/H_1 increases

(d) the spread coefficient generally increases with the increase of deformation temperature

These agree with most workers' experimental observation. It is also interesting to find that, in Fig.4-43 (a), there is little change in the spread when the $W_1/H_1 > 6$; the spread increases linearly with reduction (see Fig.4-43 (c)) and the spread shows a more complex relationship with the deformation temperature (Fig.4-43 (d)).

4.6.8 New spread formula

From the above discussion, it is clear that FEM gives an excellent prediction of the lateral profile under both laboratory and industrial rolling conditions. This shows that the laboratory or industrial experiments can be replaced totally by FEM. The advantages of such a replacement are obvious. There is no equipment limitation, the accuracy of measurement is high and little capital investment is required. We adopt a quarter model to analyse hot flat rolling process by FEM, stop the analysis when rolling reaches the steady state regime, use a powerful workstation and limit the experimental analyses. This is regarded as sufficient to construct a spread formula with high precision. The time would be shorter than the time necessary for laboratory experiments, especially when the whole experimental procedure is considered, i.e. homogenisation, rolling, machining and measurement.

From Table 14 and Table 15, it can be seen that the definition of the spread coefficient directly determines which factor should be included in any spread formula. With the consideration of reducing any possible measurement error, it was decided that equation (4-23) would be abandoned because it involves both a change in width and a change in thickness. A more satisfactory way is to use equation (4-24), where W_2 is the maximum width after deformation. The advantage of using equation (4-24) is that the spread coefficient is a simple function of reduction. If we revisit equations (2-4) to (2-8), we can see that three parameters: $\frac{W_1}{H_1}$, $\frac{W_1}{\sqrt{R * dH}}$ (where $dH = H_1 - H_2$) and $\frac{R}{H_1}$ are adopted. This suggests that S_w is a function of above three factors. In recent years, a parameter, $\frac{H_m}{L}$ the ratio of the mean roll gap thickness to the projected arc of contact, is adopted to distinguish various rolling conditions (Bünten and Karhausen 1999). The value of $\frac{H_m}{L}$ where

$L = \sqrt{R * dH}$ decreases from approximately 4 in the initial breakdown pass towards the values of 0.3 in the finishing hot rolling pass. This parameter will also be included in the new formula. The influence of temperature is neglected as suggested by the study using the Taguchi method. Hence a total of 4 factors will be involved in the new formula.

A total of 434 sets of spread data are employed to deduce the new formula. The data are taken from two sources: one is from the FE analyses for various industrial rolling conditions (50 data sets), another part is taken from Wright's laboratory experiments (384 data sets) (Wright 1978). It is expected that the new formula constructed in this way will be able to deal with both laboratory rolling and industrial rolling. The ranges of $\frac{W_1}{H_1}$, $\frac{W_1}{\sqrt{R * dH}}$, $\frac{R}{H_1}$, and $\frac{H_m}{L}$ are:

$$\begin{aligned} &1 \le W_1/H_1 \le 7 \\ &0.54 \le W_1/\sqrt{R * dH} \le 28.6 \\ &1 \le R/H_1 \le 9.48 \\ &0.42 \le H_m/L \le 4 \end{aligned} \qquad (4\text{-}33)$$

The software used to obtain the new spread formula is Microsoft Excel 97. The linear regression function "LINEST" in Excel 97 is applied for multiple linear regression. This function calculates the statistics for a line by using the "least squares" method to calculate a straight line that best fits the provided data. The equation for the line is:

$$y = m_1 x_1 + m_2 x_2 + \cdots + b \qquad (4\text{-}34)$$

where the dependent y-value is a function of the independent x-values. The m-values are coefficients corresponding to each x-value, and b is a constant value.

Note that y, x, and m can be vectors. The array that "LINEST" returns is $\{m_n, m_{n-1}, \cdots, m_1, b\}$ {mn,mn-1,...,m1,b}.

When applying the function "LINEST", one necessary condition is the knowledge of the possible form of the formula. Although four factors are ascertained above, there are countless functional combinations for these four factors. The most common function are due to linear, power and exponential relationship. From equations (2-4) to (2-8), we can see that there possibly exists an exponential relationship between S_w and $W_1/\sqrt{R*dH}$, and possibly power relationship between S_w and W_1/H_1. After many trial regression analyses, it was found that the following formula gives the best fit with the raw spread data:

$$Ln\frac{W_2}{W_1} = 0.2187 * \left(e^{0.1071*\left(\frac{W_1}{\sqrt{R*dH}}\right)} \right) \left(\frac{R}{H_1}\right)^{-0.848} \left(\frac{W_1}{H_1}\right)^{-1.481} \left(\frac{H_m}{L}\right)^{-2.6978} \tag{4-35}$$

It can be seen from equation (4-35) that H_m/L contributes more to the spread coefficient than does W_1/H_1. The reason why H_m/L is not studied as a parameter in the Taguchi method is attributed to the difficulty of controlling the variation of H_m/L. The value of H_m/L is usually calculated by

$$\frac{H_m}{L} = \frac{(H_1 + H_2)/2}{\sqrt{R*dH}} \tag{4-36}$$

where H_1 and H_2 are the thickness before and after the roll gap. From equation (4-36), it can be seen that the H_m/L is influenced by three parameters: H_1, H_2 (or dH) and R. In the above Taguchi experimental design, see table 12, the value of H_1 is fixed. W_1, R and H_2 were determined according to the levels of W_1/H_1, R/H_1 and $\Delta H\% = (H_1 - H_2)/H_1 \times 100$. Hence, in each analysis, the H_m/L is

different. That means the H_m/L, W_1/H_1, R/H_1 ,and ΔH% can not be applied together to design an orthogonal array. In order to compare with the reported work, it was decided that the H_m/L should be ignored in the orthogonal table. But this does not mean that the H_m/L is not important. On the contrary, it could be the most influencing variable.

The relation between S_w and $W_1/\sqrt{R*dH}$ is shown in Fig.4-44. It is obvious that an exponential function does exist between S_w and $W_1/\sqrt{R*dH}$. We can also observe that most data, which are taken from Wright's thesis, are situated within the range of $W_1/\sqrt{R*dH} \leq 10$. The reason is due to the roll load limit of the laboratory mill. The slab width can not be larger because of torque limitation. The fit between the prediction and the measurement is illustrated in Fig.4-45. The correlation coefficient is 0.97.

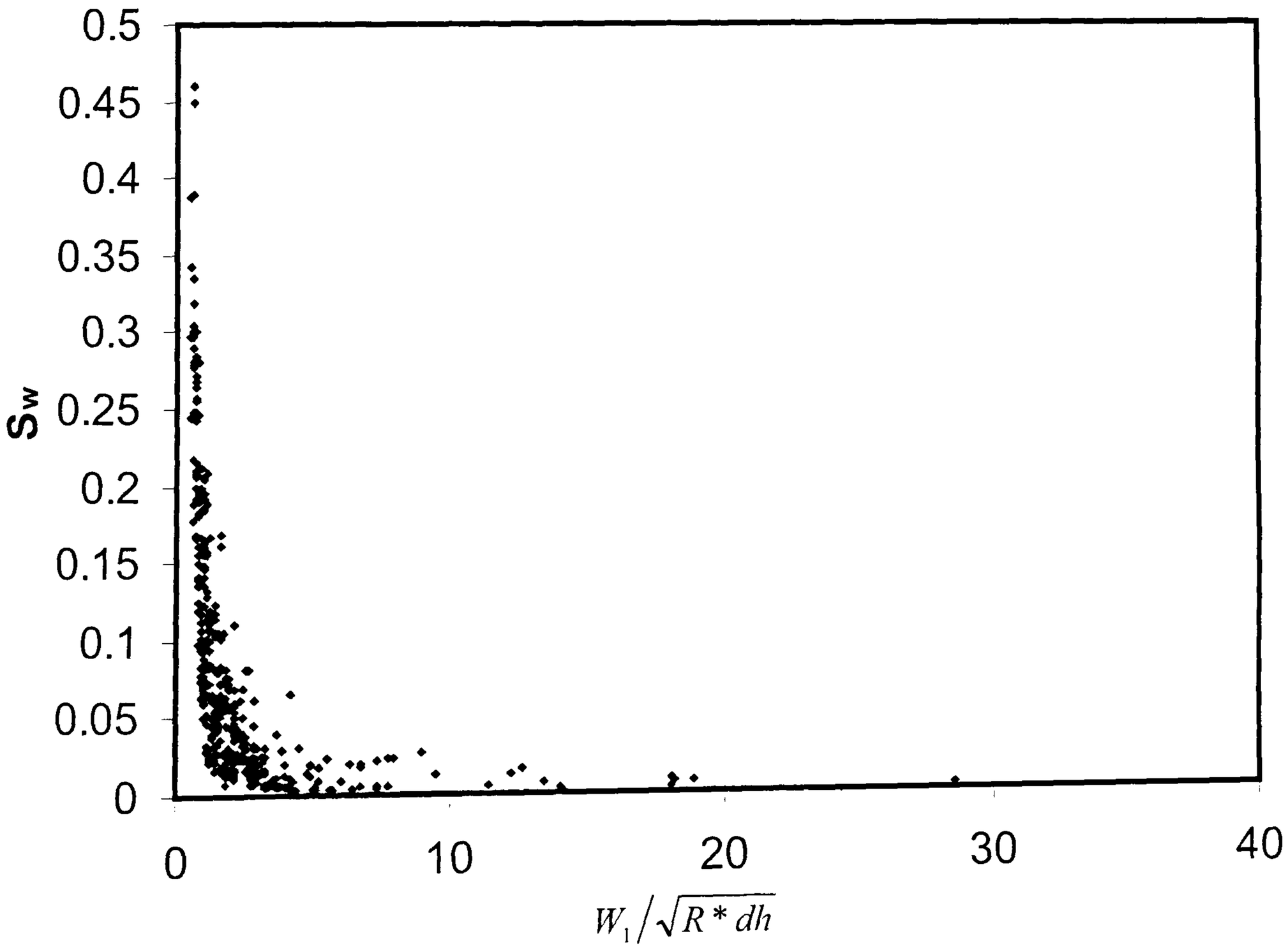

Fig.4-44 Relation between S_w and $W_1/\sqrt{R*dH}$

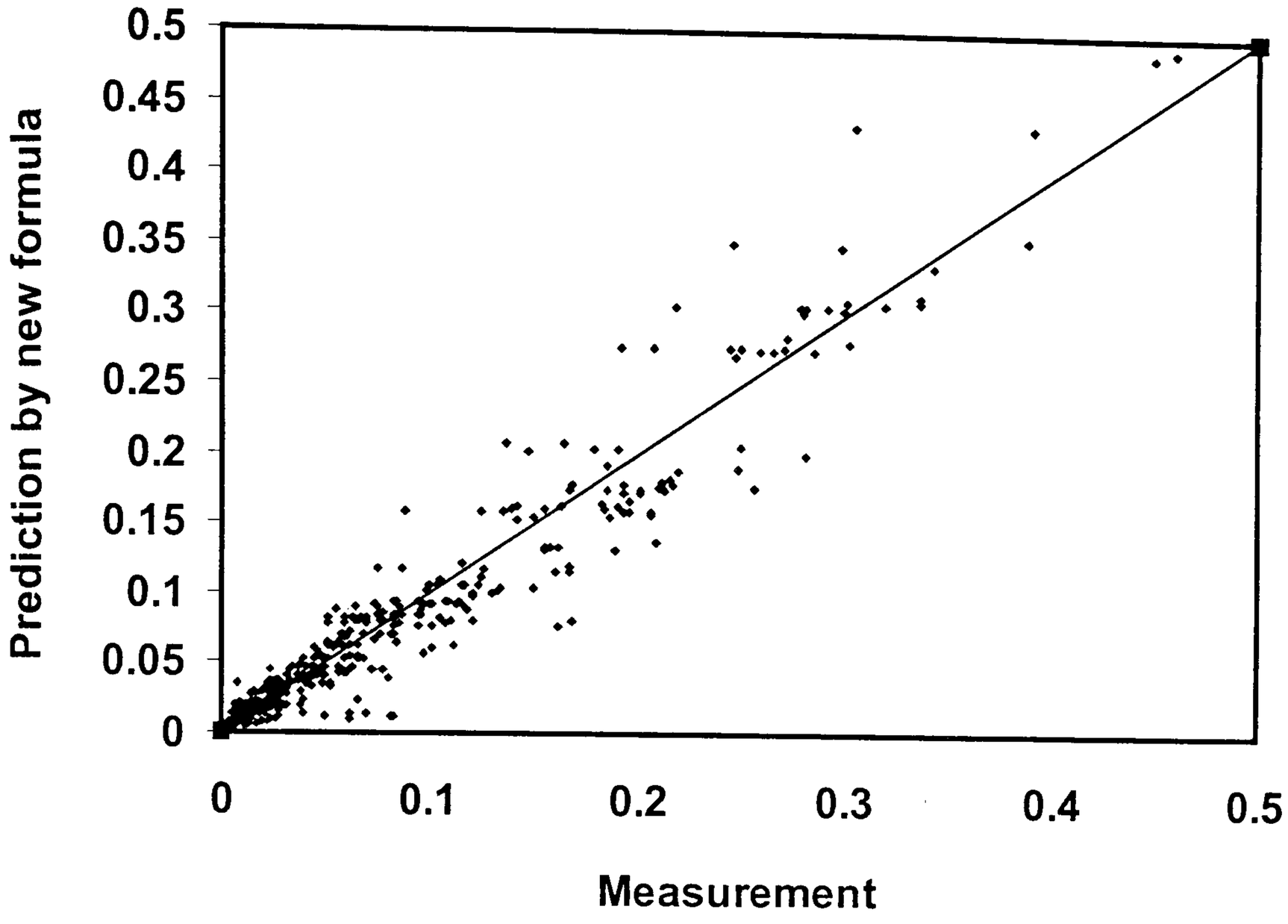

Fig.4-45 Correlation between the measured/computed spread and the predicted spread coefficient by the new formula

To check the validity of the new formula, the variation of spread coefficient of a 14-pass schedule was calculated and compared with the laboratory measurement by Winden (Winden 2000). The experiments were carried out in a laboratory mill in the University of Sheffield, but the industrial rolling conditions were reproduced through the introduction of a series of new techniques. The calculated spread coefficients are shown in Table 16. The values in the column 4 to column 7 in Table 16 are calculated by using the expression W_i/W_0 , where W_i is the width of i^{th} pass, W_0 is the initial width which is 55 mm in this particular rolling pass schedule. It is assumed here that the values given by Winden's equation can be regarded as the actual measurement because his equation is regressed from the measurement.

From Table 16, we can see that the present work shows a better prediction than Sheppard & Wright's equation and Helmi & Alexander's equation. Sheppard's work gives the greatest unrealistic values after the twelfth pass. It is believed that

this result is caused by the first term in equation (2-8) (Winden 2000). Although the present formula is regressed from nearly the same data sets as Sheppard & Wright's equation adopted, the new formula show more flexibility and accuracy due to two main reasons:

(a) The introduction of the term of $\frac{H_m}{L}$ in equation (4-35)

(b) The introduction of industrial data into the regression data set

Table 16. Comparison between different spread formulae

Pass No. (Winden)	**H_1**	**H_2**	**Sheppard Eq.(2-8)**	**Helmi Eq.(2-7)**	**Winden Eq.(2-10)**	**Present work**
1	58.6	50.1	1.006	1.032	1.028	1.030451
2	50.1	48.2	1.007	1.033	1.035	1.035224
3	48.2	43.4	1.009	1.047	1.051	1.050404
4	43.4	38.7	1.013	1.063	1.066	1.065958
5	38.7	34	1.016	1.083	1.082	1.082465
6	34	29.3	1.02	1.106	1.097	1.100177
7	29.3	24.6	1.026	1.133	1.113	1.119475
8	24.6	19.8	1.034	1.168	1.129	1.141663
9	19.8	15.1	1.045	1.208	1.145	1.166637
10	15.1	11.3	1.062	1.244	1.157	1.188666
11	11.3	7.6	1.104	1.286	1.17	1.215497
12	7.6	4.7	1.298	1.323	1.179	1.241364
13	4.7	3.2	0.311	1.341	1.184	1.255344
14	3.2	2.2	0	1.353	1.188	1.266232

The present author believes that the introduction of $\frac{H_m}{L}$ into the spread calculation is vital for the success. Unfortunately, this term was ignored in all previous formulae. It is worth emphasising that even though equation (4-35) is derived for a

series of single pass deformation, it still performs quite well for multi-pass rolling process.

4.7 Prediction of damage evolution

Edge cracking is a common rolling defect occurred in the hot rolling of aluminium alloys. It is desirable to predict and eliminate the occurring of edge cracking in the design stage. Several studies have been carried out in recent years by incorporating ductile fracture criteria into the FE code (Kim et al 1995, Hartely et al 1997, Behrens et al 1999). Cockroft & Latham's criterion may be the best for practical applications, because no material constant is included in the formula (Kim et al 1995). The modified Cockroft & Latham's criterion is expressed as:

$$\int_0^{\bar{\varepsilon}_f} \frac{\sigma^*}{\bar{\sigma}} d\bar{\varepsilon} = C \qquad (4\text{-}37)$$

In Fig. 4-46, the maximum damage value is 0.21, which occurs at the edge and the slab centre. That means the edge and the centre are the most dangerous places. If the damage value reaches a critical value, either edge cracking or alligatoring may occur. Because there is no practical data nor experimental evidence to connect edge cracking or alligatoring in any aluminium alloys it is not possible to predict the fracture limit or to assess whether the maximum value of C=0.21 will produce unsound products. We can however observe that the greatest values occur at those locations most susceptible to cracking.

The rolling process is made up of a series of single passes. Similar to the strain, the damage value is inherited from pass to pass. If the damage value is computed from the first pass to the pass in which the edge cracking becomes manifest, the accumulated damage can be regarded as the critical damage value. It is suggested

that the critical damage value C could be obtained, by conducting hot compression tests.

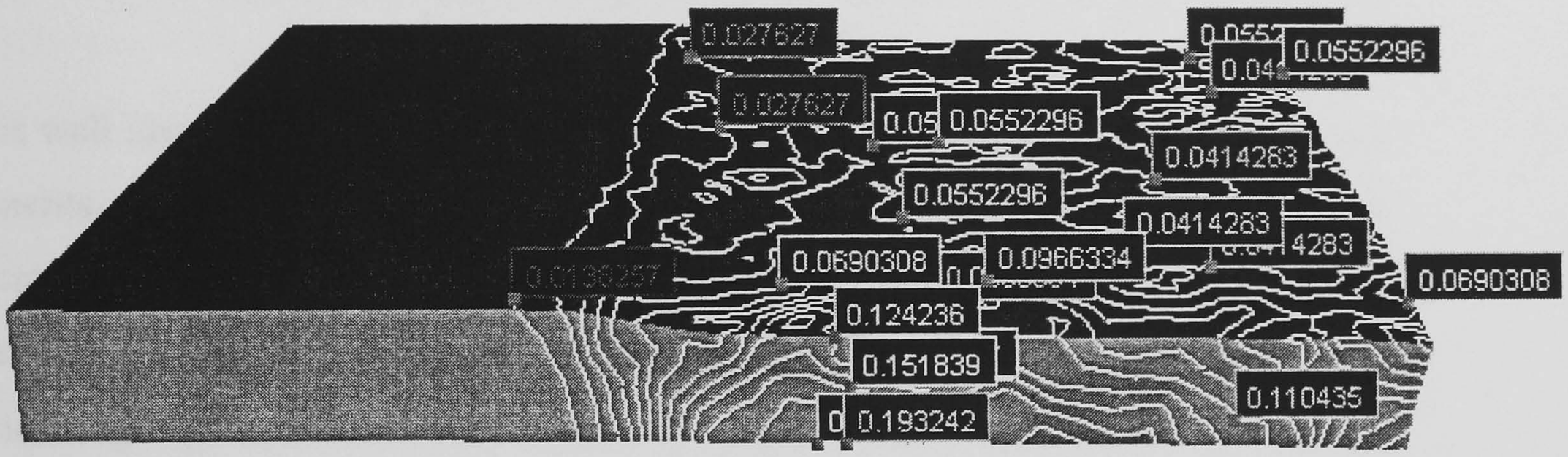

Fig.4-46 The damage value distribution in the rolled slab

PAGE

MISSING

IN

ORIGINAL

Chapter 5 Simulation of Microstructure Evolution

5.1 Modelling of subgrain size

5.1.1 Hot flat rolling of commercial purity aluminium

It is well known that the microstructure of dilute Al. alloys during hot deformation consists of subgrains within the original grain in those processes in which recrystallisation does not intervene during the deformation and during any interpass time. The subgrain distribution and the mean size have a significant influence on mechanical properties: determining the strength, ductility, texture, etc. Thus knowledge of the distribution of subgrain size is critical for quality control.

In this section, the experimental data are taken from Zaidi and Sheppard's (1982) experiment. Generally, The material specification conforms to AA1100. The slab is 25mm in thickness and 25mm in width. The rolling was performed at 500^0C and at strain rate of $2s^{-1}$ in a single stand mill with roll diameters of 250mm. The thickness reduction is 40%. The specimens were quenched within 3 seconds in ice water after deformation. The measurement locations are shown in Fig.5-1. All these points are in the symmetrical plane along width, where the plane strain deformation prevails. Therefore, a 2-D plane model is used.

The measured microstructure in the roll gap is shown in Fig.5-2. Figure 5-2 (a) is taken from a foil extracted from a position 8 mm ahead of the roll bite, indicated by A in Fig.5-1. There is no evidence of subgrains, the only substructural feature being dislocation lines which terminate either at particles or grain boundaries. This is typical of a cast and homogenised structure. At a position closer to the roll gap (location B in Fig. 5-1) but still generally considered to be outside the quasi static deformation zone, an imperfect cellular structure with ragged walls and considerable dislocation activity may be observed (see Fig.5-2 (b)). It indicates that

very low strains are required to produce sufficient activity to initiate the formation of subgrains.

Figure 5-2 (c) shows that many dislocation tangles have formed in the grain interior but that well defined sub-boundaries form only at the grain boundaries and at those positions where larger particles are located. This is because the grain boundaries are likely to be locations of the greatest stress in lightly deformed material.

At the onset of observable macroscopic deformation (position D in Fig.5-1, 1 mm into the roll bite) the electron micrograph (Fig. 5-2 (d)) indicates a structure consisting of well developed subgrain walls but containing a multiplicity of 'microcells' within each subgrain. Subgrain size in Fig.5-2 (e) is stabilised and no further change is observed after the position E in Fig.5-1.

Generally, in a billet rolled at 500^0C with 40% reduction, the average subgrain diameter decreased from ~9 to 6.4 μm within the first 10 mm of the projected length of contact. The total length of contact for such a reduction is 35 mm.

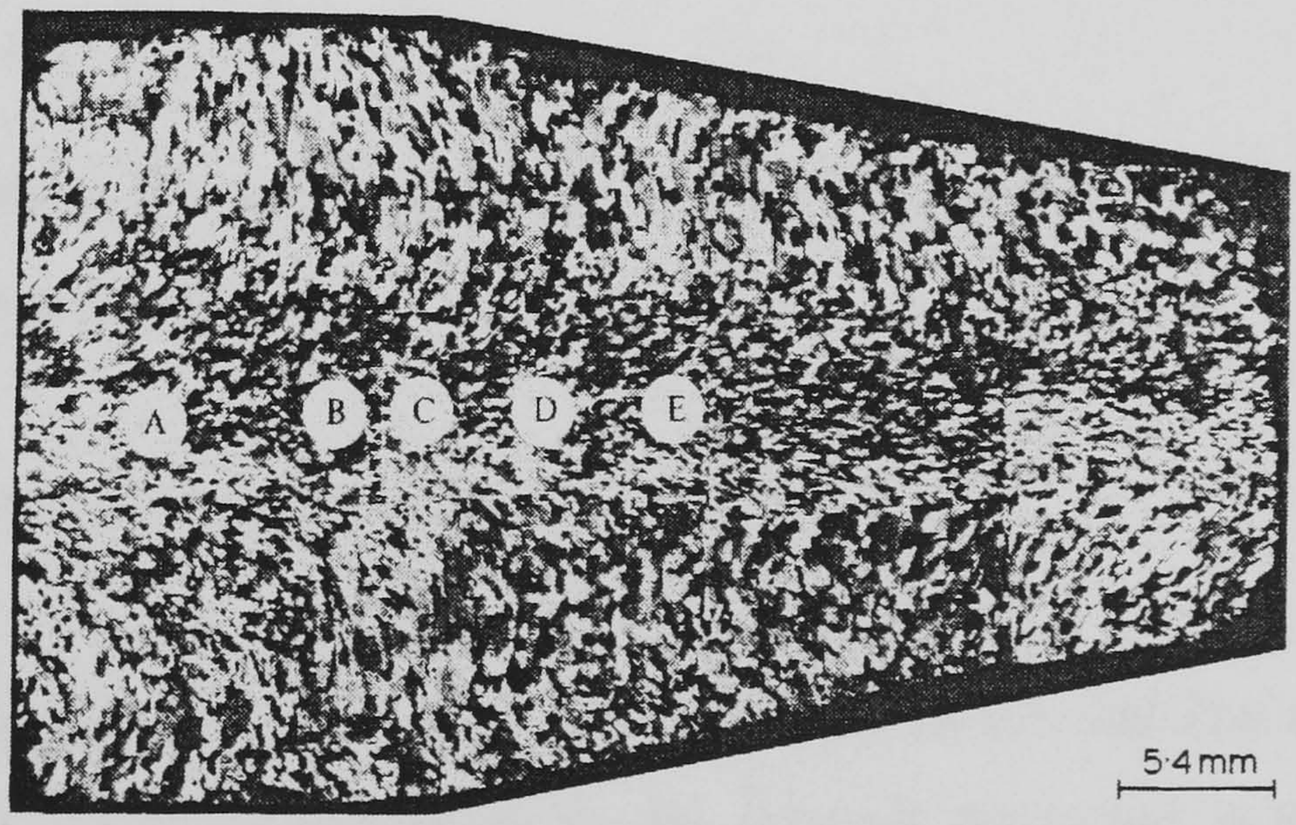

Fig.5-1 Locations of subgrain size measurement (after Zaidi and Sheppard 1982)

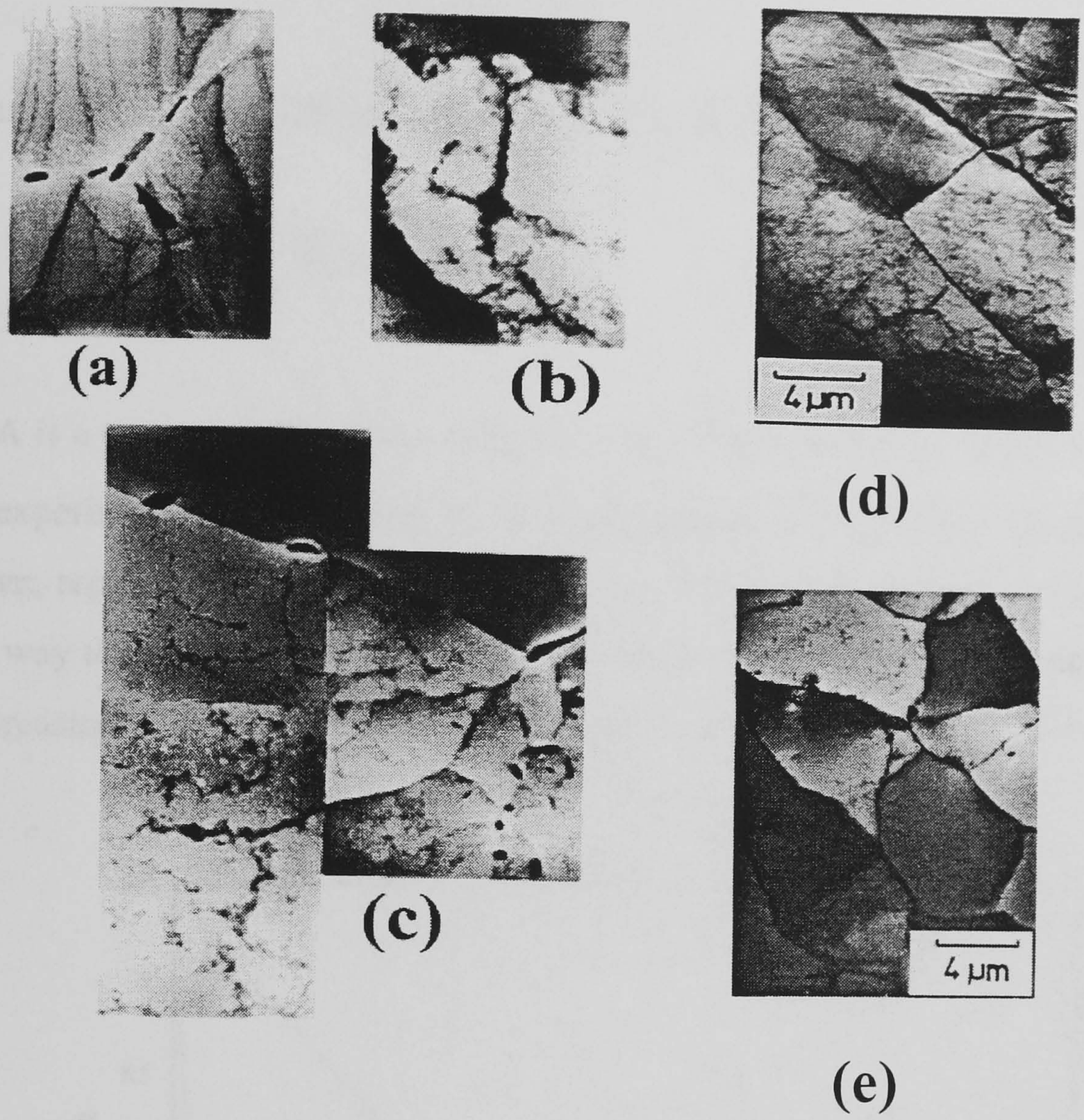

Fig.5-2 The development of a subgrain structure as material passes through the roll gap (after Zaidi and Sheppard 1982)

The relationship between the subgrain size and the deformation parameters in the steady state regime was given by:

$$\delta_{ss}^{-1} = -0.196 + 0.0153 * LnZ \tag{5-1}$$

In the following prediction of the subgrain size evolution, Sellars and Zhu's model is applied. The ε_δ, the characteristic strain for the subgrain formation, is assumed proportional to Z^{-1}, which differs from Sellars et al.'s assumption (2000).

$$\varepsilon_{\delta} = AZ^{-1} \tag{5-2}$$

Substituting equation (5-2) into equation (2-28), obtaining:

$$d\delta = \frac{\delta * Z}{\delta_{ss} * A}(\delta_{ss} - \delta)d\varepsilon \tag{5-3}$$

where A is a constant. The initial subgrain size is taken as $9\,\mu m$, which is indicated by the experimental observations. In many circumstances, the initial subgrain size is unknown, replacing the initial subgrain size by the initial grain size seems the most logical way to apply the equation (5-3). The variation of subgrain size with constant and increasing strain rate calculated by equation (5-3) is shown in Fig.5-3.

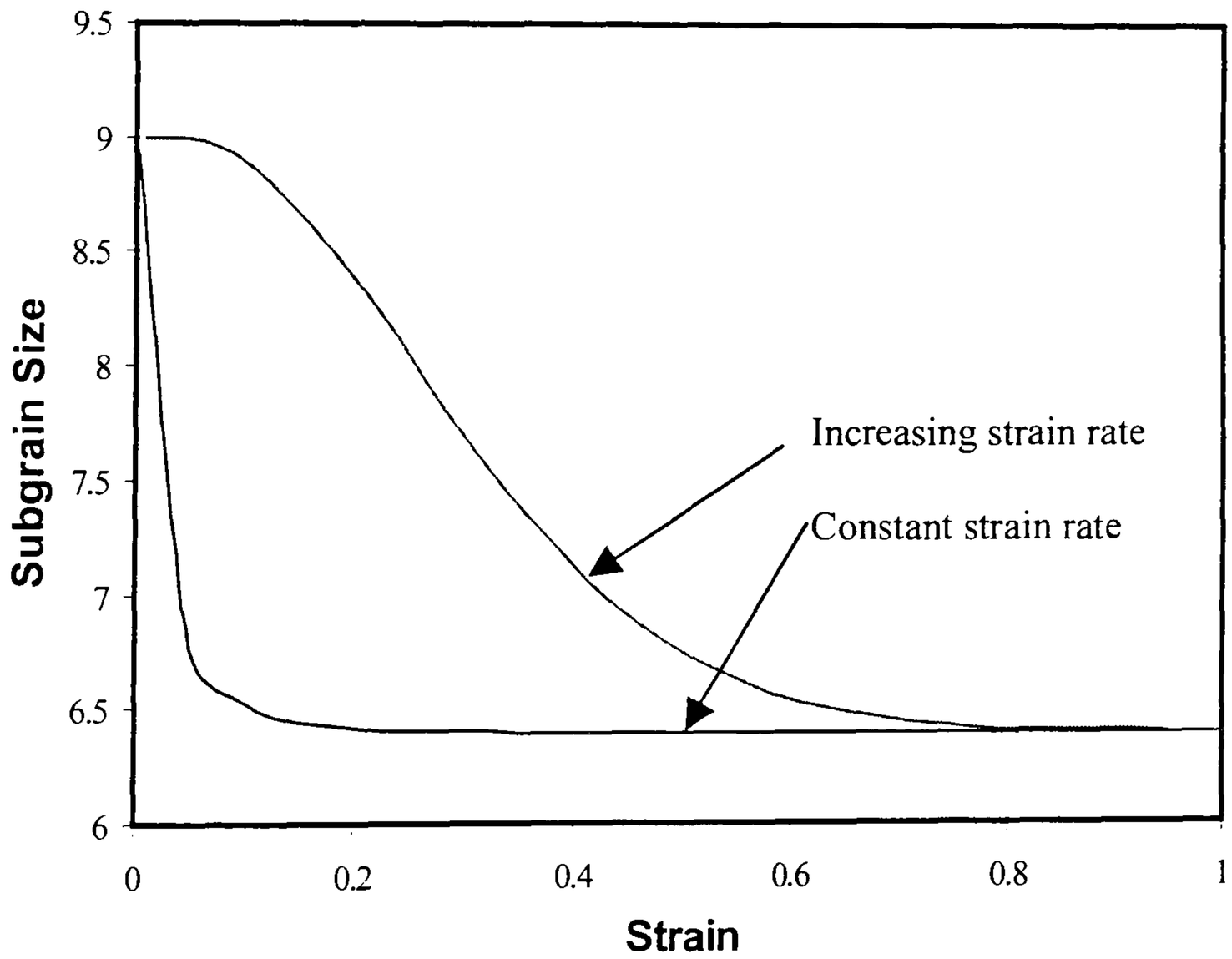

Fig.5-3 The variation of subgrain size under different strain rate conditions calculated by equation (5-3)

It is apparent that the curves presented in Fig.5-3 show similar trends to those in Fig.2-2 (e). The subgrain size decreases with increasing strain, and attains a

stabilised value of 6.4 μm . The strain needed to attain such a steady subgrain size is about 0.2 for constant strain rate and 0.8 for increasing strain rate.

The computed distribution of subgrain size using equation (5-3) by FEM is given in Fig.5-4. Obviously, Fig.5-4 shows a reasonable prediction for subgrain size: subgrain size at the surface is smaller than that at the centre and the decreases from the entry to the exit. Clearly it is constant after leaving the roll gap.

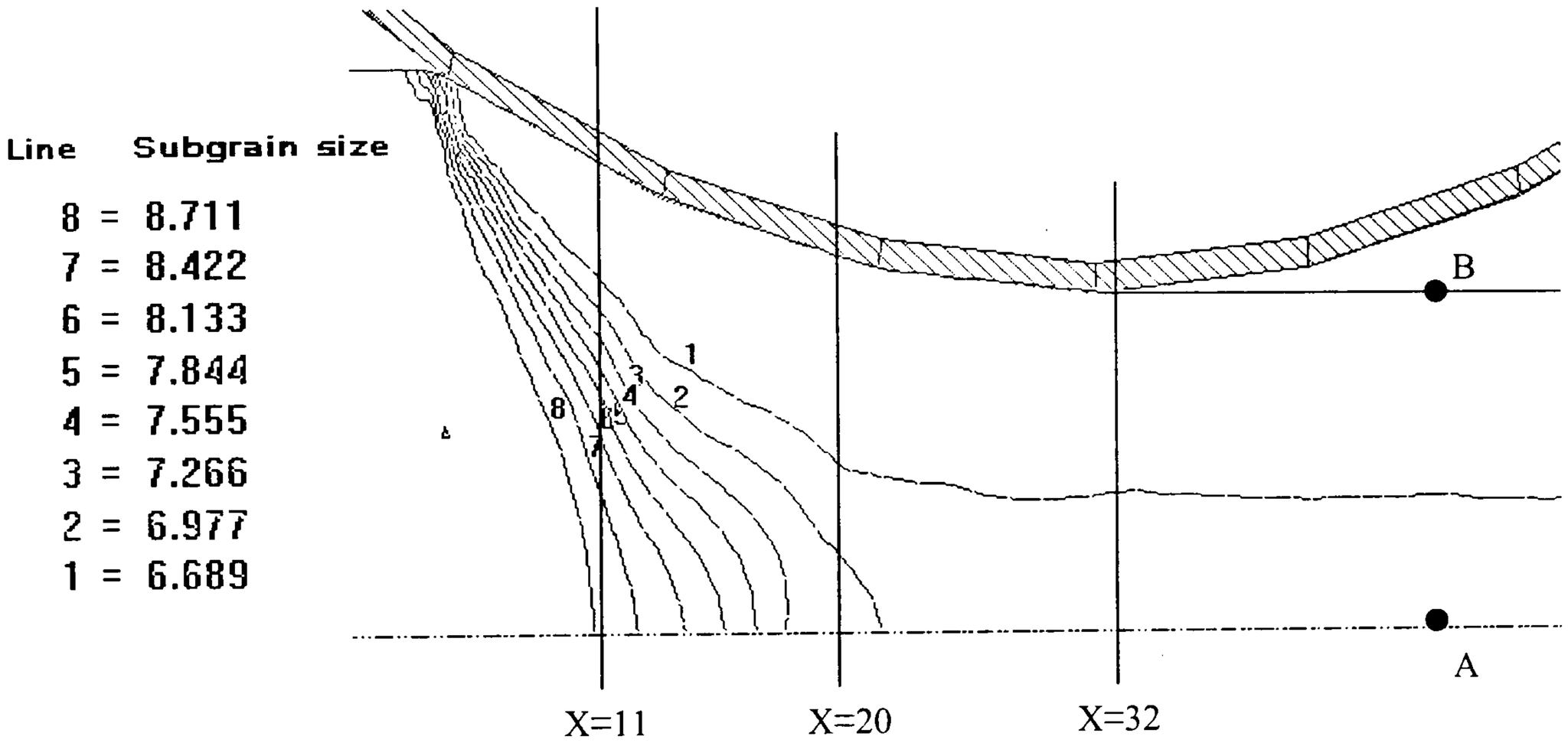

Fig. 5-4 Distribution of subgrain size computed by equation (2-28), in μm

To give a better understanding of the variation of subgrain size, the histories of point A and point B are traced from the beginning to the locations shown in Fig.5-4. The variations of subgrain size with time for these two points are shown in Fig.5-5. For the surface point, the stabilised subgrain size of 6.4 μm is first attained at a time of 0.2s, while the centre point obtains its steady state value of 6.75 μm at a time of approximately 0.4s. As discussed before, the stabilised subgrain size at the centre is 6.4 μm , the relative error between the measurement and the prediction is 5.5%. Chen et al (1990) also simulated the same rolling process by using the empirical

equation (2-23), the predicted subgrain size in the state steady regime is 5.2 μm , the relative error is approximately 20%. It is clear that the present prediction is much better than Chen et al's work.

The predicted distributions of subgrain size through the slab thickness at different locations in the roll gap are shown in Fig.5-6. X=0 corresponds to the position where the rolls just contact the workpiece before rolling. The curves marked "X=20mm" and "X=32mm" is much smoother than the curve marked "X=11mm". This implies that the difference of subgrain size between the surface point and the centre point decreases as the slab passes through the roll gap. The subgrain size at the slab surface is smaller that that of the centre point, due to the lower temperatures at the roll/surface interface.

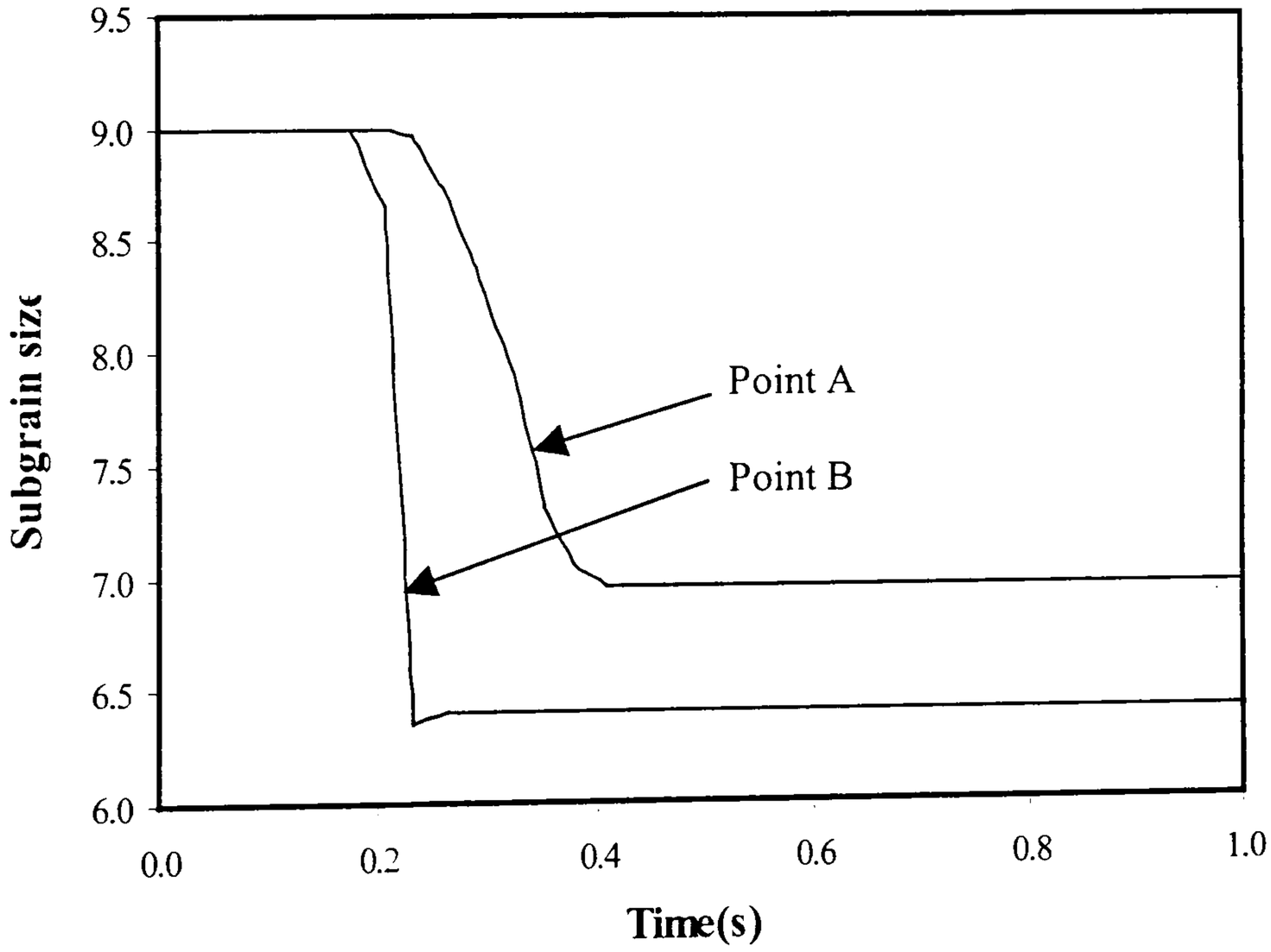

Fig.5-5 Variation of Subgrain size with time

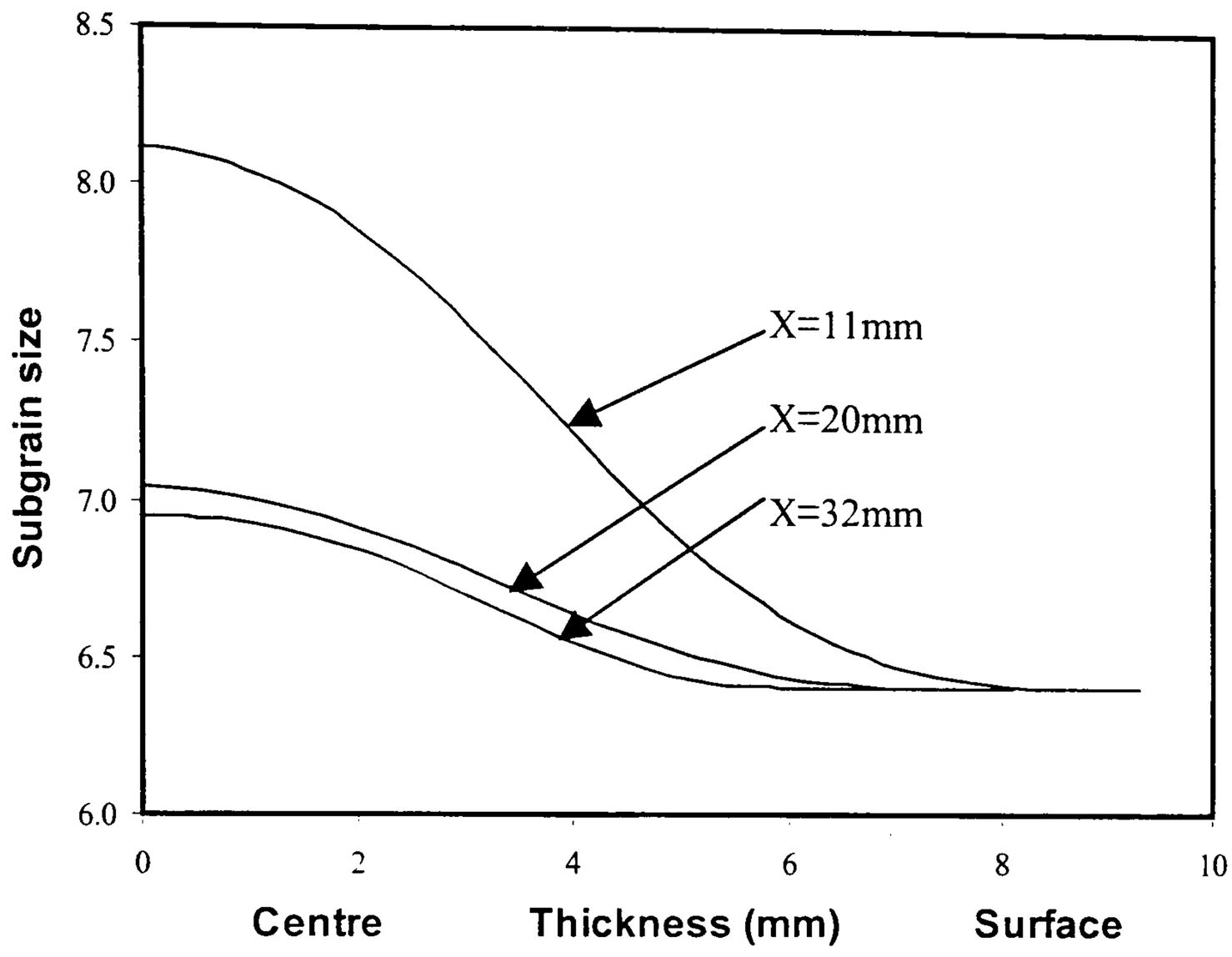

Fig. 5-6 Variation of subgrain size along the thickness

Fig. 5-7 shows the predicted distribution of subgrain size when no modification has been made to equations (2-23), i.e. substituting the instantaneous nodal strain rate and temperature directly into equation (2-23), and using normal activation energy. The range of subgrain size is between $-1549\,\mu m$ to $1004\,\mu m$. That is clearly impossible. The subgrain size can not assume a negative value nor one as large as 1004 μm. Another feature of Fig. 5-7 is that the distribution is irregular. The reason is that equation (2-23) is just a statistical relationship, which relates the subgrain size with mean strain rate and nominal rolling temperature. Critically, this equation is not suitable for the prediction of subgrain size during transient deformation, because it is constructed in the steady state regime. Therefore, it is not surprising that FEM gives unreasonable results because FEM uses the instantaneous strain rate and temperature, which vary both with the position and time.

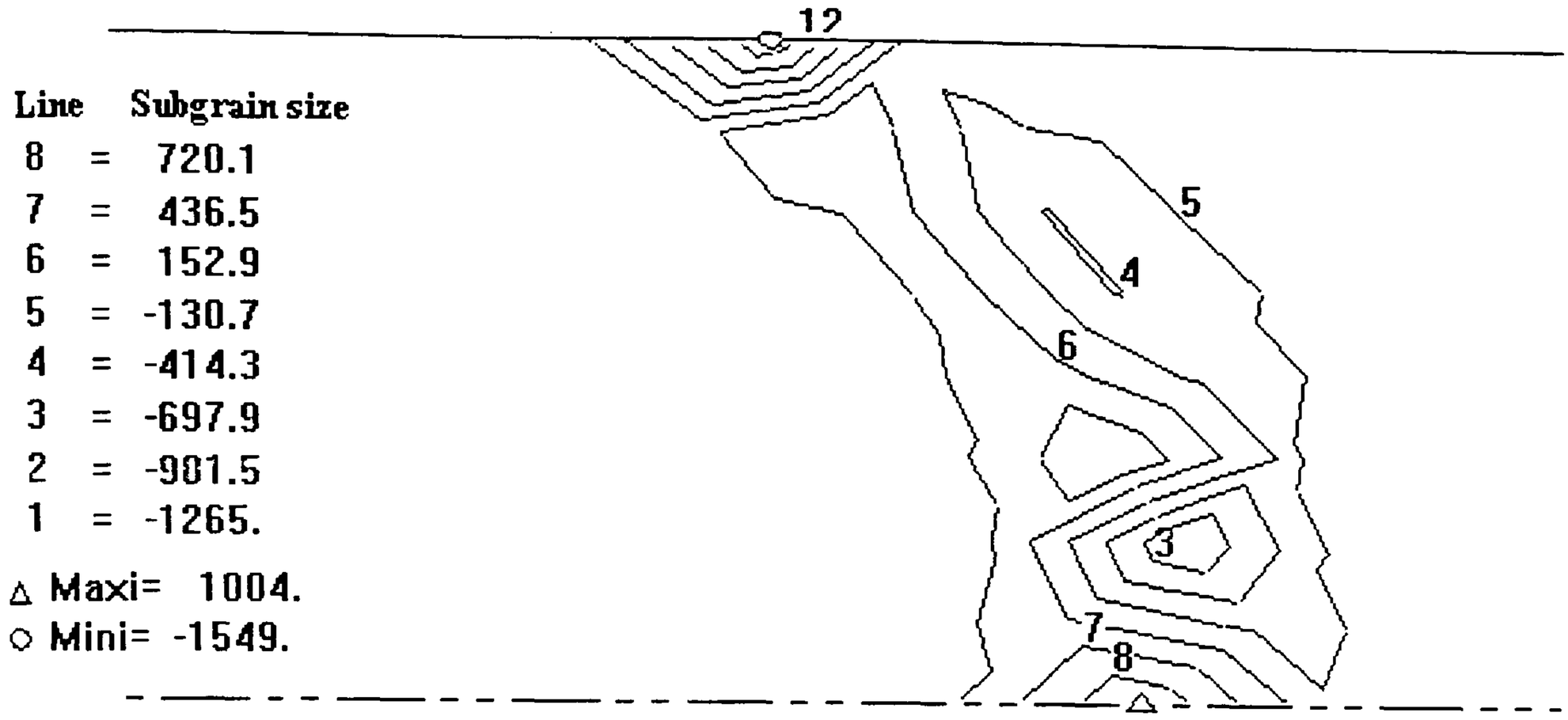

Fig. 5-7 Predicted distribution of subgrain size by equations (2-23) by using instantaneous strain rate, temperature and normal activation energy, in μm

Unlike Chen et al's work where the prediction of subgrain size based on equation (2-23) utilised a Zener-Hollomon parameter averaged over the whole deformation zone, the Zener-Hollomon parameter is calculated by using instantaneous nodal strain rate and nodal temperature in the present study.

Fig.5-8 shows the computed subgrain size using the same ideas that Chen et al (1990) adopted: strain rate is averaged over the whole deformation region at each increment during FE computation, but it also varies as deformation progresses. Comparing Fig.5-8 with Fig.5-4, it can be seen that using the physical model gives a much better prediction than using the empirical model. The predicted subgrain size at the centre in Fig.5-8 at exit is $5.15\,\mu m$, which approaches Chen et al's prediction, $5.2\,\mu m$.

Finite element analyses show that distribution of strain rate is erratic and irregular with greatest contribution at entry point. There are too much bias from entry to exit in the roll gap. The subgrain size at exit is most important. However, the strain rate at this position approaches zero. Hence it is necessary to average strain rate over the whole deformation zone.

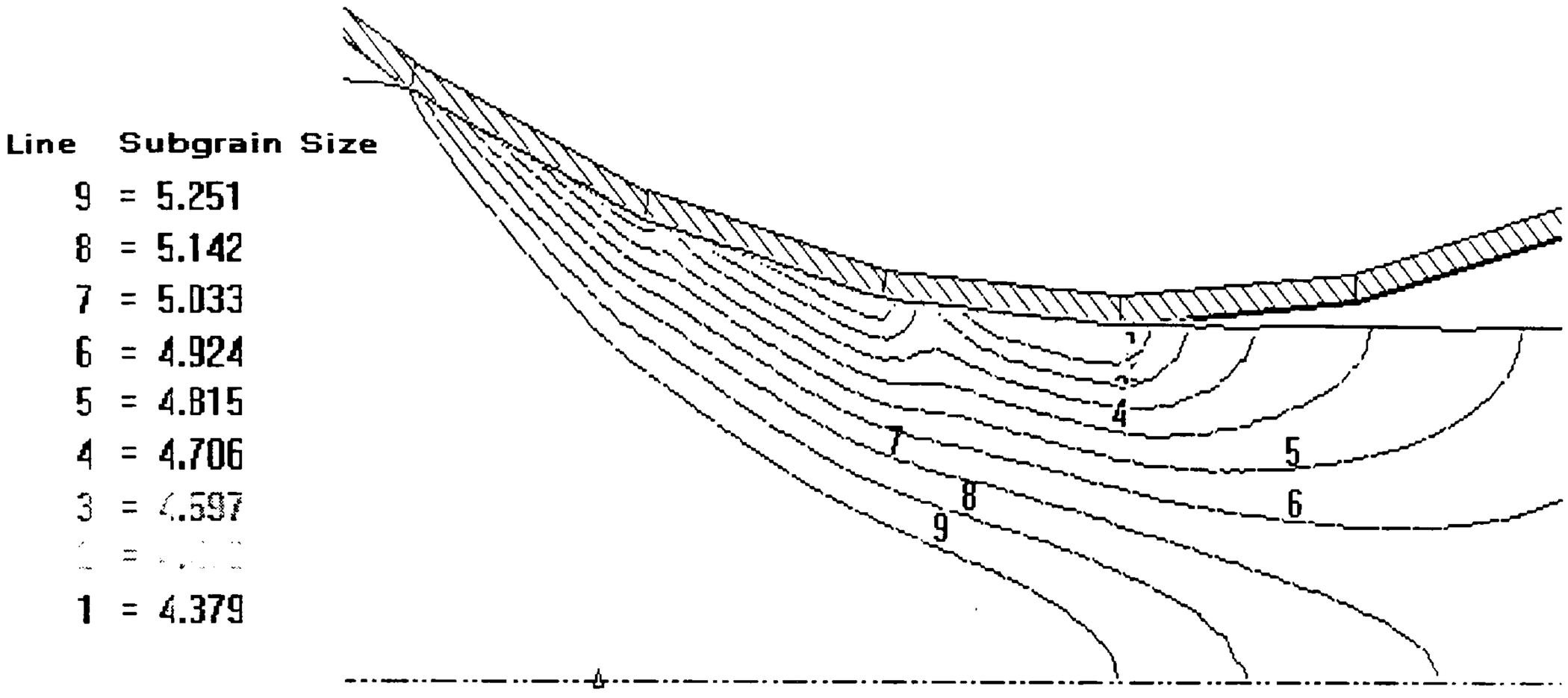

Fig. 5-8 Predicted distribution of subgrain size by equations (2-23) by using averaged strain rate, temperature and normal activation energy, in μm

5.1.2 Hot rod extrusion

Although hot extrusion is not the research topic in the present study, it would be useful to compare the subgrain size evolution with an alternative strain path. Both hot extrusion and hot rolling belong to hot bulk deformation. Theoretically, equation (2-28) should be valid for hot extrusion. The experimental model is taken from Vierod's PhD thesis (1983). The extrusion schedule is shown in Table 17. The measured subgrains size at different locations in the container, shown in Fig.5-9, are listed in Table 18.

Table 17 Extrusion schedule

Extrusion ratio	40:1
Ram velocity	6.7mm/s
Extrusion temperature	325^0C
Billet size (mm)	ϕ 73.5*95
Container size (mm)	ϕ 75
Container temperature	275^0C
Ram temperature	225^0C
Die temperature	225^0C

Table 18 Measured subgrains size

Location	Measurement (μm)	Error (±)	Predicted (μm)	Relative Error (%)
A	1.27	0.19	1.29	1.57
B	1.38	0.11	1.4	1.45
C	1.36	0.21	1.44	5.88
D	1.88	0.12	1.82	3.19
E	1.49	0.25	1.57	5.37

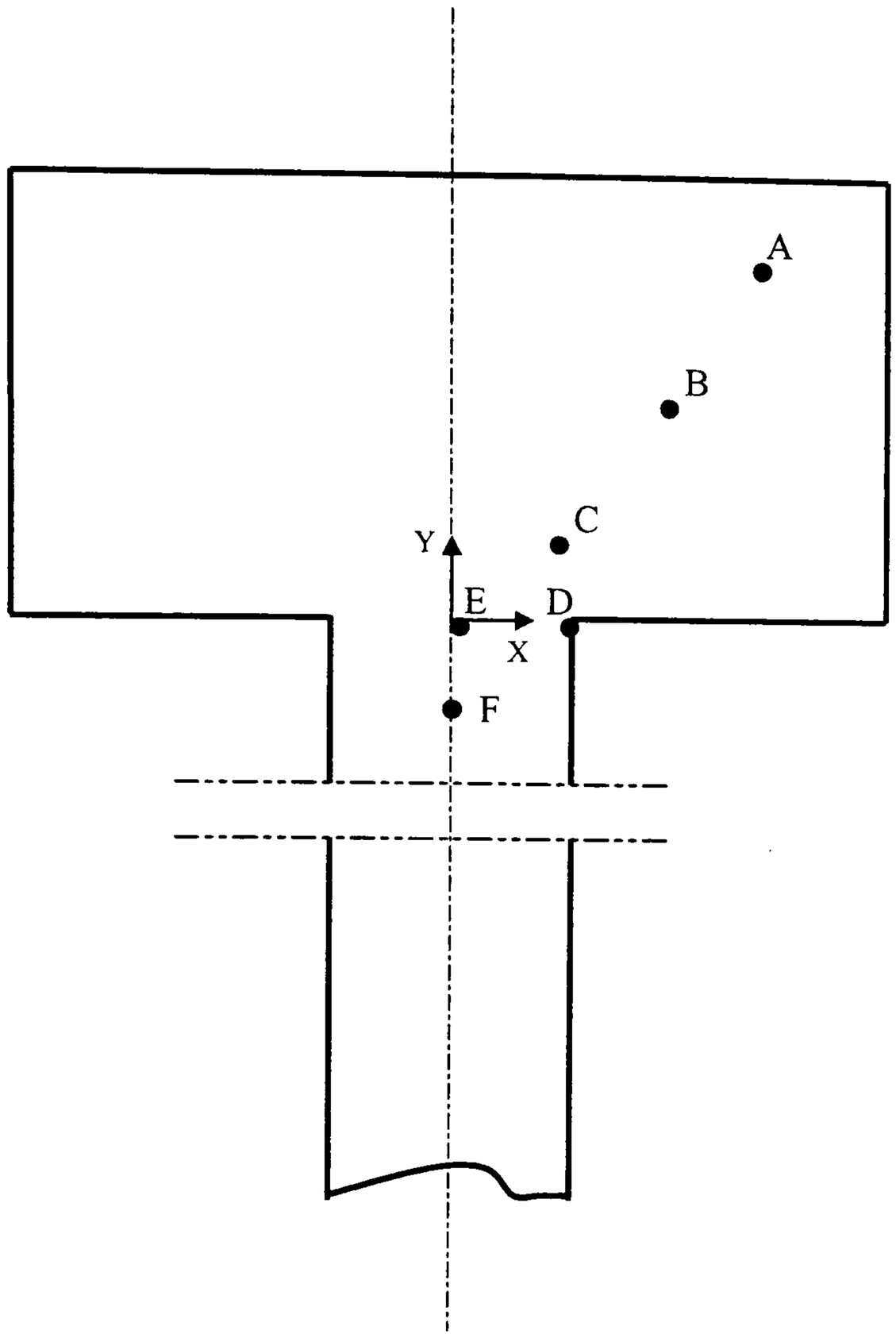

Fig. 5-9 Schematic illustration of locations of the TEM specimens

Unlike the rolling process, the subgrain size from point A to point E increases due to the inherent temperature rise. In this case, δ_{ss} is given as

$$\delta_{ss}^{-1} = -1.747 + 0.096 * \mathrm{Ln}Z \tag{5-4}$$

The computed history of the subgrain size for point F is shown in Fig.5-10. It is obvious that the subgrain size increases steadily before reaching the die mouth. When point F enters the high deformation region, the subgrain size grows rapidly. After leaving the die mouth, the subgrain size maintains an equilibrium size; any possible growth being prevented by the water quench which is usually applied. The

substructure observed at point D and E are shown in Fig.5-11 and Fig.5-12 respectively.

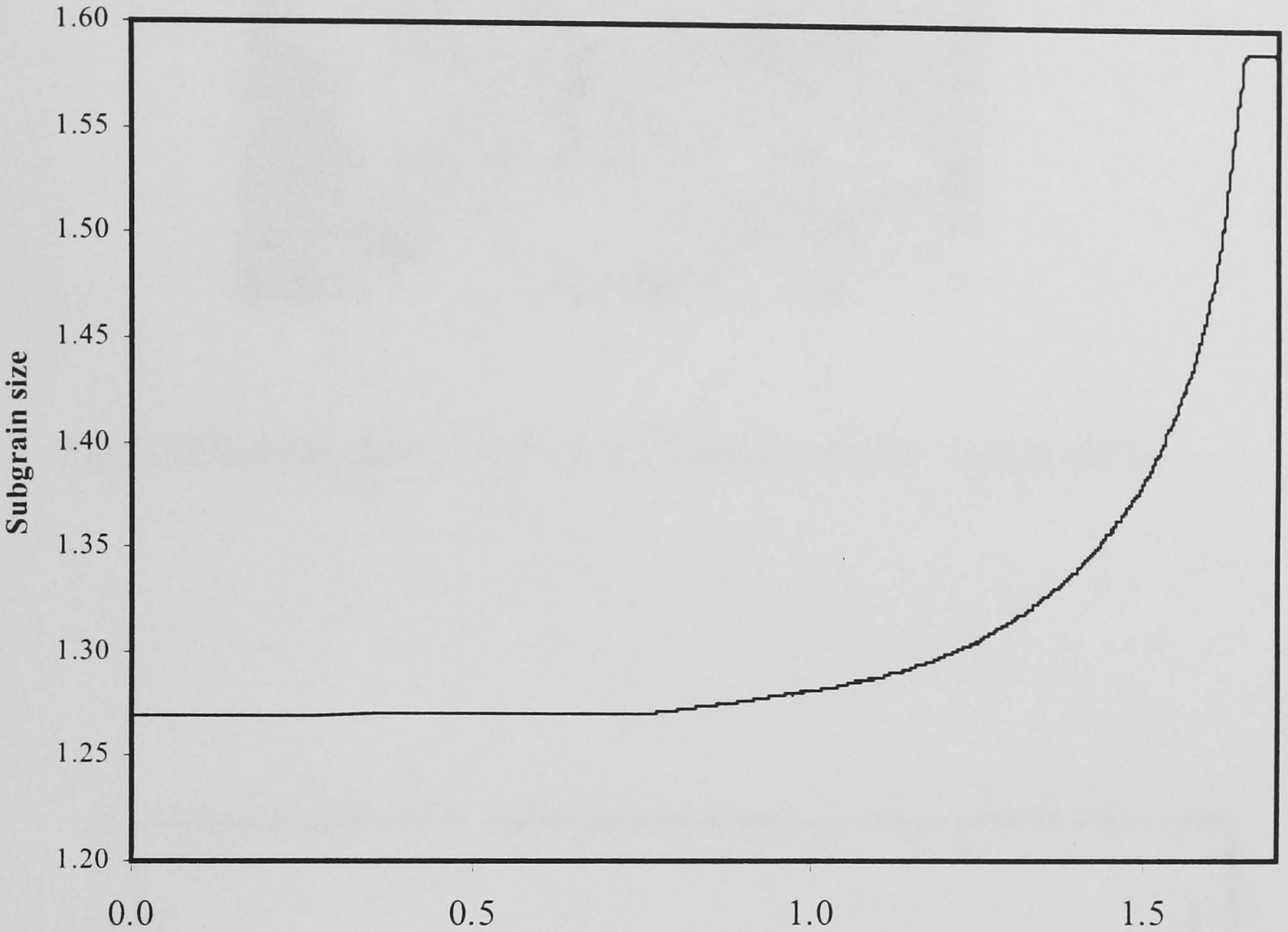

Fig.5-10 Variation of subgrain size with time for point F

Fig.5-11 Substructure observed at point D (After Vierod 1983)

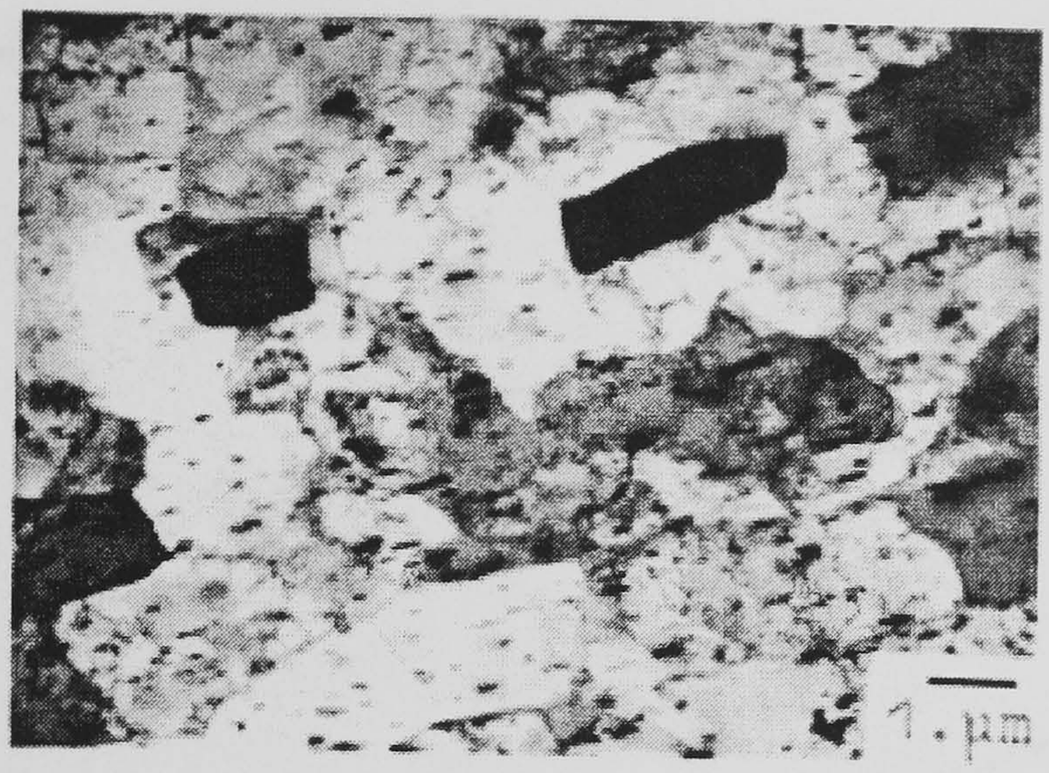

Fig.5-12 Substructure observed at position E (After Vierod 1983)

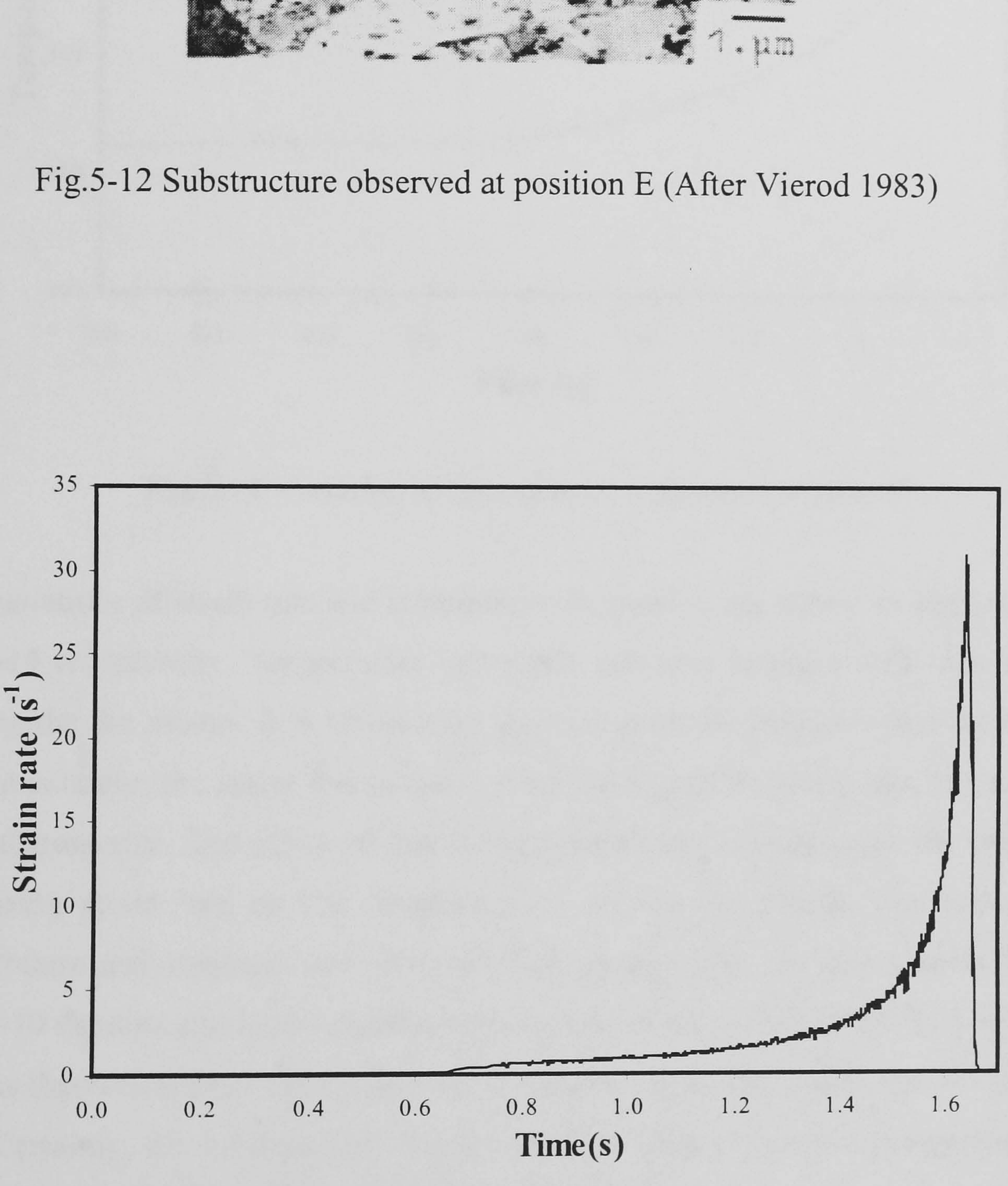

Fig.5-13 Variation of strain rate with time for point F

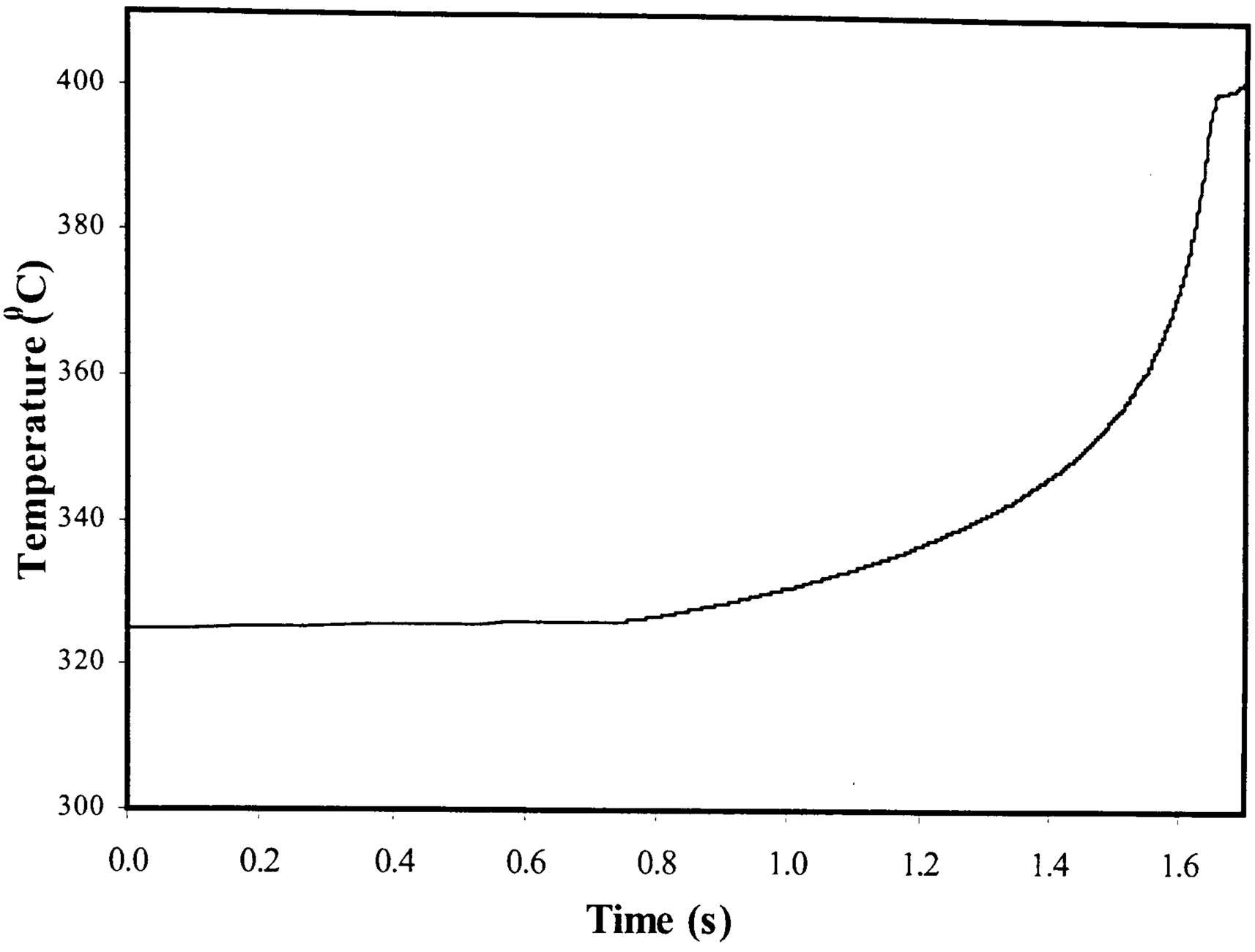

Fig.5-14 Variation of temperature with time for point F

The variations of strain rate and temperature for point F are shown in Fig.5-13 and Fig.5-14 respectively. Temperature and strain rate also increase with time before leaving the die mouth. It is obvious by inspecting all the formulae that the higher the temperature, the larger the subgrain size; the higher the strain rate, the smaller the subgrain size. The effect of increasing temperature complements the effect of increasing strain rate on the subgrain size. At the die mouth, the strain rate, temperature and subgrain size all reach their peaks. Also, the curve presented in Fig. 5-10 exhibits almost the identical shape to the curve presented in Fig.5-14. This implies that temperature must play a dominant role on the determination of subgrain size. Certainly, it's influence would appear to be greater than the precipitates and dispersoids readily identified in Fig.5-11 and Fig.5-12.

The profiles of subgrain size, strain rate, equivalent rate and temperature from point E to point D at the die mouth are shown from Fig.5-15 to Fig.5-18. The predicted

subgrains size at point E and D are 1.57μm and 1.82 μm respectively. The relative errors compared with experimental measurement are 5.4% and 3.2% respectively. The predicted subgrains size for other points are listed in Table18. It is clear that the predicted subgrain size agree well with the measured data.

The strain rate, equivalent strain and temperature at point D are all larger than those at point E, leading to a larger subgrain size at point D. It is interesting to find that there is a sharp growth in the equivalent strain near the die surface due to the strong friction effect (sticking friction condition is assumed in the present simulation). Since the die temperature is 100^0C below the initial billet temperature, there is a strong heat transfer phenomenon between the billet and the die. The combined effects of friction and heat transfer cause approximately 5 ^{0}C temperature rise between points D and E.

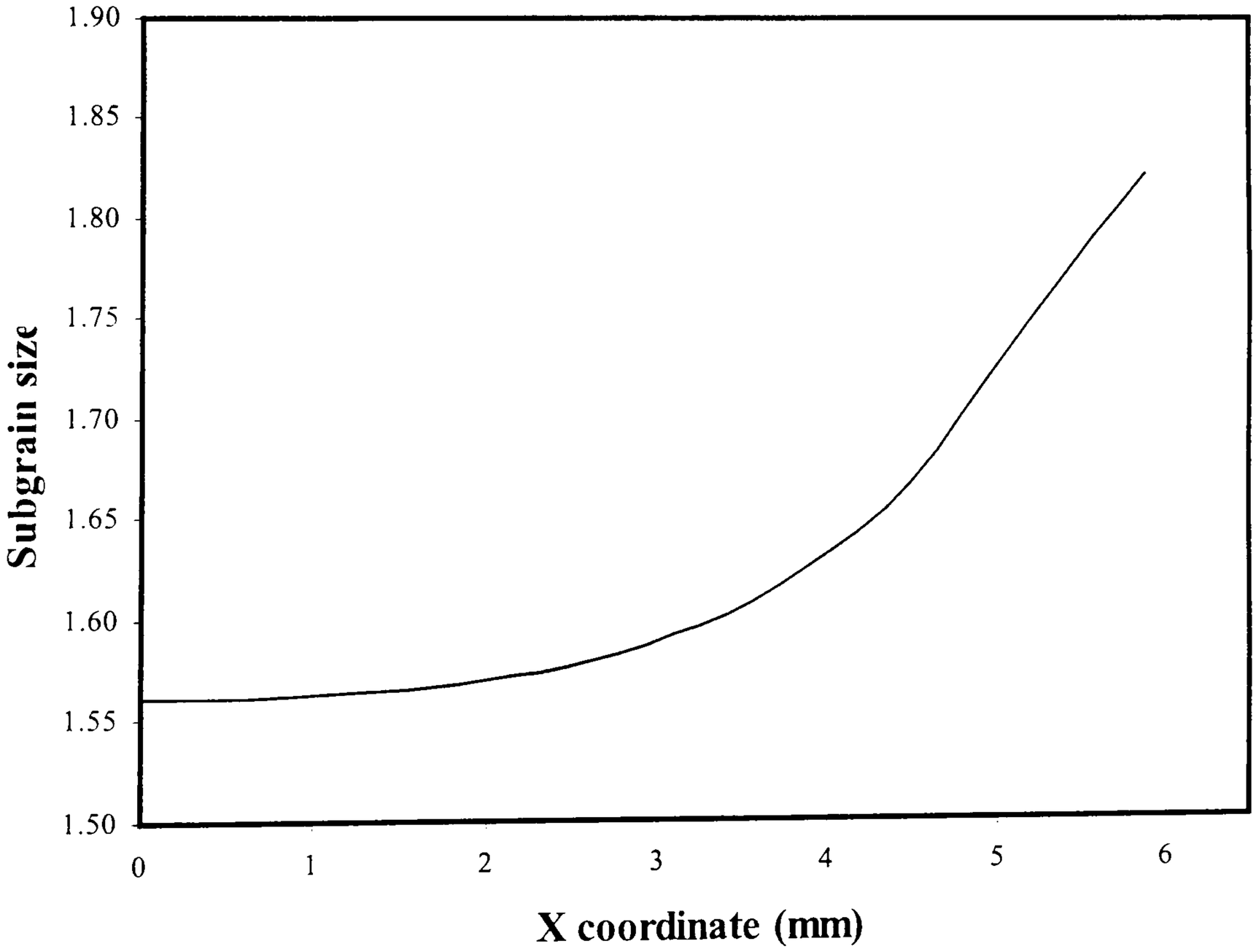

Fig.5-15 Variation of subgrain size along line ED

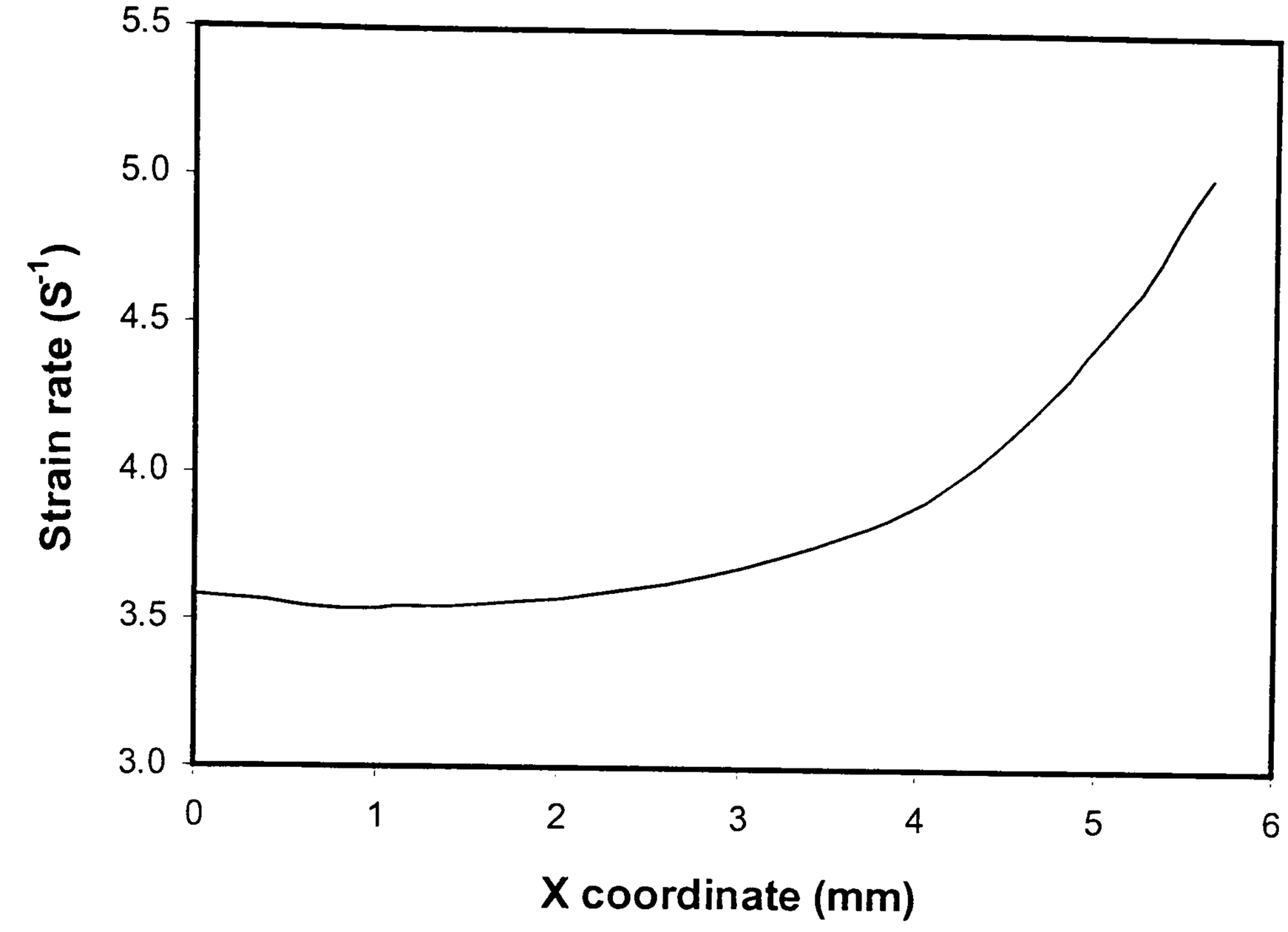

Fig.5-16 Variation of strain rate along line ED

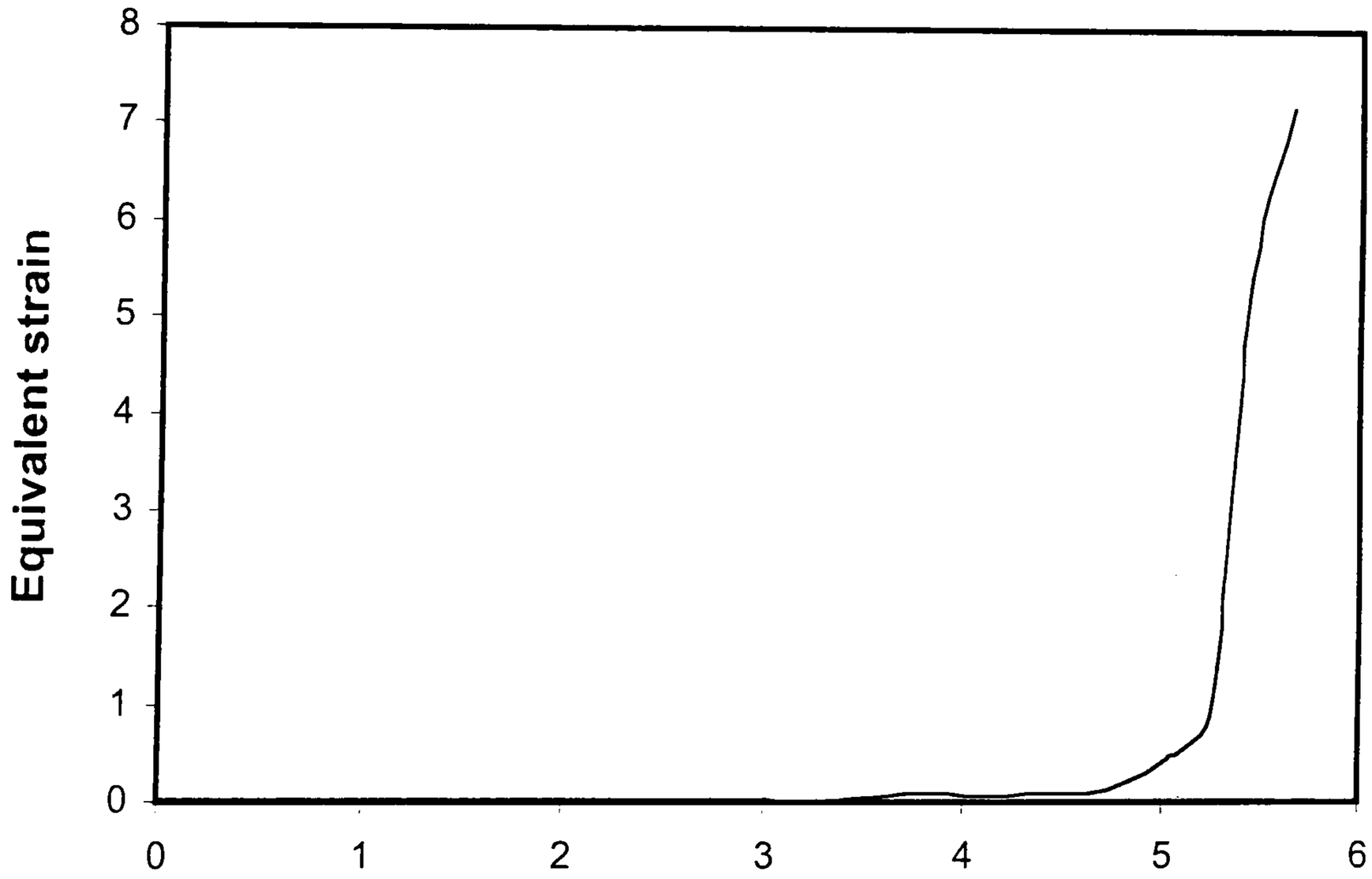

Fig.5-17 Variation of equivalent strain along line ED

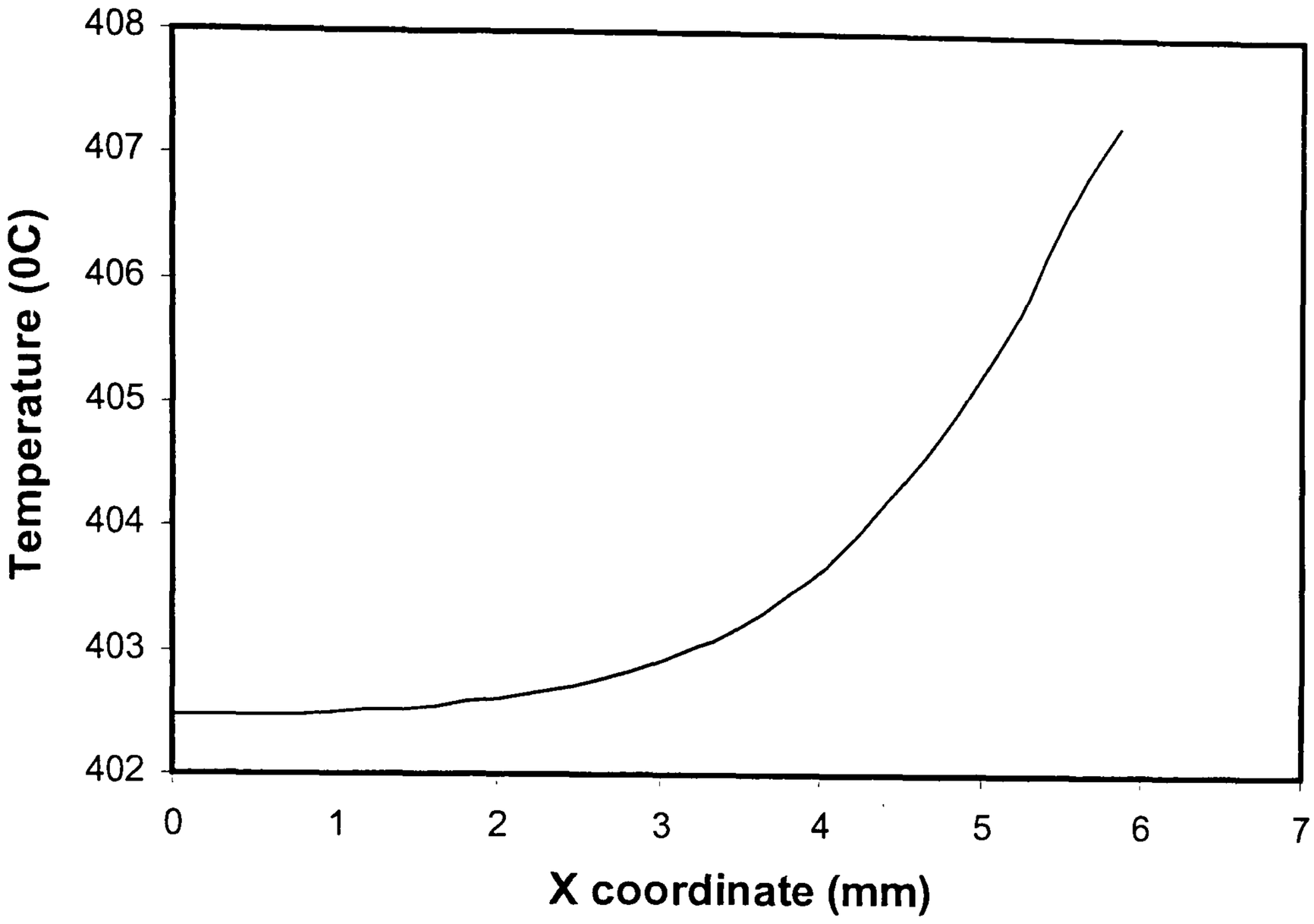

Fig.5-18 Variation of temperature along line ED

Although equation (2-28) gives a good result in the present research, it still is a half-physical model, depending upon strain, strain rate, temperature and previous state of subgrain size. As discussed earlier, the initial subgrain size is the consequence of dislocation movement and interaction. From the point of view of metallurgy, the internal dislocation density should be included or should precede equation (2-28) in the calculation. Most recently, Nes et al (Nes 1998, Marthinsen and Nes 2001) have proposed a model relating subgrain evolution with dislocation density and other metallurgical variables.

When using equation (2-28), there is a parameter which has not been clarified in Furu et al's work (see Fig.2-2). This is the determination of the initial subgrain size. In the present paper, the initial subgrains size, 9μm is extracted from the experimental measurement. Therefore, it is not a problem in this study. Regretfully, experimental work on the measurement of subgrain size from the beginning to the steady state regime is scarce.

As we know, the initial internal dislocation density usually varies from 10^8 to 10^{11} m^{-2}. According to Holt's work (1970), the relationship between internal dislocation density and subgrain size is given as

$$\delta\sqrt{\rho} = K \tag{5-5}$$

For the same K, if ρ varies from 10^8 to 10^{11} m^{-2}, the corresponding maximum value of δ_{max} is about 31.6 times the minimum value of δ_{min}. In the current stage of modelling the evolution of subgrain size, few experimental data are available. The determination of some parameters, i.e. ε_δ, is obtained by tuning to one experimental data set. Therefore, the choice of initial subgrain size will significantly affect the determination of ε_δ, and hence the predicted results of subgrain size.

5.2 Modelling of dislocation density

In this part, the internal dislocation density is computed based on Sellars and Zhu's model (2000). Since the objective of calculating dislocation density and misorientation (discussed in the later section) is to calculate the flow stress, the geometric necessary dislocation density ρ_g is neglected due to its small contribution to the flow stress. Hence, only the random dislocation density is considered and assumed to replace the internal dislocation density. The FE analysis model is the same as that described in section 5.1.

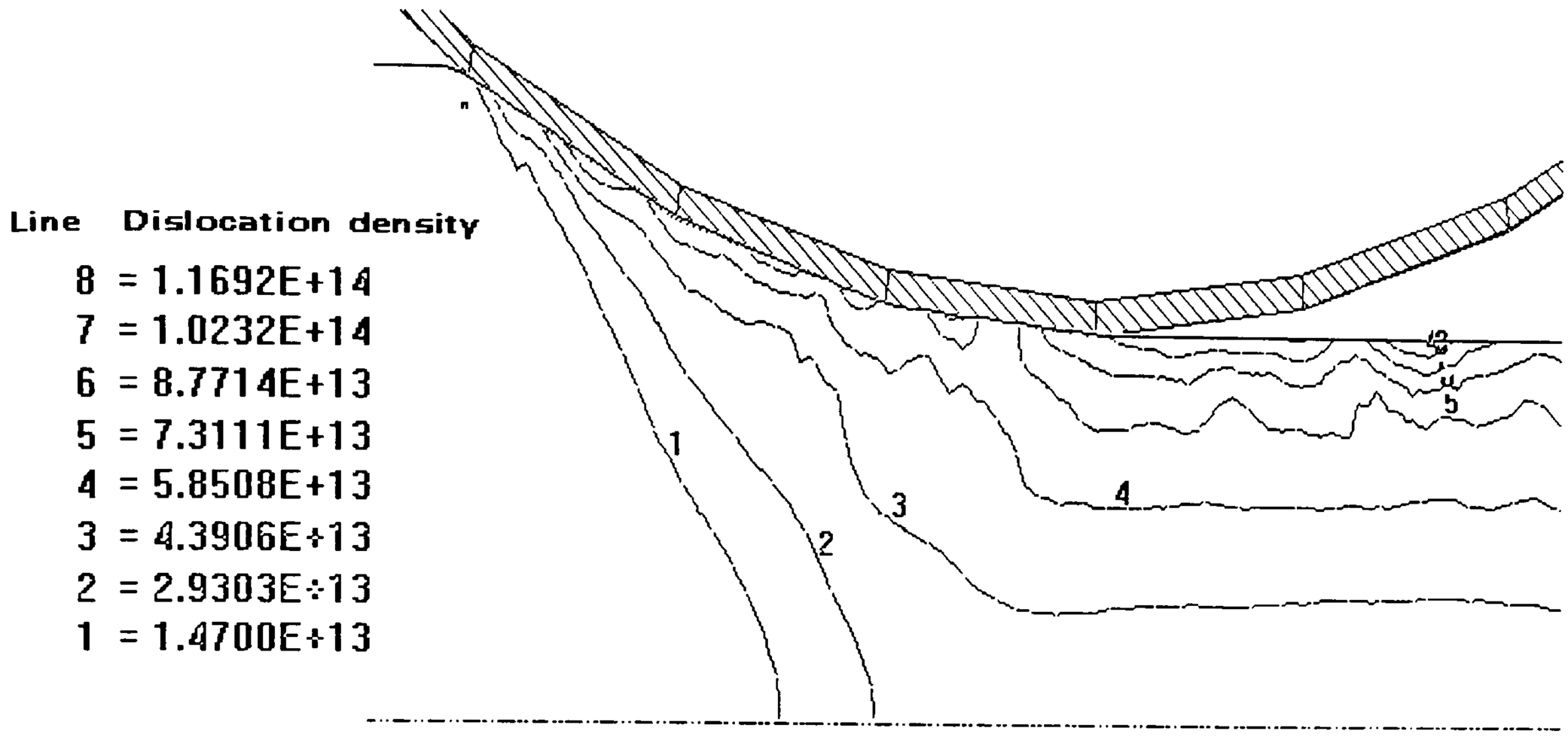

Fig.5-19 Distribution of internal dislocation density

Fig.5-19 shows the distribution of the computed internal dislocation density ρ_i. The maximum dislocation density occurs near the exit in the surface due to the effect of strong shearing since sticking friction is applied in the simulation. To understand the evolution of internal dislocation density, point A (see Fig.5-4) is traced from the beginning of the rolling to the position illustrated in Fig5-4. The variation of ρ_i of point A with the position in the roll gap is shown in Fig.5-20. The initial ρ_i is assumed to be $10^{11}m^{-2}$. It is clear from Fig.5-20 that there is a sharp rise from approximately $10^{11}m^{-2}$ to the peak value of $4\times10^{13}m^{-2}$ within a very short period, and is followed by a slightly decrease caused by dynamic recovery during deformation in the roll gap and static recovery after leaving the roll gap. Unlike subgrain size which remains constant after leaving the roll gap, the random dislocation density decreases since the generation of dislocation density stops due to the cessation of further plastic deformation, while static recovery or static recrystallisation occurs during the interpass time.

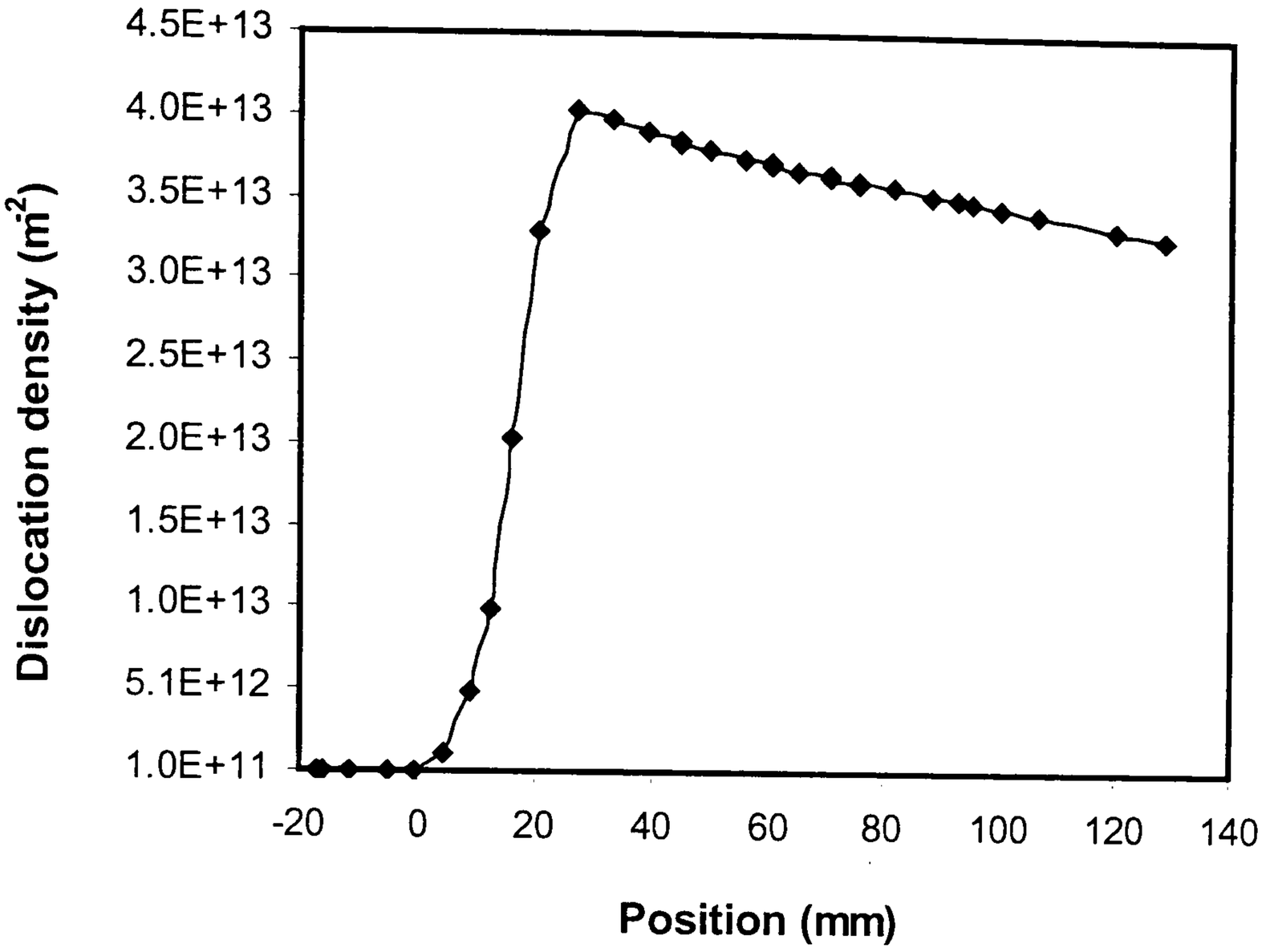

Fig.5-20 Variation of internal dislocation density for point A

The predicted profiles of ρ_i along the thickness at different location (see Fig.5-4) in the roll gap are given in Fig.5-21. We can see that as the workpiece passes through the roll gap, the values of ρ_i rise and the gradients increase due to increasing shear strain. The curves present in Fig.5-21 shows a completely reverse shape to the curve in Fig.5-6. From Fig.5-19 to Fig.5-21, it can be seen that the predictions seem reasonable with common metallurgical observation. Due to the dearth of the measured data in dislocation density, comparison between the measurement and the prediction can not be performed. Once the measured data is obtained, the constants in equation (2-20) need to be tuned to the experimental data set. The tuned model is then applied to predict the dislocation evolution.

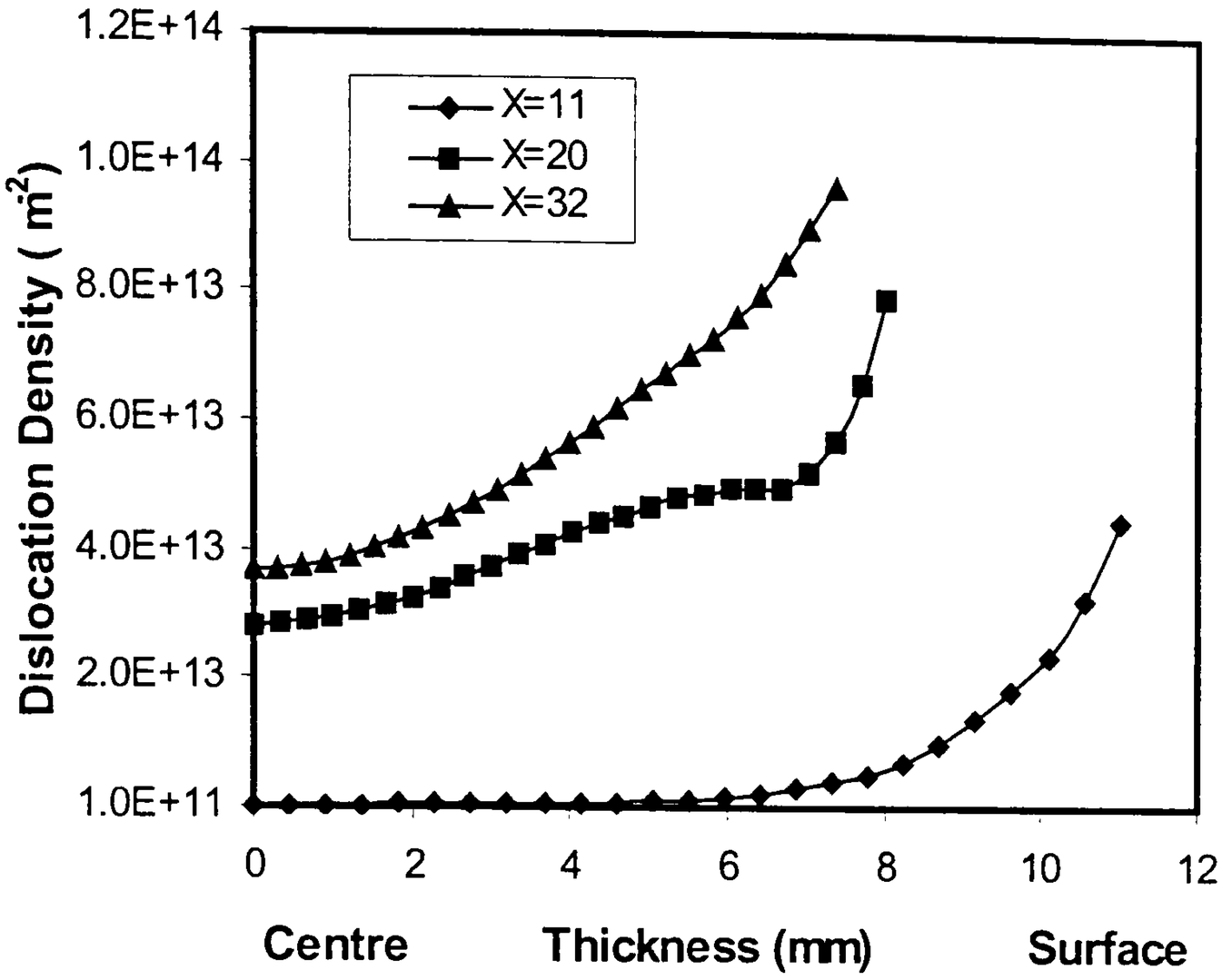

Fig.5-21 Distribution of the ρ_i through the thickness at different locations

5.3 Modelling of misorientation

The predicted distribution of misorientation θ is shown in Fig.5-22. The maximum θ of 3^0 appears at the surface, nearly the same position as that the maximum ρ_i appears. The history of θ for point A is given in Fig.5-23. θ also first remains almost constant, then increases to the peak within a short period and finally reaches a steady value of about 1.9^0. The maximum θ situated at the surface is attributed to the strong effect of shear strains, which contributes more to the equivalent strain than the other strain components, while at the slab centre, little shear strains exist. The relationship between shear strain and the equivalent strain will be detailed in section 5.5.

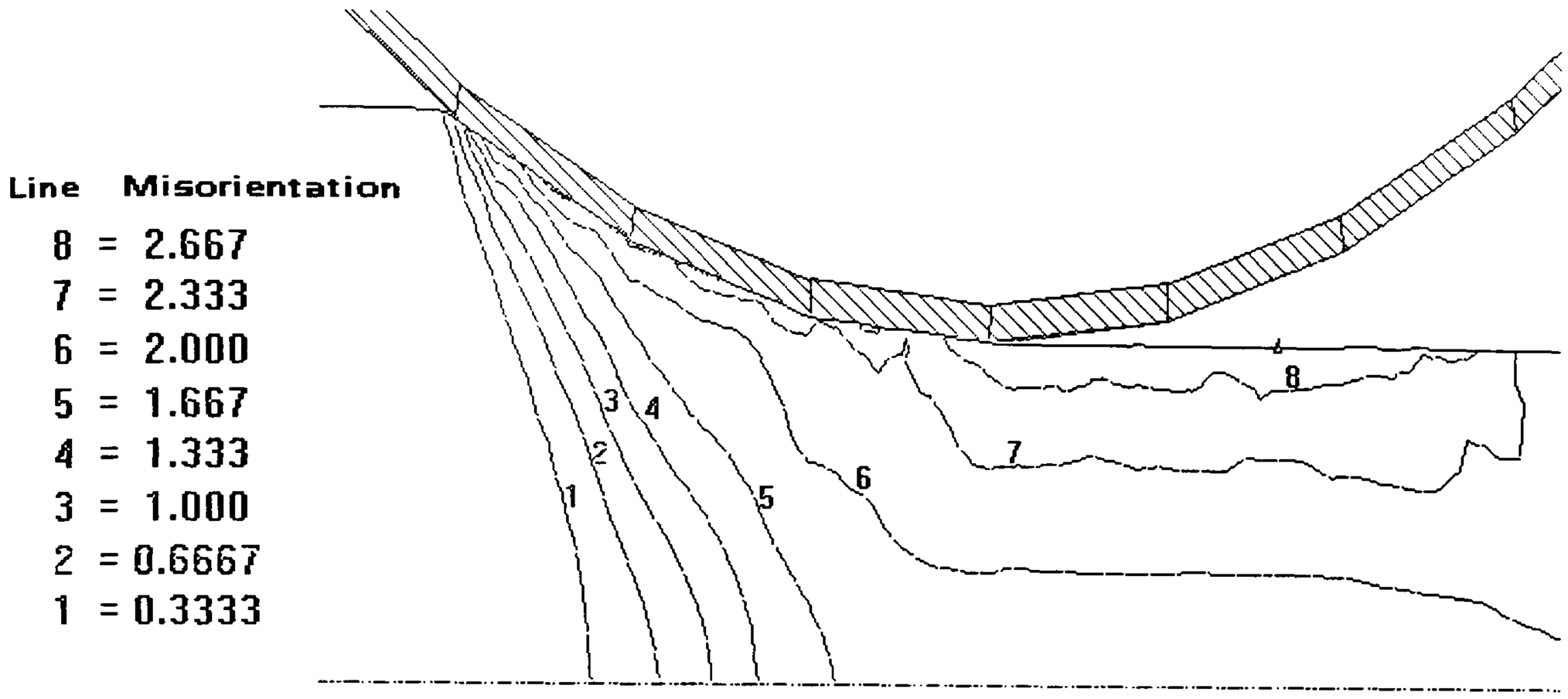

Fig.5-22 Distribution of misorientation

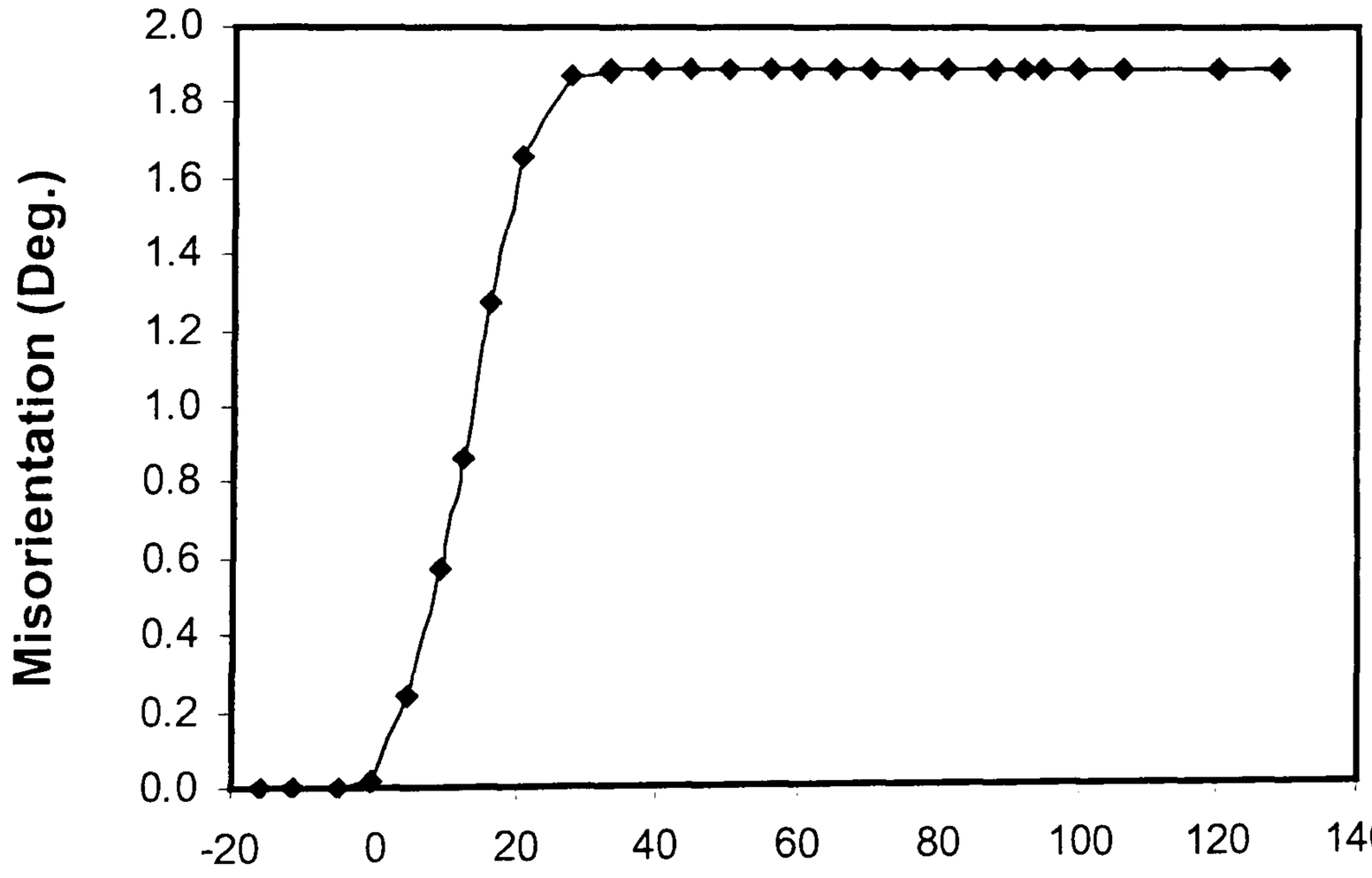

Fig.5-23 Variation of misorientation with time for point A

5.4 Modelling the flow stress based on physical model

The predicted distributions of the flow stress by equation (2-32) and equation (2-33) are shown in Fig.5-24 and Fig.5-25 respectively. Two figures show similar distribution except the magnitudes. Fig.5-24 indicates that the flow stress at the surface is about 4 times higher than the flow stress at the centre. This is caused by two effects: lower temperature at the surface (about 70^0C temperature drop from the surface to the centre, see Fig.4-25) producing a small subgrain size; strong shear strain generating high dislocation density and high misorientation. As discussed in section 4.6, this considerable gradient in the flow stress between the surface and the centre will produce a serious difference, i.e., microstructure, lateral deformation, between laboratory and industrial rolling. Fig.5-24 further confirms the explanation of the difference on the lateral deformation between laboratory rolling and industrial rolling.

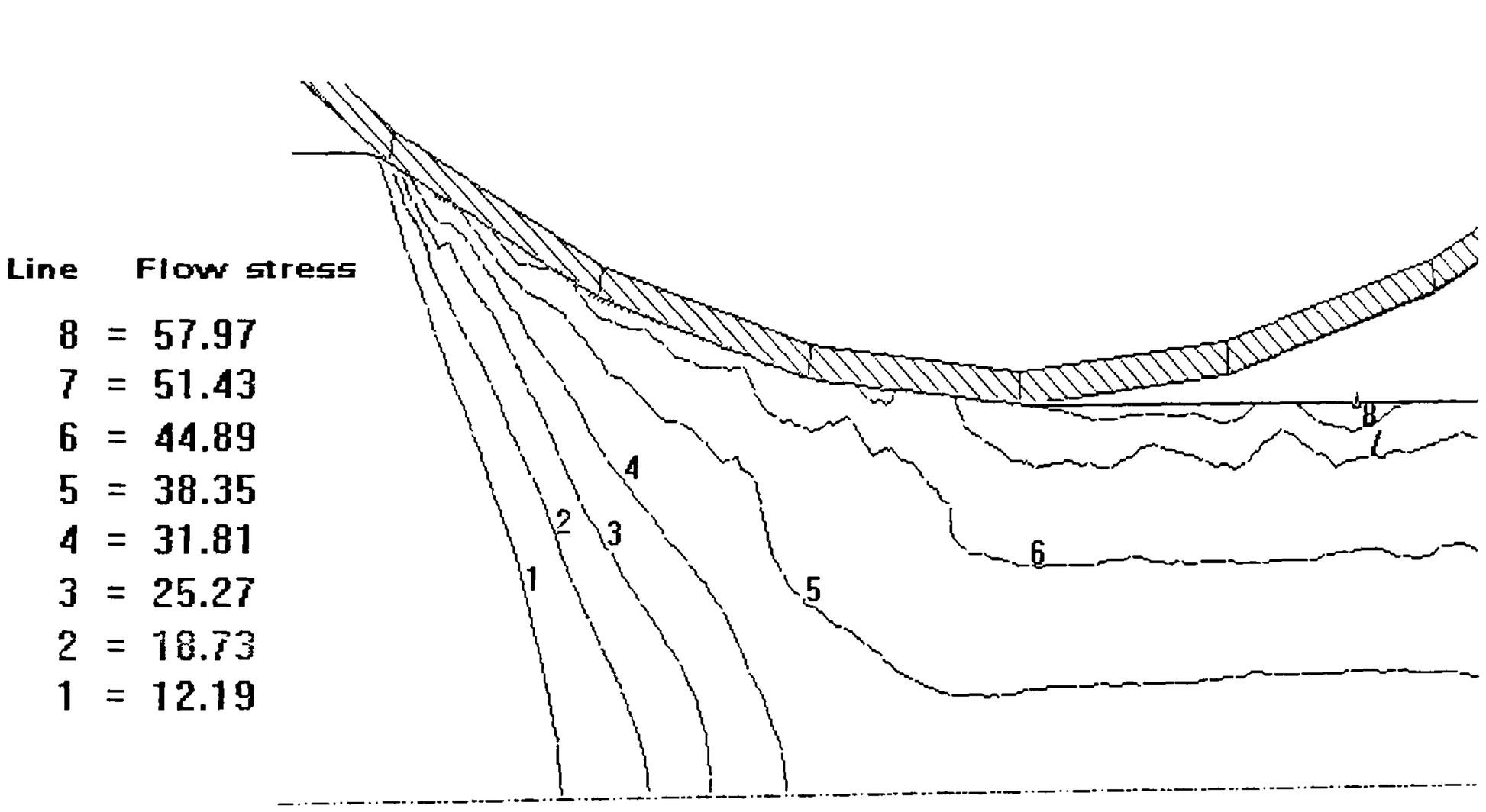

Fig.5-24 Distribution of the flow stress by equation (2-32) in MPa

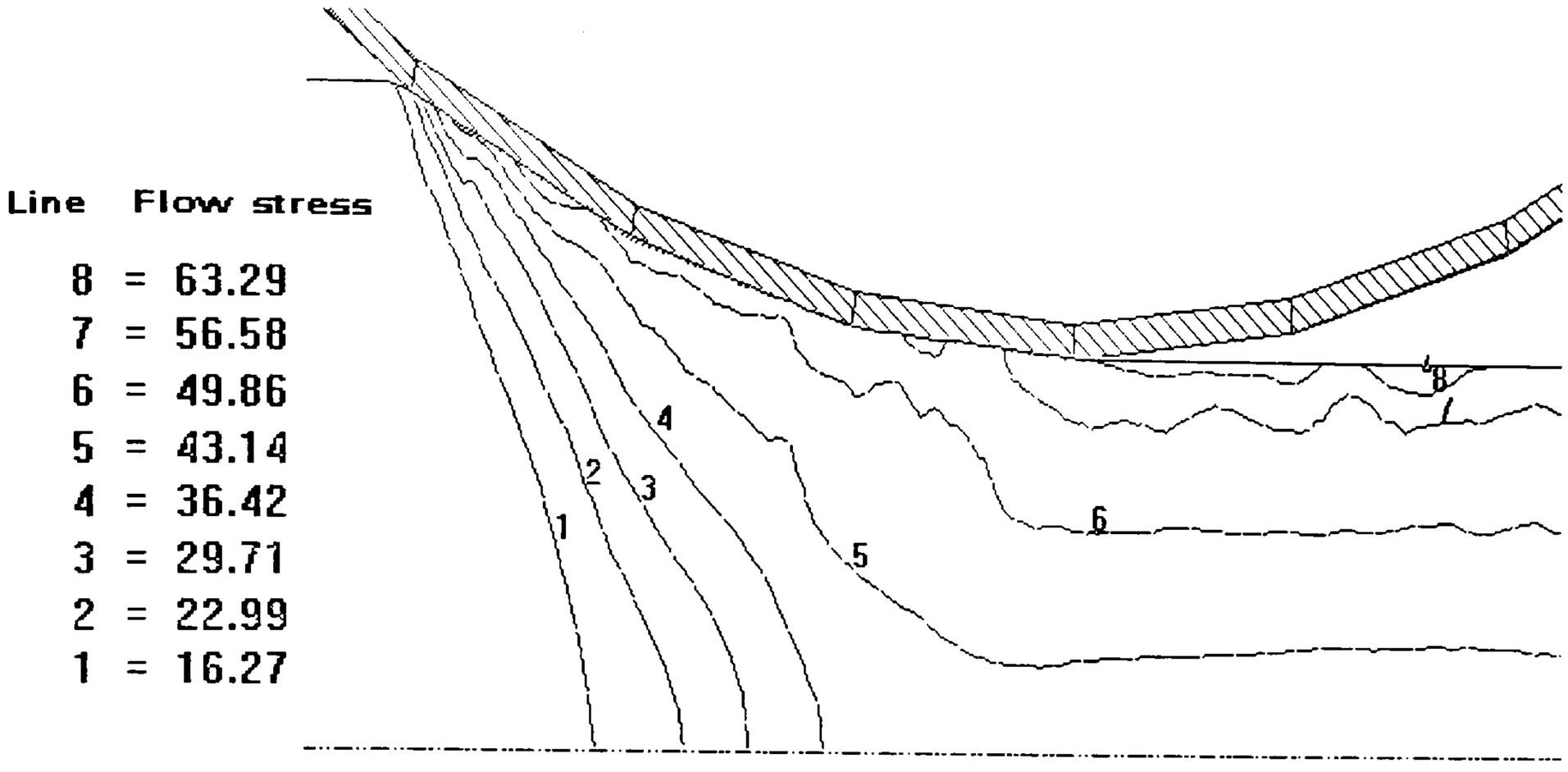

Fig.5-25 Distribution of the flow stress by equation (2-33) in MPa

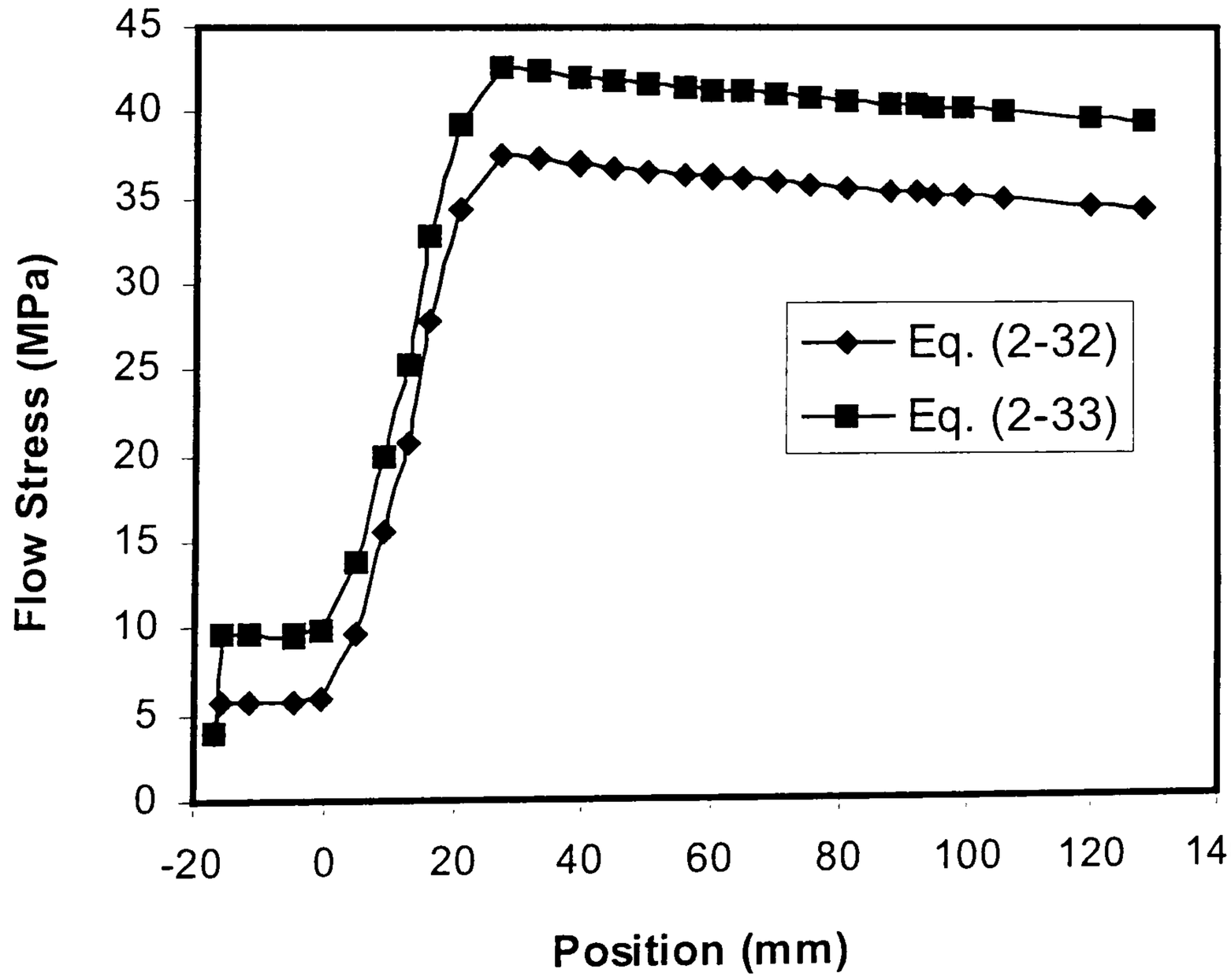

Fig. 5-26 Variation of flow stress for point A computed by different models

The comparison of the histories for point A calculated by equation (2-32) and equation (2-33) is illustrated in Fig.5-26. It is apparent that values computed by equation (2-33) are larger than the values calculated by equation (2-32). Similar results have been given in the literature (Marthinsen and Nes 2001, Nord-Varhaug et al 2000). The difference between two curves is small before the two curves reach the pseudo steady state. The flow stress declines slightly and gradually during the steady state. These curves fit with metallurgical observation. Since dynamic recrystallisation does not usually intervene, the effect of either dynamic or static recovery exert minor effects on the flow stress. The results demonstrate that the prediction is reasonable.

The curves present in Fig.5-26 exhibit almost identical shape to the curve present in Fig.5-14. This implies that dislocation density must contribute more to the determination of the flow stress than subgrain size does. Urcola and Sellars (1987) and Zhu et al (1997) have reached the same conclusion for Al-Mg alloys. However, from Immarigeon and McQueen (1969) et al's observation on substructure for superpurity aluminium rolled after 90% reduction in a single pass (see Fig.5-27 and Fig.5-28), there is little dislocation within the subgrain, especially at high temperature. The strengthening effect by subgrain size should be the major source. The modified Hall-Petch relationship, equation (2-31), should be used for the prediction of the flow stress. Therefore, the conclusion that dislocation density is the major strengthening source should be applied with extreme caution.

When the flow stress is calculated by either equation (2-32) or equation (2-33) in the present study, the values of the constants α_1 and α_2 are chosen as the same as the Nord-Varhaug et al (2001) adopted. Experiment evidences for various aluminium alloys have confirmed the validities of these parameters.

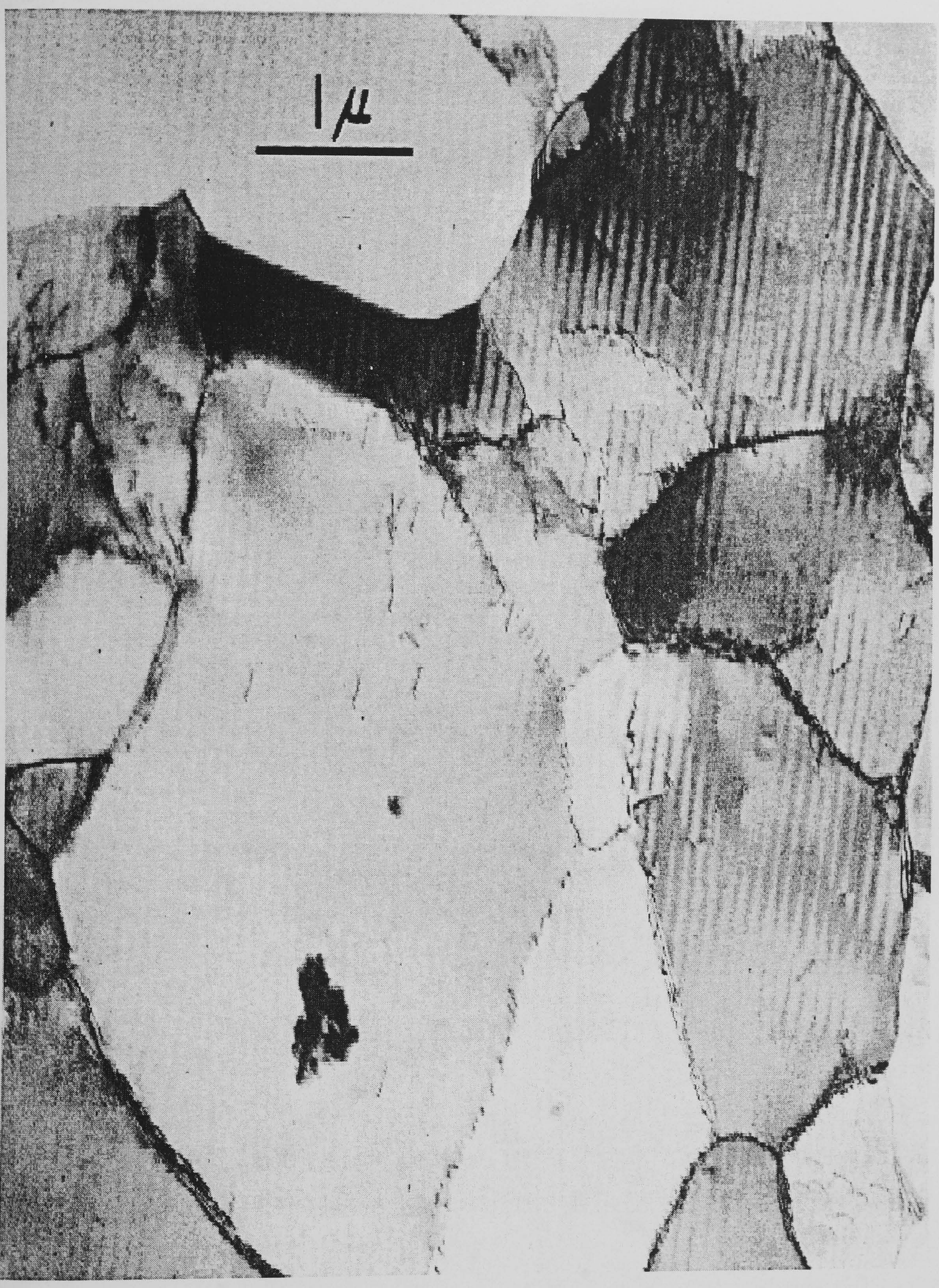

Fig.5-27 Micrograph of superpurity aluminium rolled at 0.55 T_m (After Immarigeon and McQueen 1969)

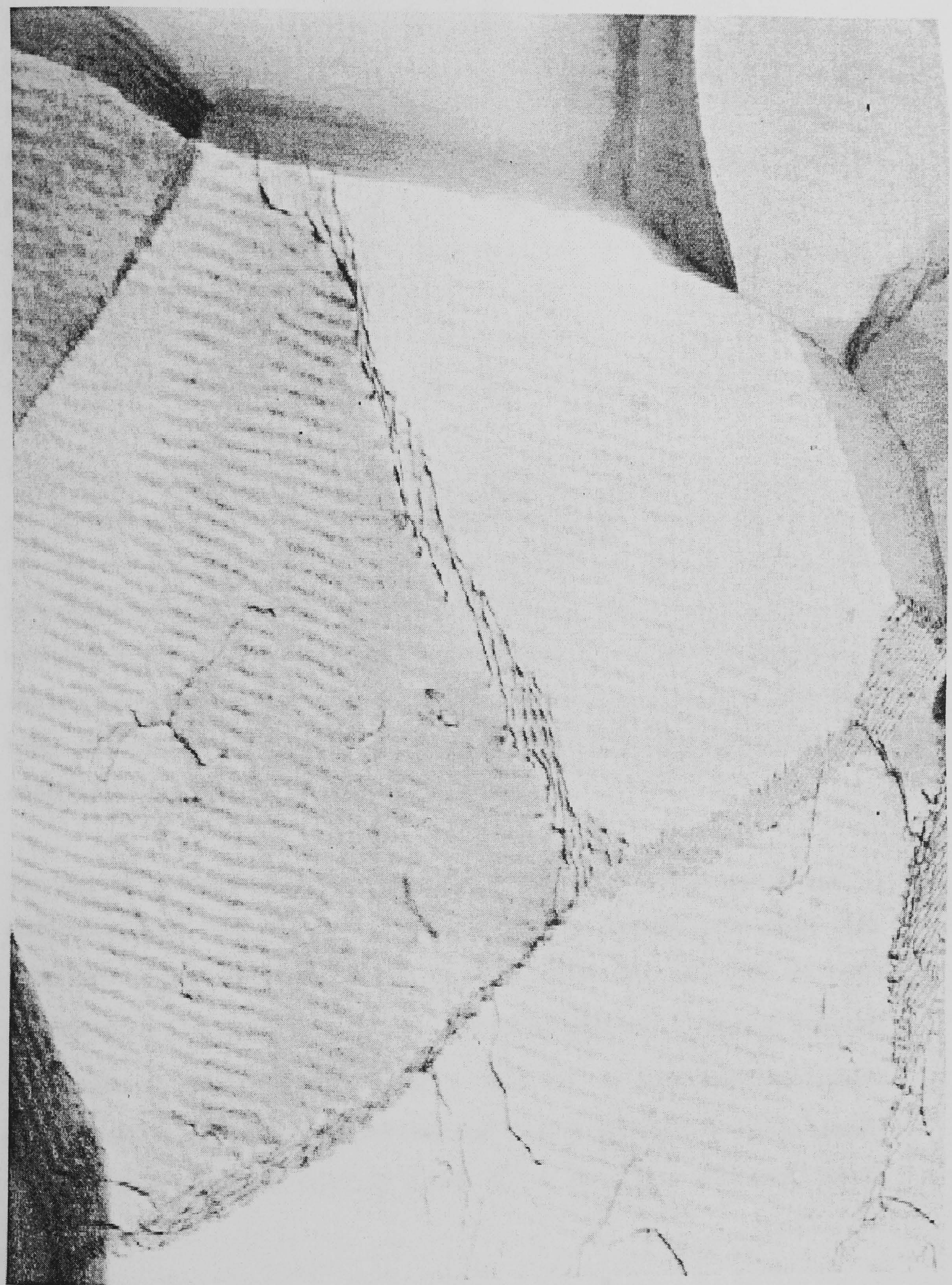

Fig.5-28 Micrograph of superpurity aluminium rolled at 0.65 T_m (After Immarigeon and McQueen 1969)

As a rudimentary study, physical models have been successfully linked with the commercial FEM code. The predicted results, i.e. subgrain size, dislocation density, misorientation and the flow stress, seem reasonable. Further work on the coupling of physical models with commercial program will focus on the validation of the predicted flow stress. A simple way is in simulating the plane strain compression (PSC) process since the macroscopic relationship between the flow stress and strain can be easily determined from PSC. Other work on the coupling between the physical models and the FEM code is feeding back the calculated flow stress in each increment to the invoking FEM code as input for the next increment.

Controlling the distribution of texture is one of the major objectives in the strip rolling of aluminium alloys. Frequent occurrence of static recrystallisation (SRX) after intermediate stages reduce the intensity of the rolling texture and final SRX texture (McQueen and Blum 1998). Due to the complexity, modelling of texture evolution is not ready to lend itself for numerical modelling even though some workers have predicted the texture by FEM. In the near future, modelling the SRX based on physical model is practical and will be helpful for a deeper understanding of SRX behaviour and its influence on the texture.

The rate of recrystallisation is dominated by the total stored energy and its distribution, the availability of nucleation and the holding temperature. The calculation of the total stored energy per unit volume, P_D, is crucial for every physical model. To obtain the value of P_D, the calculation of ρ_g need to be added in addition to the calculation of ρ_r. After P_D is calculated, subsequent recrystallisation kinetics and related reactions such as grain size and cube texture can possibly be predicted, either by Nes et al's model (1994) or Sellars's model (2000).

5.5 Modelling of static recrystallisation

This study is to improve prediction through introducing new approaches for the analysis of the FEM results and using recently proposed SRX models. The analysis model is taken from McLaren's experiment (McLaren 1994). The material, commercial purity aluminium, is rolled with an initial centre temperature of 400^0C in a single stand mill with roll diameter of 68mm. The roll peripheral speed is 0.21m/s. The initial slab thickness is reduced from 50 mm to 38mm. After rolling, the specimen is water quenched. The specimen is annealed at 400^0C, and the fractions recrystallised (X_V) are measured after annealing for 426 seconds. A plane strain deformation model is used to simulate the rolling process because the measurement of the fraction recrystallised was taken at the slab centre. Sticking friction is assumed in the finite element computation. The heat transfer coefficient between the roll and the slab is 25 $kWm^{-2}K^{-1}$. This value was obtained by matching the computed temperature history with the recorded values in the literature (McLaren 1994).

5.5.1 Calculation of equivalent strain

From equation (2-40), it is clear that the mean values of strain and Zener-Hollomon parameter at different through thickness positions are required for the prediction of the local kinetics of static recrystallisation. On the calculation of strain for $t_{0.5}$, four different methods have been proposed by McLaren and Sellars (1993) in summing the strain components. The details of the summation methods are given in the appendix 8. Two definitions of equivalent strain are used in the present study:

Strain 1

$$\bar{\varepsilon} = \int \sqrt{\tfrac{2}{3}} \sqrt{\dot{\varepsilon}_x^2 + \dot{\varepsilon}_y^2 + 2\dot{\varepsilon}_{xy}^2}\, dt \qquad (5\text{-}6)$$

Strain 2

$$\bar{\varepsilon} = \int \sqrt{\tfrac{2}{3}} \sqrt{\dot{\varepsilon}_x^2 + \dot{\varepsilon}_y^2}\, dt \qquad (5\text{-}7)$$

In equation (5-7), the contribution of the shear strain to the total accumulated equivalent strain is ignored. There are two reasons. Firstly, McLaren and Sellars's work (1993) have demonstrated clearly that "accumulated equivalent strains by summing squares of components during deformation may give grossly erroneous results if these strains are applied in equations (2-40) for recrystallisation kinetics. The accumulation of shear strains irrespective of sign appears to be incorrect in regions where significant reversals in the direction of shear occur during rolling". Secondly, when equation (2-40) is regressed from the experimental data, the strain is usually calculated by (Sheppard et al 1986)

$$\varepsilon = Ln \frac{H_f}{H_0} \qquad (5\text{-}8)$$

where H_0 and H_f are the initial and final thickness respectively. The effect of shear strain is not included in equation (5-8).

Dauda and McLaren (1999) adopted another definition of equivalent strain in their study

$$\bar{\varepsilon} = \sqrt{\frac{2}{3} \varepsilon_{ij} \varepsilon_{ij}} \qquad (5\text{-}9)$$

However, extra caution must be taken when using equation (5-9) since it is proposed for small deformations. Hot rolling is typically a large deformation process, except for the first few passes in the hot breakdown rolling. To reduce the possible error introduced by the use of equation (5-9) in FEM, the increments of

time must be set at very small values to ensure a small deformation during each increment.

5.5.2 Calculation of Zener Hollomon parameter

Presently, there are two ways to calculate the value of Z for each node in FEM computation. The first method is simply substituting the nodal strain rate and nodal temperature into equation (2-11) to calculate the history of Z. The Zener-Hollomon parameter calculated by this way is termed "instantaneous Zener-Hollomon parameter", represented by Z_{ins}, in this thesis. The second method is using the averaged strain rate and nodal temperature to derive the value of Z. The Z calculated by this way is termed " averaged Zener-Hollomon parameter", represented by Z_{ave}. The averaged strain rate is obtained by averaging strain rate over the whole deformation zone in each increment during the finite element computation (Chen et al 1992). Adopting such an average strategy is logical since the strain rate in equation (2-11), which is regressed from experimental data, is also a mean value over the whole deformation zone. Thus, in each increment during the finite element computation, all nodes have the same strain rate. The gradient of Z depends upon the gradient of temperature. According to Wells et al's study (Wells et al 1998), temperature plays an overwhelming effect on determining the microstructure when compared with roll speed (strain rate), work roll temperature, and the friction coefficient. Hence, averaging strain rate over the whole deformation is acceptable.

As reported by McLaren & Sellars (1993), the mean value of Z can be obtained by averaging the history of Z on the basis of time or strain. For the Z_{ins}, the averaged value on the basis of increments of time and strain are given in equation (5-10) and (5-11) respectively:

$$(\overline{Z}_{ins})_t = \frac{\sum Z_{ins}\Delta t}{t} \tag{5-10}$$

$$(\overline{Z}_{ins})_\varepsilon = \frac{\sum Z_{ins}\Delta \varepsilon}{\overline{\varepsilon}} \tag{5-11}$$

where Δt and $\Delta \varepsilon$ are time and strain increments respectively, t is the deformation time, $\overline{\varepsilon}$ is the final equivalent strain. For the Z_{ave}, similar definitions are given by:

$$(\overline{Z}_{ave})_t = \frac{\sum Z_{ave}\Delta t}{t} \tag{5-12}$$

$$(\overline{Z}_{ave})_\varepsilon = \frac{\sum Z_{ave}\Delta \varepsilon}{\overline{\varepsilon}} \tag{5-13}$$

5.5.3 Prediction of the fraction recrystallised for commercial purity aluminium

The predicted through thickness variation of the accumulated strains defined in equations (5-6) and (5-7) are shown in Fig. 5-29. These final nodal strains are taken from the FEM output. The lines marked "strain 1" and "strain 2" give the same value at the slab centre, where the effect of shear strain is negligible. From the centre to the surface, the difference between these two curves expands due to increase of shear strain. "Strain 1" rises gradually from the centre to the surface. However, for the line marked "strain 2", there is a steep rise near the surface. "Strain 1" is much greater than "strain 2" at the surface. This implies that there is a large shear strain generated by the contacting friction force.

The computed profiles of $(Z_{ins})_t$ and $(Z_{ave})_t$ are shown in Fig. 5-30. There also exists a significant difference between these two lines in the surface region. The

maximum value appears at the surface, and the value of $(Z_{ins})_t$ is much greater than the value of $(Z_{ave})_t$.

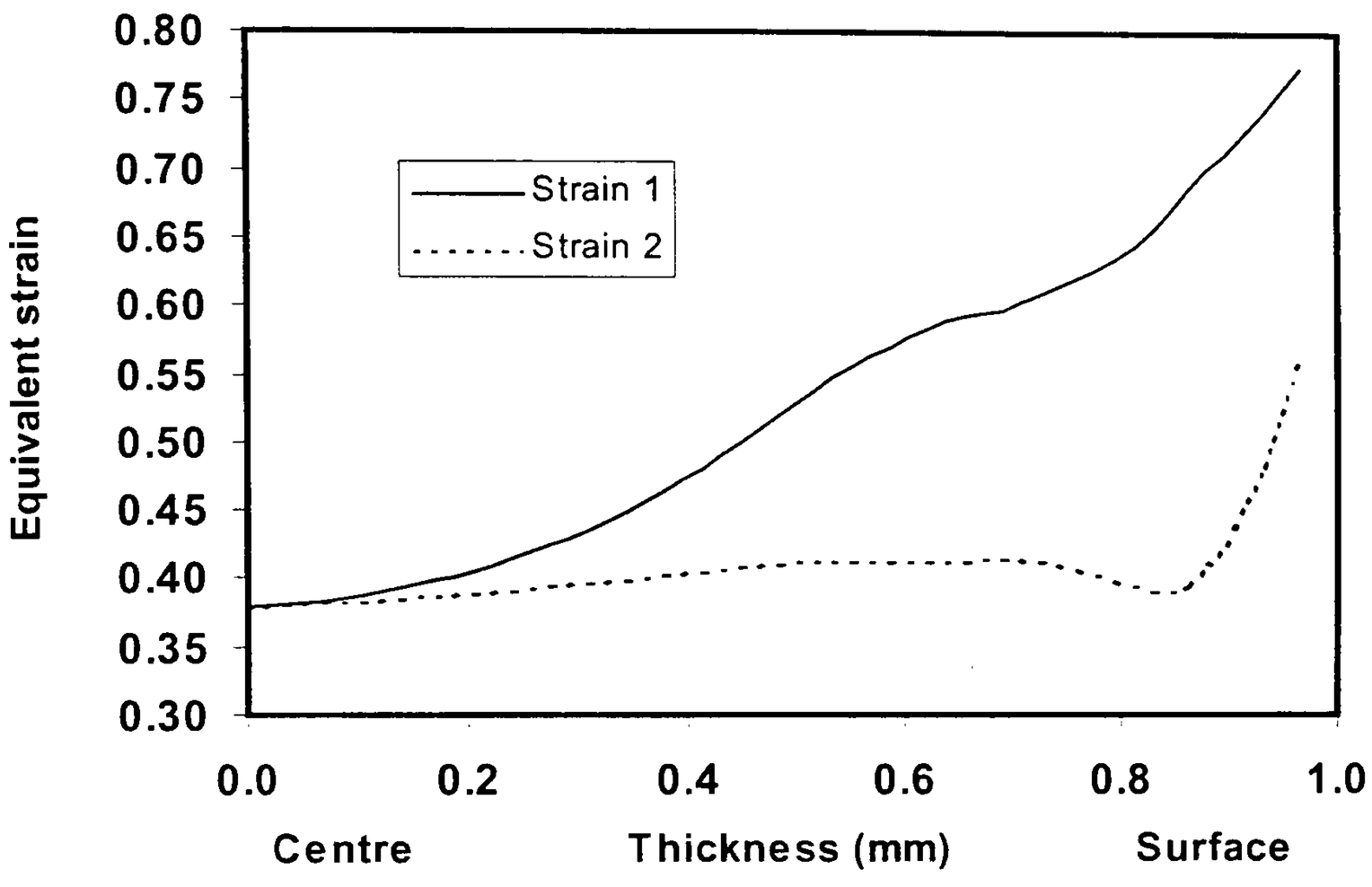

Fig.5-29 Variation of strain throughout the thickness. Strain 1 is defined by equation (5-6); strain 2 is defined by equation (5-7)

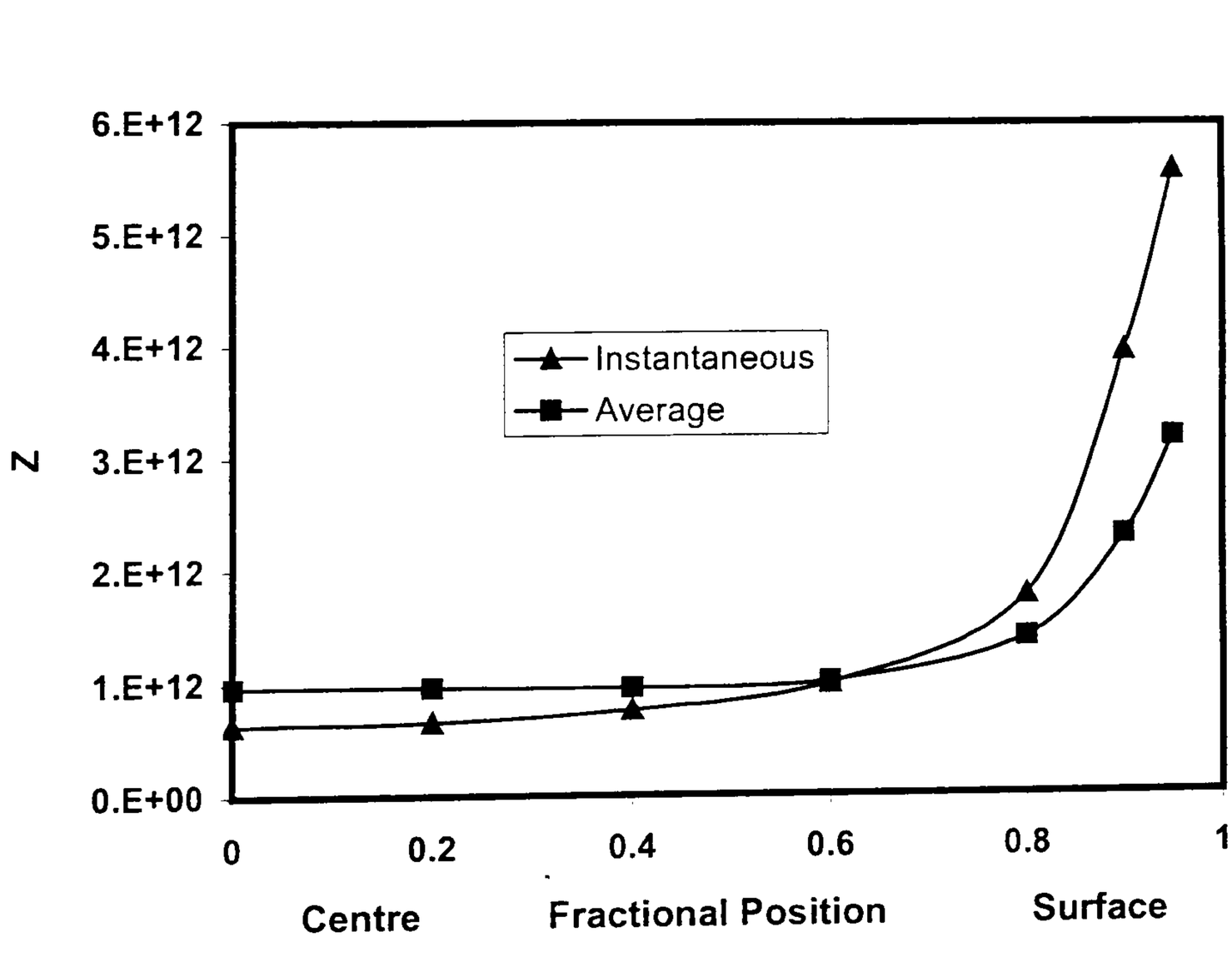

Fig. 5-30 Comparison of the predicted gradients of the Zener-Hollomon through the thickness, $(Z_{ins})_t$ and $(Z_{ave})_t$

In Fig. 5-29 and Fig.5-30, the maximum values of equivalent strain and Z are all located at the surface. Theoretically, the highest rate of recrystallisation should appear at the surface because more stored energy for recrystallisation is produced at the surface due to the low temperature, high strain rate and high strain. The stored energy can be calculated by the following model:

$$P_D = \frac{Gb^2}{10}\left[\rho_i\left(1-\ln\left(10b\rho_i^{1/2}\right)\right)+\frac{2\theta}{b\delta}\left(1+\ln\left(\frac{\theta_c}{\theta}\right)\right)\right] \tag{5-14}$$

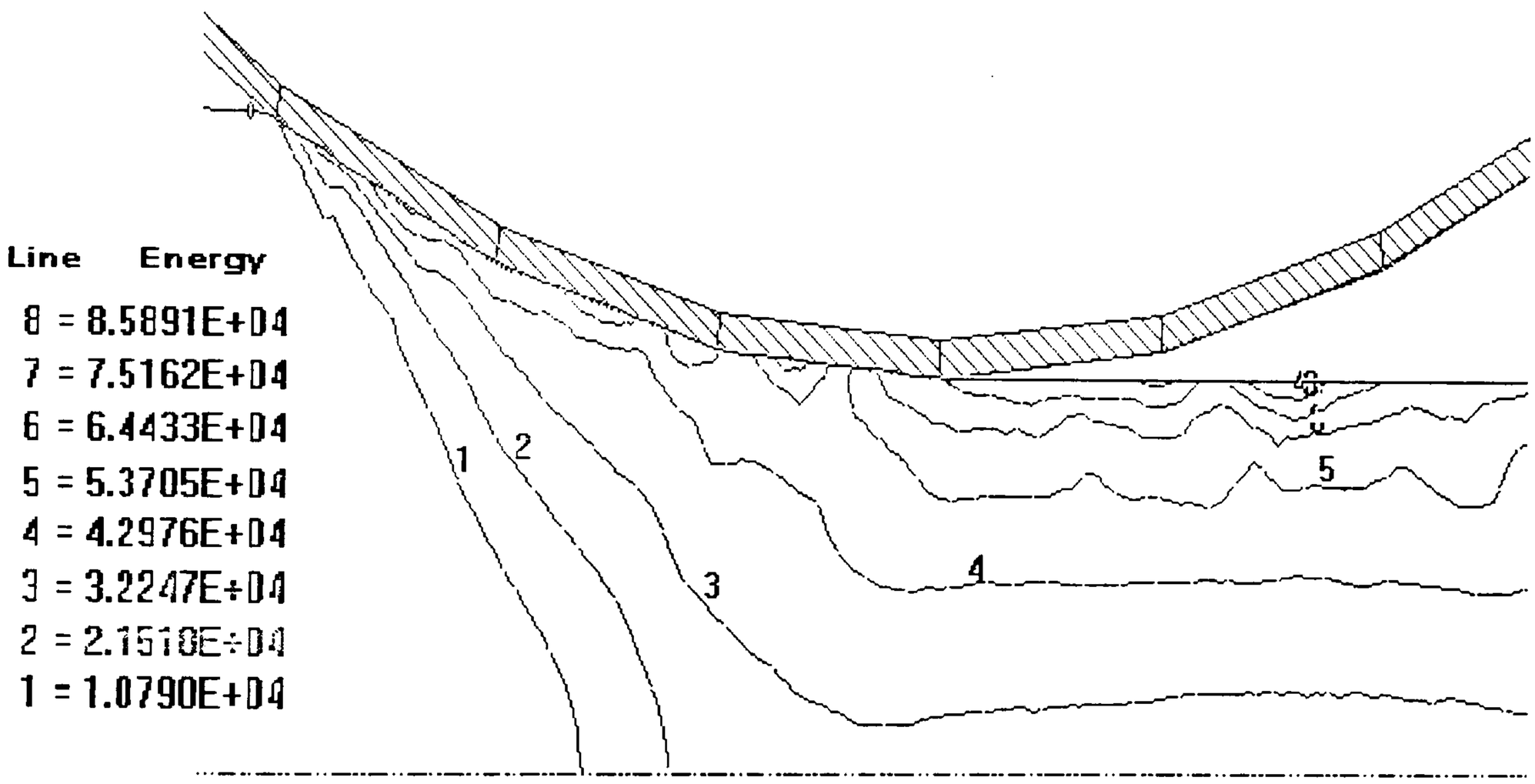

Fig.5-31 Distribution of the computed stored energy in Joules

The prediction of ρ_i, δ and θ by integrating FEM with physical models for hot flat rolling of aluminium alloys have been reported in section 5.1 to 5.3. It should be noted that calculation of ρ_g has been included in the calculation of ρ_i. The variation of $1/R_r$ with strain is taken from the literature (Baxter et al 1999). The predicted distribution of the stored energy is given in Fig.5-31. This results fit well with other researcher's calculation (Hansel and Jensen 1990). It can be seen from

Fig.5-31 that the maximum stored energy appears in the surface region. Whilst the energy decreases from the surface to the centre at exit. Therefore, we have sufficient confidence to say that the ideal fraction recrystallised should fall from the surface to the centre during normal rolling conditions when the roll is not heated intentionally.

In industrial hot rolling, the roll temperature is usually less than 100^0C which is much lower than the stock temperature, generally about 500^0C for the breakdown rolling and greater than 300^0C after tandem rolling. Under such conditions, the chilling effect becomes increasingly significant as the slab get thinner. Therefore it is very difficult to conceive why a small fraction recrystallised is predicted by FEM in the surface region for industrial rolling (Brand et al 1996, Mirza 2001). The only explanation is that the previous modelling results are incorrect.

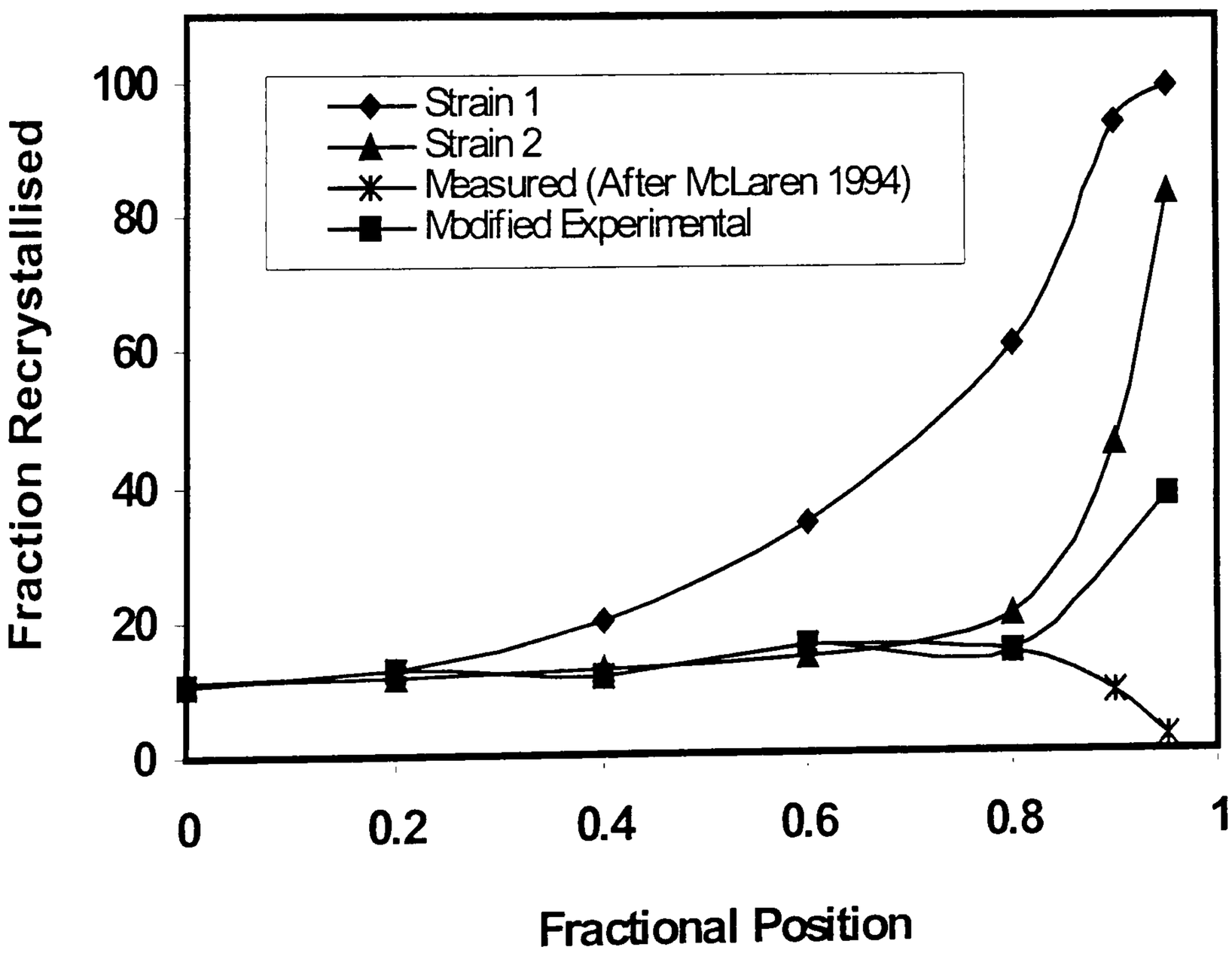

Fig. 5-32 Comparison between the measured and the predicted gradients of the fraction recrystallised by using Gutierrez et al's model with $(Z_{ins})_t$

The measured and calculated through thickness distributions of the fraction recrystallised under the conditions of annealing 426 seconds is compared in Fig.5-32 when Gutierrez et al's model (Guitierrez et al 1988) is applied with $(Z_{ins})_t$. Since the influence of the initial grain size on the kinetics of static recrystallisation is not included, Gutierrez et al's model has to be adjusted for the specific case. Here, Gutierrez et al's model is tuned on the basis of "Strain 1" by matching the predicted fraction recrystallised with the measurement at the slab centre. The tuned Gutierrez et al's model is expressed as

$$t_{0.5} = 1.45\times10^{-6}\varepsilon^{-1.5}Z^{-0.75}\exp\left(\frac{220000}{RT_a}\right) \tag{5-15}$$

This tuned equation is then applied for "strain 2". It is clear from Fig.5-32 that, the measured fraction recrystallised drops to a very low value at the surface, whereas the predicted lines give fast recrystallisation in the surface region. Although the influence of shear strain is deleted from "strain 2", the prediction is far from satisfactory. This demonstrates that changing the definition of equivalent strain does not succeed much in reducing the prediction of $X_{1'}$ in the surface region. The comparison between McLaren's measurement and the present prediction can not be considered because it is clear that some experimental error has occurred. These results must therefore be excluded when evaluating SRX.

The three reported single pass rolling conditions and measurements are shown in Table 19. It is clear that Yiu et al's experiment (Yiu et al 1990) is more practical than the other two experiments in terms of roll diameter, roll speed and rolling temperature. Comparing Dauda & McLaren's and Yiu et al's experiments, it can be seen that the fraction recrystallised increases with increase of the percent of Mg and increase of reduction. It is generally recognised that the number of nucleation sites and the stored energy are key for the occurrence of static recrystallisation. The

number of nucleation sites depends upon the precipitates, which are determined by the alloying elements and the substructure which is also a function of the alloy. In general, alloying elements tend to reduce the activation energy, making the movement of dislocations more difficult during deformation. The less the movement of dislocations, the more difficult it is for the occurrence of recovery and the easier it is for the occurrence of recrystallisation. The more reduction, the more stored energy becomes. From the above analyses, we can conclude that, in McLaren's measurement, the maximum fraction recrystallised at the surface should not exceed 39.2% and the maximum fraction recrystallised at the centre should be less than 4.5%. But McLaren reported a larger measurement at the centre and a smaller measurement at the surface than the other two measurements. Therefore we can say there is greater error in McLaren's measurement. If we assume that the measurements at the fractional position of 0, 0.2, 0.4, 0.6 and 0.8 are correct, and plus the possible maximum fraction recrystallised, 39.2%, at the surface, we can draw a "Modified Experimental" curve for McLaren's experiment, see Fig.5-32. There are two reasons to assume such a curve. Firstly, the purpose of this section is how to accurately predict at the surface. The most important point is that we know the maximum fraction recrystallised should be less than 39.2%. Secondly, all empirical models need to be tuned to the measurement at the centre.

Table 19 Comparison of the rolling conditions and measurement

	McLaren	Dauda & McLaren	Yiu et al
Roll diameter	68mm	89mm	368mm
Rolling temperature	400^{0}C	400^{0}C	460^{0}C
Relative reduction	24%	30%	48%
Roll peripheral speed	210mm/s	200mm/s	385mm/s
% Mg in the alloy	<0.001	3	4.45 in Fig.2-6a
Measured fraction	10.7%	~3%	~4.5% in Fig.2-6a
Measured fraction	2.3%	~15%	~39.2% in Fig.2-6a

In the following parts, all predictions are compared with this "modified experimental " curve not the measurement. Comparing the curves "Strain 1" and "Strain 2" in Fig.5-32, it can be seen that "strain 2" shows a better agreement with the theoretical curve than "Strain 1". But this kind of changing the definition of equivalent strain is not convincing.

Fig.5-33 shows the comparison on prediction by using $(Z_{ins})_t$ and $(Z_{ins})_\varepsilon$. The symbol "Strain 1-time" indicates that the corresponding curve is calculated by "strain 1" and $(Z_{ins})_t$. The symbol "Strain 2-strain" indicates that the corresponding curve is calculated by "strain 2" and $(Z_{ins})_\varepsilon$. It can be seen that averaging Z on the basis of strain appears to give a better prediction than that by averaging with time for both "strain 1" and "strain 2". This conclusion was also confirmed by Dauda and McLaren (1999). In the following computations, all Z, either Z_{ins} or Z_{ave}, are averaged with increments of strain.

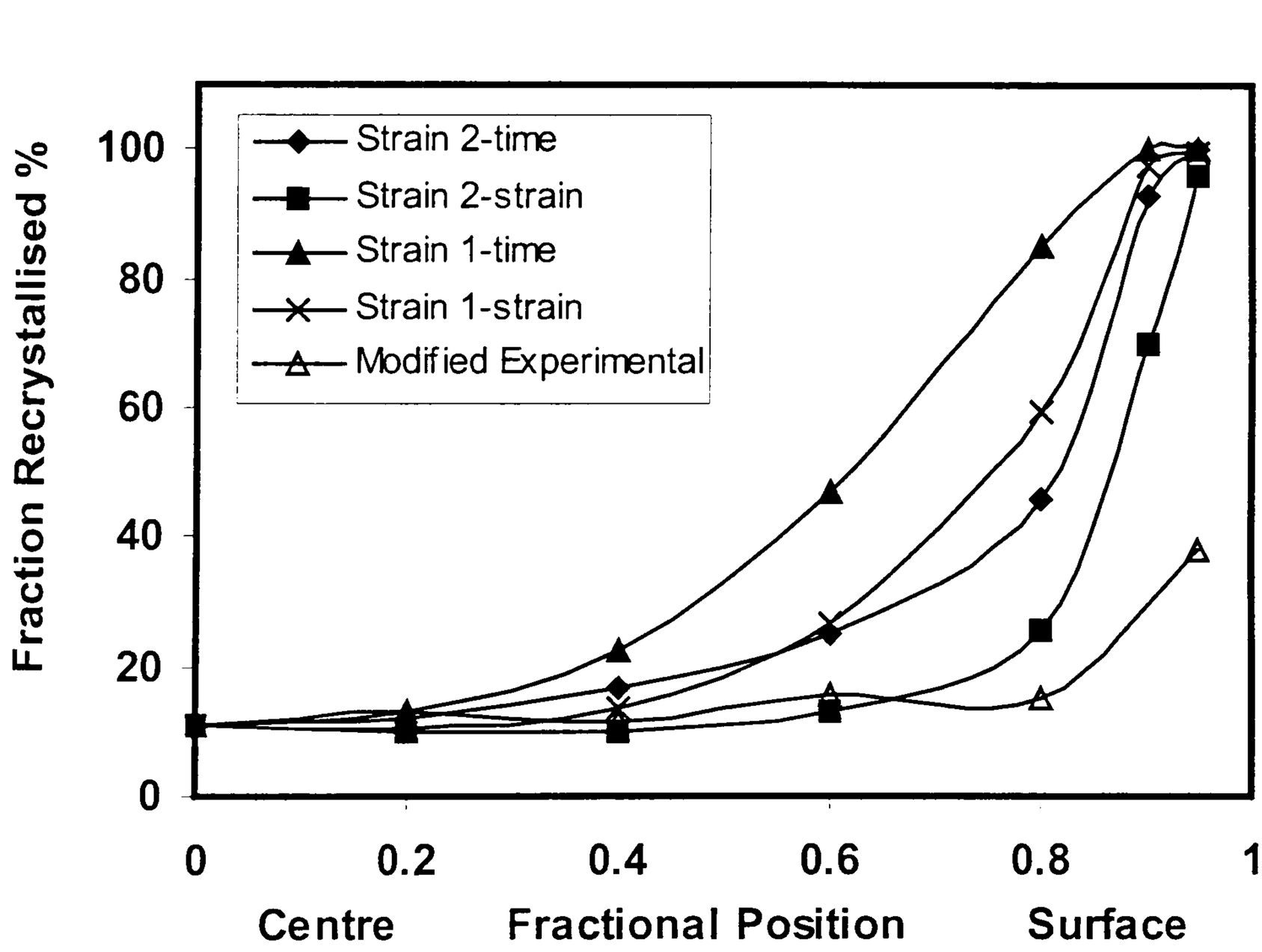

Fig.5-33 Comparison of the predicted profiles by using between $(Z_{ins})_t$ and $(Z_{ins})_\varepsilon$

All curves in Fig.5-33 still possibly overpredict the fraction recrystallised within the surface area. An alternative method to improve the prediction is a recently developed model-- Liserre and Goncalves's model (Liserre and Goncalves 1998). This model was modified from Gutierrez et al's model for commercial purity aluminium. Liserre and Goncalves's model is adjusted to "strain 1" at the centre. The computed results are shown in Fig.5-34. Unexpectedly, this model gives an irregular distribution of the fraction recrystallised through the thickness because the calculated values of $t_{0.5}$ is negative for some points on the lines. The error is introduced by the term "–6924" (See appendix). Apparently, Liserre and Goncalves's model is basically in error.

Another method to decrease the difference between the prediction and the theoretical distribution is in modifying the mode of calculation for Z. "Averaged Zener-Hollomon parameter", Z_{ave}, will be applied. Fig.5-35 shows the predicted profiles by using Gutierrez et al's model. Clearly, using Z_{ave} significantly improves the prediction for both strains.

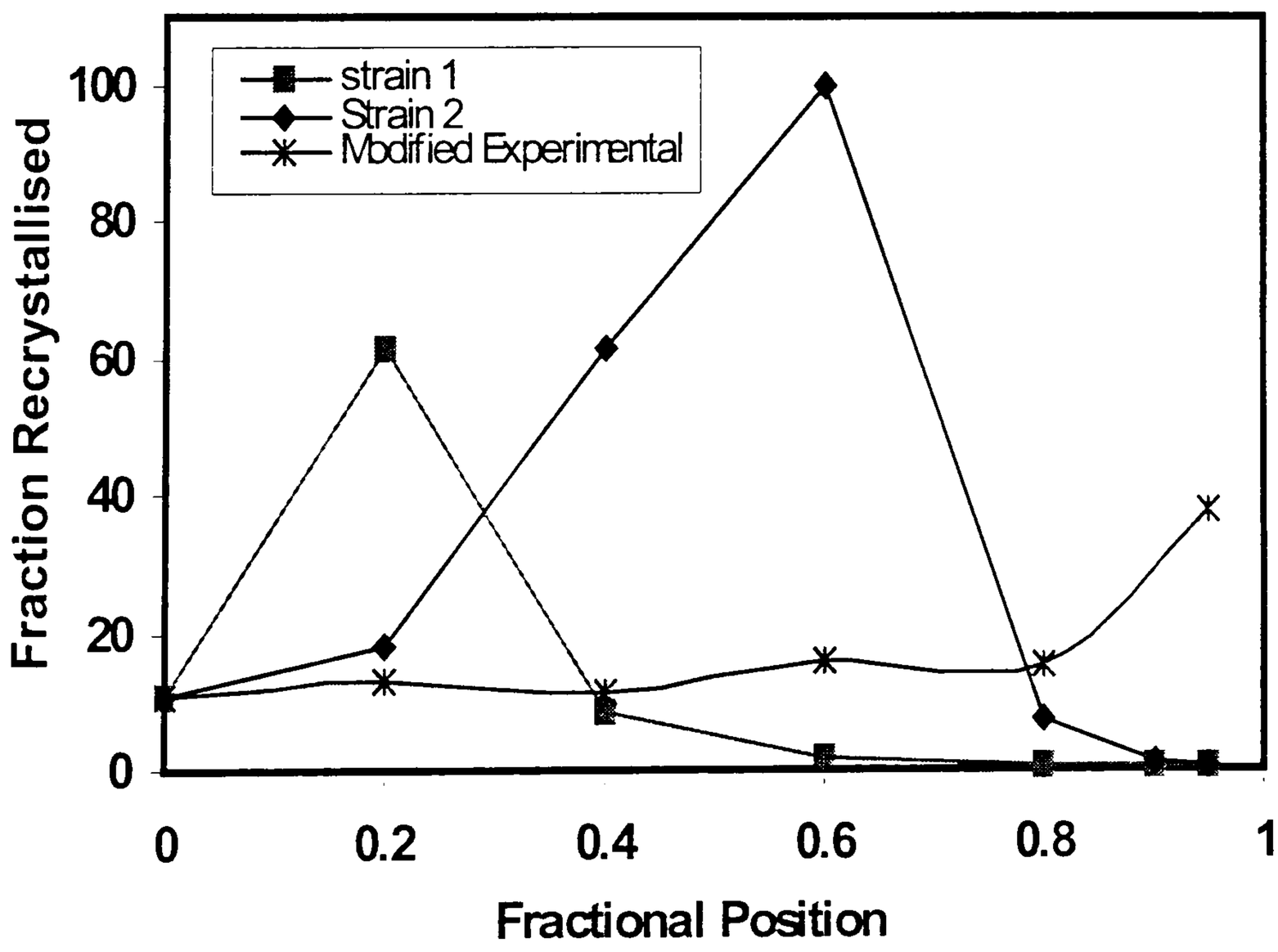

Fig. 5-34 Comparison between the measured and predicted gradients of the fraction recrystallised by using Liserre et al's model with $(Z_{ins})_{\varepsilon}$

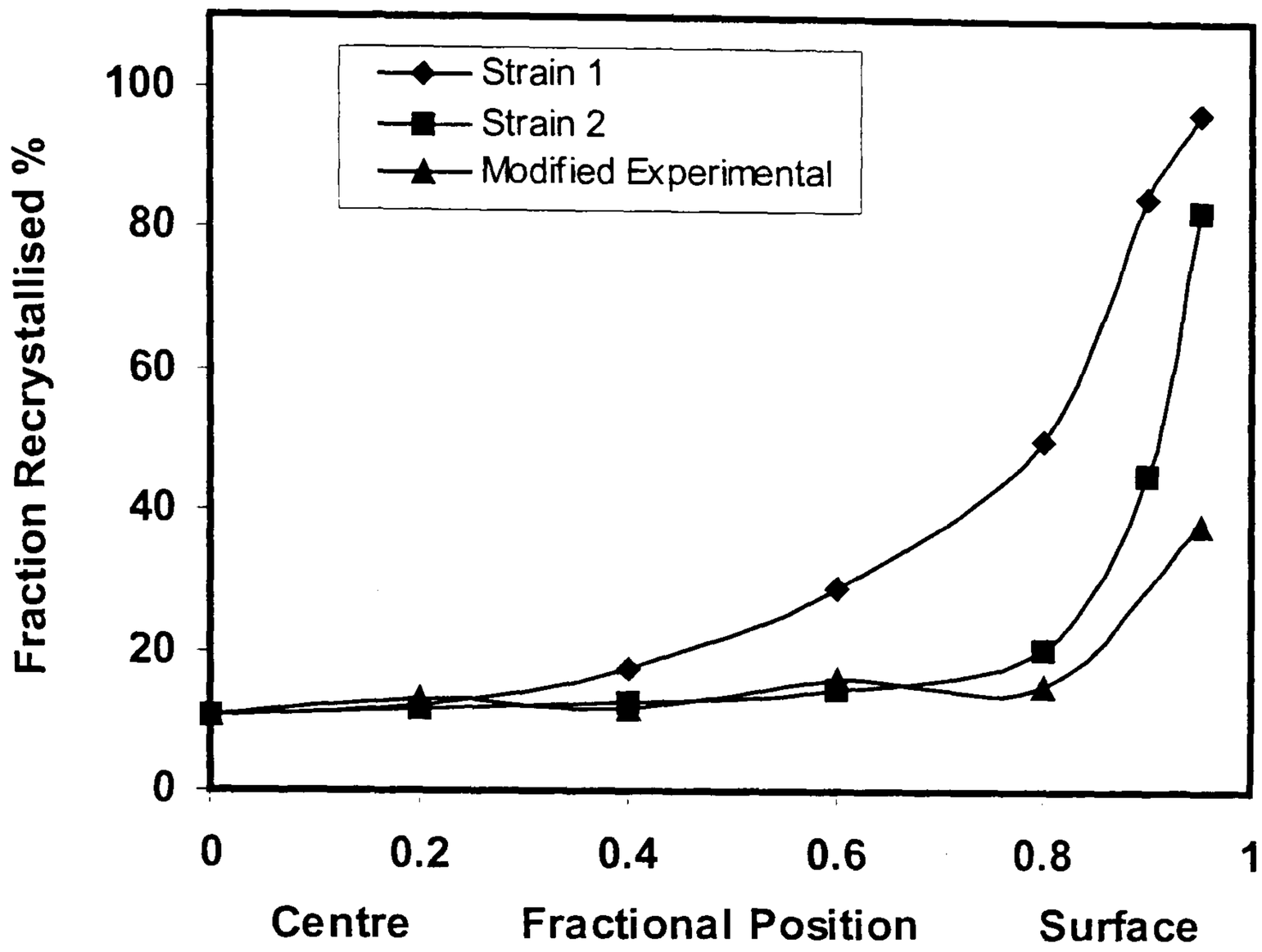

Fig. 5-35 Comparison between the measured and predicted gradients in the recrystallised fraction by using Gutierrez et al's model with $(Z_{ave})_{\varepsilon}$

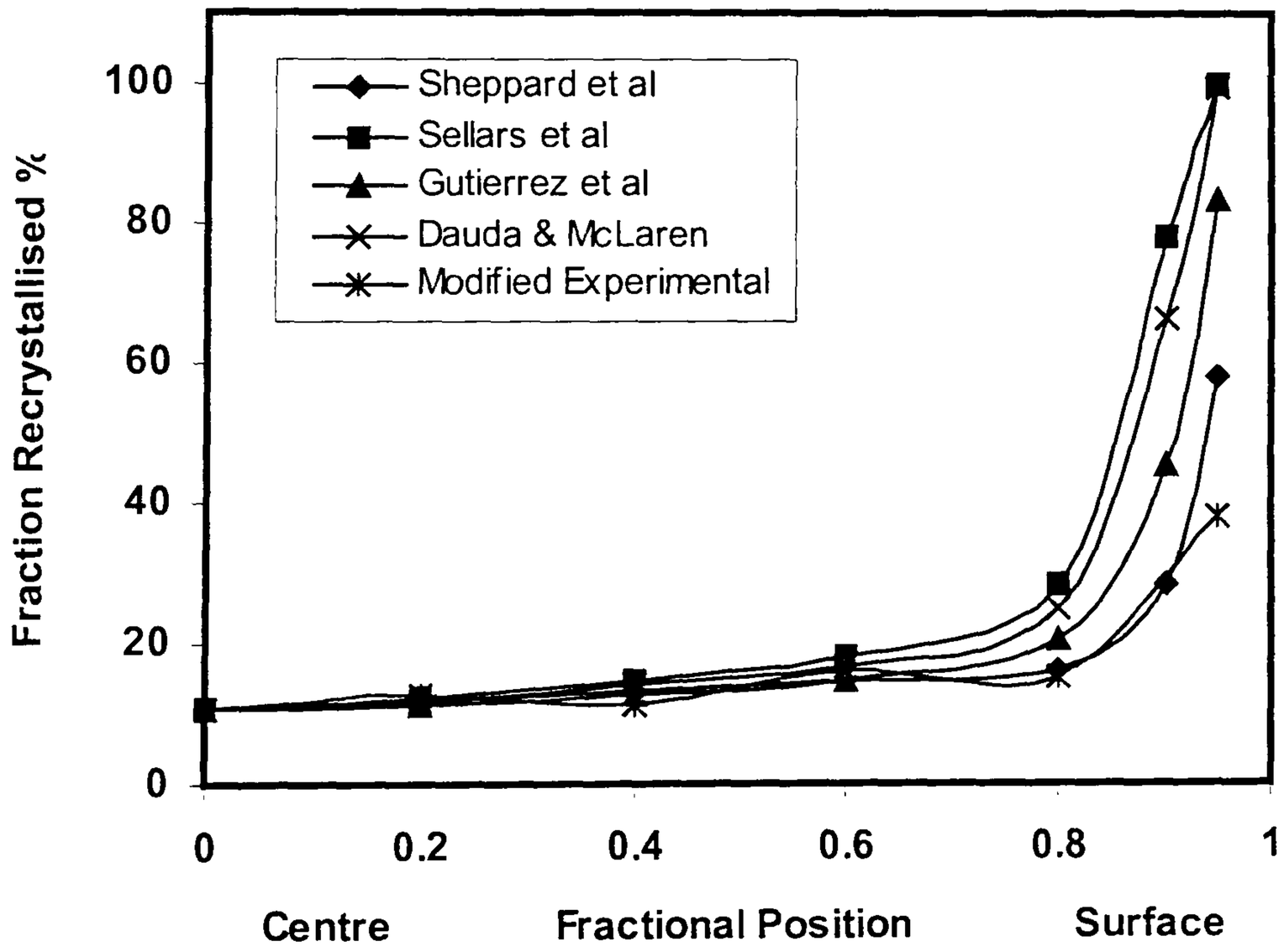

Fig. 5-36 Comparison of the predicted gradients in the fraction recrystallised by using the different normalised models with the strain 2 and $(Z_{ave})_{\varepsilon}$

The comparison of various empirical models is shown in Fig.5-36. These empirical models are all tuned with the measurement at the centre for "strain 2". Contrary to expectation, the model established for commercial purity aluminium (Gutierrez et al) does not give the best prediction for the rolling of purity aluminium. The other three models provide nearly the same prediction within 70% thickness. Sheppard et al's model (Sheppard et al 1986) proposed for aluminium alloy AA5056 gives the best agreement, particularly in the surface area. The predicted fraction recrystallised by using Sheppard et al's model is nearly half of that predicted by using Sellars et al's model. This discrepancy with other models is of considerable importance because only Sheppard et al's models are regressed from rolling tests. The other three models are established either by plain strain compression (Sellars et al's model (Sellars et al 1985)) or the torsion test (Gutierrez et al's model (Gutierrez et al 1988)).

In torsion testing, the effect of shear strain is dominant. The phenomenon that shear strain changes the direction is not included. The magnitude of shear strain is much greater than those in plane strain compression (PSC) and rolling. In PSC, the magnitude of shear strain at the surface is lower than that in the rolling test where the slab is pulled into the roll gap by the net frictional force. Although there is a direction change at the contacting face in PSC testing, a specified material point at the interface only experiences uni-directional shear strain. While in rolling, a specified material point at the surface first experiences a forward shear strain because its entering speed is lower than the roll peripheral speed. The shear strain disappears at the neutral point or neutral region. After that, the same material point experiences a backward shear strain. From the above comparison, it can be concluded that there is a considerable difference in the strain path between these testing methods. Black et al's work show that the strain path affects the static recrystallisation kinetics (Black et al 2001). Rossi and Sellars (1996) reported that PSC leads to faster kinetics of recrystallisation than rolling does by a factor of approximately 2.7, but the authors are not able to establish why this should so.

From the above discussion, it can be concluded that the empirical model should be established by the rolling test. Otherwise, the fraction recrystallised would be overpredicted.

Now, we should compare the predicted results given by McLaren (1994) with the present study. Fig.5-37 shows the predicted results with Guitierrez et al's model by McLaren. It should be noted the curves marked "strain 1" and "strain 2" were calculated from the addition of increments of shear strain, accumulated irrespective of sign through the roll gap. "Strain 1" and "strain 2" used by McLaren are different with those in equations (5-6) and (5-7). The curve "strain 3" was calculated from the net shear at exit. The curve "strain 4" is the result of non plane strain conditions during experimental rolling. Using "strain 3" and "strain 4" do have a marked effect on the prediction. Even making so many changes to the strain, the predicted results are really not good within the 70% thickness region. Comparing Fig.5-36 and Fig.5-37, It can be seen that the present work gives a much better prediction. The reason can be attributed to the use of "strain 2" and $(Z_{ave})_{\varepsilon}$

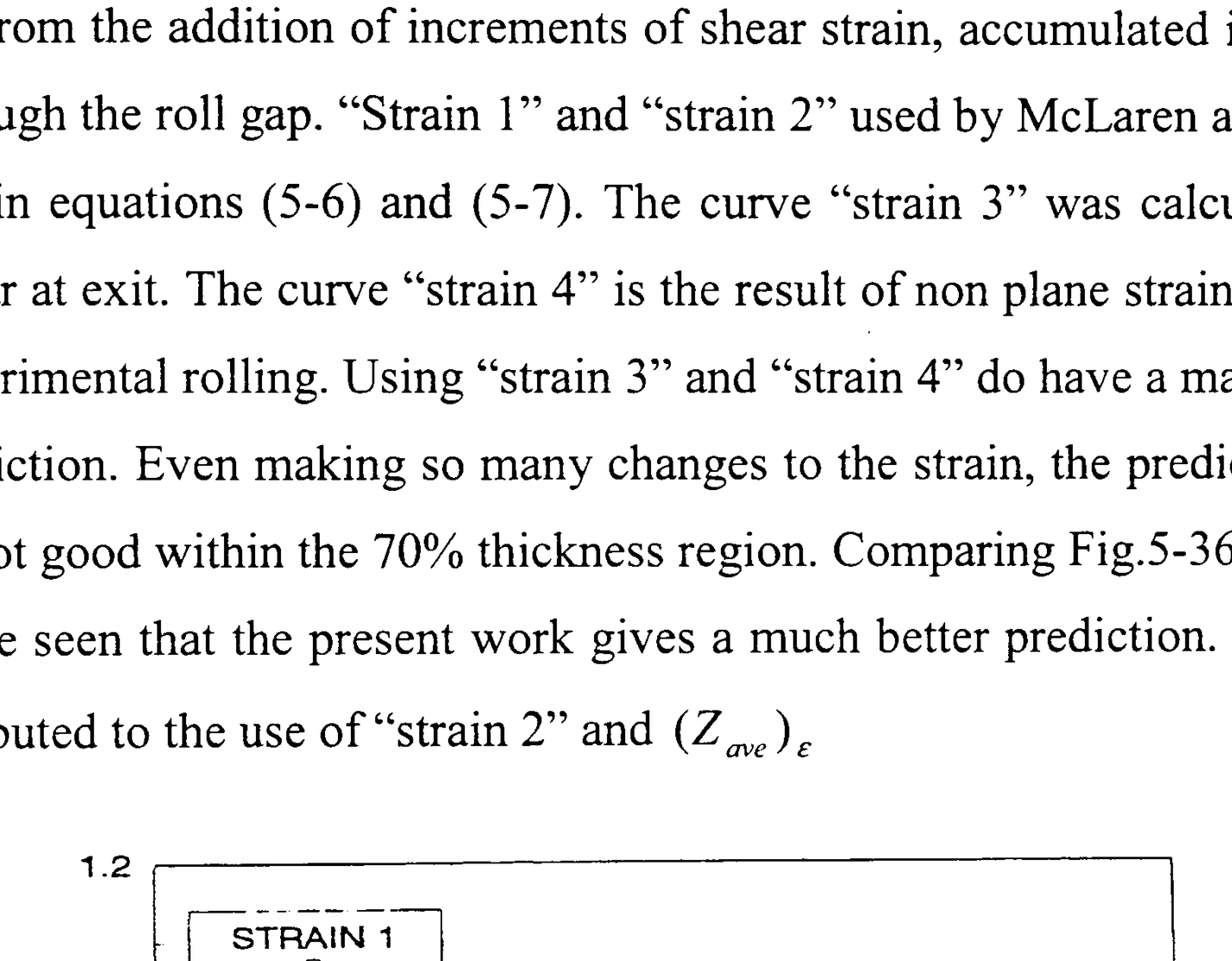

Fig.5-37 Predicted gradients in fraction recrystallised (After McLaren 1994)

Fig.5-38 shows the results by using the "strain 1", and $(Z_{ave})_{\varepsilon}$. The curve marked "Gutierrez et al" in Fig.5-37 gives a better prediction than any curves in Fig.5-37 within approximately 80% thickness, even though there is no modification to the equivalent strain (The effect of shear strain is included). We can also see that changing the mode of calculation for Z has a marked effect on improving the prediction.

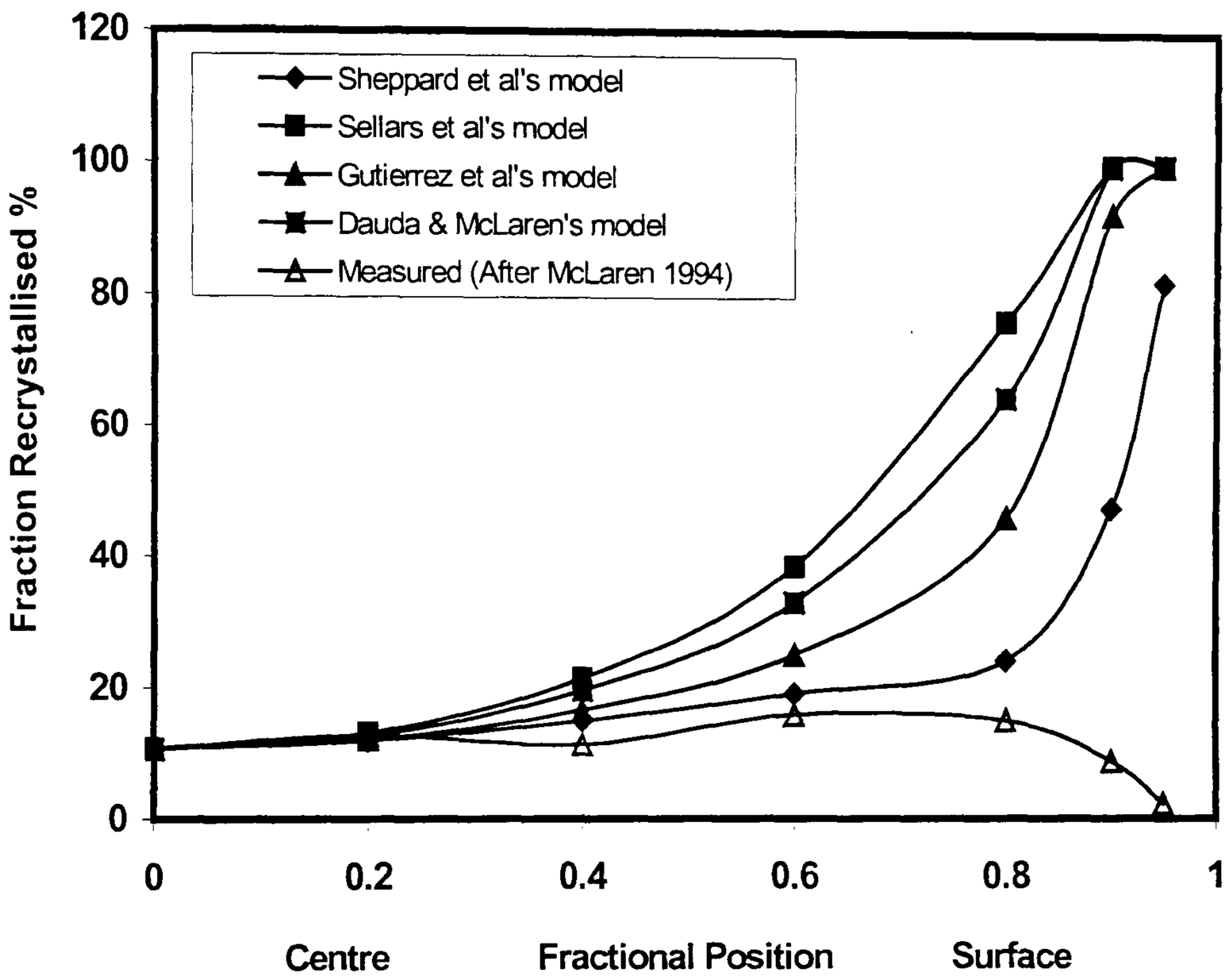

Fig. 5-38 Comparison of the predicted gradients in the fraction recrystallised by the different normallised models with the "strain 1" and $(Z_{ave})_{\varepsilon}$

If we check Sellars et al's and Dauda & McLaren's model in the appendix 2, it is clear that two models have the same powers for ε and Z. That may be the reason why the two models predict very close results, see Fig.5-36 and Fig.5-38. Based on the observation of microstructural changes of Al-1Mg, Rossi and Sellars (1996) found that the slight difference in alloy constitutions had a profound effect on static recrystallisation. Fig.2-6 presented in Chapter 2 also indicates the significant influence of alloying element on the recrystallisation behaviour. This means that we can not build up an empirical model for a new material in such a way: modifying

the constant A but retaining the constants b and c in equation (5-40) from existing models which were constructed for differing materials. If so, incorrect result will be given by the simulation (Mirza et al 2001). Simulation by physical modelling seems essential for future research work.

5.5.4 Prediction of the fraction recrystallised for AA5083

The analysis model is established based on the experimental work by Timothy et al (Timothy et al 1991). The material, aluminium alloy 5083, is rolled with an initial centre temperature of 460^0C in a single stand mill with roll diameter of 368mm and roll temperature of 20^0C. The roll peripheral speed is 0.192m/s. The initial slab thickness is reduced from 30 mm to 15.9mm. The specimen was rolled to completion and held for 15s after deformation before being water quenched. The predicted histories of various deformation variables are shown in Fig.5-39 to Fig.5-41. The predicted maximum temperature rise for the centre point is ~23^0C, which approaches Timothy et al's theoretical calculation and FEM prediction of ~26^0C (Timothy et al 1991). The minimum sub-surface temperature of ~365^0C corresponds very well with their measurement. The temperature rise for the quarter and centre point is caused because the heat generation due to plastic deformation and the interface friction work outweighs the heat loss to the roll and the surrounding. Aluminium alloys have a very good heat conductivity. The temperature of the whole section becomes approximately uniform within a very short time of about 0.5s.

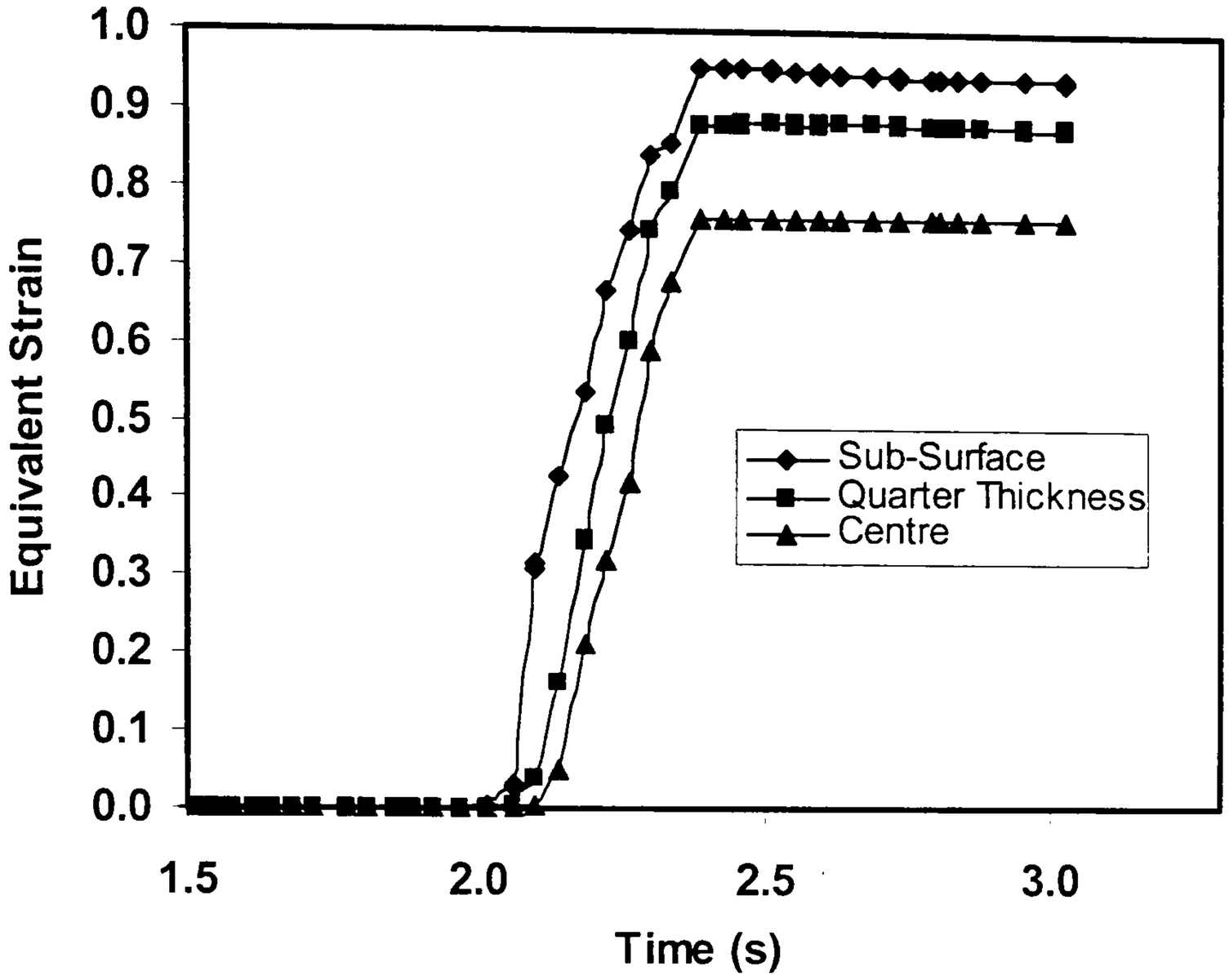

Fig.5-39 The history of temperature

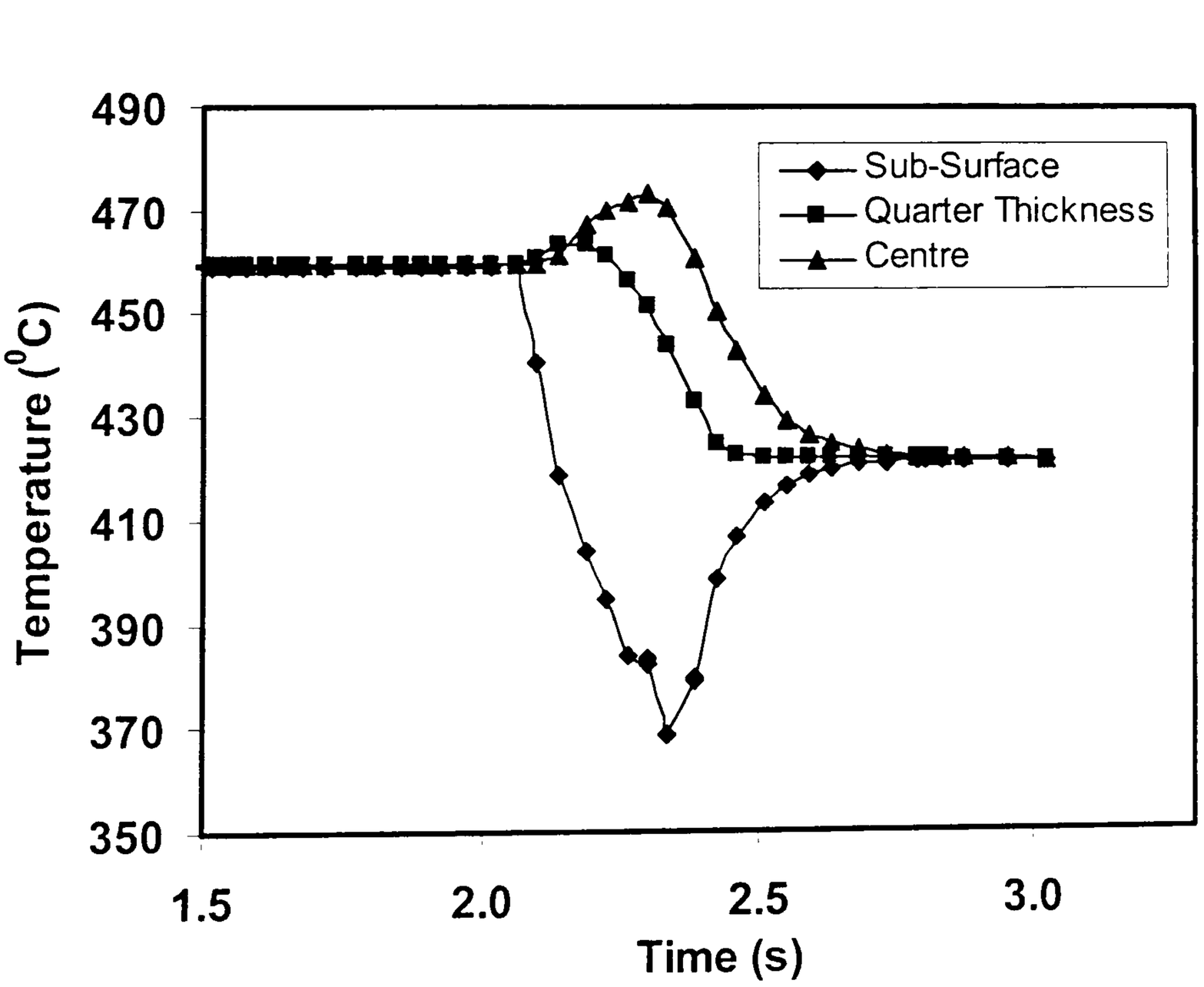

Fig.5-40 The history of equivalent strain

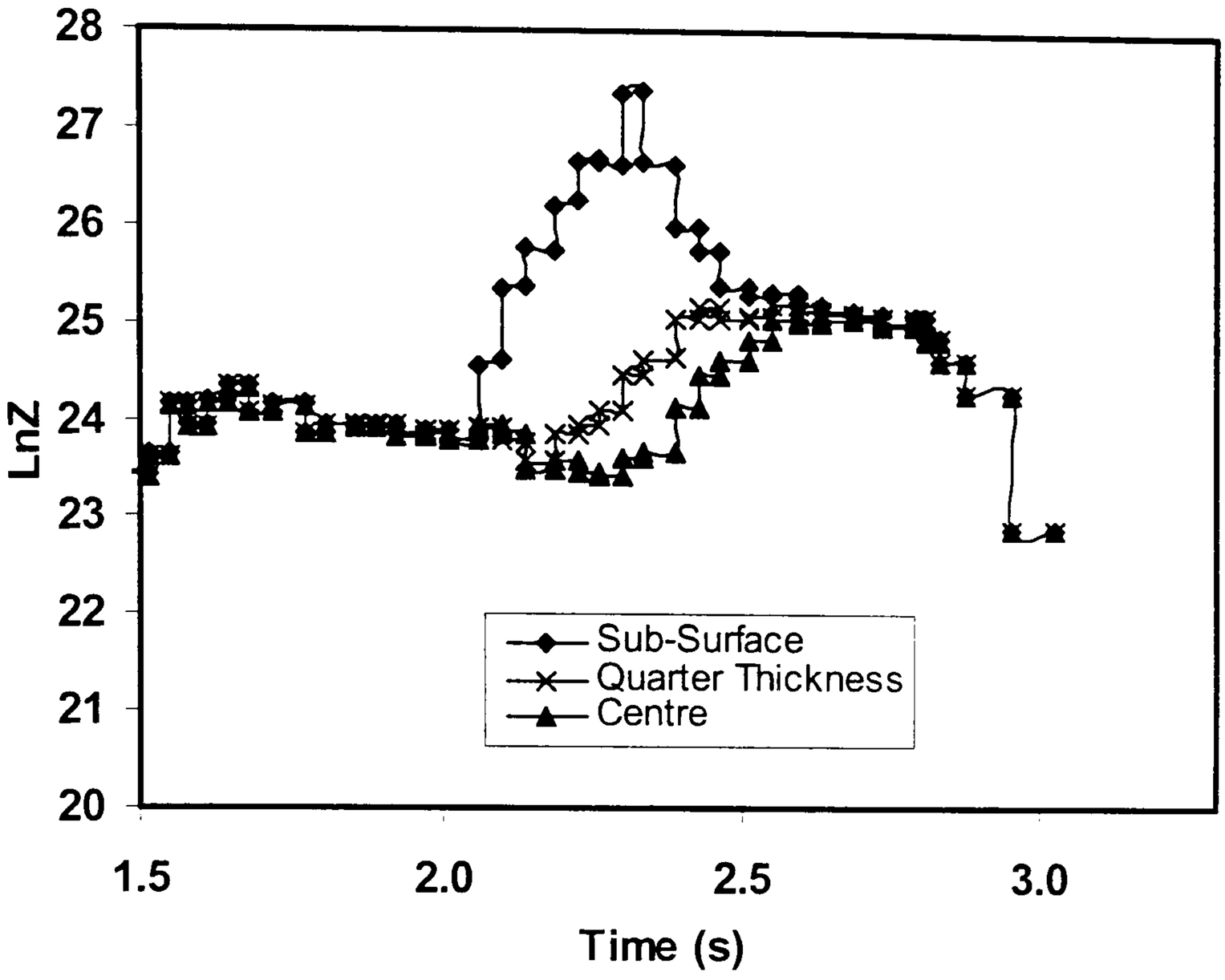

Fig. 5-41 Predicted history of Zener Hollomon Parameter

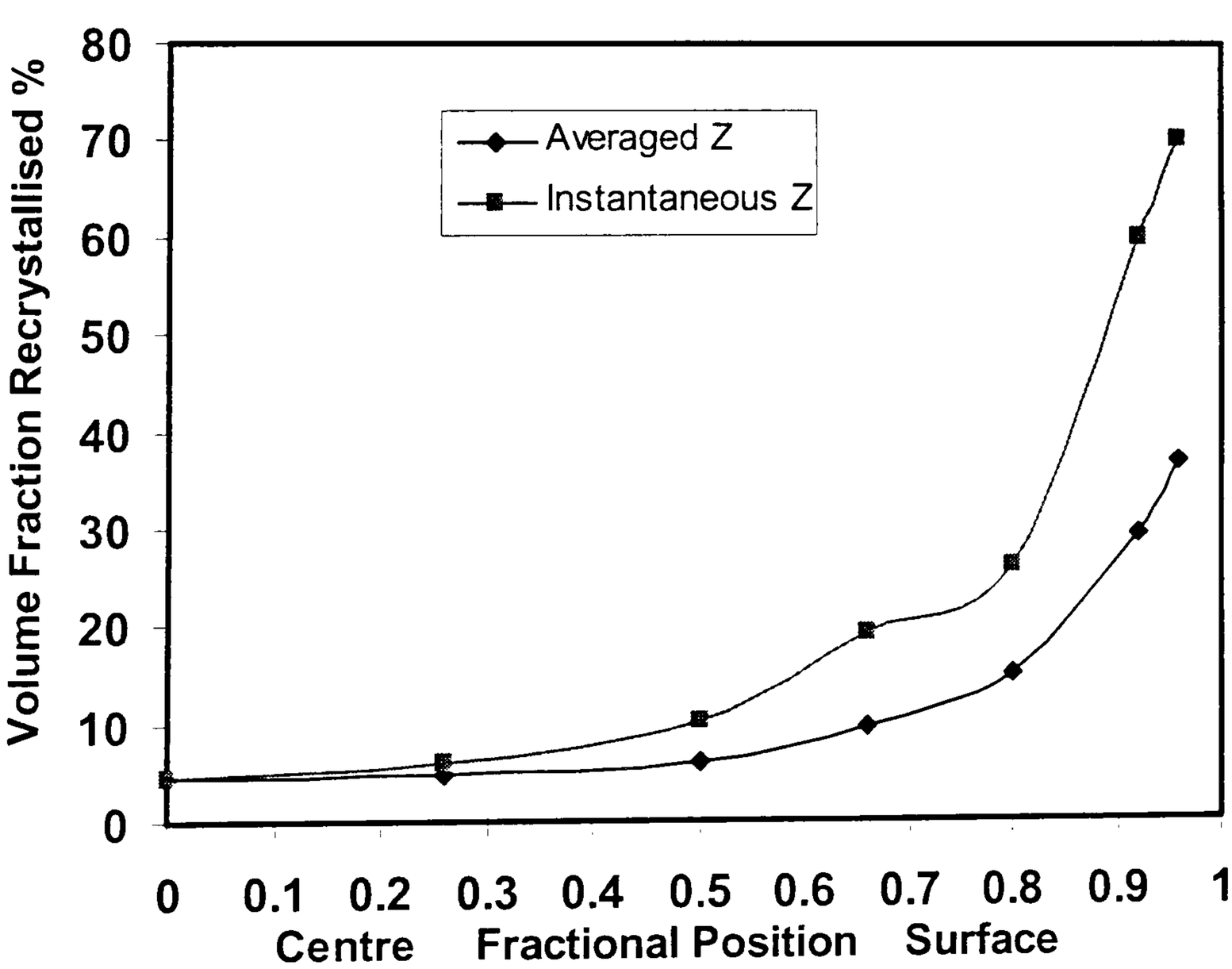

Fig. 5-42 The distribution of X_1

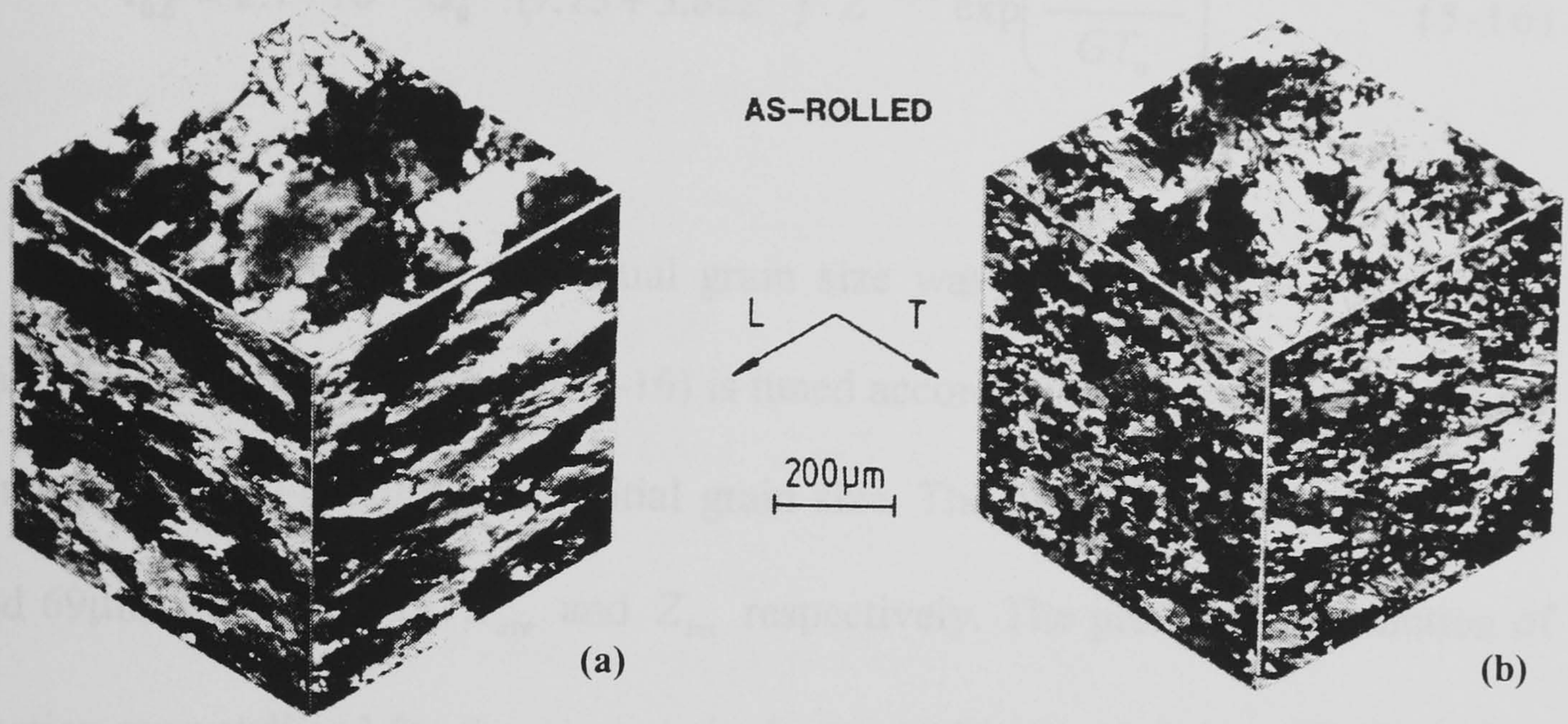

Fig.5-43 Measured micrographs at (a) centre, (b) surface (After Timothy et al 1991)

Fig. 5-40 shows an obvious difference in the final equivalent strain when leaving the roll gap. The value decreases from the surface to the centre. This phenomenon is caused by the distribution of shear strain, which is strong at the surface due to the roll-stock contact, and vanishes at the stock centre due to the geometrical symmetry. The predicted history of Z is plotted in Fig.5-41 by the use of a logarithm function. It can be seen that Z also decreases from the surface to the centre. It is generally recognised that higher strain and Z tend to accelerate the SRX because they produce more stored energy. Therefore, the X_V should decreases from the surface to the centre.

The reported formula for the calculation of the $t_{0.5}$ for AA5083 in the literature was given by (Sheppard et al 1986):

$$t_{0.5} = 2.7 * 10^{-10} d_0^{2.45} \left(9.75 + 3.82\bar{\varepsilon}^2\right)^{-1} Z^{-0.58} \exp\left(\frac{183000}{GT_a}\right) \qquad (5\text{-}16)$$

In Timothy et al's paper, the initial grain size was not reported. To predict the fraction recrystallised, equation (5-16) is tuned according to the measurement at the centre (4.5%) by changing the initial grain size. The tuned initial grain size is 86 and 69μm for the use of Z_{ave} and Z_{ins} respectively. The predicted distribution of fraction recrystallised for the present single pass rolling is shown in Fig.5-42. The two curves give the same trend but differ in value. The measured X_V is 39.2% and 4.5% for the surface (at the 0.95 fraction position) and centre point respectively. The corresponding micrographs for these two points are shown in Fig.5-43. It is clear that using the Z_{ave} gives a better prediction than the use of Z_{ins}.

The formula for the calculation of the recrystallised grain size, d_{rex}, was also reported in the literature (Sheppard et al 1986)

$$d_{rex} = 4.79 d_0 Z^{-0.075} / \left(3.72 + 1.12\bar{\varepsilon}^2\right) \qquad (5\text{-}17)$$

The predicted distribution of d_{rex} through the thickness is shown in Fig.5-44. The d_{rex} decreases from the centre to the surface. For the curve predicted by using Z_{ave}, the d_{rex} at the centre is 15.6μm which fits well with the measurement of 16μm at

this position. The computed d_{rex} at the surface is 12.6μm, which is also close to the measurement of 16μm. It is inconsistent that the same d_{rex} was measured for both the centre and the surface point. There are significant differences on the deformation histories through the thickness, see Fig.5-39 to Fig.5-41. Theoretically, d_{rex} should decrease from the centre to the surface.

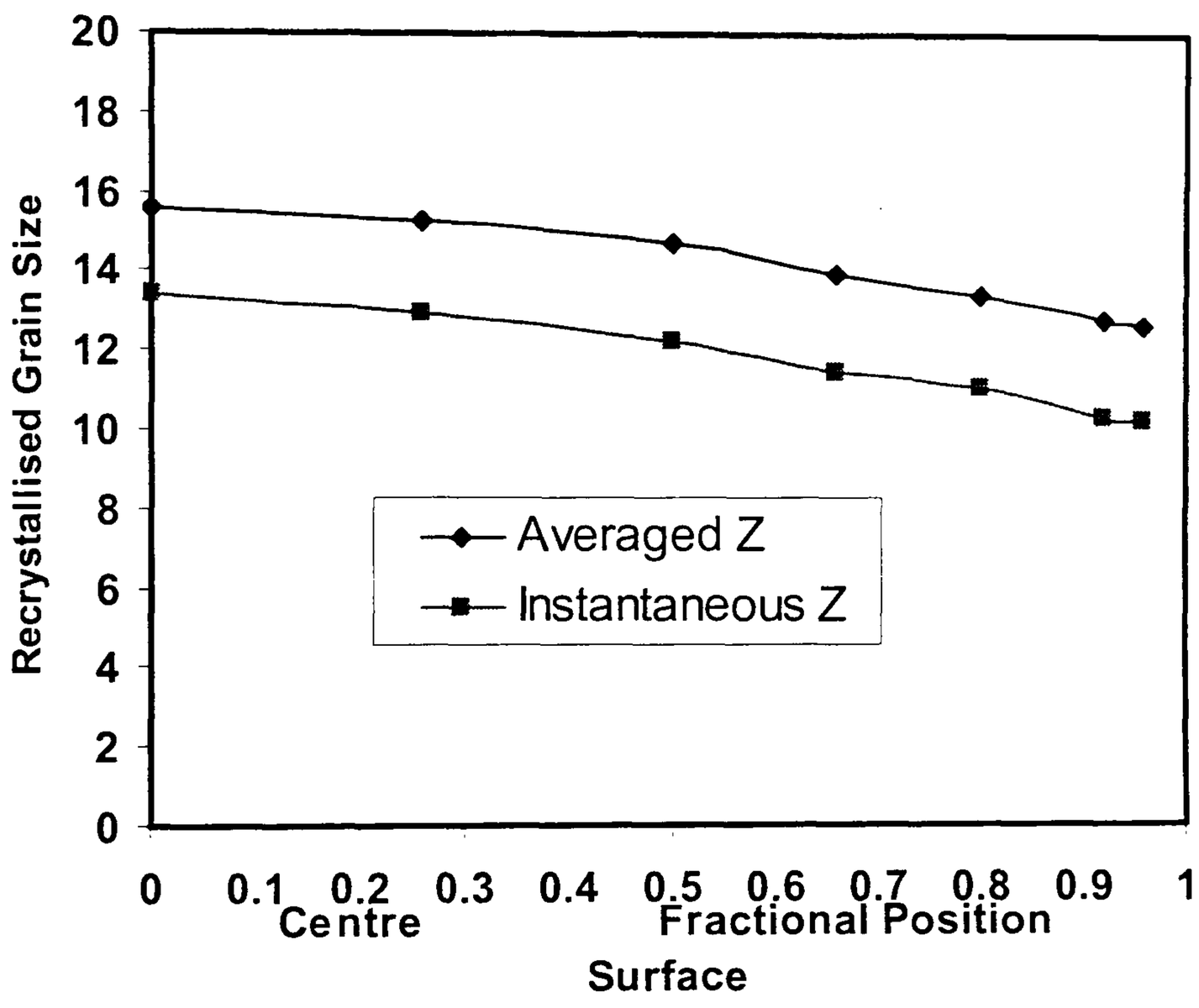

Fig.5-44 Predicted distribution of the recrystallised grain size

5.5.5 Determination of the influence of rolling parameters on the X_V

From the curve marked "Averaged Z" presented in Fig.5-42, it is clear that FEM gives an excellent prediction. This indicates that we can replace the experiment by FEM. The advantages of such a replacement are obvious. There is no equipment limitation, the accuracy of measurement is high, little capital investment is required and it is fast.

There are several types of parameters that have influence on the $X_{I'}$. They are initial geometry parameters (width/thickness, length/thickness), deformation zone parameters (draft, the contact length), process parameters (temperature, roll speed) and material parameters (component). Four variables, the ratio of the mean thickness to the contact length ($\frac{H_m}{L} = \frac{H_1 + H_2}{\sqrt{R(H_1 - H_{2)}}}$), the roll temperature (T_{roll}), roll speed (V) and the slab temperature (T) that are easily controlled, are selected for the study. Each parameter has three values, also called three levels. These values are shown in Table 20. For the ratio H_m/L, the values are 0.4283, 0.627 and 0.813 (equivalent to 50%, 30% and 20% thickness reduction respectively since the roll radius R and the initial thickness H_1 are fixed. The values are the same as those described in section 5.5.4). For the ratio of T_{roll}, the values are 20^0C, 60^0C and 100^0C. The designed orthogonal table $L9(3^4)$ is shown in table 21. $L9(3^4)$ indicates that there are four parameters, each parameter has three levels and total 9 test runs need to be conducted. The simulated material is aluminium alloy AA5083.

Table 20 Test parameters and their levels

Level	H_m/L	T_{roll} (^{0}C)	V(mm/s)	T(^{0}C)
1	0.428	20	100	400
2	0.627	60	200	450
3	0.813	100	300	500

Table 21 Experimental design and the predicted fraction recrystallised

Run No.	H_m/L	T_{roll} (^{0}C)	V(mm/s)	T(^{0}C)	$X_{V'}$ %(Centre)	$X_{V'}$ %(Surface)
1	0.428	20	100	400	14.174	62.360
2	0.428	60	200	450	0.863	3.692
3	0.428	100	300	500	0.073	0.159
4	0.627	20	200	500	0.059	0.411
5	0.627	60	300	400	2.873	6.798
6	0.627	100	100	450	0.278	1.520
7	0.813	20	300	450	0.219	0.779
8	0.813	60	100	500	0.017	0.090
9	0.813	100	200	400	1.107	2.949

The objective of this section is to show the relative contribution of each parameter on the $X_{V'}$. This task is obtained through the analysis of variance (ANOVA). ANOVA uses the sum of squares to quantitatively examine the deviation of the control factor effect responses from the over all experimental mean response (Fowlkes and Creveling 1995).

For each level, the mean of quality characteristic response is calculated by

$$\bar{y} = \frac{1}{n}\sum_{i=1}^{n} y_i \tag{5-18}$$

where y_i is the quality characteristic response. In this study, it refers to the $X_{V'}$. n is the number of experiments that include the level. In the array $L_9(3^4)$, n is a constant 3.

The calculated mean values at different levels for each factor are shown in the Table 22 under the column $\bar{y}$. It can be seen from Table 22 that level 1 of H_m/L is included in test runs 1, 2 and 3.

Table 22 Level average response analysis using S/N ratio for the centre point

Variables	Level	Runs	y	$\bar{y}$	S/N	$\overline{S/N}_{ij}$
H_m / L						
		1	14.1735		-23.0295	
Level 1	0.428	2	0.862902	5.03649	1.280774	0.325616
		3	0.073067		22.72562	
		4	0.059329		24.53467	
Level 2	0.627	5	2.872739	1.07006	-9.16592	8.828117
		6	0.278112		11.1156	
		7	0.219293		13.17951	
Level 3	0.813	8	0.016918	0.447636	35.43283	15.91059
		9	1.106695		-0.88056	
T_{roll}						
		1	14.1735		-23.0295	
Level 1	20°C	4	0.059329	4.817375	24.53467	4.894878
		7	0.219293		13.17951	
		2	0.862902		1.280774	
Level 2	60°C	5	2.872739	1.250853	-9.16592	9.18256
		8	0.016918		35.43283	
		3	0.073067		22.72562	
Level 3	100°C	6	0.278112	0.485958	11.1156	10.98689
		9	1.106695		-0.88056	
V						
		1	14.1735		-23.0295	
Level 1	100mm/s	6	0.278112	4.822844	11.1156	7.839629
		8	0.016918		35.43283	
		2	0.862902		1.280774	
Level 2	200mm/s	4	0.059329	0.676309	24.53467	8.311628
		9	1.106695		-0.88056	
		3	0.073067		22.72562	
Level 3	300mm/s	5	2.872739	1.055033	-9.16592	8.913068
		7	0.219293		13.17951	
T						
		1	14.174		-23.0295	
Level 1	400°C	5	2.873	6.050979	-9.16592	-11.0253
		9	1.107		-0.88056	
		2	0.863		1.280774	
Level 1	450°C	6	0.278	0.453436	11.1156	8.525294
		7	0.219		13.17951	
		3	0.073		22.72562	
Level 1	500°C	4	0.059	0.049771	24.53467	27.56437
		8	0.017		35.43283	

Level 3 of the rolling temperature is involved in test runs 3, 4 and 8. When performing level average analysis for one level of one parameter, all the influence from different levels of other parameters will be counterbalanced because every

other parameter will appear at each different level once. Thus the effect of one parameter at one level on the experimental results can be separated from other parameters. In this way, the effect of each level of every parameter can be viewed independently.

Table 23 Analysis of variance of fraction recrystallised for the centre point

	Centre	Surface
H_m / L	13.7%	13.9%
T_{roll}	2.2%	5.9%
V	0.1%	2.9%
T	84%	77.3%
Total	100%	100%

In the Taguchi method, the signal-to-noise (S/N) ratio is adopted to analyse the test results. The S/N ratio can reflect both the average (mean) and the variation (scatter) of quality characterics under one trial condition. The S/N function is defined by

$$S/N = -10 * LOG(MSD) \tag{5-19}$$

where the MSD stands for the mean square deviation. The purpose of using the constant 10 is to magnify the S/N value for easier analysis. In this investigation, the MSD is expressed as:

$$MSD = y_i^2 \tag{5-20}$$

The overall mean S/N ratio of the OA is expressed as:

$$\overline{S/N} = \frac{1}{9}\sum_{i=1}^{9}(S/N)_i \tag{5-21}$$

The sum of the squares due to variation about overall the mean is:

$$SS = \sum_{i=1}^{9} \left(S/N_i - \overline{S/N} \right)^2 \tag{5-22}$$

For the i[th] factor, the sum of the squares due to variation about the mean is

$$SS_i = \sum_{j=1}^{3} M_j * (\overline{S/N}_{ij} - \overline{S/N})^2 \tag{5-23}$$

Where M_j is the number of experiments at the each level. It is a constant of 3 in this study. The percentage of contribution of i[th] factor to the X_V can be calculated by

$$SS_i\% = SS_i / SS * 100\% \tag{5-24}$$

Using the same method described in chapter 4.6.7, the relative contribution of each method on the X_V at both the surface and centre can be calculated and shown in Table 23. It can be seen that, for both the surface and centre point, the same order is given. For the centre X_V, the rolling temperature contributes 84% to the X_V, about 6 times the contribution of the H_m / L. The influences of roll temperature and roll speed on the X_V are negligible. In Wells et al's study (Wells et al 1998) by the use of sensitivity analysis, the contribution of the rolling temperature to the X_V is about 70%, which fit very well with the present work. Roll temperature and roll speed exert slightly more influence on the X_V at the surface than at the centre. That is

because the temperature and strain rate in the sub-surface region are easily affected by the change of boundary conditions. Table 23 also indicates that to control X_V, accurate prediction of the temperature evolution during multi-pass hot rolling is vital.

It should be noted that the aforementioned analysis in Table 23 is only valid within the experimental parameters setting ranges. For the H_m / L, it decreases from approximately 4 in the initial breakdown pass towards the values of 0.3 in the finishing hot rolling pass. Raghunathan and Sheppard reported that, for AA5056, at least 15% thickness reduction is required to ensure that SRX occurs (Raghunathan and Sheppard 1989). To ensure the occurrence of SRX, the minimum reduction is set 20% (equivalent to 0.813 of H_m / L) in the present study. Due to the limitation of the laboratory mill, the roll speed can not be assigned a very large value. The range from 100mm/s to 300mm/s is equivalent to from 5.2rpm to 15.6 rpm. Comparing those roll speeds with industrial rolling, the values appear to be small. When the roll speed increases, far greater influence could be exerted by the roll speed.

The average effect of each parameter level on the spread is shown in Fig.5-45. From the Fig.5-45, it can be seen that X_V increases with the decrease of all parameters. This agrees with most workers' experimental observation.

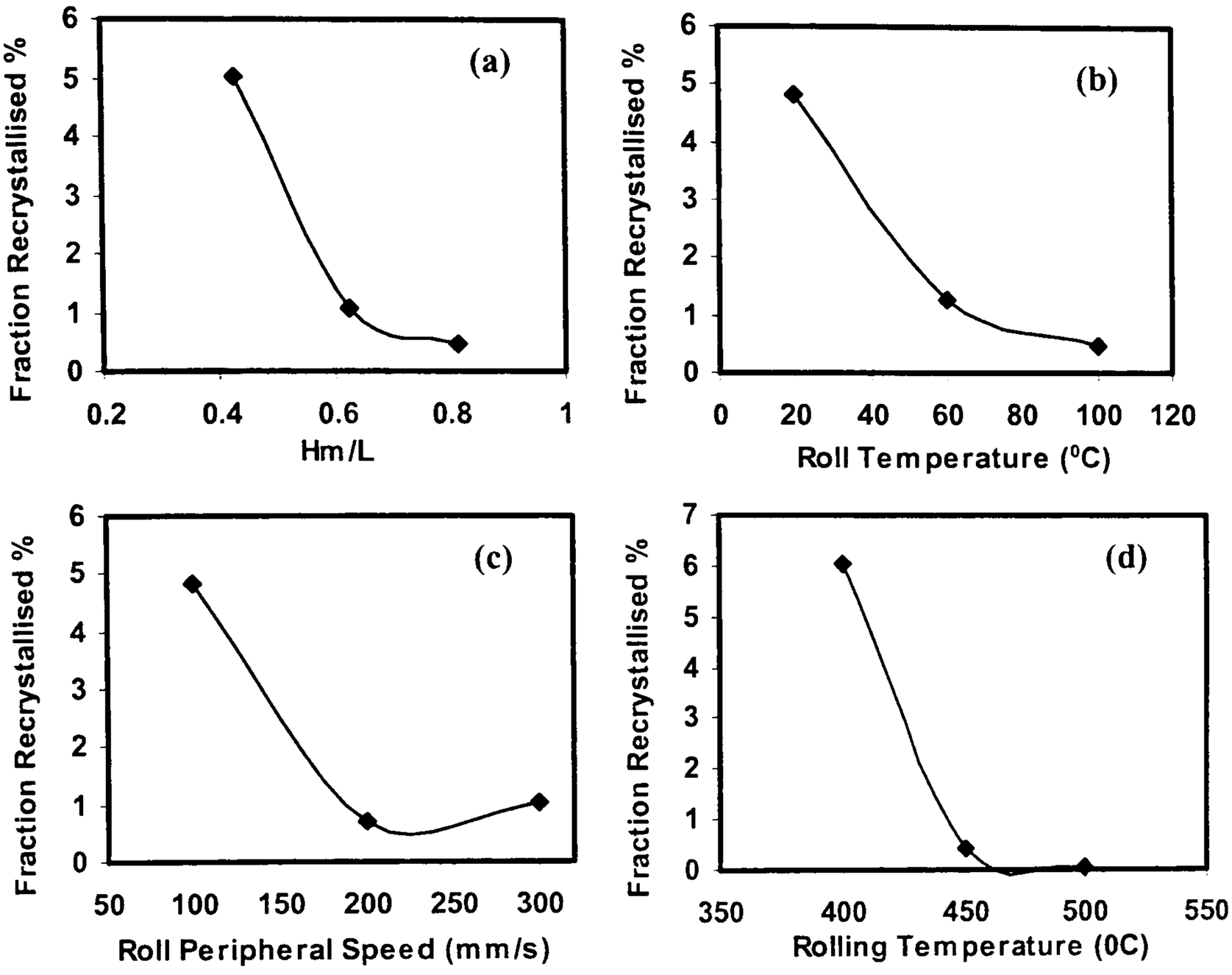

Fig.5-45 Plots of response of each parameter level on the predicted fraction recrystallised for the centre point

Chapter 6 Design of rolling pass schedules

As the described in Chapter 2, designing a rational rolling pass schedule is critical if the product quality (i.e. strip profile, mechanical properties and texture) is to be controlled. Presently, the design of rolling pass schedule depends on the accuracy of various empirical models. These models are usually difficult to apply to a new product while the FEM appears to be universal if the correct material properties and boundary conditions are applied. Compared with the design by various empirical models, the disadvantage of applying FEM in the design of pass schedule is obvious: time consumption. In order to have a better understanding and control of the whole rolling process and to apply the FE modelling more effectively and approximately, the knowledge of how a rolling pass schedule is designed would be very useful. In this study, the results from FEM are used as one of the standards by which the calculated rolling pass schedule may be compared.

The procedure and formulae, which are presented in the following sections, are extracted from a rolling pass schedule package, which was first developed by Terry Sheppard, and has been modified by Terry Sheppard and the present author. Due to the lack of sufficient industrial data and the complicated nature of practical industrial rolling, optimising the rolling pass schedule either by intelligent methods, such as expert system and neural network, or by the conventional constrained optimisation method, is not practical for the present author. Shape control is not considered. Some factors associated with the shape control such as the design and control of roll camber and thermal camber is therefore not considered. At the end of this chapter, three examples are shown. In the first two pass schedules, the computed rolling load, power and pass temperature are compared with industrial measurements. The third pass schedule is designed for a new production line. The computed rolling load and pass temperature are compared with the predictions from other industrial models.

6.1 The procedure of designing rolling pass schedule

The procedure of designing an initial schedule can be divided into 6 main steps:

(1) Preparing the input data

Input data fall into two categories: mill stand and driving data, and rolling stock data. Mill stand and driving data include the roll diameter, the roll barrel length, the roll material, the maximum roll force, the maximum roll torque, the maximum bending force and the maximum power. The rolling stock data include density, final dimensions, heat expansion coefficient, specific heat capacity, heat conductivity, emissivity, Young's modulus and temperature.

(2) Calculating the slab length and width

The length is calculated based on the principle of volume equality. The width after a pass deformation is calculated by the new spread equation described in chapter 4.6.8. Although in some passes, edge trimming or end shearing may occur, the principle of volume equality will still be applied at least when end shearing occurs

(3) Calculating the yield strength

The calculation of the yield strength plays a vital role in ensuring the success of the design of a rolling pass schedule. The yield strength depends on many factors: the reduction (determining strain), the roll speed (determining strain rate), and temperature.

(4) Setting the draft and speed

The roll force and torque, and the power required are determined by means of the respective existing models. If any limit, particularly force and power, is

exceeded, the draft is reduced and all variables are recomputed. The process is repeated until an acceptable pass is found. The determination of the roll speed mainly depends on the productivity required. But it is also retrained by the mill capacity and perhaps by structural and mechanical requirements.

(5) Determining the roll/slab contact time and setting the idle time

The determination of interpass time depends mainly upon the time to adjust to the exit gauge and in the initial passes the time to reverse the motor. In normal rolling, the shorter the idle time and the contact time, the less the temperature loss. This ensures lower rolling force and power for the next pass.

(6) The calculation of the temperature for the next pass.

The control of temperature changes over the entire schedule is of particular importance. Firstly, temperature has the major impact on the calculation of the roll force; secondly, the structure of the finished product is considerably influenced by the final deformation temperature. The ways in which the workpiece can lose or gain heat include heat conduction with the roll (including cooling and lubricant emulsion) and air, deformation, radiation, and coolant. None of the constants involved in these mechanics are well documented in the literature.

Step 1 to step 6 is repeated until the last pass exit gauge is just greater than the specified finished coil gauge. The draft for this pass is adjusted to meet the target gauge. If the last pass reduction is too small or too large to give an acceptable rolling load or good shape, an ideal last pass reduction is determined. The drafts on the previous passes are altered slightly to accommodate the ideal last pass.

6.2 The formulae used in the design of schedule

To assistant the reader to readily interpret the symbols used in this paper, a schematic diagram of parameters in the roll gap is given in Fig.6-1.

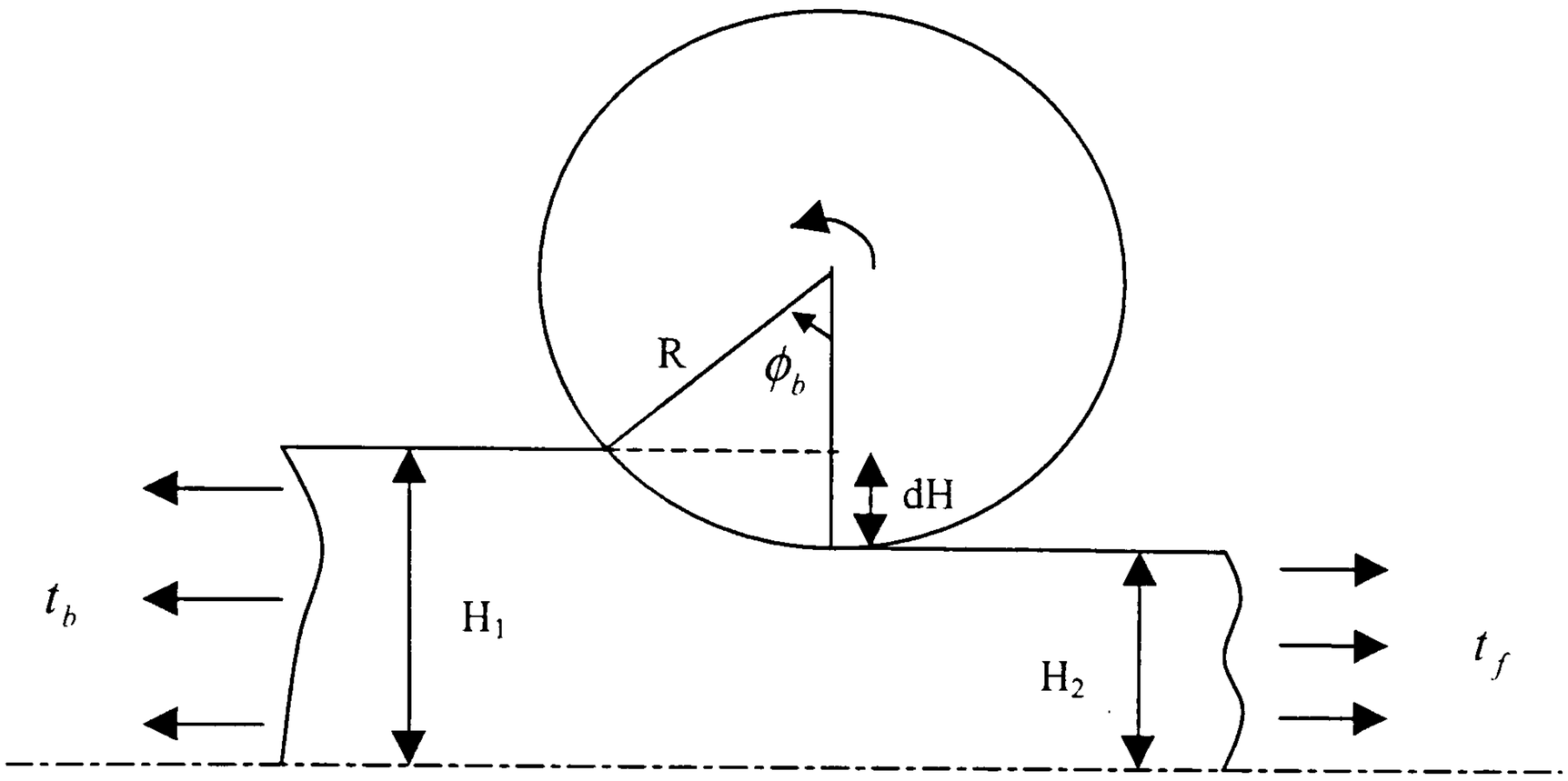

Fig.6-1 Schematic diagram of parameters in the roll gap

6.2.1 Maximum reduction

The rolls pull the slab into the roll gap through the net frictional force at entry to the roll bite. Since energy is dissipated in overcoming friction, thus, increasing friction means increasing force and power requirements. More seriously, high friction could damage the slab surface. Therefore, a comprise has to be made to ensure a friction coefficient balancing the reduction and the damage it could cause. The maximum thickness reduction dH_{max} may be calculated by equating the horizontal forces to yield

$$dH_{\max} = \mu^2 * R \tag{6-1}$$

where μ is the friction coefficient, R is the roll radius. Thus, the higher the friction, the larger the roll radius, the greater is the maximum possible thickness reduction. In hot rolling, the practical reduction is much lower than this formula indicates. Propelling the slab into the roll bite becomes more dependent on the operator' experience and confidence.

6.2.2 Determination of the exit thickness H_2

The value of thickness reduction dH is assigned directly within the range $0 < dH < dH_{max}$

$$H_2 = H_1 - dH \tag{6-2}$$

The reduction of the first pass is often assigned a value much lower than the maximum possible draft. There are several reasons for this. The first purpose is to produce satisfactory gauge and an acceptable slab surface since the flatness of the cast ingot may not be perfect nor the gauge precise. In this context it is also necessary to ensure that the roll emulsion acts efficiently as a lubricant. The second purpose is to produce compressive residual stresses on the surfaces to improve the fatigue life. The stress state and deformation distribution in the roll gap of the first pass in the breakdown rolling has been discussed in chapter 4.4. The third purpose, the major reason, is to assure a certain thickness value after the first deformation since the thickness of the cast and the result of any scalping is usually as not accurate as should be expected.

6.2.3 Calculating the average strain rate in the roll gap

This average strain rate is simply derived by dividing the total equivalent strain over the total time passing through the roll gap.

$$\dot{\bar{\varepsilon}} = \frac{2\pi N}{60} * \sqrt{\frac{R}{dH}} * Ln\left(\frac{H_1}{H_2}\right) \tag{6-3}$$

6.2.4 Calculating the Zener-Holloman parameter Z

As discussed below, this parameter strongly influences control and calculation of both continuum and structural mechanics.

$$Z = \dot{\bar{\varepsilon}} \cdot \exp\left(\frac{Q_{def}}{8.314T}\right) = A[\sinh(\alpha\bar{\sigma})]^n \tag{6-4}$$

where T is the temperature in degree Kelvin, Q_{def} is the thermal activation energy, A and α are constant, σ_f is the flow stress. The prevailing Zener-Hollomon parameter is imperative for the calculation of the flow stress and many structural parameters. Although the microstructural model is not incorporated in the current scheduling package, the calculation of Z provides the possibility to do so in the future.

6.2.5 The flow stress $\bar{\sigma}$

Two commonly used constitutive equations are introduced.

The hyperbolic sine function is written

$$\bar{\sigma} = \frac{1}{\alpha} * Ln\left\{\left(\frac{Z}{A}\right)^{1/n} + \sqrt{\left(\frac{Z}{A}\right)^{2/n} + 1}\right\} \tag{6-5}$$

It can be seen that the work-hardening effect, which is obvious in cold rolling or when the rolling temperature drops below 250^0C, is not considered in equation (6-5). So that for the case of cold rolling or when the temperature is below 250^0C, the constitutive equation must be modified to involve a strain sensitivity term. The Norton-Hoff Law could typically be applied.

$$\bar{\sigma} = K \cdot \exp(\beta T) \cdot \dot{\bar{\varepsilon}}^m \cdot (\bar{\varepsilon} + \bar{\varepsilon}_0)^n \tag{6-6}$$

6.2.6 Calculating the spread coefficient S_w

There are several formulae available for this calculation. The performance of each formula for laboratory and industrial rolling has been reported in chapter 4.6.6. The new spread coefficient formula is written:

$$S_w = Ln\frac{W_2}{W_1} = 0.2187 * \left(e^{0.1071*\left(\frac{W_1}{\sqrt{R*dH}}\right)} \right)\left(\frac{R}{H_1}\right)^{-0.848}\left(\frac{W_1}{H_1}\right)^{-1.481}\left(\frac{H_m}{L}\right)^{-2.6978} \quad (6\text{-}7)$$

It should be noted that this equation is only valid for the ratio $W_1/H_1 \leq 8$, where the formula is regressed. When the ratio $W_1/H_1 \succ 8$, no width variation is allowed because plane strain deformation prevails.

6.2.7 The slab width after the roll gap

$$W_2 = W_1 * \exp(S_w) \quad (6\text{-}8)$$

6.2.8 The slab length after deformation

If the operation of edge trimming and shear copping are ignored and the cross section after deformation remains rectangular, according to the principle of volume equality, the workpiece length after leaving the roll gap can be expressed by:

$$L_2 = \frac{L_1 W_1 H_1}{W_2 H_2} \quad (6\text{-}9)$$

Allowance for edging trimming or shearing can be dealt with at the appropriate pass.

6.2.9 Rolling load models

There are three commonly used formulae for the calculation of rolling load during hot flat rolling (Larke 1957). They are Sim's equation, Orowan-Pascoe's equation and Ekelund's equation. Larke found that rolling loads calculated by Sim's equation are always more in accordance with measured data than those

obtained by use of the Orowan-Pascoe and the Ekelund equations (Larke 1957). Hence Sim's equation is adopted in the present scheduling program.

$$P = \sigma^* \cdot W \cdot \sqrt{R(H_1 - H_2)} \cdot Q_S \tag{6-10}$$

where W is the stock width, R is the roll radius, the Q_S factor is defined as

$$Q_S = \frac{1}{2}\sqrt{\frac{H_2}{(H_1 - H_2)}}\left[\pi \cdot \tan^{-1}\sqrt{\left(\frac{H_1 - H_2}{H_2}\right)} - \left(\frac{R}{H_2}\right)^{\frac{1}{2}} \cdot Ln\left(\frac{H_n^2}{H_1 H_2}\right)\right] - \frac{\pi}{4} \tag{6-11}$$

where H_n is the thickness at the supposed neutral point in the roll gap. The symbol σ^* in equation (6-10) is called the modified plane strain yield stress. In hot rolling, especially in the hot rough rolling, there is a strong friction between roll and stock, the through thickness shear stress distribution is not uniform. To take into account this effect, σ^* is defined by (Atack et al 1988):

$$\sigma^* = m_1 m_2 \frac{2}{\sqrt{3}}\bar{\sigma} \tag{6-12}$$

where m_1 can be calculated by Lalli's expression (Lalli 1984):

$$m_1 = \left(1 - m^2 c^2\right)^{0.5} \tag{6-13}$$

In equation (6-13), m and c are constant. Generally. The value of m_2 is associated with the inhomogeneous distribution of strain (rate) through thickness. The empirical formula for the calculation of m_2 is given by (Atack et al 1988):

$$\begin{aligned} m_2 &= 0.75 + 0.25 * H_m/L && \text{for } H_m/L \geq 1 \\ and \quad m_2 &= 1 && \text{for } H_m/L \prec 1 \end{aligned} \tag{6-14}$$

When coiling is operated, the influence of tension on the rolling load should be considered. The rolling force can be calculated by (Larke 1962)

$$F = P\left(1 - \frac{\left(t_f + t_b\right)\sqrt{3}}{2\bar{\sigma}}\right) \tag{6-15}$$

where P is the rolling load when no tension is applied defined in equation (6-11), t_f is the front coiling tension and t_b is the back coiling tension.

6.2.10 Calculating the deformed roll radius R' (Larke 1957)

Due to the elastic deformation of the roll, the phenomenon of roll flattening occurs. An assumption is made that the arc of contact remains circular in shape, its radius of curvature is R' being greater than R, the nominal radius of the roll.

$$\frac{R'}{R} = 1 + \frac{C * P}{W_1 * \left(H_1 - H_2\right)} \tag{6-16}$$

where $C=16(1-\nu^2)/\pi E=2.1*10^{-5}$. Typically, in hot rolling, 5 iterations are the maximum required to converge on a deformed roll radius (Lalli 1984). The present authors found that just 3 iterations were sufficient.

6.2.11 Calculating the modified rolling load using Sim's equation

$$P' = \sigma'' \cdot W \cdot \sqrt{R' \cdot \left(H_1 - H_2\right)} \cdot Q_S \tag{6-17}$$

where σ'' is calculated by the expression $\sigma'' = m_1 m_2 \frac{2}{\sqrt{3}} \bar{\sigma}'$, where $\bar{\sigma}'$ is the modified flow stress.

6.2.12 Calculating the lever arm

When $W_1 / H_1 < 9$, the experience shows that the lever arm can be calculated by

$$a = \sqrt{R * dH} - x_n \tag{6-18}$$

where $\sqrt{R * dH}$ is the contact length, x_n is the distance from the entry to the neutral point. When $W_1 / H_1 > 9$, the lever arm can be calculated by

$$a = \left[0.5\sqrt{\frac{R}{R'}} - (0.5 - \lambda')\sqrt{\frac{R'}{R}} \right] \sqrt{R' * dH} \tag{6-19}$$

where $\lambda' = 0.43$ for rolls used during the preparatory stages of rolling and $\lambda' = 0.48$ for finishing rolls (Larke 1957).

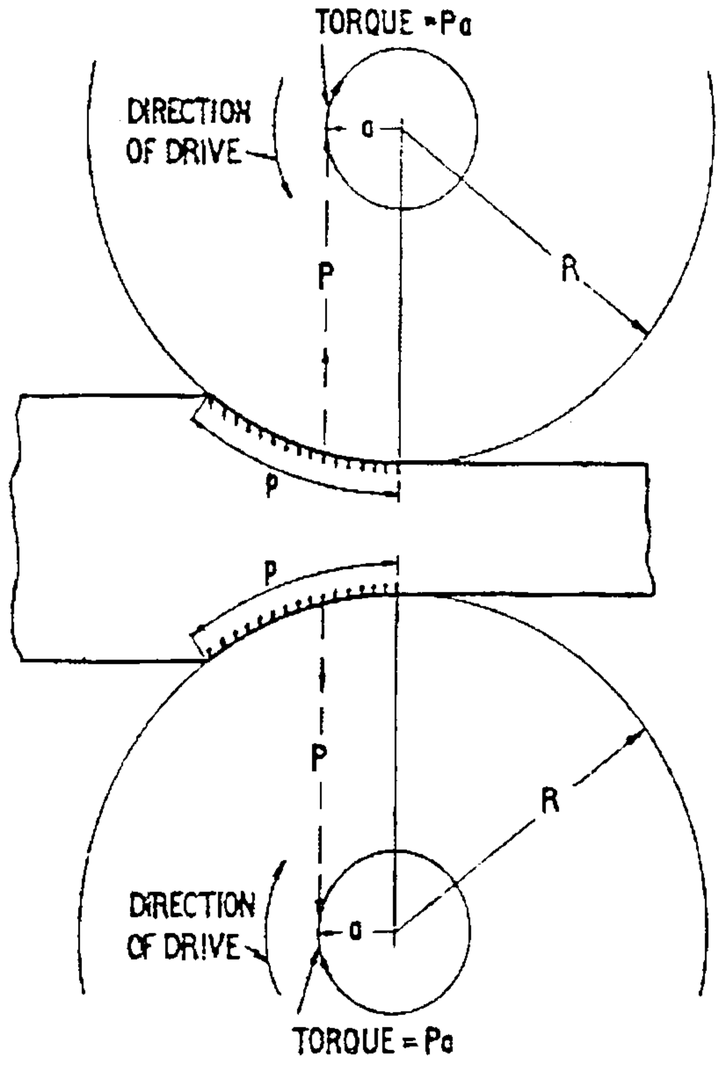

Fig. 6-2 Basic torque for both rolls equals 2Pa, work done for both rolls per revolution equals 4πPa (After Larke 1962)

6.2.13 The torque J

$$J = 2P'a \tag{6-20}$$

A schematic diagram is given in Fig.6-2 to illustrate the calculation of torque and the work.

6.2.14 Calculating the work done

$$w = 2J\phi_b \tag{6-21}$$

6.2.15 Entry bite angle (in radians)

$$\phi_b = \cos^{-1}\left(\frac{R' - 0.5 * dH}{R'}\right) \tag{6-22}$$

6.2.16 Volume of the material in the roll gap

$$V_{bite} = \frac{H_1 + H_2}{2} * \frac{W_1 + W_2}{2} * \sqrt{R' * dH} \tag{6-23}$$

6.2.17 Temperature rise of the slab due to plastic deformation

$$\Delta T_{mat} = \frac{\eta * J * \phi_b}{\rho c V_{bite}} \tag{6-24}$$

where η=0.95 is the coefficient of energy converted from the plastic deformation energy to heat, ρ is the slab density, c is the heat capacity.

6.2.18 Temperature loss to the rolls

$$\Delta T_{roll} = \frac{2\left[H_R\left(T_{mat} - T_{roll}\right)\right]\left(W_2\sqrt{R' * dH}\right)\left(\frac{\sqrt{R' * dH}}{V}\right)}{\rho * c * \left(W_2 * \sqrt{R' * dH}\right) * H_2} \tag{6-25}$$

where H_R is the conductive heat transfer coefficient between the rolls and the slab, T_{mat} is the last pass stock temperature in degree Kelvin.

6.2.19 Temperature loss at the slab tail

$$\Delta T_{tail} = \frac{\left(\sigma_r \lambda_r \left[T_{mat}^4 - T_{amb}^4 \right] t_{tail} . W_2 . L_2 + H_C \left[T_{mat} - T_{amb} \right]^{1.25} . t_{tail} . W_2 . L_2 \right)}{\rho * c * . \left(W_2 . L_2 . h_2 \right)} \tag{6-26}$$

where T_{amb} is the ambient temperature degree Kelvin, t_{tail} is the time of the slab tail exposed in air, H_C is the convective heat transfer coefficient between the stock and outside media such as rolling emulsion and air, σ_r is the Stephan-Boltzmann constant, λ_r is the emissivity.

6.2.20 Temperature loss at the slab leading edge

$$\Delta T_{lead} = \frac{\left(\sigma_r \lambda_r \left[T_{mat}^4 - T_{amb}^4 \right] t_{lead} . W_2 . L_2 + H_C \left[T_{mat} - T_{amb} \right]^{1.25} . t_{lead} . W_2 . L_2 \right)}{\rho * c * . \left(W_2 . L_2 . h_2 \right)} \tag{6-27}$$

6.2.21 The average pass temperature for the next pass T

$$T = T_{mat} + \Delta T_{mat} - \Delta T_{roll} - \left(\frac{\Delta T_{lead} + \Delta T_{tail}}{2} \right) \tag{6-28}$$

6.2.22 Power required for deforming the slab

$$K_{def} = \frac{4\pi N}{60} a P' \tag{6-29}$$

6.2.23 Power absorbed by the bearings

$$K_{bearing} = 4\pi * \frac{P'}{2} * \mu' * /10^3 * \frac{2\pi N}{60}(D_1 + D_2) \tag{6-30}$$

The friction coefficient μ' varies with the material of bearing. D_1 and D_2 are the diameters for work roll and back-up roll bearings respectively.

6.2.24 Total power required

$$K_{total} = K_{def} + K_{bearing} \tag{6-31}$$

6.2.25 The overload coefficient of power

$$O_p = K_{total} / K_{\lim} \tag{6-32}$$

where $K_{\lim}$ is the maximum power limit.

6.2.26 Time for the slab passing through the roll gap

$$t' = \frac{L_2}{V} \tag{6-33}$$

where V is the tangential roll speed.

6.2.27 Total time for an arbitrary pass

$$t_{total} = t' + t_{tail} \tag{6-34}$$

6.3 Verification by an industrial schedule

6.3.1 Hot rolling of AA3003

This design method for working rolling pass schedules is applied to an industrial rolling pass schedule in this section. The whole rolling pass schedule is given in

Table 24, from which the predictions and the measurements in terms of workpiece temperature, rolling load and total power are compared. The rolled material is aluminium alloy AA3003. The cast ingot is 580 mm thick, 5000 mm long and 1800 mm wide. The starting rolling temperature is 560^0C. The required exit thickness is 3 mm. Rolling is performed in a single stand four-high reversing mill. The nominal working roll diameter is 990mm. The diameters of working roll bearing and the supporting roll bearing are 660 mm and 950 mm respectively. The maximum roll load is 30MN, and the maximum power available is 7.360 kW.

From table 24, it can be seen that a total of 19 passes are required to produce a satisfactory product. The relative reduction for each pass increases steadily from the beginning to the end. To achieve a satisfactory rate, the roll speed also increases from the first pass and remains at the speed limit after pass 12 where plane strain conditions prevail. A coiling operation is performed in pass 17, 18 and 19. The shearing operation is conducted after pass 14. The definition of the gauge where shearing occurs and which passes are coiled are usually determined during the initial design of the mill.

The variations of the computed pass temperature, rolling load and total power for each pass are plotted in Fig.6-3 to Fig.6-5. It can be seen that Fig.6-3 shows that the temperature drops slowly for the first 12 passes where the slab is not long. Less time is spent on passage through the roll gap and exposes in the interpass time. As rolling continues, the slab gets longer. More time is spent on passing through the roll gap, hence the slab is exposed to air for a longer period. At the same time, as the slab gets thinner, the roll chilling effect becomes increasingly significant, resulting in a large temperature drop.

Table 24 Comparison between the prediction and the industrial measurement for hot rolling of aluminium alloy AA3003

Pass	H1 mm	H2 mm	DH mm		Roll Speed m/s	T (^{0}C) (Prediction)	T (^{0}C) (Measurement)	Load (MN) (Prediction)	Load (MN) (Measurement)	Power (kW) (Prediction)	Power (kW) (Measurement)
1	580	540	40		2.073451	560	560	8.499382	8.11	6.611	6.585
2	540	500	40		2.073451	556.8	555	8.464431	8.36	6.589	6.739
3	500	460	40		2.073451	553.3	550	8.438998	8.61	6.575	6.884
4	460	420	40		2.488141	549.5	545	8.746589	8.69	8.186	8.256
5	420	380	40		2.488141	546.3	540	8.703246	8.77	8.155	8.239
6	380	340	40		2.488141	542.8	535	8.680498	8.85	8.146	8.207
7	340	300	40		2.488141	538.9	530	8.687257	8.94	8.168	8.157
8	300	260	40		2.488141	534.6	525	8.737683	8.61	8.235	7.713
9	260	220	40		2.488141	529.6	520	8.855642	9.12	8.373	7.796
10	220	180	40		2.850995	523.8	515	9.320998	9.12	8.097	8.767
11	180	140	30		3.006504	517.5	510	9.737082	8.86	8.086	8.654
12	140	110	20		4.146902	509.9	496	9.441774	7.90	9.472	8.875
13	110	80	30		4.146902	504.2	484	8.829542	7.90	8.858	8.336
14	80	60	20	Shearing	4.146902	496.2	480	7.977888	6.45	6.658	5.237
15	60	45	15		4.146902	482.0	470	8.060992	7.76	5.917	5.145
16	45	30	15		4.146902	470.7	460	10.32844	10.86	7.547	6.73
17	30	15	15	Coiling	4.146902	454.8	450	14.05089	13.96	10.286	8.363
18	15	7	8	Coiling	4.146902	428.0	420	15.08451	13.59	8.641	5.947
19	7	3	4	Coiling	4.146902	405.0	380	11.99352	11.21	4.975	3.469

PAGE NUMBERING AS ORIGINAL

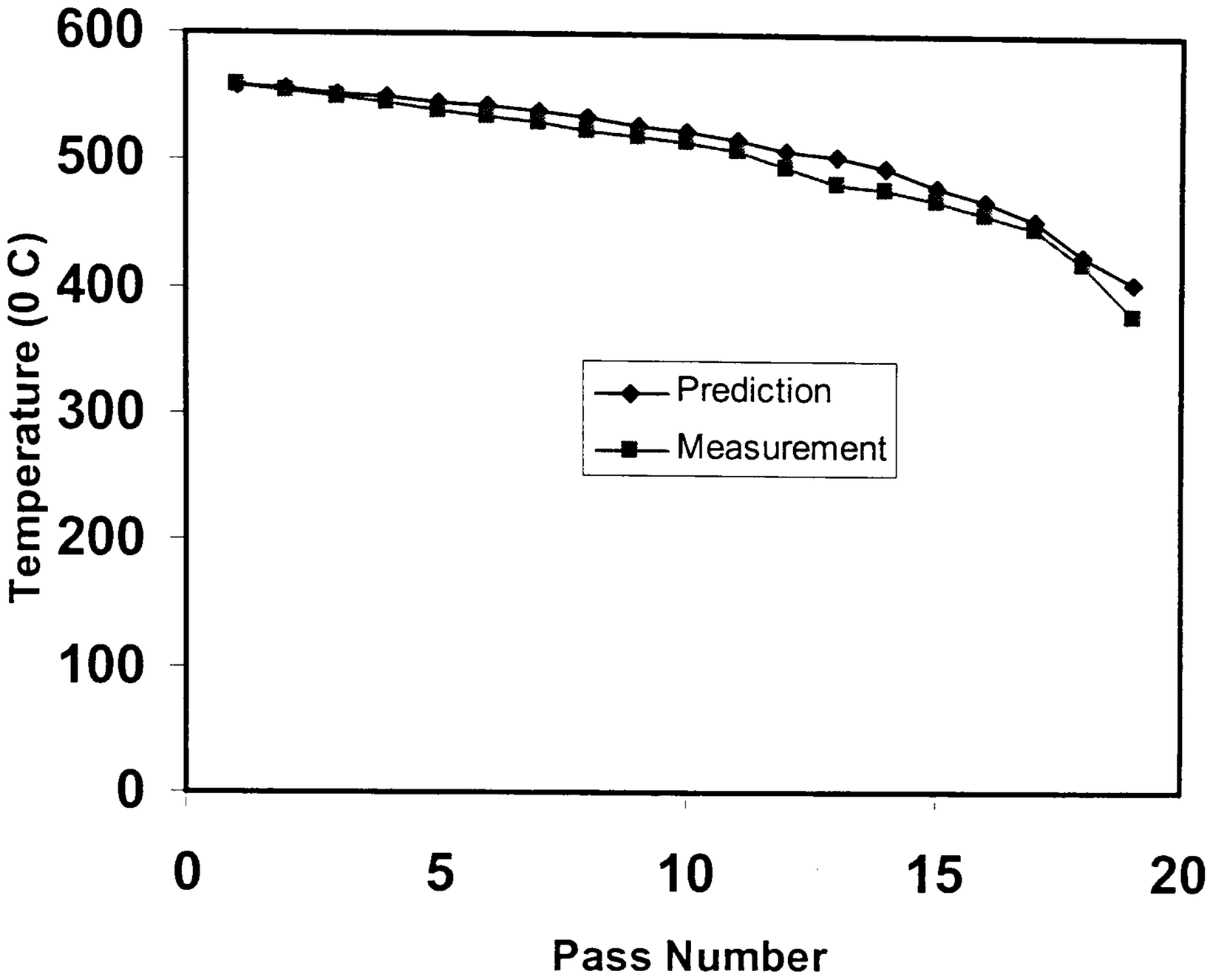

Fig.6-3 Comparison of the pass temperature for hot rolling of aluminium alloy AA3003

The predicted temperature corresponds very well with the industrial measurement in Fig.6-3. It should be noted that the measurement of temperature was conducted by radiation pyrometer. This implies that the measurement points locate at the surface. However, the calculated value of temperature is an average value, therefore it is not surprising that the calculated temperature is greater than the measurement. The difference between the two curves increases as the pass number increases. As reported in previous work chapter 4.5.4, the calculated temperature drop for the first two passes by using FEM is approximately 5^0C. This value fits with the measurement very well.

The heat transfer coefficient between the rolls and the slab used in the calculation of the average pass temperature is 100 $kWm^{-2}K^{-1}$. The choice of heat transfer coefficient in industrial hot rolling has been discussed in chapter 4. Here, only one point is emphasised: this coefficient varies with rolling conditions considerably. Other constants used in the formulae are chosen as

m=0.6,c=0.6, T_{roll}=373K, T_{amb}=313K, $\sigma_r = 5.67\times10^{-8}$, $\varepsilon_r = 0.5$, H_C=20 $kWm^{-2}K^{-1}$. Cooling time due to mill adjustment is set at 10 seconds between passes.

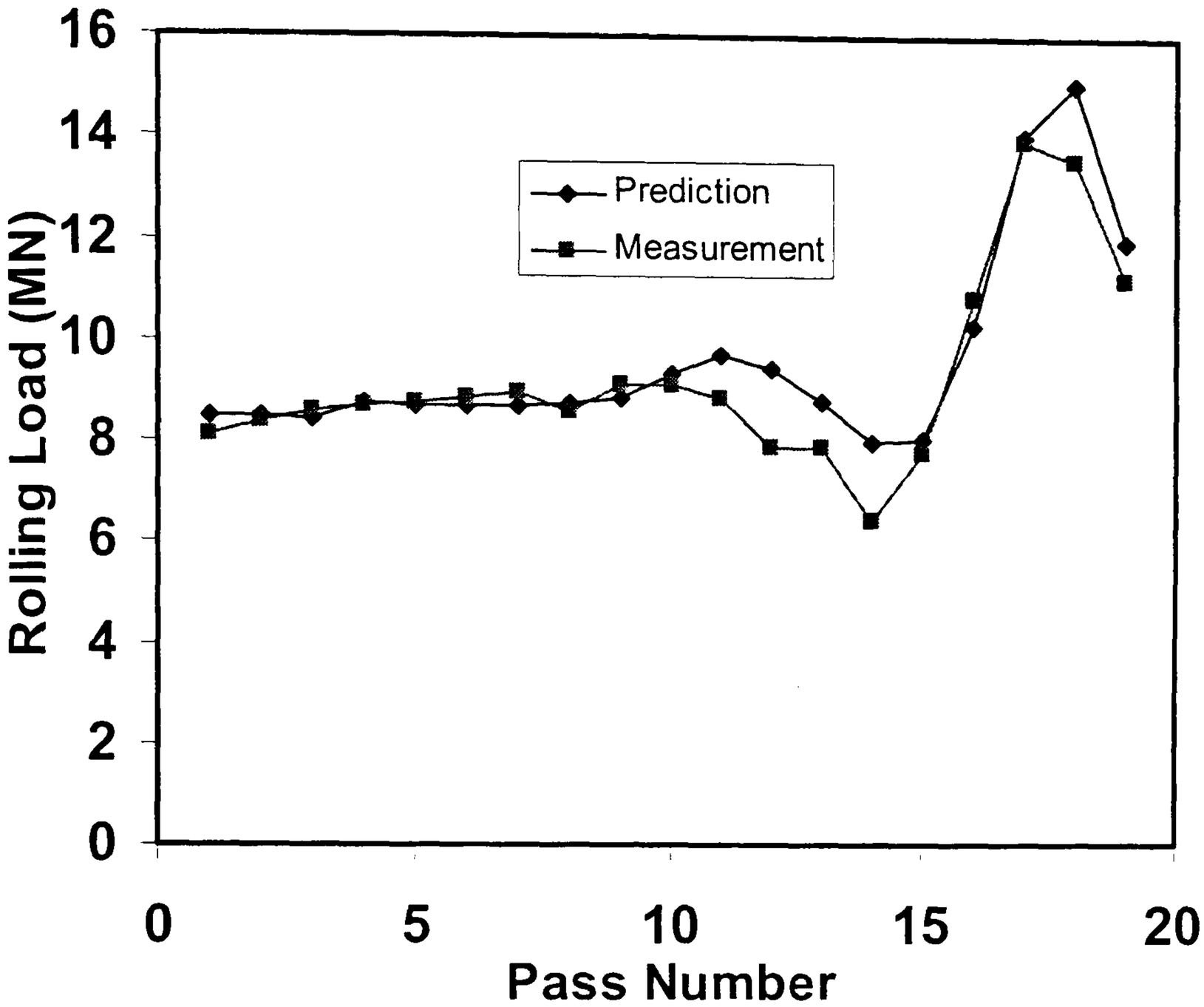

Fig.6-4 Comparison of the rolling load for hot rolling of aluminium alloy AA3003

Fig.6-4 clearly shows that the predicted rolling load also agrees very well with the measurement except pass 12 and pass 14. All rolling loads are less than the rolling load limit, 30MN. In this pass schedule, the power limit becomes the main constraint. To control the temperature variation and preventing edge cracking, the reduction can not be chosen by simply satisfying the limit of rolling load and power limit to pursue a maximum productivity, especially for the first few passes. This process is usually repeated several times to find the appropriate reduction and roll speed. Therefore, designing a pass schedule is not a simple mathematical optimisation problem. Many aspects must be considered and adjusted properly. The calculation of the rolling load is of paramount importance for industry. The greater the accuracy in the predicted rolling load, the less effort necessary is required in use of the gauge automatic control system. Higher product quality and less investment become a possibility.

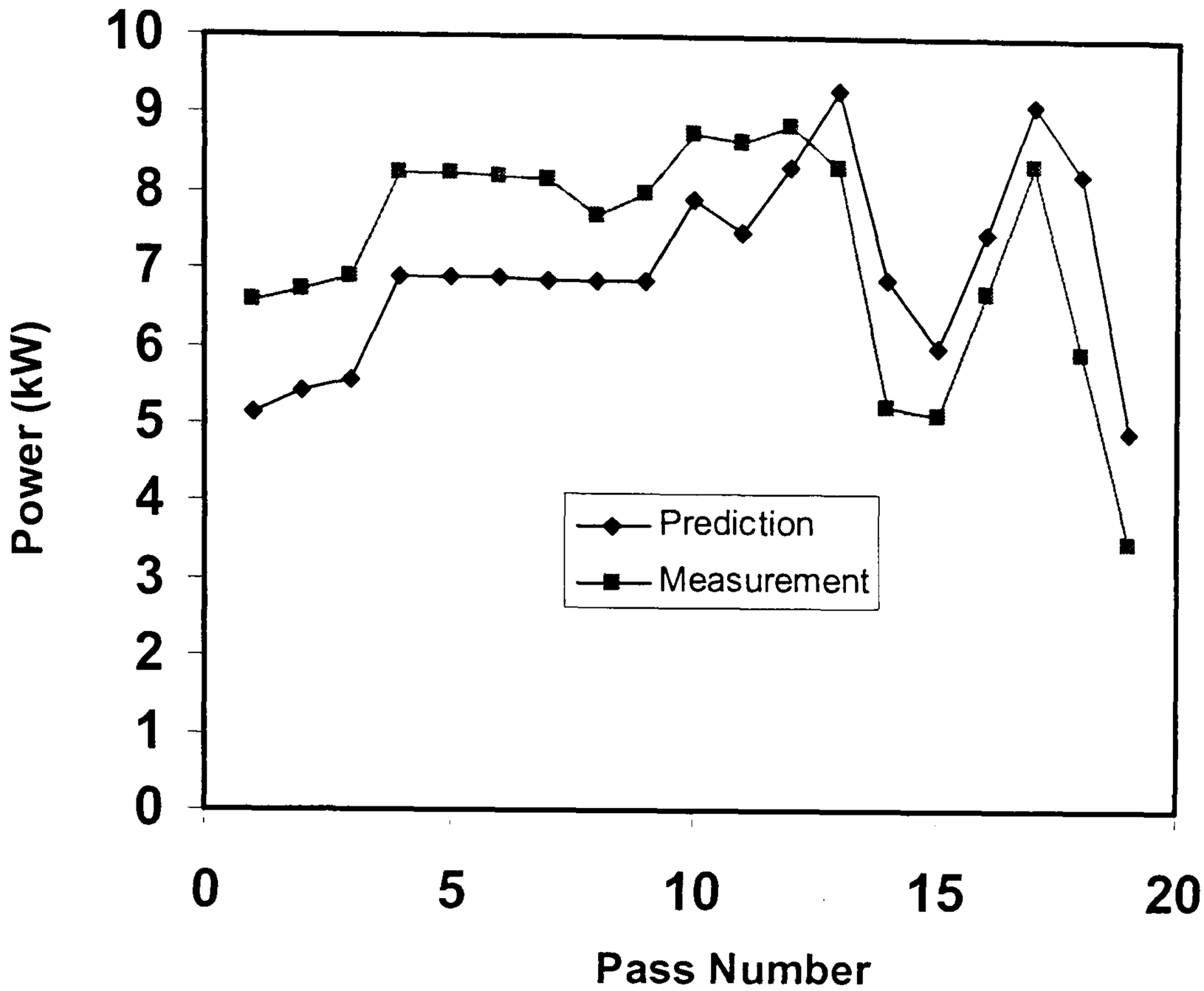

Fig.6-5 Comparison of the power for hot rolling of aluminium alloy AA3003

Fig.6-5 shows the comparison between the predicted and the measured power. A very good agreement is given. Generally, the prediction is slightly higher than the measurement. An underpowered unit is the most obvious risk since this will lead to a reduction in productivity due to stalling. Thus we must ensure that the motor is more than adequate for any immediate or future workloads.

6.3.2 Hot rolling of AA5052

This 19-pass schedule, see Table 25, is taken from the literature (Atack et al 1988). The material is aluminium alloy AA5052. The cast ingot is about 540 mm thick, 8173 mm long and 1371 mm wide. The starting rolling temperature is approximate 522^0C. The required exit thickness is 3.81 mm. Rolling is performed in a single stand four-high reversing mill. The nominal working roll diameter is 965mm.

The heat transfer coefficient between the rolls and the slab used in the calculation of the average pass temperature is 50 $kWm^{-2}K^{-1}$. Other constants used in the formulae are chosen as m=0.6, c=0.6, T_{roll}=373K, T_{amb}=313K, $\sigma_r = 5.67\times10^{-8}$, $\varepsilon_r = 0.5$, H_C=20 $kWm^{-2}K^{-1}$. Cooling time due to mill adjustment is taken from the measurement. The measurement of temperature was conducted by radiation pyrometer. Thus it is not surprising that higher predictions are given for the last few passes than the measurement.

The comparison of the computed histories of temperature, rolling load and power are shown in Fig. 6-6 to Fig.6-8. From these figures, it can be seen that a very good agreement with the measurement is shown.

From the above two examples, one conclusion can be drawn: the present temperature, rolling load and power model are reliable and show a fairly high accuracy.

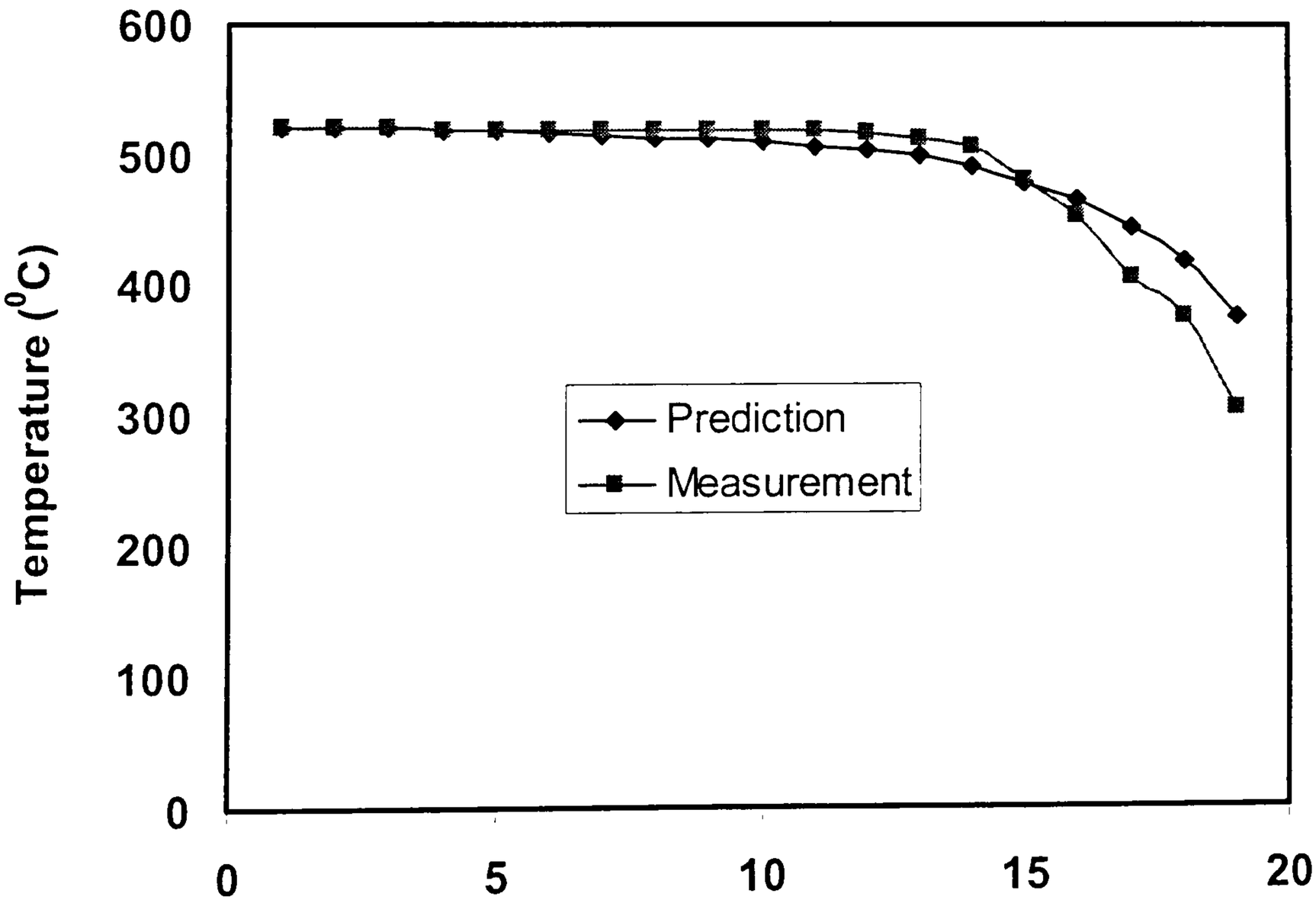

Fig.6-6 Comparison of the pass temperature for hot rolling of aluminium alloy AA5052

Table 25 Comparison between the prediction and the industrial measurement for hot rolling of aluminium alloy AA5052

Pass	H1 mm	H2 mm	DH mm	Roll Speed m/s	T (^{0}C) (Prediction)	T (^{0}C) (Measurement)	Load (MN) (Prediction)	Load (MN) (Maximum Measurement)	Load (MN) (Average Measurement)	Power (kW) (Prediction)	Power (kW) (Maximum Measurement)	Power (kW) (Average Measurement)
1	539.3	526.6	12.69	1.651	521.7	521.667	9.835781	10.51	9.244164	3.122	4.178	4.235
2	526.6	507.6	19.04	1.651	520.9	520.56	9.215166	10.36	9.099015	3.607	4.608	4.245
3	507.6	488.5	19.04	1.651	519.9	520	9.146797	10.15	8.835933	3.582	4.562	4.162
4	488.5	456.8	31.73	1.651	518.8	519.44	10.56121	11.6	10.52329	5.313	7.28	6.84
5	456.8	418.7	38.07	1.651	517.6	518.89	11.07683	11.81	10.73194	6.118	8.24	7.678
6	418.7	374.3	44.42	1.651	516.3	518.89	11.5454	12.11	10.65029	6.918	9.38	8.379
7	374.3	329.9	44.42	1.651	514.9	518.89	11.41874	11.5	10.47793	6.860	8.86	8.325
8	329.9	285.5	44.42	1.651	513.1	518.89	11.33675	11.4	10.27835	6.834	8.72	7.869
9	285.5	241.1	44.42	1.651	511.2	518.33	11.31863	10.74	10.11506	6.853	8.32	7.96
10	241.1	196.7	44.42	1.651	508.9	518.33	11.40419	11.05	9.842903	6.949	8.31	7.569
11	196.7	152.2	44.42	1.651	506.2	517.78	10.72411	11.11	9.842903	6.597	7.86	7.385
12	152.2	107.8	44.42	1.651	502.7	516.11	11.56029	12.16	10.49607	7.208	8.35	7.35
13	107.8	73.60	34.26	1.651	498.2	512.78	11.55488	12.91	9.770329	5.528	6.49	5.082
14	73.60	43.15	30.46	1.651	490.9	505	13.71904	16.75	12.6098	6.162	8.5	6.23
15	43.15	25.63	17.51	1.651	477.9	479.44	13.15413	16.08	12.26507	4.551	5.44	4.317
16	25.63	13.58	12.06	1.91516	464.9	451.67	15.57777	22.17	16.1478	5.210	5.25	4.855
17	13.58	8.63	4.95	2.02692	442.6	405.56	12.47336	17.86	11.72077	3.014	2.49	2.322
18	8.63	5.58	3.05	2.09804	417.9	375	13.29338	17.52	13.58048	2.840	2.32	2.085
19	5.58	3.81	1.78	2.13868	374.8	304.44	11.81982	14.57	10.18763	2.407	1.55	1.339

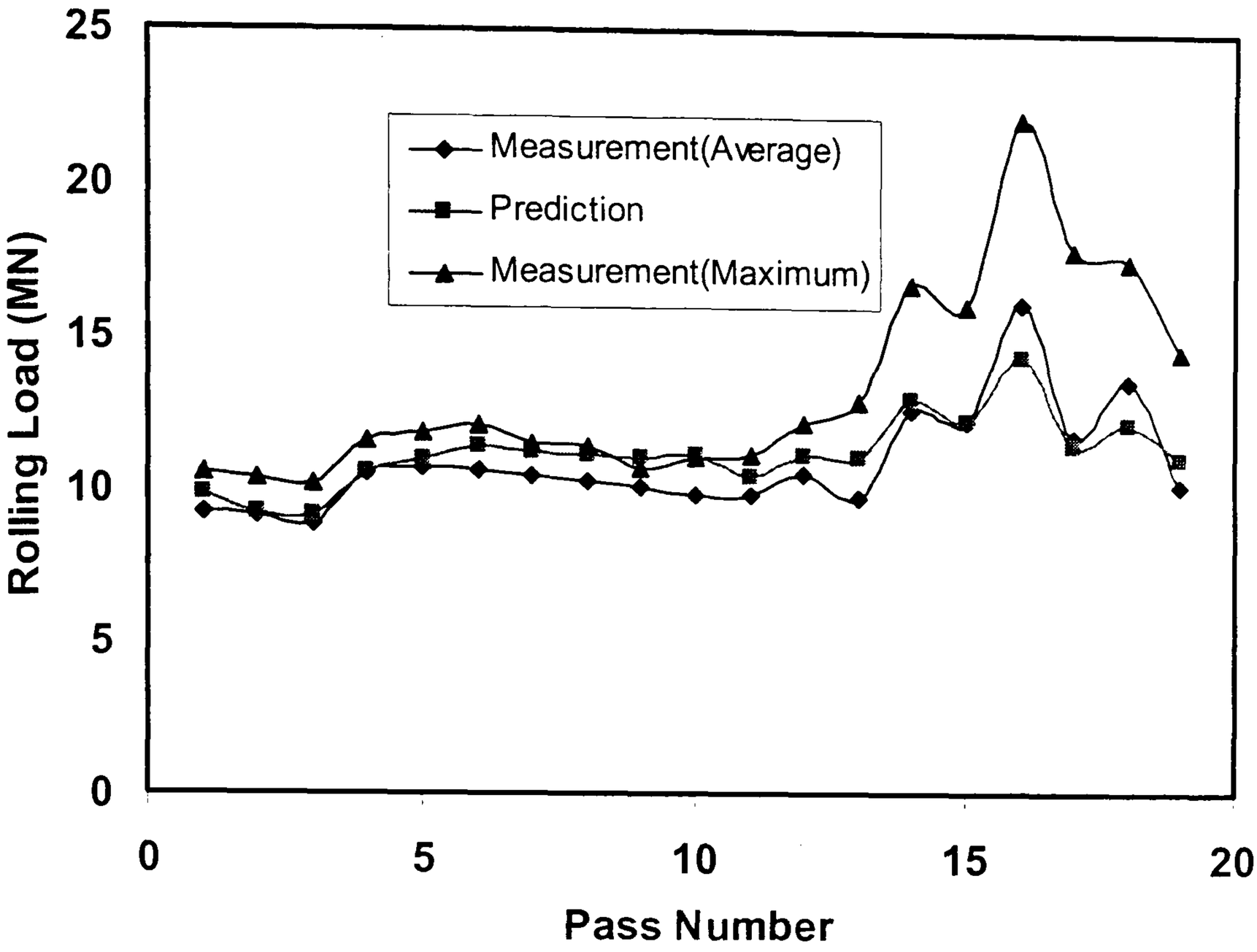

Fig.6-7 Comparison of the rolling load for hot rolling of aluminium alloy AA5052

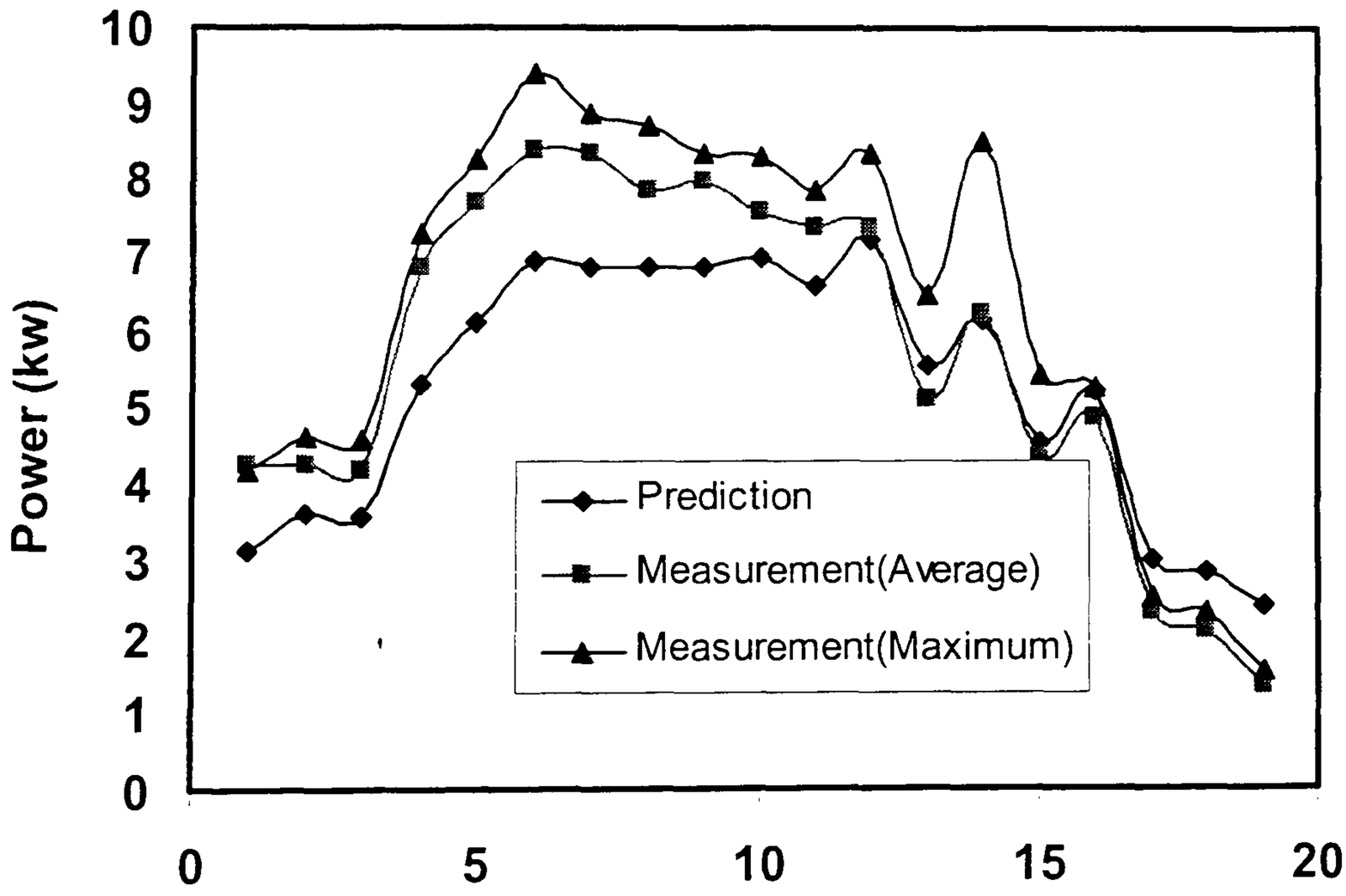

Fig.6-8 Comparison of the power for hot rolling of aluminium alloy AA5052

6.4 Comparison with industrial models

In this part, the rolling load of each pass of an industrial rolling pass schedule is also calculated by using the formulae presented. The results are then compared with those values predicted by using industrial models and FEA. This pass schedule was generated to produce a new kind of aluminium alloy plate in a single stand four-high reversing mill. No industrial measurements were conducted.

To avoid any possibility of leaking industrial sensitivity, some necessary mill setup parameters, such as the roll speed, the entry and exit thickness can not listed here. Only the computed rolling load and the average workpiece temperature are shown. For simplicity, predictions from two industrial models are abbreviated as "Ind1" and "Ind2" in the following figures. These two models are from two international well-known aluminium companies. It should be emphasised here that the present author knows nothing about their models. Only the predicted results are provided.

Table 26 Comparison between different rolling models

Pass	T (^{0}C) Present	T (^{0}C) "Ind1"	T (^{0}C) "Ind2"	P (MN) Present	P (MN) "Ind1"	P (MN) "Ind2"	P (MN) FEA
1	283	283	276	17.1215	18.45	15.5	18.33
2	277.698	279	270	17.6393	18.76	15.3	19.07
3	276.065	277	267	24.9643	26.26	22	27.26
4	277.376	278	263	23.9578	25.92	21.33	27.24
5	277.962	279	256	23.0938	25.3	20.33	27.41
6	277.789	279	252	22.3626	24.6	19	24.91
7	276.818	277	244	21.7006	23.89	18.17	22.47
8	274.972	275	239	21.0306	22.03	16.67	19.72
9	274.963	274	233	20.1967	21.03	15.6	17.54
10	273.853	271	226	19.4054	20.04	15	15.81
11	271.552	268	218	18.7377	19.16	13.67	14.03

This is plate rolling. The initial plate thickness is 50mm and the exit gauge after pass 11 is 15.81mm. The initial width and length are 2100mm and 2000mm respectively. After pass 11, the plate length is approximately 6.3m. There is no coiling operation. The ratio W_1/H_1 equals 42. Hence no width variation is assumed. A plane strain model is used in the FEM simulation. The rolling pass schedule is analysed pass by pass. The effects of softening caused by either static recrystallisation or recovery are ignored. Hence, the equivalent strain is accumulated from the beginning to the end. The rolled material is aluminium alloy AA5083. The calculated rolling load and pass temperature are shown in Table 26. The comparison of the rolling load is given in Fig.6-9. From this figure, it can be seen that the load curve given by the present work locates between two industrial predictions, approaches the curve "Ind1" more closely. This indicates that the present load model is comparable with those industrial models. The computed load curve by using FEA shows similar shape and corresponds very well with the curve "Ind1" before pass 9, and approaches the curve "Ind2" in the remaining passes. The result seems to be a comprise between the curve "Ind1" and the curve "Ind2".

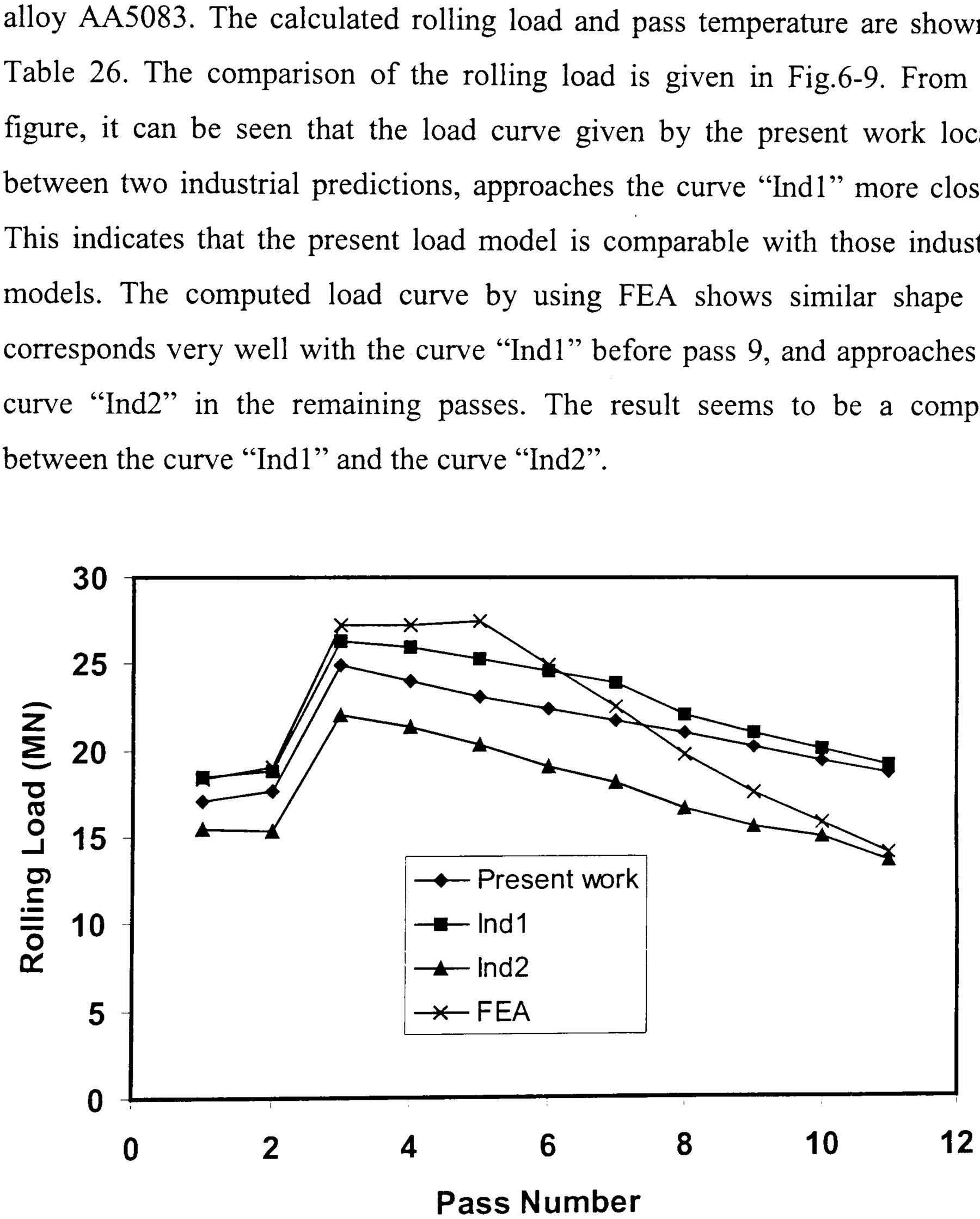

Fig.6-9 Comparison of the rolling load predicted by different methods (Ind1 and Ind2 are the abbreviation of industrial model 1, and industrial model 2 respectively)

The change of pass temperature in the whole rolling chain is illustrated in Fig.6-10. The heat transfer coefficient between the rolls and the stock used in this pass schedule is 40 $kWm^{-2}K^{-1}$. Other constants are chosen as m=0.6, c=0.6, T_{roll}=358K, T_{amb}=313K, $\sigma_r = 5.67\times10^{-8}$, $\varepsilon_r = 0.5$, H_C=20 $kWm^{-2}K^{-1}$, $d_0 = 100\ \mu m$. Cooling time due to mill adjustment is set as 10 seconds between passes. The temperature values predicted by the use of present method are nearly the same as those predictions by "Ind1". Industrial model "Ind2" predicts low temperature values than other two models, and controversially gives however gives a much lower rolling load, especially in the latter passes. There are great differences between the two industrial models. This shows that the design of rolling pass schedule is not an easy task even for those larger companies who have a considerable amount of industrial data.

It should be noted that static recrystallisation is not considered in the calculation by using the aforementioned schedule models because the rolling is carried out at lower temperature. The static recrystallisation is also not taken into account in the FEA.

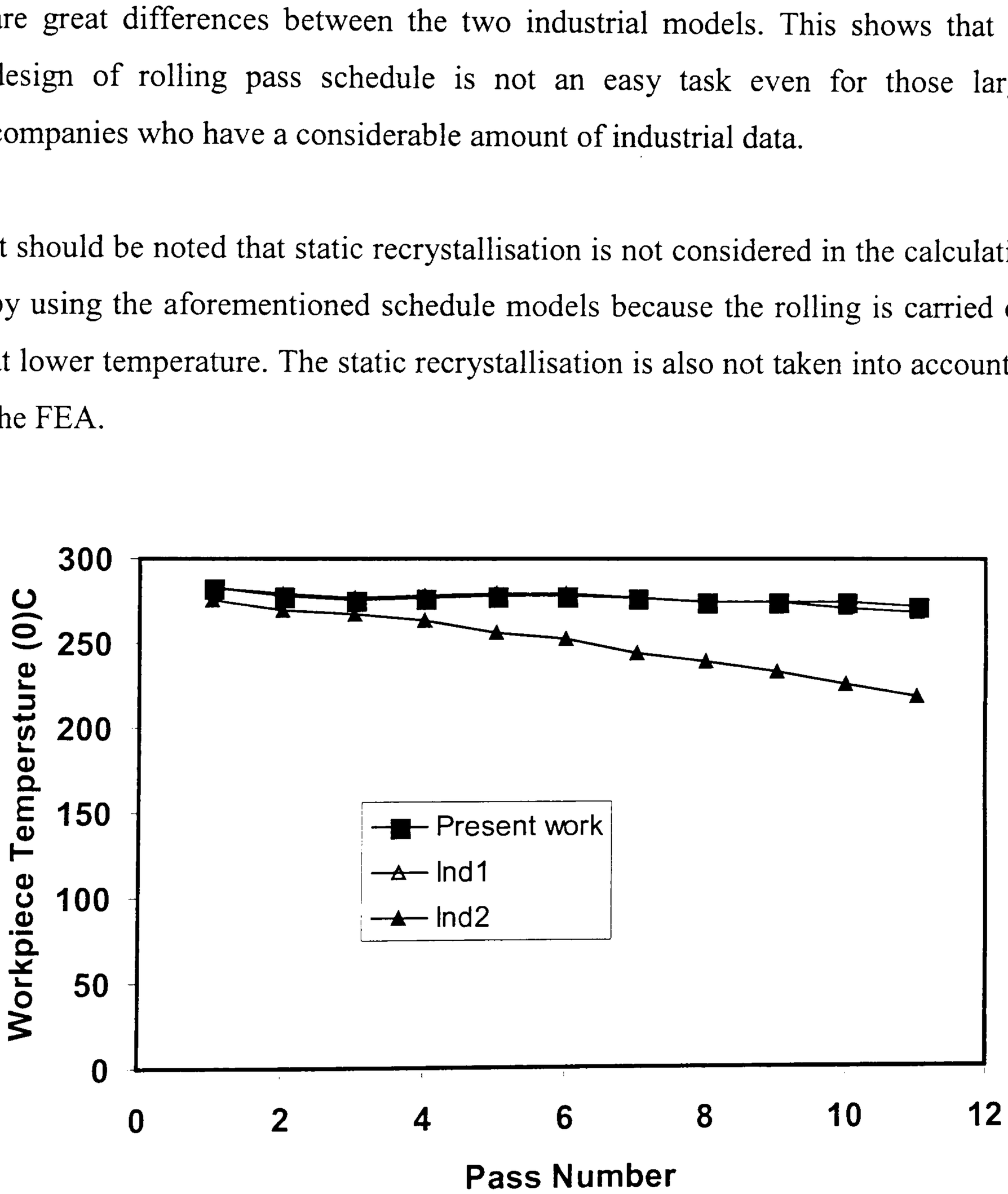

Fig. 6-10 Comparison of the workpiece temperature(Ind1 and Ind2 are the abbreviation of industrial model 1, and industrial model 2 respectively)

6.5 Problems in the multi-pass simulation by using FEM

Modelling the multi-pass hot rolling by using FEM is not an easy task. The complicated relationship of the flow stress, microstructure, temperature, and the equivalent strain all has to be considered simultaneously. Lack of precise data of any aspect may cause computing errors. However, due to the dearth of sufficient industrial data and the complex nature, the work in the simulation of multipass hot rolling of aluminium alloys is an emerging technology. It is therefore normal to ignore one or two factors.

The main drawback of the finite element analyses in this pass schedule is the difficulty of consideration of static recrystallisation and recovery between passes. In other words, the influence of the microstructure variation on the flow stress is not fully taken into account. From the view of finite element computation, the problem is reflected in how to deal with the accumulated equivalent strain. In hot rolling process, it is generally accepted that the softening mechanism is mainly caused by recrystallisation. Recovery only plays a very minor role and hence it is always omitted. If recrystallisation is assumed to have little effect on the flow stress, the strain can be accumulated pass by pass. If recrystallisation occurs and is considered, the total strain will be reduced by the X ($0 \le X \le 1$)*100 percent of the recrystallisation. The remaining strain passed into next pass is $(1-X)\varepsilon_T$, where ε_T is the total strain.

According to the work by Winden (1999) and Mirza et al (2001) static recrystallisation does not occur during the first six passes in the industrial hot rolling of AA3104. Hence the strain can be accumulated directly. For the first seven passes, the computed rolling load from FEA should not be doubted if all boundary conditions, and the mechanical and thermal properties are applied properly. From Fig.6-9, it can be seen that the FEA slightly overpredicts the rolling load for the first seven passes. The reason is that the local deformation variables, such as temperature and strain rate, are adopted for the calculation of the flow stress in FEA. In the plate surface, the local strain rate is usually greater

than the averaged value in the roll gap and the local temperature is lower than the averaged pass temperature. Hence the calculation of load by FEA is likely to be greater than by the normal pass schedule. These pass schedules are usually subjected to arbitrary constants to overcome this problem.

The effect of the accumulated equivalent strain on the computed rolling load is accomplished by changing the flow stress through two ways. For those kinds of constitutive equations that include the strain term, such as Norton-Hoff law (see equation (6-6)), the influence of the strain on the flow stress is obvious. The second way is more complicated. In metal forming, it is generally accepted that more than 90% deformation energy is dissipated into heat. The plastic deformation work can be simply calculated by

$$W = \bar{\sigma} * \bar{\varepsilon} \tag{6-35}$$

This means that the greater the accumulated equivalent strain, the more plastic deformation work is done, the more heat is generated, and hence the possibility of higher temperatures. The flow stress is therefore reduced. This description can reasonably explain the decline of the rolling load curve predicted by FEA for the later rolling passes in Fig.6-9.

According to the latest study on multi-pass simulation for aluminium alloy AA3104 by Mirza et al (2001), "the formation of statically recrystallised material would not significantly change the actual flow stress behaviour in the subsequent passes". This conclusion indicates that the simulation of static recrystallisation can be omitted. Although this conclusion is very helpful for the present authors because of lack of data, the reader should wary of such an assumption. There are several dubious points in Mirza et al's work and those problems could contradict his conclusions. It is essential and urgent to carry out the relevant work on the microstructural evolution during multipass rolling either by empirical models or physical models.

Chapter 7 Conclusions and Recommendation for Further Work

7.1 Conclusions

On the friction, pressure, stress and strain in the breakdown rolling

The Viscoplastic friction law is slightly better than the Coulomb and Tresca friction law in terms of predicting rolling load and torque. The maximum pressure in the roll gap occurs near the entry. The deformation is mainly concentrated near the roll/slab interface and does not penetrate into the slab centre. There are two dimensional tensile stress in the slab centre, which might tend to cause microcracks if the slab quality is not good, or if a small reduction is applied.

On the temperature changes during multi-pass rolling

The FD and the analytical approach always under-predict the surface temperature of the slab, and when the ratio of roll radius/slab thickness decrease, the predicted precision improves. The predicted temperature value in the slab centre by the FD fits well with the measured temperature, but there is a high level of error when using the analytical approach due to the omission of heat generation and friction work. The temperature distribution in the slab predicted by the FEM would appear to be the most accurate.

Due to the limitation of equipment capacity, the slab used in laboratory experiments is usually small. The thermal mass of the slab is much lower than the thermal mass of rolls. The chill effect is significant, resulting in a large temperature drop even in the slab centre. In the early passes of industrial rolling, the thermal mass of the slab is of the same order as the rolls and the chill effect is not obvious. Contrary to laboratory rolling, the temperature in the slab centre remains sensibly constant even after 2 passes. To minimise the striking difference in temperature between

laboratory and industrial rolling, new experimental techniques such as SMART (Winden 1999) could be used.

Thermomechanical coupled FEM is essential for simulating the laboratory rolling, where there is a great temperature difference from surface to centre. Since FEM may also deal more easily with three-dimensional problems, it should also be the preferred method for industrial application. Computer times may be significantly reduced by the use of the inverse method coupled with the omission of very fine meshes.

On the lateral deformation

The significant difference in spread behaviour between the slab surface and the slab centre confirms the need to employ a three-dimensional FEM programme to analyse the slab rolling processes.

The equation $\frac{\sqrt{R\delta}}{H1} < C \pm 0.06$ is valid for the prediction of the lateral profile. For the early passes in the industrial rolling practice, all existing spread formulae, except Winden's formula, fail to predict the spread. However Winden's formula does not give a good prediction for laboratory experimental result and may not be applicable when considering a variety of mills and roll passes because it only considers the less important influence factors, the reduction, but neglects the most important factor, the ratio of width to the slab thickness.

The lateral profile is sensitive to the change of friction coefficient in industrial rolling but not in laboratory rolling. The reason may arise from the different

temperature distribution through the slab thickness promoting sticking at the slab/roll interface.

It is a common phenomenon that the slab profile appears to be concave in commercial rolling. FEA can replace the laboratory or industrial experiments totally for the development of a spread formula.

Through integrating FEA with the Taguchi experimental design method, it is found that the ratio of width to thickness has overwhelming influence on the spread, followed by the thickness reduction, the ratio of the roll radius to thickness and the slab temperature.

Based on a large amount of FE analyses and the carefully measured experimental data from the literature, a new spread formula is constructed. The new formula is capable of dealing with both laboratory and industrial rolling with high accuracy. The new formula is written as

$$Ln\frac{W_2}{W_1} = 0.2187 * \left(e^{0.1071*\left(\frac{W_1}{\sqrt{R*dh}}\right)} \right) \left(\frac{R}{H_1}\right)^{-0.848} \left(\frac{W_1}{H_1}\right)^{-1.481} \left(\frac{H_m}{L}\right)^{-2.6978}$$

On the prediction of subgrain size

Subgrain size can be modelled accurately by FEM provided that the correct methodology is followed. In the prediction of microstructural evolution, accurate prediction of temperature is vital. Aberrant results are given when empirical models are applied directly into FEM without any modification. Previous work by Dashwood et al and Chen et al. all failed to give rational explanation to the modification made to these two equations. The empirical model is not suitable for the prediction of subgrain evolution since it is established in the steady state regime

and is just a statistical relationship. The physical model based on temperature, increment of strain, strain rate and previous state of subgrain size can predict accurate distribution of subgrain size under hot working conditions and widely varying parameter. Metallurgical experiments are essential to determine some parameters, such as the steady state subgrain size, the initial subgrain size, and the characteristic strain. The equation $\mathrm{d}\delta = \frac{\delta}{\varepsilon_\delta \delta_{ss}}(\delta_{ss} - \delta)\mathrm{d}\varepsilon$ is still not mature. More metallurgical work is required to relate the subgrain size with internal dislocation density.

On the modelling of dislocation density, misorientation and the work hardening behaviour

Various physical models have been successfully linked with the commercial FEM code. The predicted results, i.e. subgrain size, dislocation density, misorientation and the flow stress, fit well with the experimental observation. It indicates that the present research thoughts are feasible. Integrating the physical models to the FEM code enables simulation to be more precise. It provides industry with a powerful tool to improve and optimise the existing processes.

On the modelling of static recrystallisation

Altering the strain, or using the "instantaneous Z", or averaging the "instantaneous Z" with time can not reconcile the prediction with the measurement effectively, while averaging the "averaged Z" on the basis of strain can significantly improve the prediction accuracy. Averaging the history of Z on the basis of increments of strain gives better prediction than averaging Z on the basis of time. Changing the methods in summing strain components is not recommended since all equivalent strains should theoretically be the same if the time increment is small enough in FEA. Except Liserre and Goncalves's model, all remaining empirical models give

reasonable prediction after tuning the models for the measurement value at the centre. Sheppard et al's model gives the best agreement with the experimental measurement. This implies that the empirical model should be established by rolling test. It also indicates that the empirical models available are not appropriate for the prediction of the kinetics of static recrystallisation when numerical computation is adopted. The analysis of variance shows that the most significant SRX parameter is the rolling temperature, which accounts for 84% for the X_{V} at the centre and 77.3% at the sub-surface, followed by the H_m / L. The influence of roll temperature and roll speed have negligible influence on the X_V.

On the design of rolling pass schedule

Good agreement with FEM results and the industrial measurement shows that the present method for the design of a rolling pass schedule is reliable and is comparable with those models used by large companies. The marked difference between predictions by the use of different industrial models indicate that the design of rolling pass schedule is not an easy task even for those industrial company that have access to huge amounts of industrial data. The temperature, rolling load and power model given in this chapter show very high accuracy.

7.2 Recommendation for further work

On the flow stress

Neither the Norton-Hoff law or the hyperbolic sine function is the best choice for the whole breakdown rolling process where the temperature varies from 560^0C to 300^0C. There are two other more suitable empirical models which are worth trying:

Hensel and Spittel's and Voce's model. We should note that Hensel and Spittel's model has been set as one of the default constitutive equations in the latest version of FORGE3 and FORGE2. A new material database has also been provided for various aluminium alloys.

The ideal way to cope with the flow stress is in using the physical model, which is based on dislocation density, subgrain size and misorientation.

On the simulation of the breakdown rolling

The prediction precision can further be improved by adopting a function of heat transfer coefficient, and a function of friction coefficient. Using a mean value for heat transfer coefficient can not reflect the actual conditions that the heat transfer coefficient experiences. A function of pressure and temperature should be established for heat transfer coefficient. The condition for friction is even more complicated. The function of temperature, reduction should also be established for the friction coefficient.

On the simulation of microstructure evolution

A series of experiments need to be carried out to validate the prediction of dislocation density, misorientation and the flow stress. The mechanism of initial development of subgrains (i.e from individual dislocations to networks to subgrains) should be established. Various testing methods (i.e. plane strain compression, rolling and torsion) should be systematically studied, and establish procedures for experimental testing to establish reliable SRX models. Further work is using the physical to simulate SRX and texture evolution.

On the design of rolling pass schedule

The accuracy of the power model needs to be improved. A new formula for the calculation of lever arm should be proposed. Extending the present pass scheduling package from for a single stand reversing mill to for three or four stands tandem rolling is the next object. Designing an expert system and making the package friendly to the user would make the design package more commercial.

Appendix 1. Constants used in equation (2-23)

Material.	a	b	m	Process of measurement	Equation	Reference
AA1100	-0.196	0.0153	1	rolling	Eq. (23)	Zaidi et al 1982
AA2014	-1.747	0.096	1	Direct extrusion	Eq. (23)	Vierod 1983
AA2014	-1.586	0.085	1	Indirect extrusion	Eq. (23)	Vierod 1983
AA2024	-0.5778	0.0378	1	Direct extrusion	Eq. (23)	Subramaniyan 1989
AA2024	-0.6457	0.0426	1	Indirect extrusion	Eq. (23)	Subramaniyan 1989
AA3003	-0.76	0.045	1	rolling	Eq. (23)	Hollinshead 1986
AA3004	-1.24	0.058	1	Rolling	Eq. (23)	Hollinshead 1986
AA3004	0.026	0.06			Eq.(27)	Vatne 1995
AA5056	0.062	0.205	1	rolling	Eq. (24)	Raghunathan 1986
AA5056	1.667	0.03	1	rolling C=0.32	Eq. (25)	Raghunathan 1986
AA5083	0.059	0.122	1	rolling	Eq. (24)	Raghunathan 1986
AA7075	-0.54	0.023	2	Direct extrusion	Eq. (23)	Dashwood 1996
Al-1%Mg	-3.36	0.136	1	Plane stain compression	Eq. (23)	Furu et. al. 1999

Appendix 2 Various empirical models for static recrystallisation

The time to 50% recrystallisation

$$t_{0.5} = A d_0^a \varepsilon^b Z^c \exp\left(\frac{Q_{rex}}{RT_a}\right) - B$$

The fraction of static recrystallisation (X)

$$X = 1 - \exp\left\{-\ln 2\left(\frac{t}{t_{0.5}}\right)^k\right\}$$

Material	A	a	b	c	Q_{rex}	k	B	Source
Commercial Purity Aluminium	1.5×10^{-4}	0	-1.5	-0.75	220000	2	0	Gutierrez et al 1988
Commercial Purity Aluminium	9.85×10^{-6}	0	-1.5	-0.75	220000	2	-6924	Liserre et al 1998
High purity Al-3%Mg	?	0	-2.7	-1.1	205000	1.75	0	Dauda & McLaren 1999
Commercial Al-1%Mg	9.8×10^{-6}	1.35	-2.7	-1.1	230000	2	0	Sellars et al 1985
AA5182	8.34×10^{-7}	1.35	-0.93	-0.73	200000	2	0	Wells et al 1998
AA5052	1.25×10^{-6}	1.35	-1.023	-0.66	200000	2	0	Wells et al 1998

Sheppard et al's formulae (1986)

The time to 50% recrystallisation

$$t_{0.5} = A d_0^a \left(B + C\varepsilon^b\right)^c Z^d \exp\left(\frac{Q_{rex}}{RT_a}\right)$$

The fraction of static recrystallisation (X)

$$X = 1 - \exp\left\{-\ln 2\left(\frac{t}{t_{0.5}}\right)^k\right\}$$

Material	A	B	C	a	b	c	d	Q_{rex}
AA5056	9.1×10^{-12}	0.0286	1.8	1.52	2	-1	-0.35	212000
AA5083	2.7×10^{-10}	9.75	3.82	2.45	2	-1	-0.58	183000

Appendix 3

Constants in the constitutive equation for some Al-alloys

(Sheppard 1999)

$$\bar{\sigma} = \frac{1}{\alpha} Ln\left\{\left(\frac{Z}{A}\right)^{\frac{1}{n}} + \sqrt{\left(\frac{Z}{A}\right)^{\frac{2}{n}} + 1}\right\} \quad \text{and} \quad Z = \dot{\bar{\varepsilon}} \cdot \exp\left(\frac{Q_{def}}{GT}\right)$$

Alloy	α	n	Q_{def}	G	lnA	Remarks
1S	0.04	3.84	157000	8.314	26.66	
1050	0.037	3.84	156888	8.314	26.69	
1100	0.045	5.66	158300	8.314	24.67	
2011	0.037	3.712	142000	8.314	19.2	
2014	0.0128	5.13	131309	8.314	22.23	
2014*	0.0152	5.27	144408	8.314	24.41	PH.-SS
2014**	0.0283	3.49	128913	8.314	21.959	4% Cu
2024	0.016	4.27	148880	8.314	19.6	
3003	0.0316	4.45	164800	8.314	26.9	
3004	0.0344	3.6	193850	8.314	28.21	
3005	0.0323	4.96	183100	8.314	29.87	
3105	0.0248	4.83	179300	8.314	29.98	
4047	0.04	2.65	129300	8.314	20.47	
5005	0.029	5.8	183576	8.314	26.65	
M57S	0.02	5.1	155000	8.314	24.20	
5052	0.016	5.24	155167	8.314	24.47	
5054	0.015	5.43	173600	8.314	26.61	
5056	0.015	4.82	166900	8.314	23.05	
5083	0.015	4.99	171400	8.314	23.11	
5182	0.062	1.35	174200	8.314	22.48	
5456	0.0191	3.2	161177	8.314	23.5	
6061	0.045	3.55	145000	8.314	19.3	
6063	0.04	5.385	141550	8.314	22.5	
6105	0.045	3.502	145000	8.314	20.51	
7004	0.035	1.28	153000	8.314	20.12	
7050	0.0269	2.86	151500	8.314	22.85	
7075H1	0.0141	5.41	129400	8.314	20.75	24hr.Soak
7075H2	0.01	6.14	158432	8.314	26.32	Sl.Ht.-F.Cool
7075H3	0.012	7.8	155336	8.314	27.54	F.Ht-Sl.Cool
7075H4	0.01	8.5	156325	8.314	27.14	F.Ht-F.Cool
7150H1	0.01	5.7	161402	8.314	29.8	F.Ht-F.Cool
7150H2	0.013	6.1	158806	8.314	29.2	F.Ht-Sl.Cool
7150H3	0.01	5.5	159832	8.314	30.7	Sl.Ht-F.Cool

Appendix 4

Chemical composition of various aluminium alloys used in the present thesis, in weight%

Material	Si	Fe	Cu	Mn	Mg	Cr	Zn	Ti	Al.	Reference
Purity Al.	0.04	0.15	0.001	0.002	0.001		0.012	0.012	Bal.	Zaidi 1982
Purity Al.	0.11	0.2	0.001	0.004	0.001	0.002	0.002	0.013	Bal.	McLaren 1994
AA2014	0.78	0.2	4	0.78	0.47		0.02	0.013	Bal.	Vierod 1983
AA3003	0.21	0.63	0.13	1.14	0.01		0.01	0.01	Bal.	Hollinshead 1985
AA5051	0.17	0.3	<0.01	0.26	2.0		0.01	0.01	Bal.	Wright 1978
AA5083	0.2	0.2	0.05	0.7	4.45	0.15	0.125	0.075		
AA7075	0.4	0.5	0.6	0.3	3		4	0.2	Bal.	Wright 1978

Appendix 5

Experimental data of the flow stress measured by hot torsion for 4% Cu binary 2014 alloy (Vierod 1983)

Strain rate (s^{-1})	Temperature (^0C)	Actual stress (Mpa)
0.032	300	50.23
2.507	303	93.13
28.768	311	115.85
28.443	312	115.23
0.032	350	32.69
2.633	357	69.46
28.443	360	93.45
28.443	360	93.45
0.032	390	23.37
0.305	391	38.05
2.669	395	55.83
8.567	397	66.65
29.129	400	78.27
0.032	430	17.06
0.305	431	28.67
2.687	433	44.64
8.567	436	54.28
29.472	436	66.4
0.032	475	12.34
0.31	476	21.26
2.76	477	34.64
8.567	478	43.41
29.472	480	54

Appendix 6 Measured width profile (after Wright 1978)

D8A	KG3A	KG3B	KG7A	KG7B	KG13A	KG13B	KG13C
0	0	0	0	0	0	0	0
0.63	1.5	2	3	2	4	9	3
1.1	2	2.5	4	4	8	13	5
1.45	2	3	5	5	12	16	8
1.77	1	1	7	6	14	18	10
2	-1	-0.5	6	6	15	20	12
2.16	-3	-2	7	6	18	22	13
2.3	-4	-4	8.5	6	21	22	15
2.35	-6	-8	7.5	6	23	25	15
2.37	-9	-10	7.5	5.5	26	26	17
2.35	-10	-11	8	5	28	27	17.5
2.25	-11	-13	8	5	28	29	19
2.11	-11	-14	8	5	29	30	20
1.9	-12	-15	8	6	30	30.5	20
1.66	-13	-15	8.5	6	33	31.5	20
1.35	-13	-14	7.7	5	33	32	20
0.95	-13	-13	7.7	5	34	33	21
0.88	-12	-12	7.5	5	35	33	21
0	-11.5	-9	7.5	5	35	34	21
17.5*	-10	-7	7.5	5	36	34	21
25.58**	-8.5	-5	7.7	5.2	36	35	20
25.44***	-7	-2	7.7	5.4	36	35	20
	-5	-0.5	8	5.5	36	34	20
	-1	0.5	8	6	36	35	20
	-1	1	7.5	6	36	34	19
	1	0	7.5	6	35	34	18
	1.2	206*	7.2	6	35	33	17
	1.5	1188**	7	6	34	33	16
	0	1188***	7.5	6	33	32	15
	228*		7.3	5	33	31	13
	1179**		7	5	31	30	12

	1179***		5	3.2	30	29	10
			5	0	28	27	9
			4	253.4*	27	27	7
			2.5	1326**	25	24	4
			0	1326***	23	22	0
			286*		21	20	275*
			1319*		19	19	11.48**
			1319**		16	16	11.48***
					13	13	
					10	10	
					6	0	
					3	299*	
					0	1137**	
					316*	1137***	
					1132**		
					1132***		

Note:

For D8A, the width profile are measured every 1 mm through the thickness from the bottom

For the remainder rolling, width profiles are measured every 7.69mm through the thickness from the bottom

* : The slab thickness (mm)

**: : Top width (mm)

*** : Bottom width (mm)

Appendix 7

Different definitions of equivalent strain accumulated along a streamline at exit to the roll bite (McLaren 1993)

Strain 1:

$$\bar{\varepsilon}_A = \sqrt{\tfrac{2}{3}}\sqrt{(\varepsilon_x - \varepsilon_y)^2 + \varepsilon_x^2 + \varepsilon_y^2 + 6\varepsilon_{xy}^2}$$

where ε_x is the strain in the rolling direction, ε_y is the strain in the thickness direction, and ε_{xy} is the shear strain on a plane containing these directions, computed with a fixed x y co-ordinate system.

Strain 2:

$$\bar{\varepsilon}_B = \sqrt{\tfrac{2}{3}}\sqrt{(\varepsilon_s - \varepsilon_n)^2 + \varepsilon_s^2 + \varepsilon_n^2 + 6\varepsilon_{sn}^2}$$

where ε_s is the strain in the rolling direction, ε_n is the strain in the thickness direction, and ε_{sn} is the shear strain on a plane containing these directions, computed with an s n co-ordinate system which rotates to maintain s parallel to, an n normal to the streamline.

Strain 3:

$$\bar{\varepsilon}_B = \sqrt{\tfrac{2}{3}}\sqrt{(\varepsilon_s - \varepsilon_n)^2 + \varepsilon_s^2 + \varepsilon_n^2 + 6|\varepsilon_{sn}|}^2$$

where $|\varepsilon_{sn}|$ is the shear strain along a streamline, accumulated irrespective of sign through the roll bite.

Strain 4:

$$\bar{\varepsilon}_D = \int\sqrt{\tfrac{2}{3}}\sqrt{\dot{\varepsilon}_x^2 + \dot{\varepsilon}_y^2 + 2\dot{\varepsilon}_{xy}^2}\,dt$$

Appendix 8

Measured microstructural gradients in Aluminium slabs

(McLaren 1994)

Annealing 426s			Annealing 787s		
Fractional Position	Recry. Fraction%	95% Conf. limit	Fractional Position	Recrys. Fraction%	95% Conf. Limit
0	10.7	±2.2	0	31.8	±3.2
0.2	12.8	±2.3	0.2	31.2	±3.2
0.4	11.4	±2.2	0.4	32.4	±3.2
0.6	15.9	±2.5	0.6	34.5	±3.3
0.8	15.1	±2.5	0.8	32.1	±3.2
0.9	8.8	±2.0	0.9	28.3	±3.1
0.95	2.3	±1.2	0.95	12.7	±2.9

Appendix 9

The selection of constitutive equation

This work on finite element analysis commenced in January 2000. At that time, the Norton-Hoff law was the only available constitutive equation. However, the author had the constitutive equation expressed by the hyperbolic sinh function. To use FORGE3®,the hyperbolic sinh function was utilised to regress into the Norton-Hoff law excluding the strain hardening term. All analyses in sections 4.2, 4.3, 4.4 and 4.5 were carried out by the use of the Norton-Hoff law without the strain hardening term.

Since the virtual manufacturing group at Bournemouth University bought the FORTRAN program, **Compaq Visual Fortran 6**, in June 2000, the second development on FORGE2/3® became possible. The hyperbolic sinh function was added into FORGE2/3®. In order to compare the difference between the hyperbolic sinh function and the Norton-Hoff law regressed from the hyperbolic sinh function, work in section 4.1 was carried out. It was found that the hyperbolic sinh function gives slightly better results that the Norton-Hoff law does. Hence the hyperbolic sinh function was adopted in the following analyses, such as those in section 4.6 and 4.7, and chapter 5 and Chapter 6.

When this thesis was completed, new versions of FORGE2/3® were launched. A new material database, "FPD-Base", is enclosed with the new versions. A new constitutive equation, the Hansel & Spittle's model, was made available for various aluminium alloys. In order to study the influence of strain hardening ((elastic deformation) on the computed rolling load and temperature, some two dimensional analyses were conducted by the use of the Hansel & Spittle's model, the Norton-Hoff law and the hyperbolic sinh function. These results are then analysed and compared. To keep the structural consistency of the original thesis, section 4.1 was rewritten in the form of a short communication and put independently. It should be noted that there are still some minor problems in this communication, such as the time difference in attaining the steady state for the different constitutive models. The present author has referred this problem to the developer, TRANSVALOR. A satisfied reply has not been received.

The Influence Of the Constitutive Equation On Finite Element Analysis

X.Duan and T.Sheppard
DEC, Bournemouth University, Studland House, Bournemouth, BH1 3NA, UK

Abstract: In this short communication, the differences of three commonly used constitutive equations (the Norton-Hoff law, the hyperbolic sine function and Hansel & Spittel's model) are compared with respect to changes of temperature and strain rate. Applying these three equations into a commercial FEM program—FORGE2®, the predicted rolling load and temperature in hot flat rolling are compared with experimental measurements. The differences between these three equations when incorporated into the FEM code, are analysed with respect to the fundamental laws, governing the performance of discretisation in the FEM code. The effect of the derivative of the flow stress with the equivalent strain rate is emphasised.

1. Introduction

The research focus in the simulation of hot flat rolling has progressed from the prediction of load and torque to the modelling of microstructure evolution. Previous work shows that temperature plays a more important role in the development of final microstructure than any other plastomechanical parameters, such as strain, strain rate and stress. In most rolling experiments, the measurement of the microstructure has been carried out at the stock centre where plane strain deformation prevails. The finite element method (FEM) technique for two-dimensional (including axisymmetric) problems has reached a mature stage. The analysis errors caused by the inaccuracy of the input physical data now become a major factor. One of the most important physical parameters is the material flow stress. Three constitutive equations, the Norton Hoff law, The hyperbolic sine function and the Hansel & Spittle's model, have usually been adopted in the simulation of hot flat rolling [1-3]. It would be useful to determine the most suitable equation for aluminium alloys in the simulation under hot working condition. In this communication, these questions, which are of concerned to FEM analysts, are answered. A commercial FEM program, FORGE2®, is run for two hot flat rolling processes. The computed rolling load and temperature are then compared with experimental measurements.

2. Constitutive equations

The exponential form of Norton-Hoff law used in FORGE2® is written as:

$$\bar{\sigma} = K \cdot \exp(\beta T) \cdot \dot{\bar{\varepsilon}}^{m} \cdot (\bar{\varepsilon} + \bar{\varepsilon}_0)^{n} \tag{1}$$

where K, β are material constants, m is the strain rate sensitively index, n is the strain-hardening index, $\bar{\varepsilon}$ is the equivalent strain, $\dot{\bar{\varepsilon}}$ is the equivalent strain rate, $\bar{\varepsilon}_0$ is a small constant. For Aluminium alloy AA5083, K=2160.29 Mpa, β=-0.00524, m=0.0198, n=0.11.

The hyperbolic sine function can be written:

$$\bar{\sigma} = \frac{1}{\alpha} Ln\left\{\left(\frac{Z}{A}\right)^{1/n} + \sqrt{\left(\frac{Z}{A}\right)^{2/n} + 1}\right\} \tag{2}$$

A, α ,n are constants. Their physical interpretations are given in the literature [4]. Z is termed the temperature compensated strain rate, with a definition as $Z = \dot{\bar{\varepsilon}} \exp\left(\frac{Q_{def}}{GT}\right)$, where Q_{def} is the

activation energy for deformation, G is the universal gas constant. For aluminium alloy AA5083, Q_{def} =145101 kJ/mol, A=1.02E10, α=0.014, n=3.65.

The Hansel & Spittle's model is expressed:

$$\overline{\sigma} = Ae^{m_1 T}\overline{\varepsilon}^{m_2}\dot{\overline{\varepsilon}}^{m_3}e^{m_4/\overline{\varepsilon}} \tag{3}$$

A, m_1, m_2, m_3, m_4 are constant. For AA5083, there are 953.655 Mpa, -0.00524, 0.01407, 0.11 and -0.00913.

3 Finite element analysis model

In this paper, aluminium alloy AA5083 is investigated. Two single-pass rolling processes are analysed. The rolling conditions are shown in Table 1. The relative thickness reductions for these two processes are 6.7% and 48% respectively. Plane strain deformation is assumed. Due to symmetrical conditions, only the top half stock is modelled. The element sizes in the roll gap are 2.5 mm and 1.5 mm respectively. The 6-node triangle element is used.

Table 1 Rolling pass schedules

No.	Entry thickness	Exit thickness	Rolling temperature	Roll speed	Roll radius	Measured pressure
1	50mm	47.13mm	283^{0}C	10 rpm	460mm	0.879 ton/mm
2	30mm	15.6mm	485^{0}C	10 rpm	184mm	

4 Result analysis and discussion

Curves of the flow stress vs. equivalent strain under different temperature and strain rate are shown in Fig.1, in which "Hansel_283_0.81" indicates that the curve is a plot using the Hansel & Spittle's model at the rolling temperature of 283^{0}C and the strain rate of 0.81. Similarly, "Hyperbolic_485_2.45" indicates that the curve is plot by the use of the hyperbolic sine function at the rolling temperature of 485^{0}C and the strain rate of 2.45. It can be seen that there are significant differences between the Hansel & Spittle's model and the hyperbolic sine function when the equivalent strain is less than 0.1 and temperature is 283^{0}C. The difference decreases with increase of temperature. There are small differences between these three constitutive equations during steady state deformation. We would expect that the predicted results, such as the temperature history and rolling load, would show a great difference between the use of these constitutive equations at a lower temperature than at the high temperature, especially when the deformation is small.

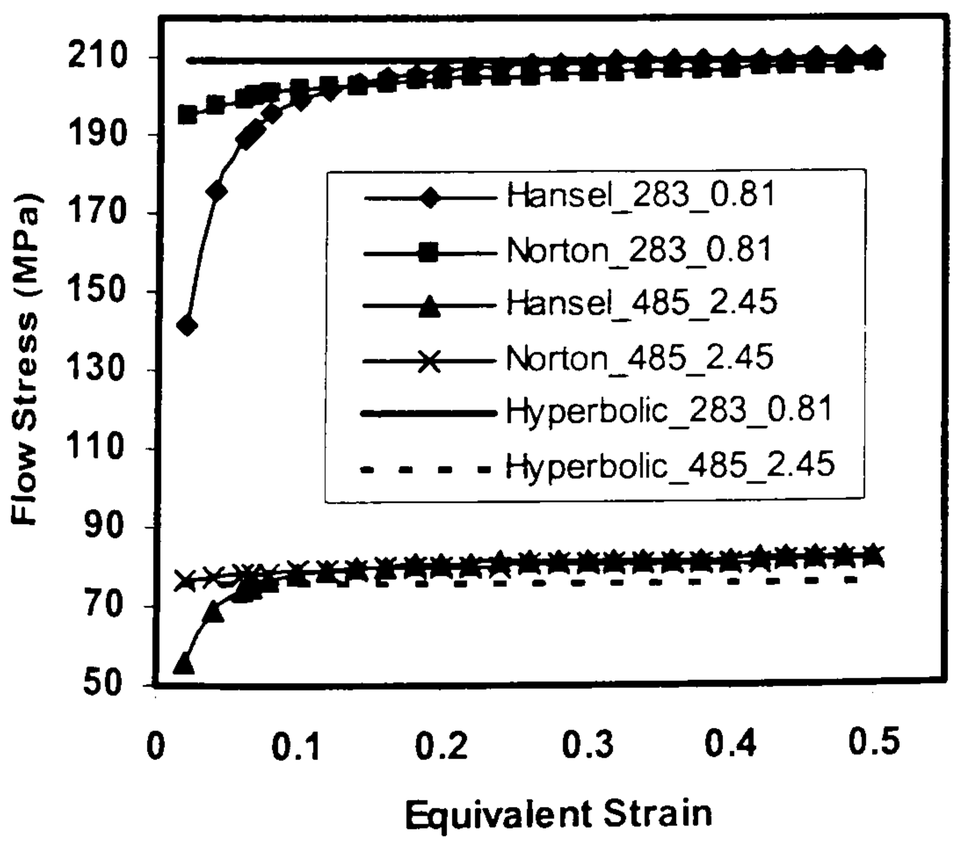

Fig.1 Curves of the flow stress vs. equivalent strain

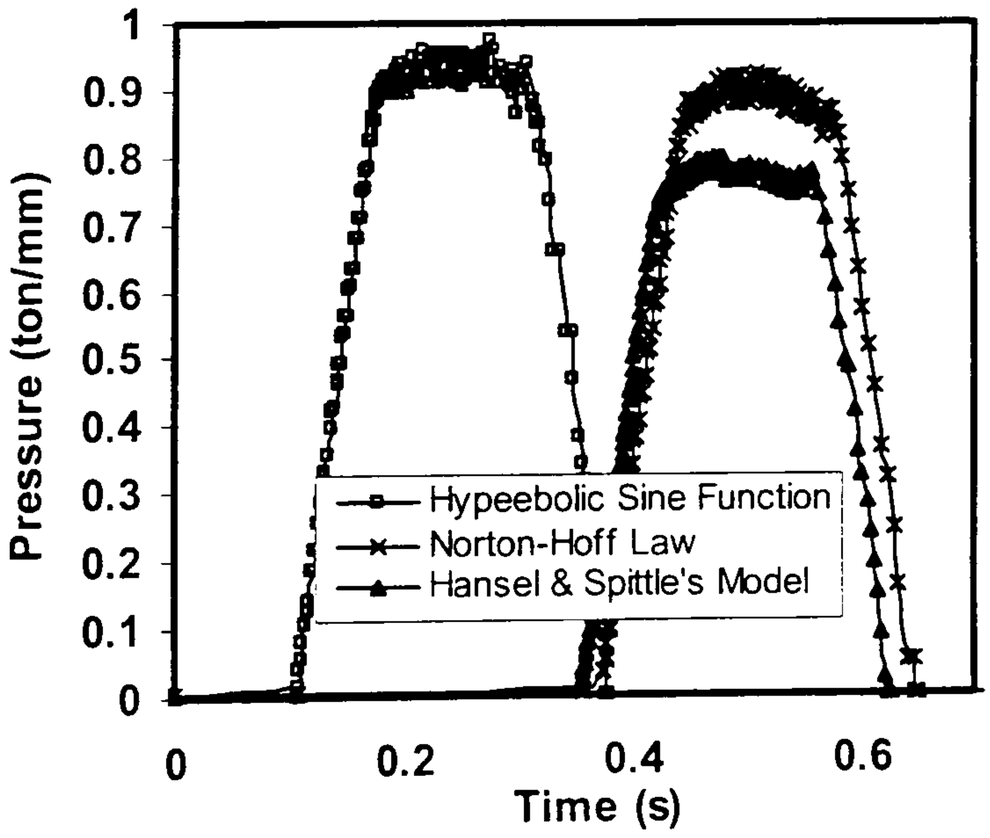

Fig.2 Comparison of the computed rolling pressure for the first pass

The critical strain to reach the steady state regime in Fig.1 is 0.26 and 0.12 for the deformation at 283^0C and 485^0C respectively. After the critical strain, the effect of work hardening balances the effect of softening, the flow stress does not change thereafter. Most aluminium alloys show a similar curve to that given by the Hansel & Spittle's model in Fig.1 [5-7]. The major difference between different Al. alloys is the value of the critical strain required to achieve a steady state deformation. The magnitude of critical strain depends mainly on the deformation conditions. The value usually varies from 0.01 during creep to less than 0.5 under hot deformation. If the flow stress still increases with increase of equivalent strain when the equivalent strain is greater than 0.5, it is usually regarded that errors have occurred in the experiment.

The predicted rolling pressures for the first rolling pass schedule is compared in Fig.2. The mean equivalent strain of this pass can be calculated by

$$\bar{\varepsilon} = \frac{2}{\sqrt{3}} \ln\left(\frac{H_0}{H_1}\right) = \frac{2}{\sqrt{3}} \ln\left(\frac{50}{47.13}\right) = 0.068 \tag{4}$$

The mean strain rate of this pass is

$$\dot{\bar{\varepsilon}} = \frac{2\pi N}{60} * \sqrt{\frac{R}{dH}} * Ln\left(\frac{H_1}{H_2}\right) = 0.81 \tag{5}$$

The measured rolling pressure during the steady state stage is 0.879 ton/mm. The predicted averaged rolling pressures are 0.897, 0.933 and 0.777 ton/mm for the Norton Hoff law, the hyperbolic sine function and Hansel & Spittle's model respectively. The relative computation errors are 2%, 6.2% and 11.5% respectively. The Norton-Hoff law gives the best fit with the measurement. It also can be seen that the hyperbolic sine function slightly overpredicts the rolling loads and the Hansel & Spittle's model underpredicts the rolling load. The answer can easily be found from the curves presented in Fig.1. In practical industrial rolling, the relative thickness reduction is usually less than 10% for the first few breakdown rolling passes. The distribution of deformation through the slab thickness is inhomogeneous. In most regions, steady state deformation is not achieved. If the hyperbolic sine function is applied, we would expect that the rolling load would be overpredicted [8]. Fig.2 also indicates that using a complicated constitutive equation as Hansel & Spittle's model does not necessarily mean that the result will be better than the use of a simple model such as the hyperbolic sine function. One obvious advantage of the hyperbolic sine function is due to its' physical background, such as the term of Q_{def}, the activation energy for the deformation.

It can be seen that there are significant differences in the time to reach the roll bite for these three constitutive equations. But, the time spending on the passage of the roll gap is the same. The reason for this phenomenon is due to the convergence problem. It should be noted that FORGE2® has been developed based on the Norton-Hoff law [9-10]. The other two constitutive equations are the later extensions.

It is understandable that there is a difference in the computed rolling load between different models. The problem is that, the difference of the computed rolling pressure between the Norton-Hoff law and Hansel & Spittle's model, see Fig.2, appears to be fairly large. Since at the nominal rolling temperature 283^0C with a strain of 0.068 and a strain rate of 0.81, two curves correspond very well (see Fig.1). The difference between the two flow stress curves is 3.94%. However, the computed rolling pressure difference by the use of these two models is 9.5%. The reason could be attributed to the derivative of the flow stress vs. strain rate. To have a clear understand of how the flow stress function affects the computed results, it will be useful to briefly review the fundamental formulae of the rigid-viscoplastic finite element method [11].

For rigid-viscoplastic materials, the following functional exists:

$$\pi = \int_V E(\dot{\varepsilon}_{ij})dV - \int_{sF} F_i u_i dS \tag{6}$$

The first order of variation of above functional is:

$$\delta\pi = \int_V \overline{\sigma}\delta\dot{\overline{\varepsilon}}dV - \int_{SF} F_i \delta u_i dS = 0 \tag{7}$$

Where $\overline{\sigma} = \overline{\sigma}\left(\overline{\varepsilon}, \dot{\overline{\varepsilon}}\right)$. The incompressibility constraint on admissible velocity fields in equation (7) is removed by using the penalised form of the incompressibility as

$$\delta\pi = \int_V \overline{\sigma}\delta\dot{\overline{\varepsilon}}dV + K\int_V \dot{\varepsilon}_V \delta\dot{\varepsilon}_V dV - \int_{S_F} F_i \delta u_{idS} = 0 \tag{8}$$

from the arbitrariness of δV_I, a set of algebraic equations (stiffness equations) are obtained as

$$\frac{\partial\pi}{\partial V_I} = \sum_j \left(\frac{\partial\pi}{\partial V_I}\right)_{(j)} = 0 \tag{9}$$

Linearising Eq. (9) by Taylor expansion near an assumed solution point $\mathbf{V} = \mathbf{V}_0$, namely

$$\left[\frac{\partial\pi}{\partial V_I}\right]_{V=V_0} + \left[\frac{\partial^2\pi}{\partial V_I \partial V_J}\right]_{V=V_0} \Delta V_J = 0 \tag{10}$$

The first term of Eq. (10) are expressed as

$$\frac{\partial\pi}{\partial V_I} = \int_V \frac{\overline{\sigma}}{\dot{\overline{\varepsilon}}} P_{IJ} V_J dV + \int_V KC_J V_J C_I dV - \int_{S_F} F_j N_{jI} dS \tag{11}$$

The second derivatives of π are expressed as

$$\frac{\partial^2\pi}{\partial V_I \partial V_J} = \int_V \frac{\overline{\sigma}}{\dot{\overline{\varepsilon}}} P_{IJ} dV + \int_V \left(\frac{1}{\dot{\overline{\varepsilon}}}\frac{\partial\overline{\sigma}}{\partial\dot{\overline{\varepsilon}}} - \frac{\overline{\sigma}}{\dot{\overline{\varepsilon}}^2}\right)\frac{1}{\dot{\overline{\varepsilon}}} P_{IK} V_K V_M P_{MJ} dV + \int_V KC_J C_I dV \tag{12}$$

The term $\overline{\sigma}$ and $\frac{\partial\overline{\sigma}}{\partial\dot{\overline{\varepsilon}}}$ are involved in equation (12). The influence of different flow stress functions on the computed results thus depends both the flow stress and it's derivative.

For the hyperbolic sine function, the derivative of the flow stress with the equivalent strain rate is obtained as

$$\frac{\partial\overline{\sigma}}{\partial\dot{\overline{\varepsilon}}} = \exp\left(\frac{\Delta H}{RT}\right) \cdot \frac{1}{\alpha \cdot n \cdot A \cdot \left[\sinh(\alpha\overline{\sigma})\right]^{n-1} \cdot \cosh(\alpha\overline{\sigma})} = \frac{\tanh(\alpha\overline{\sigma})}{\alpha \cdot n \cdot \dot{\overline{\varepsilon}}} \tag{13}$$

and the Norton-Hoff law

$$\frac{\partial\overline{\sigma}}{\partial\dot{\overline{\varepsilon}}} = \overline{\sigma} \cdot m / \dot{\overline{\varepsilon}} \tag{14}$$

For Hansel & Spittle's model, we note that

$$\frac{\partial\overline{\sigma}}{\partial\dot{\overline{\varepsilon}}} = \overline{\sigma} \cdot m_3 / \dot{\overline{\varepsilon}} \tag{15}$$

Fig.3 compares the derivative of flow stress vs. temperature based on the equation (13), (14) and (15) under different temperature and strain rate conditions. There does exist a significant difference among three different models especially between the hyperbolic sine function (without strain hardening term) and the Hansel & Spittle's model or the Norton-Hoff law (including the strain hardening term). Sensitivity analysis on the mesh size was also conducted. The element size in the roll gap is reduced from 2.5mm to 1.5mm. The computed pressure histories remain the same for the three constitutive equations.

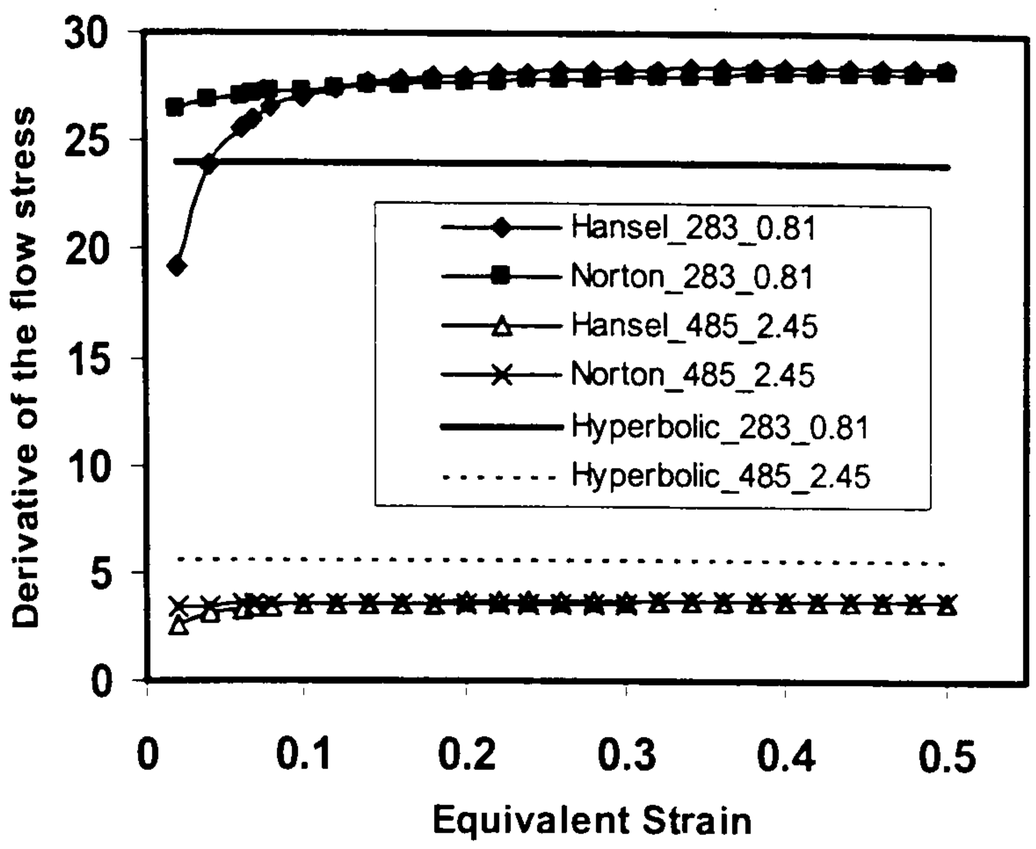

Fig.3 Comparison of the derivative of flow stress vs. equivalent strain

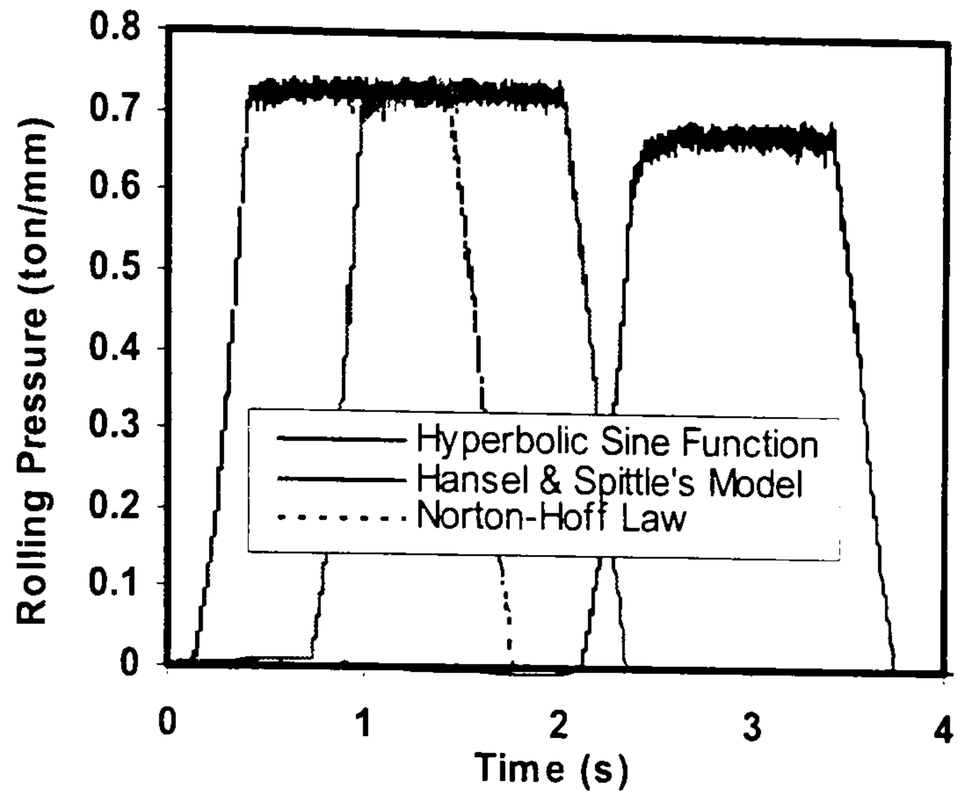

Fig.4 Comparison of the computed rolling pressure for the second rolling pass

For the second rolling pass schedule, the mean equivalent strain is

$$\bar{\varepsilon} = \frac{2}{\sqrt{3}} \ln\left(\frac{H_0}{H_1}\right) = \frac{2}{\sqrt{3}} \ln\left(\frac{30}{15.6}\right) = 0.755 \tag{16}$$

The mean strain rate of this pass is

$$\dot{\bar{\varepsilon}} = \frac{2\pi N}{60} * \sqrt{\frac{R}{dH}} * Ln\left(\frac{H_1}{H_2}\right) = 2.45 \tag{17}$$

Obviously, steady state deformation is achieved. Under such rolling conditions, three models correspond very well (see Fig.1). Comparison of the computed rolling pressures is shown in Fig.4. No measurement on the rolling pressure was conducted. The Hansel & Spittle's model gives nearly the same averaged rolling pressure, 0.727 ton/mm, as the Norton-Hoff law. The hyperbolic sine function predicts a lower value, 0.677 ton/mm. A significant difference also exists in terms of the time to reach and leave the roll gap. It should be noted that, with exception of the constitutive equation, all simulation parameters, such as the mesh size, die setup, friction law and the friction coefficient, and the heat transfer coefficient are the same for three models.

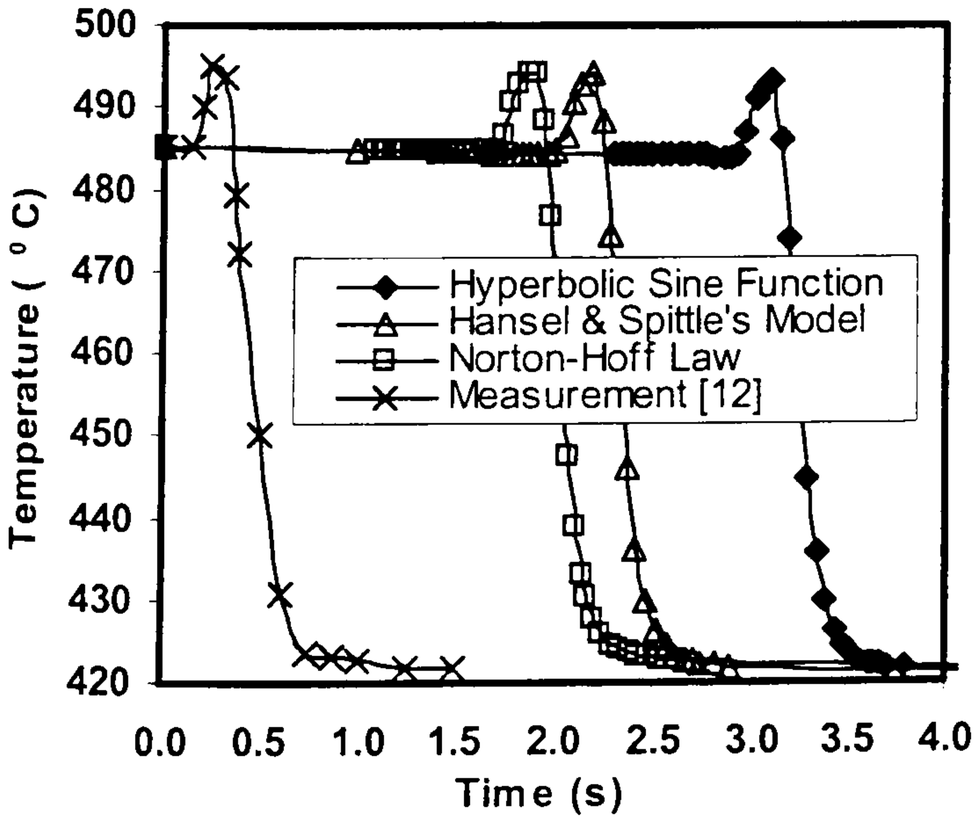

Fig.5 Comparison of the computed centre temperature histories for the second rolling pass

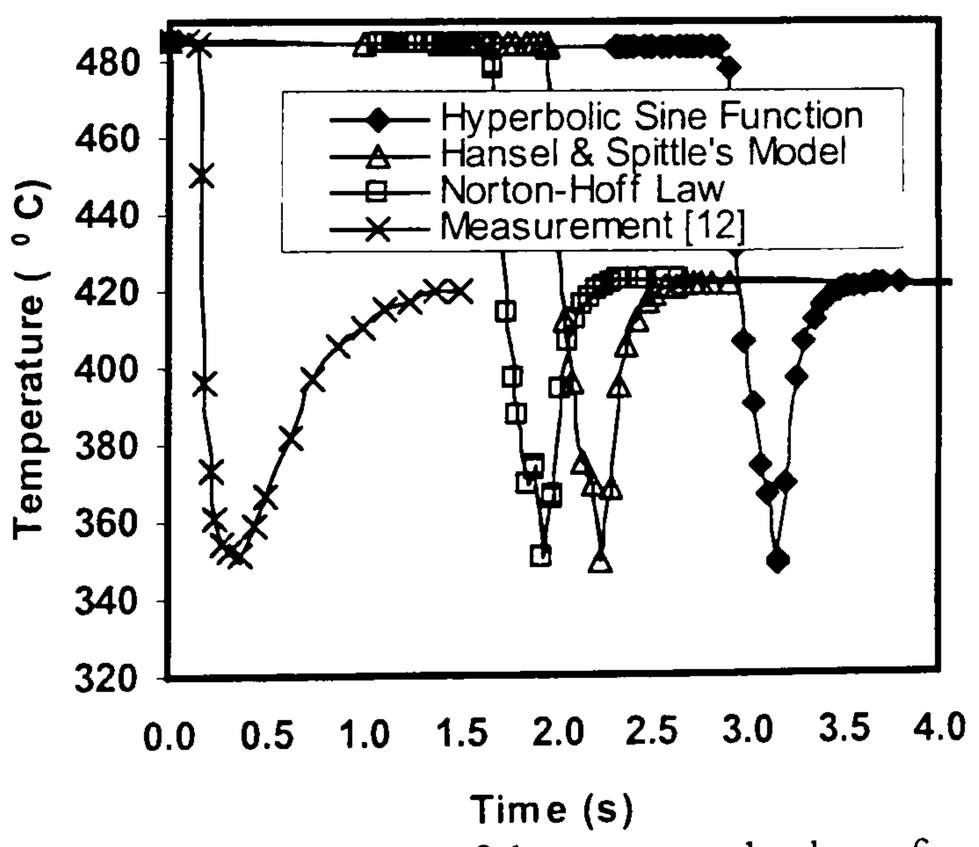

Fig.6 Comparison of the computed sub-surface temperature histories for the second pass

The predicted temperature histories are compared with the experimental measurements [12] in Fig.5 and Fig.6. Surprisingly, three models give nearly identical curve shape for both the centre and the sub-surface point. They just differ in the time taken to reach the roll bite. It should be noted that the present authors do not know the initial position of the measured points. The tracing points in FEM computation are initially located at the half-stock length. This indicates that, unlike rolling pressure, temperature is not sensitive to the constitutive equation. It is clear that an excellent agreement with the measurement has been given for three models. The heat transfer coefficient at the roll contact is set to 25 $kWm^{-2}K^{-1}$ and the free surface is set to 0.01 $kWm^{-2}K^{-1}$.

4. Conclusion

1. The selection of the constitutive equation should consider the actual deformation condition. The critical strain is an important criterion. For the small deformation, the choice of the hyperbolic sine function tends to overpredict the rolling load. The difference between the three models is negligible for the large deformation under which the steady state deformation is usually achieved.
2. The influence of different flow stress functions is introduced into the finite element analysis results, not only by the flow stress computation, but also by the derivative of the flow stress with strain rate.
3. Unlike rolling load, temperature is not sensitive to the change of constitutive equation.

Reference

1. J.L. Chenot and M. Bellet. In: Hartley P., Pillinger I. & Sturgess C.(editors). Numerical modelling of material deformation processes, Research, development and applications. 1992, London. Springer Verlag, 179-224.
2. M.A. Wells et al. Metallurgical and materials transactions B. v29B (1998), 709-719.
3. M. S. Mirza et al. Materials science and technology. 17 (2001), 874-879.
4. T. Sheppard. Extrusion of aluminium alloys. Kluwer Academic Publishers, Boston U.S.A., Dordrecht, The Netherlands1999, ISBN 0412590700.
5. K. Karhausen et al. In: J.H. Beynon et al.(editors). Modelling of metal rolling processes 3. London, 1999. 300-309.
6. J.H. Shi et al. Materials science and technology. 13, (1997), 200-216.
7. Eli S. Puchi et al. 1998. In: T. Sao et al. (editors). Sixth International conference on Aluminium alloys, Toyohashi, Japan, July 1998, 395-400.
8. X. Duan and T. Sheppard. Three dimensional thermal mechanical coupled simulation during hot rolling of aluminium alloy 3003. International Journal of Mechanical Sciences (To be published).
9. Raj Hans. et al. Engineering Computations. V9, n5, (1992), 575-586.
10. Y. Germain et al. Structural Analysis Systems: Software - Hardware - Capability - Compatibility - Applications. Volume 4: CAD/CAM & Structural Analysis in Industry, Proceedings of the SAS World Conference
11. Shiro Kobayashi, Soo-Ik Oh, Taylan Altan. Metal forming and the finite element method. Oxford university press,1989.
12. H.L. Yiu et al. The use of plane-strain compression testing to simulate the evolution of hot-rolled microstructures in aluminium alloys. In: T.G. Langdon et al (editors). Hot deformation of aluminum alloys. Proceedings of a symposium by the non-ferrous metals committee of the minerals, metals and materials society, Detroit, Michigan, October 8-10, 1990. 509-525.

Reference

Aretz, H. et al. 2000. Integration of physical based models into FEM and application in simulation of metal forming processes. Modelling Simul.Mater.Sci.Eng. 8, 881-891.

Attack, P.A. et al. 1996. Control of thermal camber by spray cooling when hot rolling aluminium. Ironmaking and steelingmaking. 23(1), 69-73.

Attack P.A et al. 1988. An adaptive scheduling and control system for a single stand reversing mill for hot rolling of aluminium. Proceedings of the Aluminium Association Rolling Mill Gauge, Shape and Profile Control Seminar, Atlanta, Georgia, USA, June 8 - 9 1988.

Atack, P.A. and Robinson, I.S.1990. Adaptation of hot mill process models. Journal of materials processing technology. 60, 535-542.

Backofen, W.A. 1972. Deformation processing. Addison-Wesley publishing company.

Barnes, Howard R. et al. 1996. Aluminium flat products –plant technology and future trends. MPT international. 6, 50-59.

Baxter, G. J. et al. 1998. Effect of magnesium content on hot deformation and subsequent recrystallisation behaviour of aluminium-magnesium alloys. In: Sao T.et al. (editors). Sixth International conference on Aluminium alloys, Toyohashi, Japan, July 1998, 1233-1238.

Baxter, G. J et al. 1999. The influence of transient strain-rate deformation conditions on the deformed microstructure of aluminium alloy Al-1%Mg. Acta material. 47(5), 2367-2376.

Behrens, A. et al. 1999. Assessment of deformation sequences using damage mechanics in cold metal forging. In: Geiger, M. (editor). Advanced technology of plasticity 99: Proceedings of the 6th ICTP, 19-24 Sept. 1999. Springer-Verlag, New York, 1999. 2311-2316.

Bertrand-Corsini C. et al. 1988. A three dimensional thermomechanical analysis of steady state flows in hot forming processes. Application to hot flat rolling and hot shape rolling. Modelling of metal forming processes. In: Chenot, J.L.and Onate, E. (editors). Modelling of metal forming processes, 1988. Kluwer academic publishers, 271-279.

Black, M.P. et al. 2001. Effect of strain path on recrystallisation kinetics during hot rolling of Al-Mn. Materials science and technology. 17, 1055-1060.

Bramely, A.N. and Mynors, D.J. 1999. The use of forging simulation tools. In: Geiger, M. (editor). Advanced technology of plasticity 99: Proceedings of the 6th ICTP, 19-24 Sept. 1999. Springer-Verlag, New York, 1999, 1583-1596.

Bryant, G.F. and Heselton, M.O. 1982. Roll gap temperature models for hot mills. Metals Technology, 9(12), 469-477.

Bünten, R. and Karhausen, K. 1999. Modelling of Al-rolling processes involving through thickness plastic inhomogeneities. In: Beynon, J.H. et al.(editors). Modelling of metal rolling processes 3. London, 1999, 323-332.

Carslaw, H.S.and Jaeger, J.C. 1959. Conduction of heat in solids. OUP, 88.

Chen, B.K.et al. 1990. Simulation of evolution of microstructure in a thermo-mechanical analysis of the hot rolling of aluminium. International journal of structural mechanics and materials science. 31(4), 455-469.

Chen, B.K., Thomon, P.F. and Choi, S.K. 1992a. Temperature distribution in the roll gap during hot flat rolling. Journal of Materials Processing Technology. 30, 115-130.

Chen, B.K., Thomon, P.F. and Choi, S.K. 1992b. Computed modelling of microstructure during hot flat rolling of aluminium. Materials science and Technology. 8, 72-77.

Chenot. J.L.and Bellet, M. 1992. The viscoplastic approach for the finite element modelling of metal-forming processes. In: Hartley P., Pillinger I. & Sturgess C.(editors). Numerical modelling of material deformation processes, Research, development and applications. 1992, London. Springer Verlag, 179-224.

Chenot, J.-L. et al. 1998. FORGE3®-a general tool for practical optimization of forging sequence of complex three-dimensional parts in industry. International conference on forging and related technology (ICFT'98), 27-28, April, 1998. Professional Engineering Publishing, Suffolk, UK, 113-122.

Chenot, J.-L. et al. 1999. Practical simulation of forging sequence of complex 3-D parts in industry. In: Geiger, M. (editor). Advanced technology of plasticity 99: Proceedings of the 6th ICTP, 19-24 Sept. 1999. Springer-Verlag, New York, 1999.1597-1612.

Chiou, Jen-Ming. 1996. A study of ductile damage in metal forming. PhD thesis, The University of Birmingham.

Chung, S.H.and Hwang, S.M.. 1999. An integrated finite element computer simulator for the prediction of the strip profile in cold strip rolling. In: Beynon, J.H. et al.(editors). Modelling of metal rolling processes 3. London, 1999, 343-349.

Chung, W.K; Choi, S.K.; and Thomson, P.F. 1993. Three-dimensional simulation of the edge rolling process by the explicit finite-element method. Journal of material processing technology. 38(1-2), 85-102.

Compaq computer corporation. 1999. Compaq Fortran languange reference manual.

Cotner, J.R. and McG, W.J. 1969. Tegart. High-temperature deformation of aluminium-Magnesium alloys at high strain rates. Journal of institute of metals. 97, 73-79.

Czlapinski Witold et al. 1989. Optimization strategy and model forming for heavy plate rolling. Metallurgical plant and technology. 12(1), 44-53.

Dashwood, R.J. et al. 1996. Computer prediction of extrusion limit diagrams. Proceedings 5th international aluminium extrusion technology seminar. Chicago, USA, 1996, 331-339.

Dauda,T.A. and Mclaren A.J. 1999. Simulation of single-pass hot flat rolling of Al-3%Mg using the finite element method and the kinetics of static recrystallisation. In: Beynon, J.H. et al.(editors). Modelling of metal rolling processes 3. London, 1999, 257-266.

Davies, Chris H.J. 2000. The cellular automaton simulation of microstructural evolution during deformation processing of metals. Materials research society symposium-proceedings. 578, 457-468.

Dean, T.A.and Hu, Z.M. 1999. The increasing requirements on empirical data for use in metal forming process simulation packages. In: Geiger, M. (editor). Advanced technology of plasticity 99: Proceedings of the 6th ICTP, 19-24 Sept. 1999. Springer-Verlag, New York, 1999. 542-550.

Edberg, Jonas. 1992. Three dimensional simulation of plate rolling using different friction models. In: Chenot, Wood & Zienkiewicz (editors). Numerical methods in industrial forming processes, 1992, Balkema, Rotterdam. 713-718.

Engler, Olaf et al. 1996. Influence of deformation temperature and strain rate on the recrystallization nucleation in Al-Mn1-Mg1. Zeitschrift fur Metallkunde. 87 (6), 454-464.

Furu, T. et al. 1996. Physical-based modelling of strength, microstructure and recrystallisation during thermomechanical processing of Al-Mg alloys. Materials science Forum. 217-222, 453-458.

Furu, T. et al. 1999. The influence of transient deformation condition on recrystallization during thermomechanical processing of an Al-1%Mg alloy. Acta material. 47(5), 2377-2389.

Gelin, J.C. et al. 1993. Identification and modelling of constitutive equations for hot rolling of aluminium alloys from the plane strain compression test. Proceedings of 1st international conference on modelling of metal rolling processes, 21-23, Sep, 1993, Imperial college, London, UK.

Grosman Franciszek. 1997. Criteria flow stress function choice for numerical simulation of plastic forming processes. In: Chandra T. and Sakai T. (editors). Proc. Intern. Conf. On Thermomechanical Processing of Steels and Other Materials (THERMEC'97), 1997, The Minerals, Metals and Materials Society, 2047-2052.

Gutierrez, I. et al. 1988. Static recrystallization of commercial purity aluminium after hot deformation within the steady state regime. Materials science and engineering A. 102, 77-84.

Hand, R.J. et al. 2000. Temperature changes during hot plane strain compression testing. Materials science and technology. 16, 442-450.

Hansen, Niels and Jensen, D.Juul. 1990. Mechanisms of deformation, recovery and recrystallisation of aluminium. In: Langdon, T.G. et al (editors). Hot deformation of aluminum alloys. Proceedings of a symposium by the non-ferrous metals committee of the minerals, metals and materials society, Detroit, Michigan, October 8-10, 1990. 3-19.

Hartley, P. et al. 1993. Numerical modelling of rolling processes. In: Wang, Z.R. (editors). Proceeding of the fourth international conference on technology of plasticity, September, Beijing. Academic publisher, 742-747.

Hartley, P. et al. 1997. Elastic plastic finite element modelling of metal forming with damage evolution. In: Predeleanu, M. and Gilormini, P.(editors). Advanced methods in materials processing defects, 1997. Elsevier science, 136-143.

Hollinshead, P.A. 1986. Texture and mechanical property developments in aluminium alloy hot rolling. Ph.D. thesis, University of London.

Helmi, A. and Alexander J.M. 1968. Geometric factors affecting spread in hot flat rolling of steel. Journal of the iron and steel institute. 206, 1110-1117.

Holt, David L. 1970. Dislocation cell formation in metals. Journal of applied physics. 41(8), 3197-3201.

Hosford, William F. and Caddell, Robert M. 1982. Metal forming: mechanics and metallurgy. Prentice-hall, Inc., Englewood Cliffs, N.J.

Hughes, D. A. et al. 1998. Metal forming at the center of excellence for the synthesis and processing of advanced materials. JOM, 50(6), 16-21.

Hum, B. et al. 1996. Measurements of friction during hot rolling of aluminium strips. Journal of materials processing technology. 60, 331-338.

Immarigeon, J. P. and McQueen, H. J. 1968. Dynamic recovery of aluminium during hot rolling. Canadian metallurgical quarterly. 8(1), 25-34.

Jonas, J.J. et al. 1969. Strength and structure under hot-working conditions. Metallurgical reviews. 14, 1-24.

Karhausen K. et al. 1999. Determination of constitutive equations for the hot rolling of Al-alloys by combinatoric optimisation methods. In: Beynon, J.H. et al.(editors). Modelling of metal rolling processes 3. London, 1999. 300-309.

Kim, Hyunkee et al. 1995. Prediction and elimination of ductile fracture in cold forgings using FEM simulations. Transactions of NAMRI/SME, Volume XXVIII, 63-69.

Knustad, O. et al. 1985. Polarized light observation of grain extension and subgrain formation in aluminium deformed at 400^0C to very gigh strains. Praktische metallographie, 22(5), 219-229.

Kobayashi, Shiro; Oh, Soo-Ik and Altan, Taylan. 1989. Metal forming and the finite element method. London, Oxford university press.

Lalli, L.A. 1984. An analytical rolling model including through thickness shear stress distributions. Journal of engineering materials and technology, 106 (1), 1-8.

Larke, Eustace C. 1957. The rolling of strip, sheet and plate. Chapman and hall ltd.

Lehert, W. et al. 1996. Experimental and mathematical simulation of microstructural evolution during hot rolling of Al and Cu material. Journal of materials processing technology, 60, 567-574.

Lehert, W. et al. 1999. Deformation behaviour and microstructure properties evolution during hot and cold strip rolling aluminium alloys. In: Geiger, M. (editor).

Advanced technology of plasticity 99: Proceedings of the 6th ICTP, 19-24 Sept. 1999. Springer-Verlag, New York, 1999. 1941-1948.

Lehert, W. et al. 1999. Hot rolling in the process of thermomechanical treatment. In: Geiger, M. (editor). Advanced technology of plasticity 99: Proceedings of the 6th ICTP, 19-24 Sept. 1999. Springer-Verlag, New York, 1999. 1957-1966.

Lekhov, O. S. et al. 1987. Optimisation of basic parameters of rolling complex for production of billets. Steel in the USSR. 17 (2), 78-80.

Lenard, J.G. and Pietrzyk, M. 1992. Rolling process modelling. In: Hartley P., Pillinger I. & Sturgess C.(editors). Numerical modelling of material deformation processes, Research, development and applications. 1992, London. Springer Verlag, 275-303.

Lenard, J.G., Pietrzyk, M. and Cser, L. 1999. Mathematical and physical simulation of the properties of hot rolled products. Elsevier science.

Li, Guo-Ji; Kobayashi, Shiro. 1984. Analysis of spread in rolling by the rigid-plastic, finite element method. Numer Anal of Form Processes. 71-88

Liserre, G. et al. 1998. Contribution to the modelling of microstructure evolution during thermomechanical processing of commercial purity aluminium. In: Sao T.et al. (editors). Sixth International conference on Aluminium alloys, Toyohashi, Japan, July 1998, 395-400.

Liu, C. et al. 1987. Finite element modelling of deformation and spread in slab rolling. International Journal of mechanics science. 29(4), 271-283.

Lubrano, M. and Bianchi, J.H. 1996. A simple model for on-line control of skin pass from finite element analysis of rolling deformation. 2nd Int. Conf. NMRP. The IOM. London. 574-583.

Luce, R. et al. 1999. Microstructure multipass rolling simulation using physical models integrated into FEM. In: Beynon, J.H. et al.(editors). Modelling of metal rolling processes 3. London, 1999, 218-226.

Macgregor, C.W. and Palme, R.B. 1951. The distribution of contact pressures in the rolling of metals. Trans.ASME(J.Basic Eng.). 81, 669-679.

Mäntylä, P. et al. 1992. Improved thickness and shape accuracy with advanced pass scheduling in plate rolling. Journal of materials processing technology, 32, 255-263.

Marthinsen, K. and Nes, E. 2001. Modelling strain hardening and steady state deformation of Al-Mg alloys. Materials science and technology. 17, 376-388.

McLaren, A.J. 1994. Modelling of thermomechanical processing of metals. PhD thesis, University of Sheffield.

McQueen, H.J. and K. Conrod. 1985. Recovery and recrystallization in the hot-working of aluminium alloys. In: Chia, E. Henry and McQueen, H. J. (editor). Microstructural control in aluminium alloys: deformation, recovery and recrystallization. New York, 27 Feb. 1985. New York, The metallurgical society, Inc., 197-219.

McQueen, H.J. and W. Blum. 1998. Recovery and recrystallization in AL alloys fundamentals and practical applications. In: Sao T.et al. (editors). Sixth International conference on Aluminium alloys, Toyohashi, Japan, July 1998, 99-112.

Mirza, M.S. et al. 2001. Multipass rolling of aluminium alloys: finite element simulations and microstructural evolution. Materials science and technology. 17, 874-879.

Nes, E. et al. 1994. Physical modelling of microstructural evolution during thermomechanical processing of aluminium alloys. In: Sanders, T. and Starke, E.A. (eds). Aluminium alloys physical and mechanical properties (ICCA4), Altanta, 1994, 250-257.

Nes, E. 1998. Modelling of work hardening and stress saturation in FCC metals. Progress in materials science. 41, 129-193.

Nieth, T.G. et al. 1997. Subgrain formation and evolution during the deformation of an Al-Mg-Sc alloy at elevated temperatures. Scripta material. 36(9), 1011-1016.

Nord-Varhaug K. et al. 2000. Substructure strengthening in aluminium alloys. Material science forum. 331-337, 1387-1392.

Orsetti Rossi, P.L. and Sellars, C.M. 1996. Static recrystallisation of Al-1Mg during thermomechanical processing. Materials science forum. 217-222, 379-384.

Parker, B.A. and Lim, Jangho. 1996. Microstructure development during the deformation of aluminium-magnesium alloys. Journal of materials processing technology. 60, 563-566.

Pietrzyyk, M. et al. 1992. Finite element simulation of mechanical, thermal and structural phenomena in the hot rolling process. In: Chenot, Wood & Zienkiewicz (editors). Numerical methods in industrial forming processes, 1992, Balkema, Rotterdam. 749-754.

Pinna, C. et al. 1999. Modelling of the effect of lubrication on texture evolution during hot rolling. In: Beynon, J.H. et al.(editors). Modelling of metal rolling processes 3. London, 1999, 237-246.

Poschmann, I. and McQueen, H.J. 1995. Subgrain distributions in aluminium deformed under hot working conditions. Physica status solidi, 149, 341-348.

Postlethwaite, I. et al. 1996. The improved control for an aluminium hot reversing mill using the combination of adaptive process models and an expert system. Journal of materials processing technology. 60, 393-398.

Puchi, Eli S. et al. 1998. Analysis of a hot rolling schedule for commercial aluminium-1%magnesium alloy in terms of dynamic material modelling concepts.Part I:description of the constitutive behavior. In: Sao T.et al. (editors). Sixth International conference on Aluminium alloys, Toyohashi, Japan, July 1998, 395-400.

Raabe, Dierk and Becker, Richard C. 2000. Coupling of a crystal plasticity finite-element model with a probabilistic cellular automaton for simulating primary static recrystallization in alluminium. Modelling and simulation in materials science and engineering. 8, 445-462.

Raghunathan, N. 1986. Thermal and mechanical processing of commercial aluminium magnesium alloys. Ph.D. thesis, University of London.

Raghunathan, N. and Sheppard, T. 1989. Microstructural development during annealing of hot rolled Al-Mg alloys. Materials science and technology. 5, 542-547.

Raghunathan, N. and Sheppard, T. 1989. Evolution of structure in roll gap when rolling aluminium alloys. Materials science and technology. 5, 194-201.

Raghunathan, N. and Sheppard, T. 1989. Lateral spread during slab rolling. Materials science and technology. 5, 1021-1026.

Rebelo, N. and Kobayashi, S. 1980. Coupled analysis of viscoplastic deformation and heat transfer em dash. International Journal of Mechanical Sciences, 22(11), 699-705.

Roters, F. et al. 2000. Work hardening in heterogeneous alloys- a microstructural approach based on three internal state variable. Acta materialia, 48(17), 4181-4189.

Saito, Y. et al. 1999. Microstructure and texture control by novel rolling processes. In: Geiger, M. (editor). Advanced technology of plasticity 99: Proceedings of the 6th ICTP, 19-24 Sept. 1999. Springer-Verlag, New York, 1999. 1923-1930.

Sanders, Roberts E. Jr. 2001. Technology innovation in aluminum products. JOM. 53(2), 21-25.

Schöning, K.-V., Müller, M.and Bogob, P. 1999. Simulation tools in sheet metal forming—today's possibilities, tomorrow's demands. In: Geiger, M. (editor). Advanced technology of plasticity 99: Proceedings of the 6th ICTP, 19-24 Sept. 1999. Springer-Verlag, New York, 1999. 2113-2130.

Sellars, C.M. et al. 1986. Recrystallization characteristics of aluminium-1% Magnesium under hot working conditions. In: Chia, E. Henry and McQueen, H. J. (editor). Microstructural control in aluminium alloys: deformation, recovery and recrystallization. New York, 27 Feb. 1985. New York, The metallurgical society, Inc., 179-196.

Sellars, C.M. 1986. Modelling of structural evolution during hot work processes. In: Proceedings of the 7th Riso International Symposium on Metallurgy and Materials Science, 1986, Roskilde, Den. Riso Natl Lab, 167-187.

Sellars, C.M. 1990. Modelling microstructural development during hot rolling. Materials science and technology, 6, 1072-1081.

Sellars, C.M. 1992. Modelling microstructure and its effects during multi-pass hot rolling using SLIMMER. ISIJ international, 32(3), 359-367.

Sellars, C.M. and Kawai, R. 1993. The 'phantom roll' concept for modelling temperature changes during hot rolling.In: Beynon, J.H.(editor). Modelling of metal rolling processes, Imperial college, London, 21-23 September 1993, 648-659.

Sellars, C.M. and Zhu, Q. 2000. Microstructure modelling of aluminium alloys during thermomechanical processing. Materials Science and Engineering A: Structural Materials: Properties, Microstructure and Processing. 280(1), 1-7.

Semiatin, S.L., Collings, E.W. and Altan, T. 1987. Determination of the interface heat transfer coefficient for non-isothermal bulk-forming processes. Journal of Engineering for industry, Transaction ASME. 109(1), 49-57.

Sheppard, T. and Wright, D.S. 1980. Structural and temperature variations during rolling of aluminium slabs. Metals technology, 7(7), 274-281.

Sheppard, T. and Tutcher, M.G. 1981a. Effect of process parameters on structure and properties of Al-5Mg-0.8Mn alloy (AA5456). Metals Technology. 8(8), 319-327.

Sheppard, T. and Wright, D.S. 1981b. Parameters affecting lateral deformation in slabbing mills. Metals Technology. 8(2), 46-57.

Sheppard, T. and Zaidi, M.A. 1982. Deformation during multipass rolling of commercial-purity aluminium. Metals Technology. 9(2), 52-59.

Sheppard, T. et al. 1986. Structural evolution during the rolling of aluminium alloys. In: Chia, E. Henry and McQueen, H. J. (editor). Microstructural control in aluminium alloys: deformation, recovery and recrystallization. New York, 27 Feb. 1985. New York, The metallurgical society, Inc., 19-43.

Sheppard, T. 1993a. Extrusion of AA2024 alloy. Materials science and technology. 9, 430-440.

Sheppard, T. 1993b. Extrusion limit diagrams containing structural and topological information for AA6063 aluminium alloy. Materials science and technology. 9, 313-318.

Sheppard, T. and Jackson, A. 1997. Constitutive equations for use in prediction of flow stress during extrusion of aluminium alloys. Materials science and technology, 13, 203-209.

Sheppard, T.1999. Extrusion of aluminium alloys. London, Kluwer academic publishers.

Shercliff, H.R. 1997. Modelling of materials and processes. Materials modelling and technology foresight, 1997, London.

Shi J.H. et al.1997. Constitutive equations for high temperature flow stress of aluminium alloys. Materials science and technology. 13, 200-216.

Smelser, R.E. and Thompson, E.G. 1987. Validation of flow formulation for process modelling. AMD(American society of mechanical engineers, applied mechanics division), 88, 273-282.

Sparling, L.G. 1967. Research on the rolling of metals. Journal of the junior institution of engineers. 77(11), 330-434.

Svietlichnyj, D. and Pietrzyk, M. 1999. On-line model for control of hot plate rolling. In: Beynon, J.H. et al.(editors). Modelling of metal rolling processes 3. London, 1999, 63-71.

The aluminum association. 1993. Aluminum stands and data 1993. Eleventh edition.

Thiebaut, C. and Morey, J.-M. 1996. Application of a F.E.M. code to the evaluation of the friction law of a tungsten part at high temperatures. Journal of materials processing technology, 60, 475-479.

Timothy, S.P. et al. 1991. Simulation of single pass of hot rolling deformation of aluminium alloy by plane strain compression. Materials science and technology. 7, 255-261.

Transvalor S. A. 2000. FORGE3® V5.3 user guide & reference guide. Transvalor S. A.

Tseng, T.Y. et al. 1996. Improvement of physical properties for Al-1.1%Mn alloy with Taguchi method. Material science forum, 217-222(2) 1329-1334.

Turczyn, S. 1996. The effect of the roll-gap shape factor on internal defects in rolling. Journal of materials processing technology,.60, 275-282.

Urcola, J.J. and Sellars, C.M. 1987. Influence of changing strain rate on microstructure during hot deformation. Acta matallurgical.35(11), 2649-2657.

Vatne, Hans Erik. 1995. Experimental investigations and modelling of recrystallisation in two hot deformed aluminium alloys. PhD thesis, The Norwegian Institute of Technology.

Vante, H.E. 1996. Modelling recrystallisation after hot deformation of aluminium. Acta materialia, 44(1) 4463-4473.

Vatne, Hans Erik et al. 1998. Industrial hot rolling of an AA3004 alloy; experimental investigations and modelling of recrystallisation. In: Sao T.et al. (editors). Sixth International conference on Aluminium alloys, Toyohashi, Japan, July 1998, 1263-1268.

Vatne, Hans Erik et al. 2000. Industrial verification of microstructural models for theromechanical processing by application to hot rolling of AA3104. Materials science forum, 331-337, 551-556.

Vierod, R.P. 1983. Effect of copper additions on deformation processing of aluminium alloys. PhD thesis, University of London.

Vöhringer, K.-D. 1999. Metal forming- a key technology for automobile production. In: Geiger, M. (editor). Advanced technology of plasticity 99: Proceedings of the 6th ICTP, 19-24 Sept. 1999. Springer-Verlag, New York, 1999. 3-12.

Wagoner, Robert H. and Chenot Jean-Loup. 1997. Fundamentals of metal forming. John Wiley & Sons, Inc. New York, 1997.

Wehage, Harald et al. 1998a. New trends in hot flat rolling technologies and pass schedule optimization. MPT international, 4, 60-71.

Wehage, Harald et al. 1998b. Pass schedule optimization for new hot flat rolling processes. MPT international. 5, 92-104.

Wells, M. A. 1998a. Modelling the microstructural changes during hot tandem rolling of AA5XXX aluminium alloys: Part I, Microstructural evolution. Metallurgical and Materials Transactions B. 29B, 611-620.

Wells, M. A. 1998a. Modelling the microstructural changes during hot tandem rolling of AA5XXX aluminium alloys: Part I, Textural evolution. Metallurgical and Materials Transactions B. 29B, 621-708.

Wells, M. A. 1998a. Modelling the microstructural changes during hot tandem rolling of AA5XXX aluminium alloys: Part III, Overall model development and validation. Metallurgical and Materials Transactions B. 29B, 709-719.

William Y. Fowlkes and Clyde M. Creveling. 1995. Engineering methods for robust product design using Taguchi methods in technology and product development. Addison-wesley publishing company.

Wilmotte, S.et al. 1972. Stidy of the cross-profile of hot rolled strip. Metall Rep CRM, 30, 11-28.

Winden, M.R. Van der. 1999. Laboratory simulation and modelling of the break-down rolling of AA3104. Ph.D. thesis. The university of Sheffield.

Wood, Roy. 1994. The rolling of aluminium: the process and the product. TALAT lecture 1301. Aluminium training partnership.

Wright, D.S. and Sheppard, T. 1976. Observations on the mode of deformation during aluminium slab rolling. Proc. Of Mach. Tool Des and Res Conf, **3**(17),539-548.

Wright, D.S. 1978. Lateral deformation in slabbing mills. PhD thesis, University of London.

Wusatowski, Z. 1955a. A study of draught, spread and elongation. Iron & steel. February 1955, 49-54.

Wusatowski, Z. 1955b. A study of draught, spread and elongation. Iron & steel. March 1955, 89-94.

Yamada K. et al. Three-dimensional analysis of flat rolling using rigid-plastic finite element method coupled with roll deformation analysis. In: Chenot, Wood & Zienkiewicz (editors). Numerical methods in industrial forming processes, 1992, Balkema, Rotterdam, 755-760.

Yiu, H.L. et al. 1990. The use of plane-strain compression testing to simulate the evolution of hot-rolled microstructures in aluminium alloys. In: Langdon, T.G. et al (editors). Hot deformation of aluminum alloys. Proceedings of a symposium by the non-ferrous metals committee of the minerals, metals and materials society, Detroit, Michigan, October 8-10, 1990. 509-525.

Yoon, S.G. and Kim, D.W. 1991. A study on width spread in 2-high rolling of rectangular bar. Key engineering materials. 51-52, 423-428.

Yoshimura, Koji et al. Robust design of square-to-box rolling of steels rods. American society of mechanical engineers, Design engineering division. 82(1), 415-421.

Zaidi, M.A. and Sheppard, T. 1982. Development of microstructure throughout roll gap during rolling of aluminium alloys. Metals technology. 16,229-238.

Zhu, Q. et al. 1997. Modelling hot deformation behaviour based on evolution of dislocation substructures. In: Chandra T. and Sakai T. (editors). Proc. Intern. Conf. On Thermomechanical Processing of Steels and Other Materials (THERMEC'97), 1997, The Minerals, Metals and Materials Society, 2039-2045.

Zhu, Q. and Sellars, C.M. 1998. Dislocation substructures of aluminium alloys during thermomechanical processing. In: Sao T.et al. (editors). Sixth International conference on Aluminium alloys, Toyohashi, Japan, July 1998, 523-528.

Zhu, Q. and Sellars, C.M. 2001. Effect of transient strain rate conditions on recrystallisation behaviour of high purity and commercial Al-5%Mg alloys. In: The first joint international conference on recrystallization and grain growth. August 27-31, 2001, Aachen, Germany.

Zienjiewicz, O.C. et al. 1981. General formulation for coupled thermal flow of metals using finite elements. International Journal for Numerical Methods in Engineering, 17(10), 1497-1514.